Nancy-Université
Université Henri Poincaré

AVERTISSEMENT

Ce document est le fruit d'un long travail approuvé par le jury de soutenance et mis à disposition de l'ensemble de la communauté universitaire élargie.

Il est soumis à la propriété intellectuelle de l'auteur. Ceci implique une obligation de citation et de référencement lors de l'utilisation de ce document.

D'autre part, toute contrefaçon, plagiat, reproduction illicite encourt une poursuite pénale.

➢ Contact SCD Nancy 1 : theses.sciences@scd.uhp-nancy.fr

LIENS

Code de la Propriété Intellectuelle. articles L 122. 4
Code de la Propriété Intellectuelle. articles L 335.2- L 335.10
http://www.cfcopies.com/V2/leg/leg_droi.php
http://www.culture.gouv.fr/culture/infos-pratiques/droits/protection.htm

Université Henri Poincaré - Nancy 1

Ecole doctorale EMMA - **E**nergie, **M**écanique, **Ma**tériaux
Agence **D**e l'**E**nvironnement et de la **M**aitrîse de l'**E**nergie - ADEME
Région Lorraine

THESE

présentée pour l'obtention du titre de

Docteur de l'UHP

spécialité: Mécanique et Energétique

par

Julia Mainka

Local impedance in H_2/air **P**roton **E**xchange **M**embrane **F**uel **C**ells (PEMFC)
Theoretical and experimental investigations

Impédance locale dans une pile à membrane H_2/air (PEMFC)
Etudes théoriques et expérimentales

Soutenance publique prévue le 04 juillet 2011 devant le jury constitué de:

Rapporteurs:	M. Michael Eikerling	Professeur, SFU-NRC, Burnaby, Canada
	M. Yann Bultel	Professeur, LEPMI, Grenoble
Examinateurs:	M. Frédéric Maillard	Chargé de Recherches, LEPMI, Grenoble
	M. Joachim Scholta	Directeur du département PàC, ZSW, Ulm, Allemagne
	M. Denis Kramer	Docteur-Chercheur, Imperial College London, Angleterre
	M. Philippe Guillemet	Maître de Conférences, LGPMA-Université de Nantes
	M. Olivier Lottin	Professeur, LEMTA-UHP, Nancy
	M. Gaël Maranzana	Maître de Conférences, LEMTA-UHP, Nancy
Invité:	M. Jérôme Dillet	Docteur-Ingénieur de Recherche, LEMTA-CNRS, Nancy

---

Laboratoire d'**E**nergétique et de **M**écanique **T**héorique et **A**ppliquée - LEMTA
UMR 7563 CNRS Université de Lorraine
54500 Vandoeuvre lès Nancy

Preamble

Fuel cells are electrochemical devices that convert continuously the chemical energy of reactants into electrical energy and heat. The core element of a fuel cell is an ion conducting electrolyte membrane that is sandwiched between two electrodes covered by *Gas Diffusion Layers* (GDL). This set of components forms the *Membrane Electrode Assembly* (MEA). There exist different types of fuel cells which differ in their electrolyte, in the nature of the exchanged ions and in their operating conditions. Due to their high power density when adequately hydrated (300 - 1000 mW/cm^2 [OCCP06]) and to their low operating temperature ($< 90°C$), *Proton Exchange Membrane* (PEM) fuel cells are currently the most studied fuel cell type for stationary power and transport applications. However, for a widespread deployment, several improvements have to be accomplished for lowering the fabrication cost and for increasing their reliability and durability [KL09].

Within this context, one of the main issues is the minimization of the voltage losses caused by charge and mass transfer. This is not easy to achieve, because the different transport processes (protons, electrons, reactants and products) interact with each other and require different, sometimes conflicting working conditions. A first step for reducing voltage losses, is to identify their origin, which requires *in situ* measuring techniques, as well as a detailed comprehension of the physico-chemical processes occurring inside the MEA. In addition, it has been pointed out that in most cases, the geometrical structure of the cell and the usual operating parameters lead to a non-uniform electrochemical response over the MEA surface [SSF$^+$08, YWCSZ07, SKWS07]. As a consequence, the use of segmented PEMFC has become a useful tool to investigate the cell performance locally [PBSM11, YWCSZ07, MLC$^+$08].

Electrochemical Impedance Spectroscopy (EIS) is one of the most appropriate techniques for voltage loss identification, since it is non-intrusive and can be applied *in situ* with a discrete resolution by the use of segmented cells [YWCSZ07, MLC$^+$08, PBSM11]. However, in order to discriminate between different voltage loss contributions, appropriate models are required for the interpretation of the cell impedance in terms of charge and mass transport through the different MEA components. The analysis of the cell impedance should thus allow to determine optimal operating conditions and to optimize the design of the cell components.

Fuel cell impedance spectra exhibit usually two loops in a frequency range between 10^{-3} Hz and 10^5 Hz [CR01, SZWG96, DLGM$^+$98]: one at high frequencies that is commonly attributed to charge transfer and capacitive processes in the electrodes and one at low frequencies that is usually attributed to oxygen transport through the diffusive media. However, the phenomena governing the low frequency loop are not completely elucidated yet, although it is widely accepted that the oxygen reduction reaction represents the main factor limiting the electrical efficiency of PEMFC, even in optimal conditions [EK99, KLSC95, SZWG96]. The mass transport impedance that is generally used to interpret PEMFC spectra is the one-dimensional finite Warburg element [War99]. It yields surprisingly good results in the case of gas diffusion electrodes, despite of relatively simple assumptions: one-dimensional gas transport occurring only by mono-phasic Fickian diffusion and the existence of a reaction interface. However, the catalyst layer constitutes the final

stage of oxygen transport occurring first through micro-channels and through the GDL, generally in the presence of liquid water. Furthermore, the catalytic sites are distributed through the porous electrodes, which is in contradiction with the assumption of a reaction interface. In addition, experimental investigations of Schneider *et al.* [SKWS07, SFK$^+$07] pointed out that alternating currents induce concentration oscillations that propagate along the gas channel and influence the impedance measurements downstream, especially at low frequencies. According to these studies, the low frequency loop seems to be - at least to some extent - linked to AC induced concentration oscillations that propagate down the flow field by convection, which affects the local impedance response along the electrode, and consequently the cell global impedance.

This Ph.D thesis contributes to a better understanding of the origin of the low frequency loop and presents mass transport models alternative to the Warburg element.

The first chapter is a general introduction to the operation of fuel cells and more specifically of PEMFC, where the role of the different MEA components is explained. The physical processes occurring inside the MEA are highly coupled and depend on several factors including operating conditions, geometry and presence of liquid water. Thus, chapter 2 introduces the main physical phenomena that govern the operation of PEMFC and which allow to derive a realistic impedance model. Chapter 3 focuses on EIS: the principles of this measuring technique are presented, as well as the main electrical equivalent circuits used for the interpretation of the spectra. In this context, the limits of the classical Warburg impedance are analyzed. An experimental setup is developed that allows to perform locally resolved EIS along the cathode surface. With segmented cells, we are able to analyze the local distribution of impedance parameters, especially those linked to oxygen diffusion and to put forward the limits of a one-dimensional description.

The second part of the manuscript presents several expressions of the oxygen transport impedance and their impact on the interpretation of local and global impedance spectra. In chapter 4, one-dimensional models accounting for phenomena in the direction perpendicular to the electrode that are not considered in the classical Warburg approach, are developed: the first model accounts for a possible convective flux due to vapor evacuation, and the second model, based on the work of Eikerling and Kornyshev [EK99], considers oxygen consumption and the finite proton conduction in the porous catalyst layer. In chapter 5, pseudo-2D models are developed that include oxygen depletion along the air channel in terms of DC and AC effects: the first one leads to a simple alternative expression to the classical Warburg impedance that uses oxygen consumption along the flow field as an alternative boundary condition. In the second case, based on the experimental work of Schneider *et al.* [SKWS07, SFK$^+$07], concentration oscillations propagating along the air channel are considered. Finally, experimental results are presented in chapter 6. They are compared to the numerical results obtained with the models developed in chapters 4 and 5. This makes it possible to identify the values of the impedance parameters and to draw some conclusions about the origin of the main phenomena governing the low frequency loop.

Contents

1 Introduction to Fuel Cells **1**
- 1.1 Principle of Operation . . . 1
- 1.2 Main Fuel Cell Types . . . 2
- 1.3 Thermodynamics . . . 5
  - 1.3.1 Total chemical energy and reference potential . . . 5
  - 1.3.2 Reversible cell voltage . . . 6
  - 1.3.3 Fuel cell thermodynamic efficiency . . . 7
- 1.4 Actual Fuel Cell Performance . . . 8
- 1.5 The Membrane-Electrode Assembly (MEA) . . . 10
  - 1.5.1 Polymer electrolyte membranes . . . 10
  - 1.5.2 Porous electrodes . . . 20
  - 1.5.3 Gas diffusion layers . . . 24
- 1.6 Summary . . . 27

2 Main Physical Phenomena Governing the Operation of a PEM Fuel Cell **29**
- 2.1 Description of the Reaction Kinetics . . . 29
  - 2.1.1 Electrochemical half-reactions . . . 29
  - 2.1.2 Cell potential and reaction rate: Butler-Volmer law . . . 33
- 2.2 Electrical Double Layer and Double Layer Capacity . . . 40
  - 2.2.1 Electrical double layer in the vicinity of a charged surface . . . 41
  - 2.2.2 Double layer capacity in a fuel cell . . . 48
- 2.3 Modeling of the Active Layer Structure . . . 50
  - 2.3.1 Modeling approaches of the active layer geometry . . . 51
  - 2.3.2 Parameters characterizing the electrode morphology . . . 53
- 2.4 Oxygen Transport . . . 55
  - 2.4.1 Mass fluxes . . . 55
  - 2.4.2 Mass transport mechanisms . . . 57
  - 2.4.3 Modeling the presence of liquid water . . . 66
- 2.5 Summary and Conclusions of the Chapter . . . 67

3 Electrochemical Impedance Spectroscopy in PEM Fuel Cells **69**
- 3.1 Principle of Electrochemical Impedance Spectroscopy . . . 70
  - 3.1.1 Definition of the impedance . . . 70
  - 3.1.2 General pattern of EI spectra . . . 73
  - 3.1.3 Interpretation of EI spectra by electrical analogues . . . 74
- 3.2 Analytical Expression of the Faradaic Impedance . . . 79
  - 3.2.1 Definition of the faradaic impedance . . . 79
  - 3.2.2 1D cathode mass transfer impedance: the finite Warburg element . . . 81
- 3.3 Sensitivity Analysis . . . 85

3.4 Estimation of Electrode Kinetic Parameters . . . 91
3.5 Experimental Setup . . . 96
3.5.1 Fuel cells . . . 96
3.5.2 Impedance measurements . . . 97
3.6 Local EI Analyses Using the Classical 1D Warburg Approach . . . 98
3.6.1 Local impedance parameter profiles . . . 99
3.6.2 Physical interpretation of the local electrode kinetic parameters . . . 104
3.6.3 Analysis of the local diffusion impedance parameters . . . 106
3.6.4 Conclusion about the interpretation of local EI spectra with the 1D Warburg diffusion model . . . 111

4 Alternative Expressions to the Warburg Impedance: 1D Approaches 113
4.1 Influence of a Convective Flux on the Diffusion Impedance . . . 113
4.1.1 DC solution . . . 115
4.1.2 AC solution . . . 118
4.2 Bulk Electrode Impedance Model . . . 123
4.2.1 Impedance response in the absence of oxygen ($j_f(x,t) = 0$) . . . 125
4.2.2 Solution of the complete impedance model . . . 126
4.3 Conclusions about the One-Dimensional Mass Transport Models . . . 132

5 Pseudo-2D Impedance Models 141
5.1 Effect of Oxygen Depletion along the Air Channel on the Warburg Impedance . . . 141
5.1.1 Model development . . . 141
5.1.2 Comparison of the 1D and pseudo-2D approaches . . . 145
5.2 2D Diffusion Impedance Model Accounting for Convection along the Channel Direction . . . 151
5.2.1 Development of the pseudo-2D (or $1+1D$) model . . . 152
5.2.2 Comparison of diffusive and convective effects on the cell impedance response . . . 157
5.3 Conclusions about the Two-Dimensional Mass Transport Models . . . 161

6 Experimental Validation of the Models 167
6.1 Convective Oxygen Transport Perpendicular to the Electrode . . . 167
6.2 Estimation of the Local Impedance Parameters with the Pseudo 2D Impedance Models . . . 172
6.3 Analysis of Oxygen Transport with the 2D Convecto-Diffusive Impedance . . . 177
6.3.1 First results about oxygen transport through the cathode . . . 179
6.3.2 Role of Gas Diffusion Layer and Micro Porous Layer in oxygen transport . 182
6.3.3 Role of the current density . . . 189
6.3.4 Conclusion of the section . . . 190
6.4 Low Frequency Limit of the 2D Convecto-Diffusive Impedance . . . 191
6.5 Summary of the Chapter . . . 194

7 Conclusions and Perspectives 199

Appendices 205

A Determination of the Species Concentration with the 1D Warburg Diffusion Model 207

B Detailed Derivation of the Expressions of the 2D Convecto-Diffusive Impedance Model 209
B.1 Derivation of the Steady-State Oxygen Concentration 209
B.1.1 Under-saturated flow: $P_{H_2O} < P_{sat}$ 209
B.1.2 Saturated flow: $P_{H_2O} = P_{sat}$ 211
B.2 Derivation of the Convecto-Diffusive Impedance 211
B.2.1 Local amplitude of the oxygen concentration oscillations at the electrode $\Delta c_{O_2}(x, y = \delta)$ 211
B.2.2 Convecto-diffusive impedance accounting for concentration oscillations in the channel 214
B.3 Asymptotic Study 217

C Figures Completing the Experimental Study with the Pseudo-2D Impedances 219
C.0.1 Local impedance spectra measured with cell 1 219
C.0.2 Impact of the channel depth on the parameter estimation 219
C.0.3 High frequency impedance parameters identified with cell 1 220
C.0.4 Diffusion parameters D^{eff} and δ identified starting from cell 1 221

Bibliographie 224

1 Introduction to Fuel Cells

This chapter is an introduction to the operation mode of fuel cells, notably of ***P**olymer **E**lectrolyte **M**embrane **F**uel **C**ells* (PEMFC). More detailed descriptions of fuel cell basics can be found in [OCCP06, Col08, LD03].

1.1 Principle of Operation

Fuel cells are energy conversion devices that generate electricity and heat through an electrochemical reaction of liquid or gaseous fuels with pure oxygen or air. The chemical energy is directly converted into electrical energy, like in a battery. The difference between a battery and a fuel cell is that the latter produces electricity continuously as long as it is supplied with reactants, while a battery contains a limited amount of reactants.

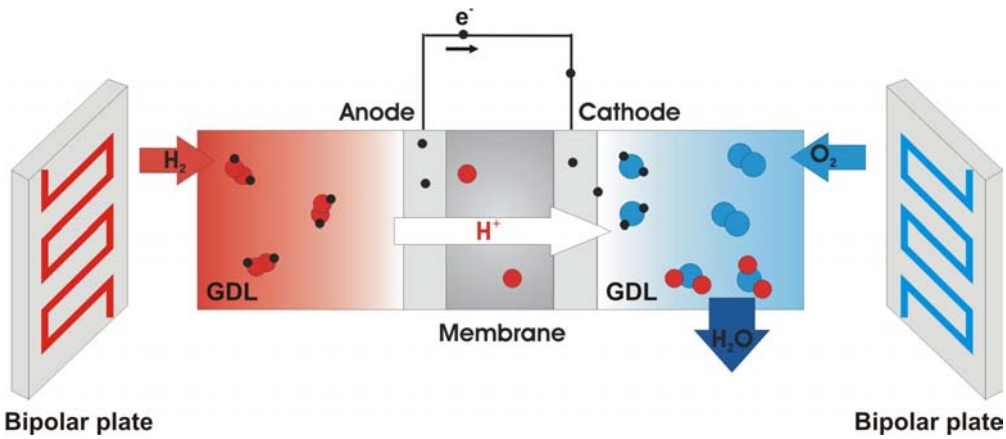


Figure 1.1: *Schematical representation of the electrochemical reaction in the MEA of a PEM fuel cell fed with pure H_2 and O_2.*

A fuel cell is composed of two electrodes, which are electronically isolated from each other by a proton conducting electrolyte that ensures the ion transport from the anode to the cathode (in the case of cations) or from the cathode to the anode (in the case of anions). The electrodes are covered by the ***G**as **D**iffusion **L**ayers* (GDL), which homogenize the gas flow to the reaction sites. This ***M**embrane **E**lectrode **A**ssembly* (MEA) is inserted between two flow field plates, which collect the current and ensure the supply of the gases as well as the cooling of the system. Figure 1.1 shows schematically the structure of the MEA and illustrates the transport of electrons in a PEM fuel cell fed with pure hydrogen and oxygen. In this case, the global electrochemical reaction that can be divided into two half-reactions, corresponds to the combustion of hydrogen (1.1), that is to say to the inverse of water electrolysis. The ***H**ydrogen **O**xidation **R**eaction* (HOR) at the anode (1.2) liberates electrons and produces hydrogen ions (protons). The electrons flow via an external circuit to the cathode and react with oxygen and with the protons flowing through the membrane to produce water (1.3) through the ***O**xygen **R**eduction **R**eaction* (ORR).

$$\text{Global reaction:} \quad H_2 + \frac{1}{2}O_2 \rightarrow H_2O \tag{1.1}$$

$$\text{HOR at the anode:} \quad H_2 \rightarrow 2H^+ + 2e^- \tag{1.2}$$

$$\text{ORR at the cathode:} \quad \frac{1}{2}O_2 + 2H^+ + 2e^- \rightarrow H_2O \tag{1.3}$$

1.2 Main Fuel Cell Types

The principle of the electrochemical reaction remains the same for all fuel cell types. However, they differ in their electrolyte and thus in the nature of the exchanged ions, as well as in their operating conditions. Fuel cells are usually classified by the nature of the electrolyte. According to this criterion, there exist 5 main fuel cell types (Figure 1.2):

- Membrane Fuel Cells (MFC) including Polymer Electrolyte Membrane Fuel Cells (PEMFC) fed with hydrogen, Direct Methanol Fuel Cells (DMFC) and Direct Ethanol Fuel Cells (DEFC) fed with methanol and ethanol respectively.
- Phosphoric Acid Fuel Cells (PAFC)
- Alkaline Fuel Cells (AFC)
- Molten Carbonate Fuel Cells (MCFC)
- Solid Oxide Fuel Cells (SOFC)

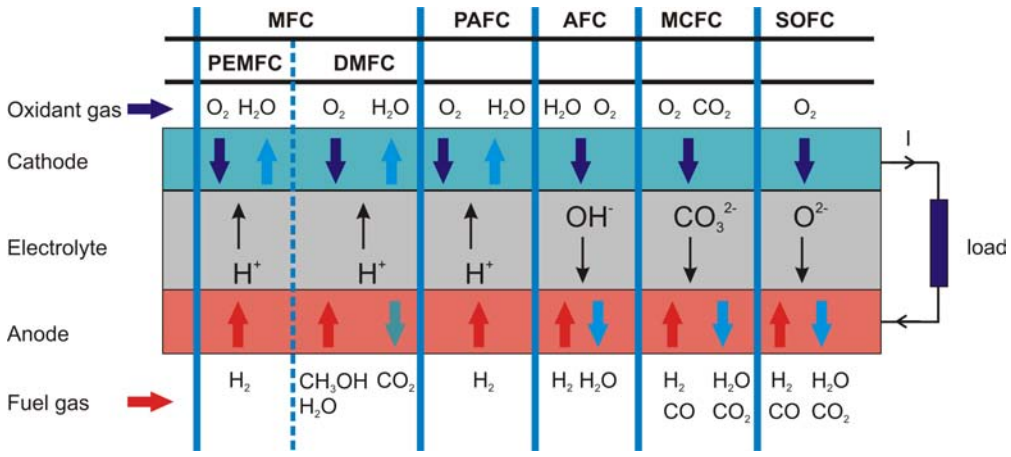


Figure 1.2: *Different types of fuel cells depending on their electrolyte and on the nature of ions exchanged through the electrolyte.*

The mobile charge carriers of each fuel cell type, as well as their tolerance to carbon monoxide are presented in Figure 1.2. More generally, the difference is made between anionic and acidic fuel cells. The anion conducting fuel cell family includes AFC, MCFC and SOFC:

In AFC, the electrolyte consists of a potassium hydroxide (KOH) solution, in which OH^- ions are the mobile charge carriers. The electrochemical half reactions at the electrodes of an AFC require low activation energies, so that nickel can be used as a catalyst. As a consequence, the cell voltage (as well as the efficiency) is high in typical operating conditions, *i.e.* it is usually between $0.8\ V$ and $0.9\ V$. This makes AFC low cost fuel cells with a high efficiency. However, they consume water at the cathode and produce twice as much at the anode, which has to be removed to avoid electrolyte dilution. The presence of CO_2 in hydrogen or oxygen must also be avoided, because it tends to dissolve in the electrolyte and decrease the OH^- concentration. As a consequence, these fuel cells have to be fed exclusively with pure H_2 and pure O_2 and a regular replenishment of the electrolyte is necessary to maintain a satisfying ionic conductivity. Due to these limitations, AFC are mostly employed in the aerospace sector which seeks mainly for highly efficient systems and where economical viability is secondary.

In MCFC, a mixture of molten alkali carbonates (Li_2CO_3, K_2CO_3) is used as electrolyte with CO_3^{2-} as mobile charge carriers. These molten salts are immobilized in a $LiOAlO_2$ matrix. MCFC operate at high temperatures ($> 600°C$), which has the advantage that less active low cost nickel based catalysts can be used. MCFC can be supplied with a variety of fuels, such as hydrogen, simple hydrocarbons (*e.g.* methane) and simple alcohols after a basic reforming stage, so that the CO present in the reformates can be used as fuel. Their high operation temperature qualifies them for heat-electricity cogeneration applications. However, the CO_2 production and consumption at the anode and the cathode (respectively) require the implementation of a recycling loop, which increases the cost of MCFC installations. Due to the thermo-mechanical stress that appears inside the electrolyte during start-up and shut-down, these fuel cells are more appropriate for continuous applications at intermediate and high power ranges.

SOFC employ oxygen ion O^{2-} conducting ceramic electrolytes (typically yttria-stabilized zirconia YSZ). Their operating temperature is usually situated between 600 and $1000°C$, which allows fuel flexibility, high electrical efficiencies of 50 - 60% [OCCP06], the use of low cost catalysts (nickel based) and the use of waste heat for cogeneration applications. With combined heat and power applications, the total efficiency can reach up to 90%. However, at these high temperatures, high cost, mechanically resistant materials are required to resist high thermal and thermal-mechanical stresses. Despite these limitations, SOFC are promising for stationnary applications from the intermediate ($1\ kW$) to the high power range ($10^5\ kW$, cf. Table 1.1), as well as for transport applications (Auxiliary Power Units APU,...).

The acidic fuel cell family includes PAFC, PEMFC and DMFC:

The PAFC contains a H^+ conducting phosphoric acid (H_3PO_4) solution embedded in a porous SiC matrix. This low cost and mechanically stable electrolyte offers a good reliability. However, due to the relatively high activation energy of the electrochemical half-reactions, PAFC employ Pt based catalysts, which makes them prone to carbon monoxide poisoning. Thus, only pure hydrogen can be used as fuel (possibly after a thorough reforming of methane) and oxygen (or air) as oxidant. PAFC operate at temperatures comprised between $130°C$ and $220°C$ and must be always maintained at sufficiently high temperatures to avoid the solidification of the phosphoric acid (pure H_3PO_4 solidifies at $42°C$) which can cause serious

damages. On the other hand, working at high temperatures entails H_3PO_4 evaporation and the electrolyte must therefore be regularly replenished. Taking these characteristics into account, PAFC are appropriate for stationary power plants only. In practice, this type of fuel cell is probably less promising than the others.

PEMFC use a proton (H^+) conducting polymer electrolyte and are usually fed with (pure) hydrogen and O_2/air (cf. chapter1.5). They reach the highest power densities ($300-1000\,mW/cm^2$ [OCCP06]) and have the best start-up/shut-down characteristics of all fuel cell types. However, because of their low operation temperature (typically $< 90°C$), they exhibit large activation energies leading to a low reaction rate. *Pt* based catalysts are thus currently essential, which makes PEMFC expensive and sensitive to *CO* poisoning. PEMFC are also demanding in terms of water management: membrane hydration is needed for achieving a satisfying proton conductivity, whereas water removal is required to avoid mass transfer limitations in the gas transport media (electrodes, GDL, gas channels). Considering these characteristics, PEMFC are the most studied and promising fuel cells for stationary and transport applications. However, for a large scale deployment, several improvements have to be made regarding their reliability and life-time, the tolerance to dry and flooded conditions and the development of Pt-free or low Pt catalysts. **DMFC and DEFC** are polymer electrolyte membrane fuel cells that oxidize directly methanol CH_3OH or ethanol C_2H_5OH (instead of H_2) at the anode to liberate electrons and protons (H^+). Water is required as an additional reactant at the anode and CO_2 is released as a product of the oxidation reaction. The oxidation of methanol and ethanol are complex reactions which exhibit large activation losses. Thus, the cell power densities are low (30 - 100 mW/cm^2 compared to 300 - 1000 mW/cm^2 for a PEMFC fed with hydrogen). As a consequence, DMFC and DEFC are mostly developed for low-power ($< 1kW$) portable applications.

Fuel cell type	Electrical efficiency $[\%]$	Power density $[mW/cm^2]$	Power range $[kW]$	Temperature range $[°C]$
PEMFC	$40-50$	$300-1000$	$10^{-3}-10^3$	$30-100°C$
PAFC	40	$150-300$	$50-10^3$	$130-220°$
AFC	50	$150-400$	$1-10^2$	$50-200°C$
MCFC	$45-55$	$100-300$	10^2-10^5	$\approx 650°C$
SOFC	$45-55$	250	$1-10^5$	$700-1000°C$

Table 1.1: *Main characteristics of the 5 fuel cell types [OCCP06, LD03].*

Table 1.1 summarizes the main characteristics of the five fuel cell types. Another classification is possible in terms of operating temperature: PEMFC, AFC and PAFC operate in the low temperature range ($50-250°C$), and MCFC and SOFC in the high temperature range ($650-1000°C$).

PEMFC, MCFC and SOFC offer the best prospects for further improvement and for a future large-scale deployment. MCFC and SOFC offer the best performance for stationary high power applications. Due to their high power density and their compact design (MEA thickness less than 1 *mm*), PEMFC seem to be the most promising for small-scale stationary, residential and portable power applications and of course for transportation.

In the recent years, a new fuel cell type - Protonic Ceramic Fuel Cells (PCFC) - has been developed [Coo03, Dai08, KJN09]. Their technology is situated between that of PEMFC and SOFC:

the membrane is a proton conducting ceramic electrolyte material. The advantage of a solid electrolyte is that it cannot dry out as with PEMFC or leak out as with PAFC. The operating temperature of PCFC is of about $750°C$ and they can be supplied with hydrocarbon fuels without former reforming. However, the major drawback of PCFC is their poor net current output (of a factor $50-100$ too small to be commercially viable [Coo03]), which could be increased by reducing the electrolyte thickness, improving the ionic conductivity and by the optimization of the electrodes [Coo03, KJN09].

1.3 Thermodynamics

Fuel cells convert most of the chemical energy of a fuel/oxidant pair into electrical energy, the other part is transformed into heat and can be directly related to voltage drops. Under ideal conditions the reversible electrical work and the reversible *open circuit voltage* OCV are functions of the working conditions.

1.3.1 Total chemical energy and reference potential

The quantity of chemical energy liberated during the global reaction of hydrogen combustion (1.1) is given by the reaction enthalpy:

$$\Delta H(T,P_i) = \Delta H_{H_2O} - \Delta H_{H_2} - 1/2\Delta H_{O_2} \tag{1.4}$$

where P_i stands for the partial pressure of species i ($i = H_2O, H_2, O_2$). The reaction enthalpy depends on the phase of water. In standard conditions ($T^0 = 298\ K$, $P^0 = 10^5\ Pa$), we have [Ram05]:

$$\begin{aligned} \Delta H^0_{liq} &= -285.8\ kJ/mol_{H_2} \\ \Delta H^0_{vap} &= -241.8\ kJ/mol_{H_2} \end{aligned} \tag{1.5}$$

The global reaction enthalpy allows to define a (virtual) reference potential E_{ref} that the fuel cell would reach if the totality of the chemical energy were transformed into electrical energy, without any heat production. This reference potential is given by:

$$E_{ref}(T,P_i) = -\frac{\Delta H(T,P_i)}{2F}, \tag{1.6}$$

where F is the *Faraday's constant* ($F = 96485\ Cmol^{-1}$) standing for the electrical charge of one mole of electrons. Like the enthalpy, the reference potential depends on temperature, pressure and on the phase of water. In standard conditions:

$$\begin{aligned} E^0_{ref,liq} &= 1.48\ V \\ E^0_{ref,vap} &= 1.25\ V \end{aligned} \tag{1.7}$$

Of course, this reference potential remains virtual. A part of the chemical energy is necessarily converted into heat, which lowers the value of the effective electrical work produced during the

reaction and thus the cell potential.

1.3.2 Reversible cell voltage

According to the 2nd law of thermodynamics, a part of the chemical energy is transformed into heat, even in reversible conditions. The parameter associated with this ideal heat production is the reaction entropy:

$$\Delta S = \Delta S_{H_2O} - \Delta S_{H_2} - 1/2\Delta S_{O_2} \tag{1.8}$$

Like the reaction enthalpy, the entropy depends on the working conditions and on the state of water. In standard (for liquid water) and saturated (for vapor) conditions [Ram05]:

$$\begin{aligned} \Delta S^0_{liq} &= -163.3\ JK^{-1}mol^{-1}_{H_2} \\ \Delta S^0_{vap}(T^0, P_{sat}(T^0)) &= -16\ JK^{-1}mol^{-1}_{H_2} \end{aligned} \tag{1.9}$$

It is worth recalling that for vapor production it is necessary to use the saturated vapor pressure at T^0, since below $100°C$ vapor cannot exist at standard pressure. The entropy variation generates a heat production that can expressed by:

$$Q = T\Delta S \tag{1.10}$$

As a consequence, the electrical energy available for the user in ideal conditions is given by the variation of the Gibbs free energy that is defined by:

$$\Delta G(T, P_i) = \Delta H(T, P_i) - T\Delta S(T, P_i) \tag{1.11}$$

which allows to define the reversible electrical work W^{rev}_{elec} (counted positively):

$$W^{rev}_{elec} = -\Delta G \tag{1.12}$$

In standard conditions:

$$\Delta G^0 = -237.1\ kJ/mol_{H_2} \tag{1.13}$$

The value of the Gibbs free energy is independent of the phase of water, although $\Delta H^{tot}_{liq} > \Delta H^{tot}_{vap}$ [Ram05]. This can be explained by the fact that in saturated conditions, the difference between these reaction enthalpies is only due to the latent heat of evaporation L_v. Since $L_v = T(\Delta S_{vap} - \Delta S_{liq})$, there is no variation in the Gibbs energy, whatever the phase of water.

The ideal cell voltage E_{th} is thus given by:

$$E_{th}(T, P_i) = -\frac{\Delta G(T, P_i)}{2F} \tag{1.14}$$

E_{th} is also called the *reversible open circuit voltage* OCV. In standard conditions, the reversible cell voltage is:

$$E^0_{th} = -\frac{\Delta G^0}{2F} = 1.23\ V \tag{1.15}$$

Assuming that hydrogen, oxygen and vapor behave like ideal gases, $\Delta G(T,P_i)$ can be obtained by [RLDM09]:

$$\Delta G(T,P_i) = \Delta G^0 - \int_{298K}^{T} \Delta S(T,P^0)\,dT + RT\ln\left(\frac{a_{H_2O}}{a_{H_2}a_{O_2}^{1/2}}\right) \tag{1.16}$$

where a_i stands for the activity of species i. For gases, the activity can be calculated knowing the partial pressure P_i, by reference to the standard pressure P^0:

$$a_i = P_i/P^0 \tag{1.17}$$

In liquid phase the water activity is considered equal to 1: $a_{H_2O,liq} = 1$. $\Delta S(T,P^0)$ stands for the reaction entropy at standard pressure. In the case of PEMFC, the temperature is close to T^0 and it is possible to neglect the variation of the entropy with respect to T in (1.16) and to consider that $\Delta S(T,P^0) \approx \Delta S^0$. Combining (1.14) and (1.16) (with the corresponding values of ΔG^0 (1.13) and ΔS^0 (1.9)) allows to derive explicit expressions of the thermodynamic voltage as a function of the temperature and pressure (concentration/activity) [RLDM09]:

$$E_{th}(T,P_i) = 1.229 - 85\cdot 10^{-5}(T-298) + \frac{RT}{2F}\ln\left(a_{H_2}a_{O_2}^{1/2}\right) \tag{1.18}$$

$$E_{th}(T,P_i) = 1.184 - 23\cdot 10^{-5}(T-298) + \frac{RT}{2F}\ln\left(\frac{a_{H_2}a_{O_2}^{1/2}}{a_{H_2O}}\right) \tag{1.19}$$

Equation (1.19) must be used in the case of vapor production; equation (1.18) must be used when water is in liquid phase. For saturated vapor ($P_{H_2O} = P_{sat}$), equations (1.18) and (1.19) yield the same result. In standard conditions, equation (1.18) returns the value of E^0 (1.15). Independently on the T deviation from standard conditions, equations (1.19) and (1.18) express the open cell voltage corrected by the loss induced by a limited gas concentration:

$$E_{th}(T,P_i) = E_{th}(T,P^0) - \frac{RT}{2F}\ln\frac{a_{H_2O}}{a_{H_2}a_{O_2}^{1/2}}, \tag{1.20}$$

This expression of the OCV is known as the *Nernst equation* and it is a fundamental equation in electrochemistry. It is worth mentioning that the actual OCV is lower than $E_{th}(T,P)$. This will be discussed in section 1.4.

1.3.3 Fuel cell thermodynamic efficiency

The reversible electrical efficiency η_{rev} of a fuel cell is given by the ratio between the maximum electrical work (*i.e.* the variation of the Gibbs energy) and the total amount of converted energy (*i.e.* the reaction enthalpy):

$$\eta_{rev} = \frac{\Delta G}{\Delta H_{vap}} \tag{1.21}$$

In (1.21) the reference enthalpy variation is the hydrogen *Lower Heating Value* (LHV) ΔH_{vap}, which gives in standard conditions $\eta_{rev} = 0.98$. By using the *Higher Heating Value* (HHV), one

would obtain $\eta_{rev} = 0.83$.

1.4 Actual Fuel Cell Performance

The actual open circuit voltage is inferior to the ideal reversible value $E_{th}(T,P)$ given by the Nernst equation (1.20). This is mainly due to internal currents, gas cross-over through the membrane and parasitic half-reactions like platinum oxidation and reactions due to the presence of impurities like carbon monoxide [ZTS$^+$06, ZZZ$^+$06]. For a PEMFC, the OCV is about 1 V which is significantly lower than $E^0 = 1.23\ V$ (1.15). Furthermore, when the cell produces a current, additional voltage losses occur due to the irreversiblity of the half-reactions, ohmic resistances and mass transfer limitations. Hence, the efficiency η_{real} of a fuel cell in operation is expressed as a function of the voltage E:

$$\eta_{real} = \frac{2FE}{-\Delta H_{vap}}. \tag{1.22}$$

These potential losses are at the origin of the shape of the fuel cell (current-voltage) *polarization curve*. Figure 1.3 presents a typical polarization curve and the influence of the different voltage losses. They can be divided into three main categories:

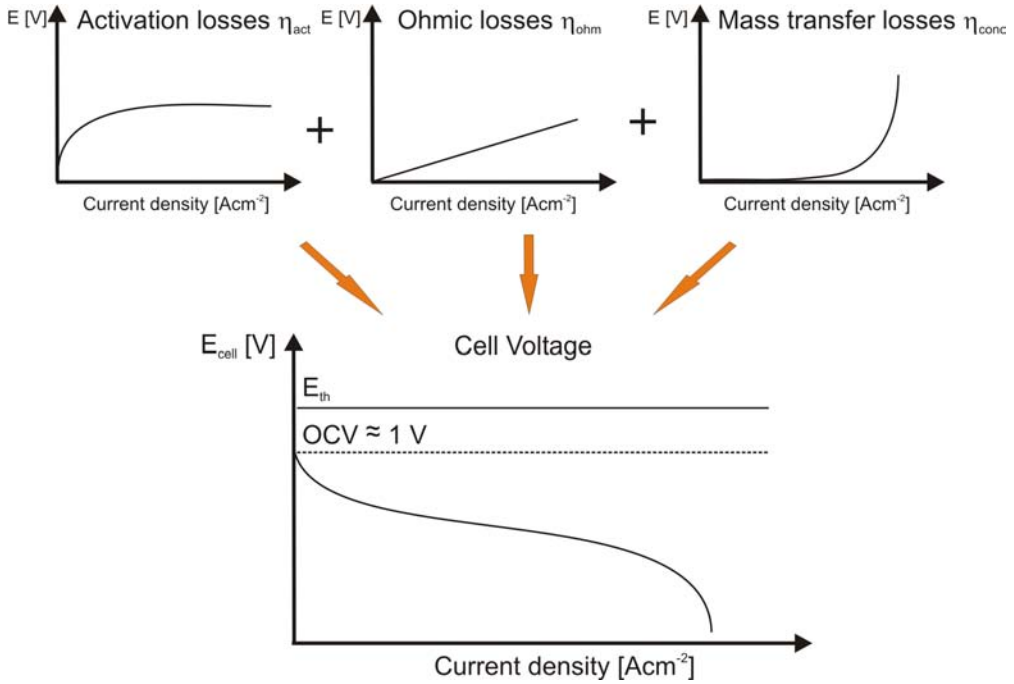


Figure 1.3: *Main factors contributing to the cell performance losses. The polarization curve can be obtained by subtracting the different overpotentials due to activation losses η_{act}, ohmic losses η_{ohm} and concentration losses η_{conc} from the OCV.*

Activation losses η_{act} are due to the finite rate of the half-reactions (Figure 1.3). These losses correspond to the voltage that is needed to overcome the activation barrier of the half-reactions. The anode potential is increased by $\eta_{act,A}$ and the cathode potential is lowered by $\eta_{act,C}$, which decreases the potential difference between the anode and the cathode and

therewith the cell voltage ($E = E_c - E_a$). For a PEMFC, $\left|\eta_{act,C}\right|$ is much larger than $\left|\eta_{act,A}\right|$, since the kinetic of the ORR is much lower than that of the HOR. The activation losses can be lowered by the use of more active catalysts and by increasing the active catalyst area, which is a major goal in catalyst layer development. The most effective catalysts for PEMFC are currently platinum based, which represents an important part of the cost of the cell.

Ohmic losses η_{ohm} are associated with the transport of charges in the cell. Their variation with the current density shows a linear-type behavior (Figure 1.3) and η_{ohm} is generally expressed by Ohm's law:

$$\eta_{ohm} = R \cdot j, \tag{1.23}$$

where R stands for the sum of all ohmic resistances appearing in the cell. The main part of η_{ohm} is due to the membrane ohmic resistance. Other resistive losses are linked with proton transport in the catalyst layers, electron transport in the other cell components (electrode, GDL, bipolar plates) and through the interfaces between them. However, these voltage losses are usually negligible (or at least neglected) compared to the ohmic losses in the membrane. As it will be shown in section 1.5.1 the membrane conductivity depends on the polymer hydration. As a consequence, R is a function of the operating conditions and it cannot be considered as strictly constant.

Concentration losses η_{conc} occur at high current densities because of mass transfer limitations (Figure 1.3). Since the gases are consumed by the electrochemical reactions, their concentration and partial pressure decrease through the gas channels, diffusion layers and electrodes, which entails voltage drops. These losses are much more important when liquid water is present in the pores of the GDL and of the active layer, which limits the gas supply: the increase in proton conductivity with increasing cell humidification is counterbalanced by higher mass transfer limitations due to pore flooding. A compromise has to be found between both effects. Concentration losses in fuel cells are generally expressed by:

$$\eta_{conc} = c \ln \frac{j_L}{j_L - j}, \text{ with } c = \frac{RT}{nF}(1 + \frac{1}{\alpha}) \tag{1.24}$$

This expression can be derived from the *Nernst equation* (1.20) and the *Tafel equation* (2.33) that will be introduced in chapter 2.1.2, supposing a purely diffusive mass transfer. j_L in equation (1.24) represents the limiting current density (when the reactant concentration in the catalyst layer drops to zero). An alternative, entirely empirical expression is proposed by Kim *et al.* [KLSC95]:

$$\eta_{conc} = m \exp(n \cdot j) \tag{1.25}$$

where m and n are constants expressed in V and m^2/A respectively. They have been estimated for a PEMFC with E-TEK electrodes and an Aciplex-S 1004 membrane working at 1 atm and 60°C using different O_2/inert gas mixtures [KLSC95]. The authors mention that the values of m cover a wide range from 10^{-19} V to 1 V, whereas those of n vary in a relatively narrow range ($10^{-2} - 10^{-3}$ m^2/A): it seems that these constants are correlated with parameters characterizing other voltage losses.

The actual cell voltage E can be expressed by starting from the ideal voltage and subtracting the different voltage drops cited above:

$$E = E_{th} - \eta_{act} - \eta_{ohm} - \eta_{conc} \tag{1.26}$$

The typical shape of the resulting polarization curve corresponds to that given in Figure 1.3.

1.5 The Membrane-Electrode Assembly (MEA)

As shown schematically in Figure 1.1, the Membrane-Electrode Assembly (MEA) is made of media (membrane, electrodes, GDL) which differ in their geometrical and physical properties. Each of these components has a well defined function: for instance, the GDL homogenize the reactant distribution and evacuate the products of the electrochemical half-reactions (charges, water and heat), whereas the membrane ensures the proton conduction between the electrodes, while preventing electronic conduction and gas cross-over. The electrons liberated by the electrochemical reaction at the anode flow through an external circuit and react at the cathode with the hydrogen ions and the oxygen to produce water. In order to optimize the cell efficiency, these components have to exhibit certain properties which are discussed in this section.

1.5.1 Polymer electrolyte membranes

The electrolyte in a PEMFC has to exhibit simultaneously a high proton conductivity and a high permselectivity for electrons and for non-ionized molecules to limit crossover of reactants. Furthermore, for the sake of reliability, the membrane has to be stable against chemical and mechanical degradation over the range of conditions experienced during operation. The solid polymer electrolytes in low temperature PEMFC (with a typical working range between $60°C$ and $80°C$) are typically perfluorosulfonic acid (PFSA) membranes, such as Nafion® (Du Pont de Nemours & Co.), Flemion® and Aciplex® (Asahi Glass), Dow (Dow Chemical Company), Membrane C (Chlorine Engineers) and Aquivion™ (Solvay). These materials exhibit currently the best proton conductivity (when adequately hydrated) in conjunction with the best chemical and mechanical stability [IPSV00, MM04]. For example, proton conductivities of about $10^{-1}\ Scm^{-1}$ can be reached with Nafion membranes at $80°C$ and a relative humidity of 100 % [TMTD00].

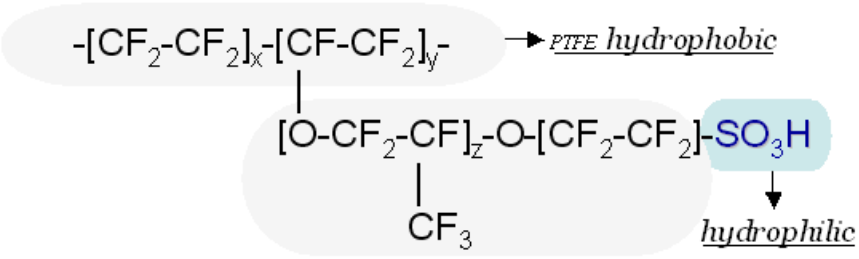


Figure 1.4: *Representation of the chemical structure of Nafion. The polymer consists of a hydrophobic "PTFE-like" backbone with side chains that are terminated by hydrophilic sulfonic acid groups SO_3H. For Nafion membranes with an equivalent weight of* $1100\ g\,mol^{-1}$; $6 < X < 10$ *and* $y = z = 1$.

The polymer structure of PFSA membranes consists in a fluorocarbonated backbone ("PTFE-like") with side chains that are terminated with sulfonic acid groups ($-SO_3H$), as represented

in Figure 1.4. The resulting macromolecule contains consequently hydrophobic and hydrophilic parts. Varying the length of ($-SO_3H$) side chains and their location on the backbone modifies the equivalent weight (EW) of the polymer membrane. The equivalent weight and its inverse, the ion exchange capacity (IEC) are defined by [FSD05, MM04]:

$$EW = \frac{1}{IEC} = \frac{\text{weight of dry polymer [g]}}{\text{number of active } SO_3H \text{ groups [mol]}} \tag{1.27}$$

The material the most used and consequently the most analyzed up to now is Nafion. Nafion membranes are classified according to their equivalent weight EW and thickness: *Nafion XYZ*. The first two digits - *XY* - designate the EW and the last digit - *Z* - the membrane thickness. For example, *Nafion 117* membranes possess an equivalent weight of $11 \times 100\ g\,mol^{-1}$ and a thickness of 7 *mil* ($1\ mil = 25\ \mu m$). The standard thicknesses of Nafion membranes are 2, 5 and 7 *mil* (50, 125 and 175 μm respectively). More generally, the thickness of perfluorosulfonic acid membranes lies between 25 μm and 250 μm. A compromise has to be found between gas impermeability and proton conduction: the thinner the membrane, the higher the proton conductivity and the higher the gas permeability. The operation range of perfluorosulfonic acid membranes is limited to temperatures below $90\,^{\circ}C$ (glass transition temperature $\approx 100-110\,^{\circ}C$ [HMT94]) in order to avoid dehydration. A more detailed description of the membrane properties can be found in a review by Kreuer *et al.* [KPSS04].

Membrane hydration

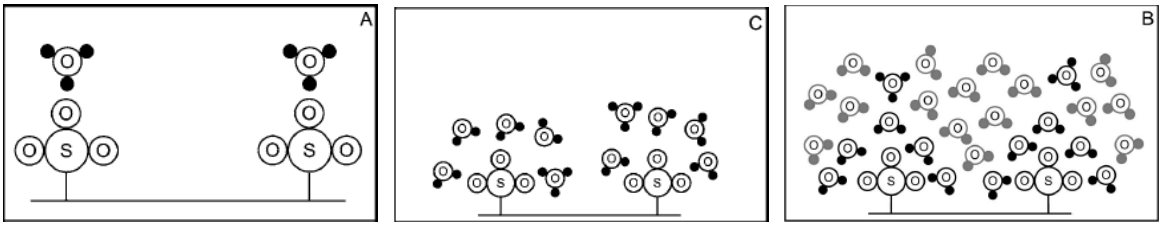
The proton conductivity σ of solid polymer electrolytes is strongly dependent on their water content. Membrane hydration is necessary in order to obtain a satisfying proton conductivity. However, the membrane swells with increasing hydration which causes mechanical stress. As a consequence, the understanding of the membrane water sorption behavior plays an important role in research and development of polymer membranes and has been the purpose of many theoretical [TMTD00, FSD05] and experimental studies [SES96, LSVZ03, SOH$^+$07, ZDR$^+$93, ZJSD$^+$93]. The water sorption is characterized by the (dimensionless) concentration λ, which represents the number of adsorbed water molecules per sulfonate head group $-SO_3^-$:

$$\lambda = \frac{n_{H_2O}}{n_{SO_3^-}} \tag{1.28}$$

where n_{H_2O} and $n_{SO_3^-}$ designate the number of adsorbed water molecules and the number of sulfonate groups, respectively. The water content λ can also be expressed as a function of the equivalent weight EW (1.27), the membrane dry density ρ_{dry} (gm^{-3}) and the concentration of water molecules present in the membrane c_{H_2O} ($molm^{-3}$):

$$\lambda = \frac{EW}{\rho_{dry}} c_{H_2O} \tag{1.29}$$

The evolution of the membrane structure with increasing water content has been the topic of several studies in the last decades [Geb00, LPZ99, RRGD02]. Ionomer membranes are generally described by ionic clusters enclosed in a polymer matrix that swell with hydration. Figure 1.5 represents schematically the different stages of hydration of Nafion according to Fourier Transform Infrared Spectroscopy (FT-IR) studies performed by Laporta *et al.* [LPZ99]. The first water molecules interact with the sulfonic groups to create hydronium H_3O^+ and SO_3^- ions (Figure



(a) $\lambda = 1$ (b) $\lambda = 5$ (c) $\lambda = 14$

Figure 1.5: *Schematic representation of different stages of hydration of Nafion membranes [FSD05].*

1.5(a)). The next water molecules aggregate with the hydronium ions to form small counter-ion clusters containing up to six water molecules (Figure 1.5(b)). According to studies by Laporta *et al.* [LPZ99], proton conduction is usually observed when excess protons can move on the counter-ion clusters, *i.e.* for $\lambda \geq 2$. When λ lies between 1 and 2, proton transport is possible but the conductivity is extremely low. When the water content exceeds $\lambda = 6$ (Figure 1.5(c)), the counter-ion clusters coalesce to form larger clusters and finally a continuous phase with properties similar to those of bulk water [LPZ99]. The structure in the diluted state of ionomer membranes is described by a dispersion of rod like polymer aggregates.

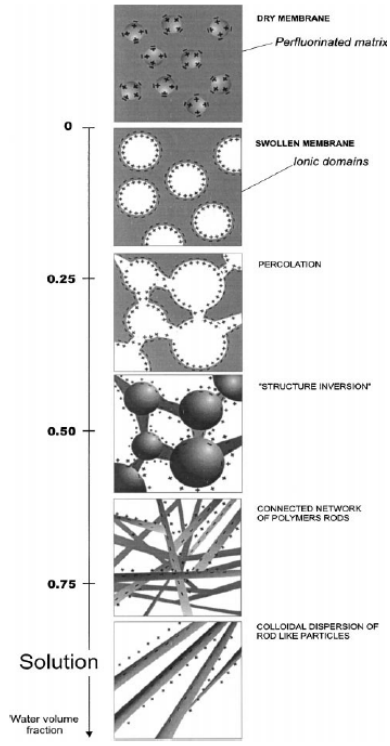


Figure 1.6: *Schematic representation of the structural evolution of perfluorosulfonated ionomers during hydration according to Gebel [Geb00].*

One of the rare models describing the evolution of the membrane structure over the complete hydration range is proposed by Gebel [Geb00]. The proposed model based on analyses of membranes at different hydration states by small angle neutron or X-ray scattering techniques (SANS and SAXS) is depicted in Figure 1.6. In this model, the ionic clusters of the dry membrane have

a size of about 15 Å in diameter. When the membrane is hydrated, the clusters swell and form spherical water pools with ionic groups at their surface that grow up to a size of about 40 Å. At this size, the clusters interconnect and form a network which is described in terms of a percolation model. In order to explain the transition between a dispersion of connected spherical ionic cluster in the polymer matrix at low water contents and a network of rod like polymer aggregates in the diluted state, Gebel evokes an inversion of the membrane structure. This model explains qualitatively the evolution of the membrane structure, but has no support from a thermodynamical model [RRGD02].

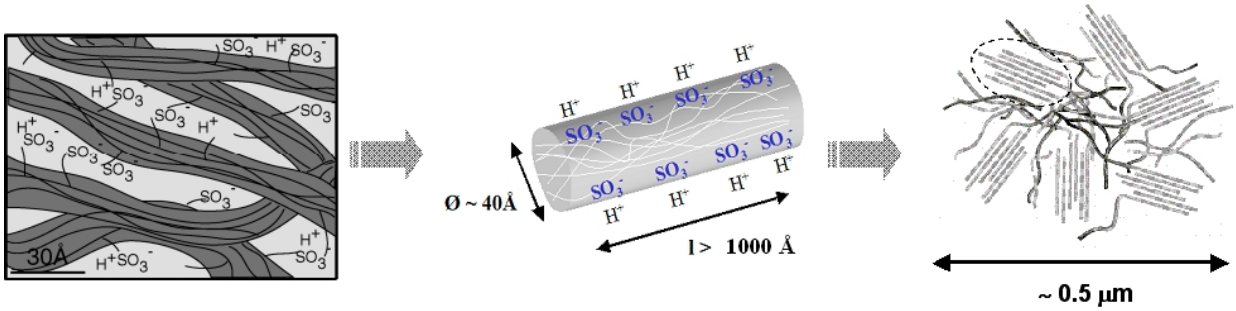


Figure 1.7: *Schematic representation of the structure of ionomer membranes in a range from 10 Å to 1000 Å according to Rubatat et al. [Rub03].*

Rubatat *et al.* [RRGD02, Rub03] propose an alternative structural model of Nafion over the entire hydration state which is represented in Figure 1.7. The model is based on investigations of the structure between 10 Å and 1000 Å using SANS and SAXS techniques. The studies revealed that, on a nanometer scale, the membrane consists of randomly orientated polymer chains with ionic groups and water molecules on their surface. The membrane is isotropic on this length scale. The polymer chains aggregate into elongated polymeric bundles surrounded by the electrolyte solution with a diameter of about 40 Å and a length exceeding 1000 Å. The elongated polymer aggregates orient themselves in larger bundles which can be further oriented by the application of strains on the membrane [VDHRD04]. This model is used for highly dilute perfluorosulfonic ionomers and can be also applied to explain the evolution of the structure of polymer electrolyte membranes.

The water uptake depends strongly on relative humidity and on the equilibration temperature. It is also sensitive to the pretreatment procedure.

Pretreatment protocol: For Nafion, different pretreatment protocols are described in the literature. They can be classified in two categories according to Alberti *et al.* [ANS08]:

- Standard treatment: the membranes are immersed successively for 1 h in a boiling solution of 0.03 *M* hydrogen peroxide, in boiling 0.5 *M* sulfuric acid and finally in boiling distilled water.
- Thermal treatment: after the standard procedure, the membranes can be dried by placing them into an oven at a certain temperature for a certain time.

Yeo and Yaeger [YY85] introduced a classification of Nafion membranes according to their pretreatment:

- Standard treatment → *expanded* or *E-form*

- Standard treatment + drying at $80°C \rightarrow$ *normal* or *N-form*
- Standard treatment + drying at $105°C \rightarrow$ *shrunken* or *S-form*
- Standard treatment + drying at $120°C$ [SES96] $\rightarrow$ *further shrunken* or *FS-form*

Experimental investigations performed by Sone *et al.* [SES96] show a decrease in the membrane conductivity with increasing thermal treatment temperature. This effect is generally explained by a shrinkage of the membrane pores [HMT94, SES96]. Alberti *et al.* [ANS08] explained the thermal memory by the fact that Nafion consists essentially of an amorphous matrix in which some microcrystalline phases are embedded. Thus, the amorphous ionomer forms only metastable phases that depend on the pretreatment temperature.

The classification introduced by Yeo and Yaeger [YY85] and completed by Sone *et al.* [SES96] remains qualitative, since it does not take the heating time into account and offers only a reference for two, respectively three temperatures. The pretreatment protocols can vary considerably, but Alberti *et al.* [ANS08] show that even for similar protocols a large discrepancy in the values of the membrane properties (σ, λ) can be found in the literature.

Sorption isotherms: For membranes equilibrated with vapor, λ_{vap} increases with increasing relative humidity RH. Surprisingly, despite the numerous studies related to the properties of Nafion, only a few expressions of sorption isotherms can be found in the literature. For instance, for Nafion 117 at $30°C$ [SZG91] and $80°C$ [HMT94] ($RH \leq 1$):

$$\lambda_{30°C}^{vap} = 0.043 + 17.81RH - 39.85RH^2 + 36RH^3 \tag{1.30}$$

$$\lambda_{80°C}^{vap} = 0.3 + 10.8RH - 16RH^2 + 14.1RH^3 \tag{1.31}$$

The relative humidity is defined by the ratio of the water partial pressure P_{H_2O} to the saturated vapor pressure P_{sat}:

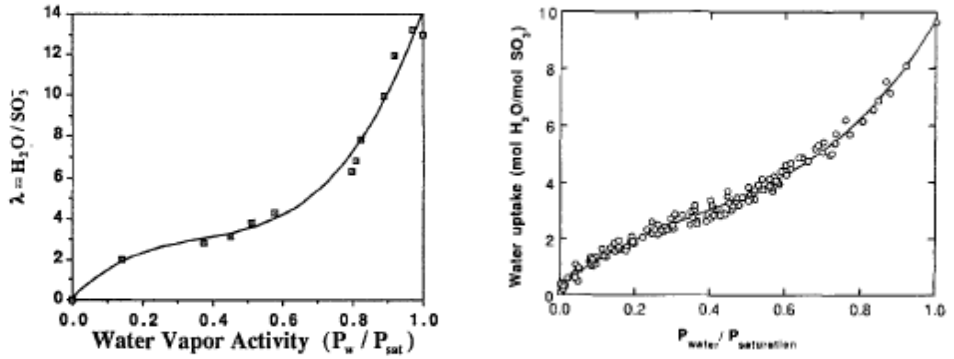
$$RH = \frac{P_{H_2O}}{P_{sat}} \tag{1.32}$$

where P_{sat} can be expressed as a function the temperature (in K) by Rankine's formula [Ram05]:

$$P_{sat} = P^0 \exp\left(13.669 - \frac{5096.23}{T}\right) \tag{1.33}$$

where P^0 stands for the standard pressure. The isotherms (1.30) and (1.31) are obtained by third-order least squares polynomial fits of experimental data measured by gravimetric methods [HMT94, SZG91]. These expressions are empirical and have therefore no physical meaning. Figure 1.8 represents experimental sorption isotherms and their corresponding fitting curve at $30°C$ (Figure 1.8(a)) and $80°C$ (Figure 1.8(b)).

The classical gravimetric method for measuring the water uptake consists in weighing the membrane sample with a micro-balance under an atmosphere that is controlled in humidity and temperature.



(a) (b)

Figure 1.8: *Membrane water content as a function of the relative humidity for Nafion 117 at (a)* $30°C$ *[SZG91] and at (b)* $80°C$ *[HMT94] and their respective fitting curve with equations* (1.30) *and* (1.31) *respectively.*

L. Maldonado of our group in LEMTA uses an alternative procedure for measuring the water uptake of PEM. Each membrane sample is preserved in an open vessel which is stored in an environment of controlled relative humidity and temperature. The water uptake is determined by weighting the whole setup (vessel + sample) before and during hydration and by subtracting the weight of the vessel. This method offers the advantage of treating multiple samples simultaneously and allows measurements over a long period of time.

	Fitting Equations (LEMTA)	
$T\ [°C]$	Linear-Exponential	R^2
30	$\lambda = 8.57RH + 1.72\ 10^{-5}\exp(13.2RH)$	0.996
40	$\lambda = 7.21RH + 4.2\ 10^{-4}\exp(10.1RH)$	0.998
50	$\lambda = 6.66RH + 4.1\ 10^{-4}\exp(10.2RH)$	0.998
60	$\lambda = 6.72RH + 2.03\ 10^{-4}\exp(10.9RH)$	0.999
70	$\lambda = 2.3RH + 7.38\ 10^{-2}\exp(5.01RH)$	0.999
80	$\lambda = 2.76RH + 7.3\ 10^{-3}\exp(7.38RH)$	0.998

Table 1.2: *Expressions used to fit the experimental data in Figure 1.9 and the corresponding residuals.*

The sorption isotherms obtained with this procedure for Nafion 115 membranes at different hydration temperatures ($30 - 80°C$) are presented in Figure 1.9. Table 1.2 shows the corresponding fit equations.

In addition to the water uptake from vapor phase, Figure 1.9 also depicts the water uptake obtained for equilibration of Nafion 115 in liquid phase. The water uptake in the presence of saturated vapor λ_{sat}^{vap} is always significantly lower than with liquid water λ^{liq}. This is in good agreement with observations reported in the literature [HMT94, ZDR$^+$93, SZG91]. For instance, for Nafion 117 membranes in equilibrium with **saturated water vapor** ($RH = 1$):

$$\begin{aligned} \text{At } 30^\circ \text{ C [SZG91]}: &\qquad \lambda_{sat}^{vap} = 14 \\ \text{At } 80^\circ \text{ C [HMT94]}: &\qquad \lambda_{sat}^{vap} = 9.2 \end{aligned}$$

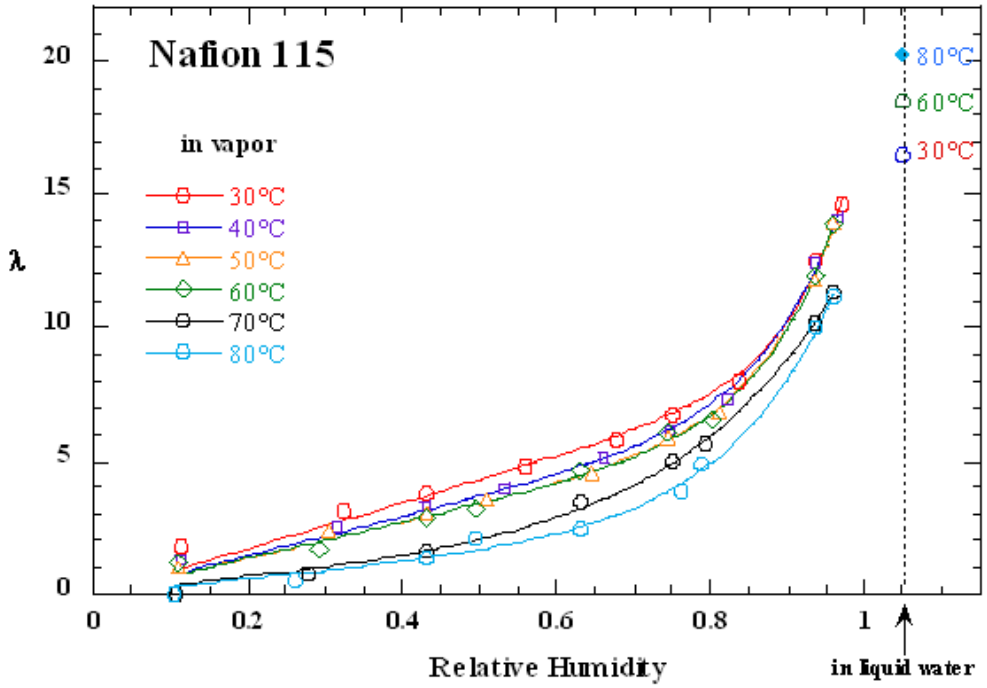


Figure 1.9: *Sorption isotherms of Nafion 115 membranes between 30°C and 80°C and their respective fitting curve obtained with the equations of Table 1.2 (experiment performed by L. Maldonado (LEMTA)). The graphs point out that the water uptake from liquid phase is significantly higher than the values obtained with saturated vapor. In addition, the graphs show an inversion of the temperature effects between vapor and liquid sorption.*

Whereas when the same membranes are immersed in **liquid water**, the measured water content is:

$$\text{In boiling water [SZG91, ZJSD}^{+}\text{93]}: \qquad \lambda^{liq} = 22$$
$$\text{At } 80°C \text{ [SZG91]}: \qquad \lambda^{liq} = 16.8$$

The difference between the amount of water sorbed from saturated vapor and with liquid water at the same pressure and temperature was first observed in 1903 by Schroeder [Sch03] and it is sometimes referred to as the *Schroeder's paradox*. Several explanations have been reported in the literature, but still no clear consensus has been obtained. Some of them are based on experimental factors linked to temperature fluctuations [ZJSD^{+}93, ZDR^{+}93] and to the discrepancy in the sorption rates from liquid and vapor phase. However, when a liquid-equilibrated membrane is removed and suspended over saturated water vapor, λ_{sat} drops from about 22 to 14 indicating that the two states are thermodynamically stable [ZDR^{+}93, TMTD00]. Zawodzinski *et al.* [ZJSD^{+}93] explain the Schroeder paradox by the fact that sorption from vapor involves water condensation on the hydrophobic backbone of the polymer electrolyte, whereas sorption from liquid phase is direct and fills all the pores. Another interpretation is given by Choi and Datta [CD03], who developed a physicochemical model of water sorption that describes the entire sorption isotherm. In their model, the water uptake

is governed by a balance of forces between the swelling (or osmotic) pressure reducing the pore diameter which results from the stretching of the polymer chains upon water uptake and the pressure within the pore liquid. In the case of water uptake from vapor phase, it is supposed that vapor condenses within the pores before being sorbed, which entails an additional pressure on the liquid by the curved vapor-liquid interface within the pores. As a consequence, the water sorption is lower from vapor than from liquid phase.

In Figure 1.9, it can be noticed that λ^{liq} increases with the immersion temperature, whereas λ^{vap} decreases with the temperature. This is in good agreement with some results of the literature [HMT94, SZG91, ANS08, BE97b], whereas other authors put forward an increase of λ^{vap} with the temperature [JCD05].

Temperature dependency: The sorption isotherms of vapor-equilibrated Nafion 117 membranes at $30°C$ and at $80°C$, as well as those of Nafion 115 membranes measured in our group (Figure 1.9) show that the humidification temperature has a significant effect. However, the variations of the water uptake over the whole relative humidity range are more important than those observed between $30°C$ and $80°C$ at a fixed RH.

There seems to exist only two analytical expressions of the water uptake from liquid phase λ^{liq} [HMT94]. Hinatsu *et al.* [HMT94] measured the water uptake in liquid phase of Nafion 117 membranes (with different thermal histories) from $25°C$ to $130°C$. They report that the E-form of Nafion 117 sorbs more water at $25°C$ than the forms dried at high temperature (N, S). However, with increasing immersion temperature, λ_{liq} increases for the N- and the S-form, while it remains independent of the temperature for the E-form. For temperatures up to about $110°C$, the N-form sorbs more water than the S-form. By increasing the immersion temperatures further above $110°C$, which is close to the glass transition temperature of Nafion ($\approx 130°C$ [Ker01]), the water uptake becomes independent of the membrane form and follows the same tendency as the S-form. These results indicate that structural changes caused by the different pretreatment processes are eliminated at immersion temperatures approaching or above the glass transition temperature. For the N- and the S-form, Hinatsu *et al.* [HMT94] obtained the following best fit equations,

$$N-form: \quad \lambda^{liq} = 9.38 + 0.138(T-273) \tag{1.34}$$

$$S-form: \quad \lambda^{liq} = 10.0 + 1.84\ 10^{-2}(T-273) + 9.90\ 10^{-4}(T-273)^2 \tag{1.35}$$

which are in good agreement with studies performed by Zawodzinski *et al.* [ZDR$^+$93, ZJSD$^+$93]: they observed that λ^{liq} of Nafion 117 membranes dried at room temperature and then treated at $105°C$ under vacuum is temperature dependent, whereas the water uptake of membranes that have been dried only at room temperature is independent of the temperature and twice as high as for membranes dried at high temperature.

Membrane ionic conductivity

The main criterion characterizing the performance of polymer electrolyte membranes in fuel cells is their ionic conductivity σ (in Scm^{-1} or Sm^{-1}). The higher the proton conductivity at given temperature and relative humidity, the more promising is the membrane as an electrolyte for PEMFC.

The ionic conductivity strongly depends on several parameters like its thermal history, the temperature, the water uptake and therefore the relative humidity. The proton conductivity of Nafion membranes varies from about 10^{-7} Scm^{-1} for very low water uptakes ($\lambda^{vap} < 2$) up to about 10^{-1} Scm^{-1} when equilibrated with saturated vapor ($\lambda^{vap}_{sat} = 14$) [TMTD00]. For instance, Zawodzinski *et al.* [ZJSD+93] measured $\sigma = 0.06$ Scm^{-1} at $30°C$ and 100% RH for Nafion 117 membranes.

Reference	Ionic conductivity σ $[Sm^{-1}]$
[SZG91]	$\sigma = (0.514\lambda - 0.326) \cdot \exp\left[1268\left(\frac{1}{303} - \frac{1}{T}\right)\right]$, for $\lambda > 1$
[Cos01]	$\sigma = (0.58\lambda - 0.5) \cdot \exp\left[1268\left(\frac{1}{303} - \frac{1}{T}\right)\right]$, for $\lambda > 1$
[Kul03]	$\sigma = 0.5738\lambda - 0.7192$, for $\lambda > 1.253$
[ME04]	$\sigma = (0.46\lambda - 0.26) \cdot \exp\left[1190\left(\frac{1}{298.25} - \frac{1}{T}\right)\right]$, for $\lambda < 30$
[SDFP04]	$\sigma = 0.421\lambda - 1.722$, at $T = 298$ K

Table 1.3: *Examples of empirical relations given in the literature for the ionic conductivity of Nafion membranes.*

Experimental investigations of Sone *et al.* [SES96] with Nafion 117 revealed that σ decreases with increasing drying temperature. They explained this behavior by considering the porous structure of Nafion. According to them, for pretreatment temperatures close to the glass transition temperature, the pores tend to shrink, which results in a lower water uptake and therefore in a lower ionic conductivity. Table 1.3 summarizes some of the relations found in the literature. They represent best fit results of experimental data.

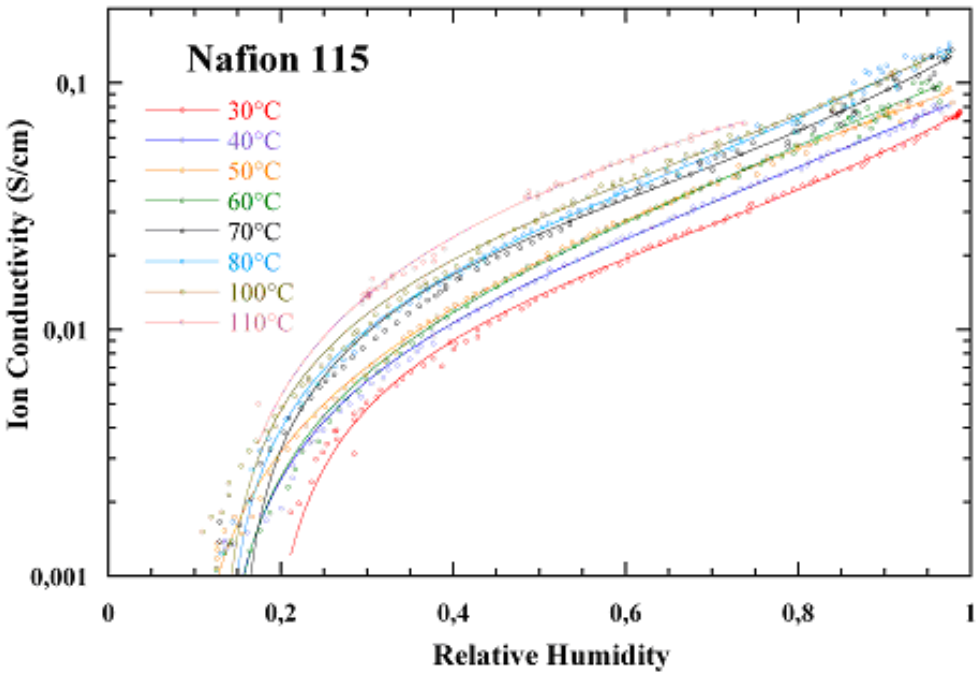


Figure 1.10: *Ionic conductivity vs. relative humidity of Nafion 115 membranes from 30°C to 80°C (L. Maldonado(LEMTA)).*

Figure 1.10 presents preliminary experimental results obtained by L. Maldonado (LEMTA) on

Nafion 115 membranes at different temperatures for a relative humidity ranging from 0.2 to 0.95. The increase of σ with the relative humidity is in good agreement with the results of Sone *et al.* [SES96], as well as other predictions from the literature (Table 1.3).

The ionic conductivity of the curves in Figure 1.10 increases continuously over the whole temperature range (30 - 110°C), whereas experimental investigations of Sone *et al.* [SES96] on Nafion 117 membranes with different pretreatment protocols show an inversion of the sorption behavior at 45°C: σ decreases for temperatures between 20 and 45°C and increases for temperatures between 45 and 80°C. They explain this behavior with experimental results obtained on the evolution of the water uptake with temperature. They observed a decrease of λ with increasing temperature for temperatures between 20°C and 45°C, while above 45°C, the water uptake remains rather constant. Sone *et al.* [SES96] conclude that, for $T < 45°C$, the decrease of the ionic conductivity with the temperature is due to a decrease of λ. Above 45°C the water uptake remains constant and σ can be expressed by an Arrhenius equation.

The temperature dependency of the proton conductivity of Nafion membranes is generally described by an *Arrhenius relation* [SES96, ZDR$^+$93, ZJSD$^+$93]:

$$\sigma = A \exp(-\frac{E_A}{RT}) \tag{1.36}$$

where A, E_A and R denote the frequency factor (high temperature limit of the ionic conductivity depending on λ, thermal pretreatment, etc.), the activation energy (for ionic conduction) and the gas constant, respectively. The values of the activation energy E_A reported in the literature show a large dispersion, which confirms the effect of the heterogeneity of the preparation procedures on the ionic transport properties. For Nafion 117 for instance, a review of the literature yields values of E_A that vary between 2 $kJmol^{-1}$ and 40 $kJmol^{-1}$ [SES96, ZDR$^+$93, SDFP04, CES94, TCB00]. However, most of the data are comprised between 9.6 and 11 $kJmol^{-1}$ [SDFP04, CES94, TCB00].

All of the above cited expressions for the ionic conductivity are empirical relations, but there exist a few theoretical models. Thampan *et al.* for instance [TMTD00], derived a numerical expression, which is referred to as the *TMT expression*:

$$\sigma = \frac{F^2}{RT}(\varepsilon - \varepsilon_0)^q \left(\frac{D^e_{12}}{1+\delta}\right) c_{HA,0}\alpha \tag{1.37}$$

where ε and ε_0 denote the volume fraction of water in hydrated membranes and the percolation threshold, respectively. q, δ, $c_{HA,0}$ and α stand for the Bruggeman coefficient, the ratio of the binary D^e_{12} to the bulk effective diffusion coefficient D^e_{1M}, the concentration of acid groups in the membrane and the degree of acid-group dissociation, respectively.

The most common way to determine the ionic conductivity remains experimental by using impedance methods with four or two electrodes [SES96]. Usually, the resistance of the membrane R_{el} is measured at a fixed signal frequency and the ionic conductivity is given by:

$$\sigma = \frac{l}{R_{el}S} \tag{1.38}$$

where l represents the distance between the reference electrodes and S denotes the cross-sectional area of the membrane. σ stands thereby for the ionic conductivity in the in-plane directions. There exist also AC impedance spectroscopy methods to determine the proton conductivity of the membrane [XSA$^+$06]. The AC impedance of an isolated polymer membrane is generally purely resistive or shows a negligible imaginary part, so that equation (1.38) is sufficient for determining

the proton conductivity. However, with a membrane integrated in a fuel cell, R_{el} cannot be determined directly from the impedance spectrum, since the high frequency resistance R_{hf} is the sum of the electrolyte resistance, the resistances of the ionomer in the electrodes and the various electric contact resistances between the MEA components.

1.5.2 Porous electrodes

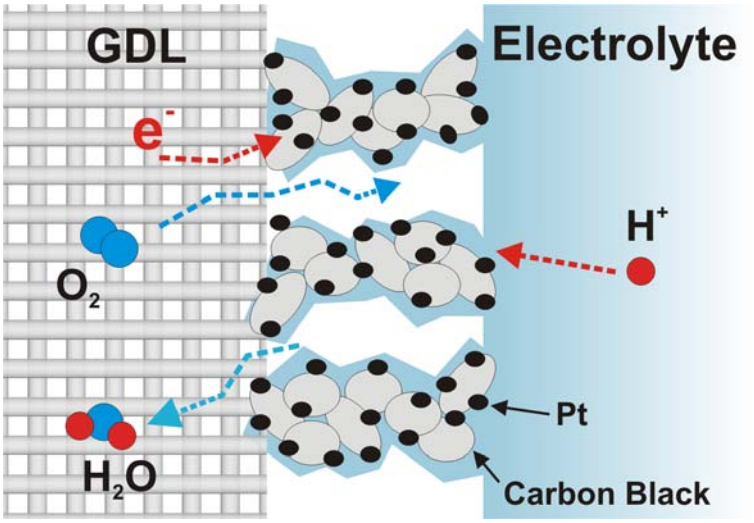


Figure 1.11: *Schematic representation of the transport processes in the porous active layer of a PEMFC. The electrons flow through the solid phase consisting of a mixture of carbon powder with catalyst particles (mostly Pt) that are embedded in the electrolyte, which ensures the hydronium ion transport. The gases and liquid water flow through the pores between the C/Pt clusters.*

The electrodes are considered herein as the components of the MEA that span from the membrane to the GDL (Figure 1.11). They are also referred to as *active layers* or *catalyst layers*. The reaction rates in PEMFC are limited by the low temperature ($< 100°C$) and the subsequent low reactivity of the gases, especially of oxygen. Thus, the utilization of a catalyst (usually platinum or platinum alloys) is necessary to limit performance losses. In state of the art PEMFC using carbon supported Pt catalyst (Pt/C) electrodes, about $2/3$ of the voltage losses at high current density ($1.5\ Acm^{-2}$) are due to slow ORR kinetics [GBLG09]. From Figure 1.11, it can be deduced that in addition to the charge separation, the electrodes are the place of complex coupled transport phenomena [LM04]:

- Transport of the reactants (hydrogen, oxygen) and products (vapor and liquid water) between the catalyst sites and the GDL.
- Proton transport between the active sites and the membrane.
- Electron transport between the reaction sites and the GDL.

The gas and liquid transport is realized *via* the porous structure of the catalyst layer. Proton conductivity is ensured by the ionomer, while electron transport occurs through the Pt and carbon particles (carbon black, typically Vulcan XC72, E-TEK Inc.). That is the reason why the electrochemical reaction should take place at the interface between three phases or materials: a fluid and

2 solids. In the literature, the reaction sites are often referred to as *triple phase boundaries* (TPB) or *triple phase zones* [OCCP06], which does not mean that there exists a well defined reaction interface. Figure 1.11 shows schematically that the reaction sites are dispersed inside the catalyst layer. One of the main issues in terms of electrode design is the optimization of the structure of the active layer in order to minimize transport losses. In parallel, another major issue is to minimize the quantity of platinum in active layers of PEMFC in order to reduce the cost of the cells. This can be obtained by:

- Increasing the specific catalyst activity (in Acm_{Pt}^{-2}) through the development of alternative catalyst materials (non-platinum metals) and/or alloying of platinum with transition metals.
- Increasing the active area of the catalyst by optimizing the carbon support (porosity, distribution of different phases, nano-structured supports) which can be obtained by improving the fabrication processes for catalyst layers.

In addition to these improvements, increasing the performance of the electrodes requires the optimization of several properties of the active layers, such as the reactant diffusivity, the ionic and electronic conductivity and to facilitate the removal of liquid water. Most of the current and emerging electrode preparation techniques are cited in a review by Litster and McLean [LM04]:

The PTFE-bound method was the standard fabrication method of PEMFC catalyst layers before the thin-film method. It consists in bounding catalyst particles with a hydrophobic PTFE structure. In order to ensure ionic transport to the reaction sites, the PTFE-bound catalyst layers are impregnated with Nafion by brushing or spraying. With this method, electrode catalyst loadings of 0.4 mg_{Pt}/cm^2 can be obtained [TDRS88, LM04]. Nevertheless, the platinum utilization in these catalyst layers does not exceed 20% [MHM94, CYH$^+$99].

In the thin-film method, the hydrophobic PTFE is replaced by the hydrophilic perfluorosulfonate ionomer to bind the carbon supported catalyst particles. Thus, the binding material in the active layer is that of the membrane, which increases the platinum utilization from 22 % up to 45.4 % [CYH$^+$99]. The platinum charge is also lower than in PTFE-bound catalyst layers (down to 0.1 mg_{Pt}/cm^2) [CL99].

Vacuum deposition methods include chemical, thermal or physical vapor deposition and sputtering. The sputtering of catalyst layers is a vacuum evaporation process that removes portions from a coating material (the catalyst material) to deposit a thin film of the target material onto a substrate, which can be the GDL or the membrane. Sputtering yields thin catalyst layers ($< 10\ \mu m$), with high power densities and low platinum loadings ($0.04 - 0.01\ mg_{Pt}/cm^2$)[OLCP02, CEM$^+$09]. O'Hayre *et al.* [OLCP02] compared the power density of a commercial coated MEA with a platinum loading of 0.4 $mgcm^{-2}$ to a sputter-deposited MEA with a platinum loading level of 0.04 $mgcm^{-2}$. The results showed that the maximum power output of the sputtered cell reached $3/5$ of the commercial cell performance, but with only $1/10$ of the catalyst loading. However, the performance of PEM electrodes with sputtered catalyst layers depends strongly on the catalyst film thickness [OLCP02] and suffers from the fact that Pt is deposited as a uniform film on the substrate [YCP$^+$08]. In recent years, it has been shown that highly porous catalyst layers with an average particle size of 8.9 *nm* can be obtained using a high-pressure (200 *mTorr*) sputtering method in a gaseous mixture of Ar and He. Yoo et al. [YCP$^+$08] showed that it is possible

to enhance the active surface of the porous Pt nanocatalyst layer of about 250 % by using a high-pressure sputtering technique.

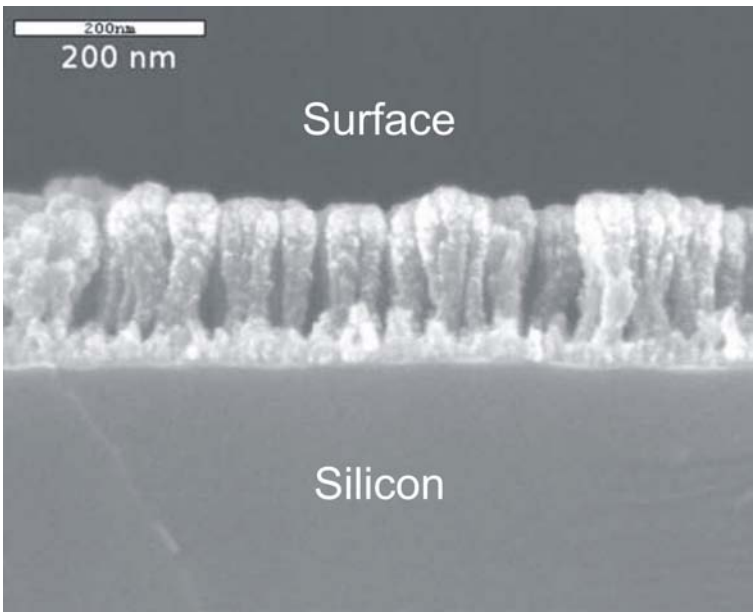


Figure 1.12: *SEM image of nanostructured C/Pt films on silicon wafers performed by Rabat et al. [RAB$^+$09] with a low pressure (< 1 Pa) sputtering process. The Pt particles (bright regions) are coated on the columnar carbon structures that have been deposited on a first sputtering step. The SEM micrograph is reproduced from Rabat et al. [RAB$^+$09].*

The methods cited above consist of plasma sputtering deposition of Pt particles on carbon electrodes. Alternative sputtering methods allowing the production of nanostructured electrodes with ultra-low Pt loading are developed and tested at the GREMI (*Groupe de Recherche sur l'Energétique des Milieux Ionisés*) in Orléans [CEM$^+$09, RAB$^+$09]. Rabat *et al.* [RAB$^+$09] deposited Pt/C nanostructures on silicon wafers with a low pressure (< 1 Pa) sputtering process, which allows to control the catalyst content and location (Figure 1.12). The catalyst layers are deposited in two steps: carbon is deposited first, forming a columnar structure on which the Pt particles are dispersed in a second sputtering process. This fabrication method yields catalyst layers with a good Pt dispersion and a low Pt loading (0.1 mg_{Pt}/cm^2) [RAB$^+$09]. However, the electrochemical performance of these catalyst layers has still to be evaluated. Cavarroc *et al.* [CEM$^+$09] manufactured ultra-low Pt content PEMFC electrodes by using magnetron co-sputtering of carbon and platinum on commercial uncatalyzed gas diffusion layers (E-TEK). In this deposition method, Pt is growing on carbon particles as clusters with a mean size lower than 2 nm to make catalyst layers with a Pt loading of 0.01 mg_{Pt}/cm^2. With such a low Pt loading, a PEMFC performance of 400 $mW cm^{-2}$ (corresponding to a specific power of $20 kW g_{Pt}^{-1}$) has been obtained with a MEA using a Nafion 212 membrane [CEM$^+$09]. Theses ultra-low Pt content MEA are currently tested in our laboratory.

Electrodeposition has been the focus of several studies in the last years as an alternative method for the preparation of PEMFC electrodes [VAT92, AlB$^+$10, KSP04, SSP$^+$10, SKVK09], since it allows to control the size, the amount and the distribution of the catalyst particles.

The principle of this electrode preparation technique is represented in Figure 1.13 according to Verbrugge [Ver94]:

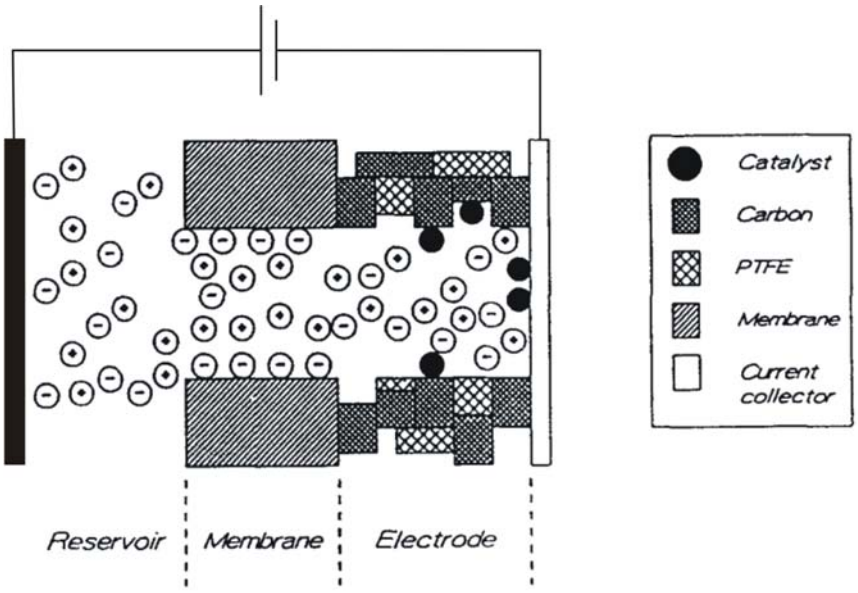


Figure 1.13: *Scheme of electrode preparation by electrodepostion based on the work of Verbrugge [Ver94]: an electrical current is applied between a platinum electrode and a current collector on which is placed the uncatalyzed MEA to reduce Pt ions. The Pt ions migrate through the acid-plating bath onto the carbon surface of the active layer.*

An uncatalyzed porous carbon substrate which is coated with Nafion on one side, is placed into a platinum acid-plating bath along with a platinum counter electrode. An electrical DC (or pulse) current is applied between both electrodes to reduce Pt ions that migrate onto the Nafion coated side of the GDL. The other side of the carbon substrate is usually covered to form a non-conductive surface, which prevents the deposition of catalyst ions. This method allows to produce electrodes with a very low catalyst loading (0.05 mg/cm^2 [VAT92]), as platinum is only deposited on regions that are impregnated with the perfluorosulfonate ionomer. State of the art electrodeposited active layers contain Pt loadings of about 0.3 mg_{Pt}/cm^2 [SSP$^+$10, AlB$^+$10, KSP04] and reach peak power densities of about 400 $mWcm^{-2}$ in H_2/O_2 PEMFC operated at 1 atm [KSP04]. Saibuathong *et al.* [SSP$^+$10] showed that pulse plating at low frequencies ($\approx 1\ Hz$) increases the ORR kinetics in PEMFC compared to an electrodeposition at constant DC current, since smaller catalyst particle sizes can be obtained, which increases the active area. Recently, Saminathan *et al.* [SKVK09] electrodeposited Pt nanoparticles on carbon nanotubes. With a Pt loading of 0.13 mg_{Pt}/cm^2, they obtained PEMFC performances (with Nafion 212 membranes) of 441 $mWcm^{-2}$ at 80°C using pure H_2 and O_2 at 1 atm and 90% RH.

Another way to reduce the amount of Pt in PEMFC electrodes without performance loss is the development of either non-platinum catalysts or more active platinum-catalysts. Two ways are proposed in the literature to improve the Pt mass activity:

- In core-shell concepts, a Pt monolayer is supported on non-platinum nanoparticles, which leads to a high active area and therefore to a high specific activity [AZS$^+$07]. Another way consists in applying ultra-thin Pt (alloy) coatings on nano-structured supports [DSVA06].

- Alloying Pt particles with transition metals, such as *Ni*, *Co*, *Ti* or *Fe* [SM09, CSY$^+$09, MMGL02, DMC$^+$10][Dubau2010a]. A surprisingly high specific activity was observed for the (111) surface planes of platinum alloys (especially of $Pt_3Ni(111)$ single crystals) [SM09, SFM$^+$07].

In this regard, Dubau *et al.* [DDM$^+$] analyzed the degradation mechanisms of nano-structured Pt_3Co/C particles and their impact on the catalytic activity of ORR in PEMFC. They found out that at low current densities (high cathode potentials), the composition of the particles changes as a result of a fast *Co* surface diffusion (Kirkendall effect). Initially homogeneous Pt_3Co/C particles turn into spherically shaped "hollow" nanoparticles with thick *Pt*-shells and with a higher intrinsic activity than the fresh catalyst.

The catalyst layer characteristics (thickness, porosity, Pt charge, etc.) are not uniform, but depend strongly on the fabrication method and the catalyst loading. Table 1.4 gives typical ranges of the main characteristics of platinum based catalyst layers.

Parameter	Unit	Numerical value	Ref
layer thickness δ_{al}	$[\mu m]$	$4-20$	[SWG93, BE97a]
C particle size d_C	$[nm]$	$10-100$	[YW08, Eik06]
Pt particle size d_{Pt}	$[nm]$	$2-3$	[SPK05a, EK99, SENVS03]
pore size d_{pore}	$[nm]$	$10-100$	[EAP98, GJL$^+$03, Eik06, LE08]
porosity ε_{al}	$[-]$	$0.2-0.35$	[FJW98, EAP98, IJL$^+$02]

Table 1.4: *Typical values of the main characteristics of PEMFC active layers.*

These structural properties are usually determined by *ex situ* methods, such as scanning electron microscopy (SEM), transmission electron microscopy (TEM), X-ray scattering techniques, mercury porosimetry, ... They can also be determined by *in situ* methods, such as cyclic voltammetry (CV) and electrochemical impedance spectroscopy (EIS). It has to be mentioned that EIS is used rather to analyze charge and mass transfer kinetics through the cell and that the geometrical properties of the active layer are usually taken as model parameters. Nevertheless, it is possible to estimate the geometrical characteristics *via* EIS, which could be a good way to test the reliability of this technique.

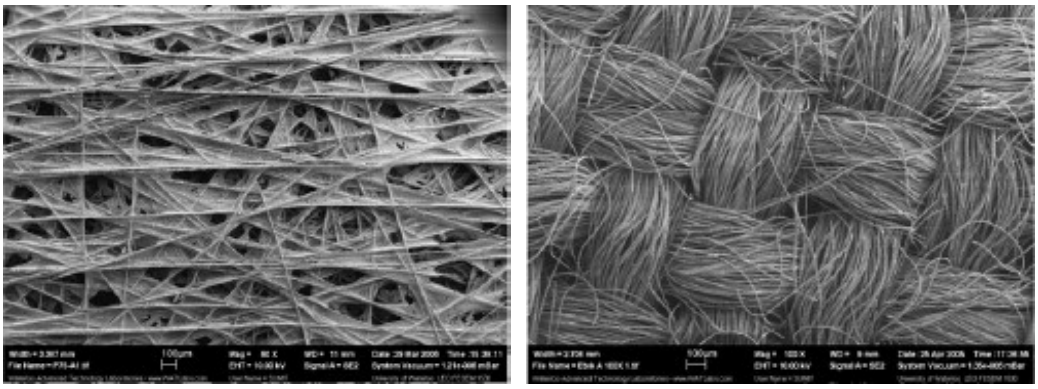
1.5.3 Gas diffusion layers

The *gas diffusion layers* (GDL) or *backing layers* homogenize the fluxes and the mechanical constrains between the gas channels of the bipolar plates and the catalyst layers. In addition, these layers serve often as physical support for the catalyst layers. Therefore, ideal GDL have to satisfy sometimes conflicting requirements [WBB$^+$04, PW04b, LM04]:

- Thin backing layers with a high fiber density have a better electronic and thermal conductivity, as well as low electrical contact resistances with the adjacent media.

- On the other hand, an efficient transport of reactants and products between the gas channels and the catalyst layers requires a high porosity and an hydrophobic coating is often needed in order to improve the ability of the GDL to evacuate liquid water.

GDL are necessarily porous media. By increasing their porosity, mass transfer can be improved at the cost of a drop in the electronic conductivity. In addition, the MEA is subjected to mechanical pressure aiming at establishing an intimate contact between its different components and limiting electrical contact resistances. However, this reduces the GDL thickness and porosity, which decreases the gas permeability [LHVZM99, DJK$^+$03]. All these factors have to be considered for the choice of a GDL.



(a) Ballard P75 carbon paper GDL (b) E-TEK Cloth'A' carbon cloth GDL

Figure 1.14: *SEM images of examples of carbon paper (a) and carbon cloth (b) [GFP$^+$06].*

Most of the GDL are fabricated from carbon paper or carbon cloth [WBB$^+$04, PW04b, LM04, GFP$^+$06] produced for instance by SGL Carbon Group, Toray Corporation, E-TEK Inc. or Ballard. Carbon papers (such as the Ballard P75 shown in Figure 1.14(a)) consist of straight or convoluted carbon fibers, whereas carbon cloth (such as the E-TEK Cloth 'A' in Figure 1.14(b)) consist of woven bundles of fibers called *tows*. The average pore size in carbon papers ranges from about 10 to 50 μm [PWC05, AST99], whereas the cloth weave offers relatively large openings between the bundles that range between 50 μm and 100 μm [AST99]. The carbon fibers have a mean thickness of about 10 μm [GFP$^+$06]. The typical thickness of the GDL varies from 200 to 400 μm [GFP$^+$06, WBB$^+$04] (cf. Table 1.5).

Gostick *et al.* [GFP$^+$06] found out that carbon papers with the most aligned fibers show the most pronounced anisotropy in permeability, which was expected considering the SEM pictures in Figure 1.14. In the case of carbon cloth, the tows have a lower permeability than the overall woven structure [GFP$^+$06]. Because of the layer's anisotropy, the through-plane and the in-plane permeabilities have to be distinguished. The permeabilities of commercial GDL are typically comprised between 1×10^{-12} m^2 and 50×10^{-12} m^2 [GFP$^+$06].

GDL	Porosity ε_{GDL} $[-]$	Thickness δ_{GDL} $[\mu m]$	Fiber diameter $[\mu m]$	Thermal conductivity $[Wm^{-1}K^{-1}]$
SGL 10BA	0.88	400	9.2	0.23 [RDLM08]
Ballard AvCarb® P75	0.85	210	7.4	1.3 [BAL]
Toray 090	0.80	290	9.2	1.6 [RL01, TI]
E-TEK Cloth 'A'	0.78	360	9.9	0.2 [VK04]

Table 1.5: *Thermophysical properties of a series of GDL used in PEM fuel cells [GFP$^+$06].*

The GDL porosity ε_{GDL} is most of the time determined by *mercury intrusion porosimetry* (MIP). An alternative method consists in weighing the sample before and after immersion in a wetting liquid, which fills the totality of the pores (*e.g.* decane). Both methods yield the same porosity values of about 0.8 [GFP$^+$06, WBB$^+$04, TI]. Some results are reported in Table 1.5. In operating fuel cells, ε_{GDL} is lower as a consequence of the MEA compression. The compressed porosity cannot be determined by external measuring methods. However, Springer *et al.* [SZWG96] estimated that the compressed porosity of an E-TEK backing layer (initially: $\varepsilon_{GDL} = 0.78$) could vary between 0.2 and 0.6. Taking into account a further influence of liquid water accumulation, they suggested that the mean value of the effective porosity could drop to about 0.4.

Beside the gas flow, the GDL ensure the electron and heat transport between the catalyst layer and the bipolar plates. Even if the main part of ohmic losses in a fuel cell is due to proton conduction through the membrane, the electron conductivity through the GDL is finite. For Toray TGPH-120 backing layers for example, an in-plane resistivity of about 0.005 Ωcm has been measured [WBB$^+$04, TI], which corresponds to an electronic conductivity of about 12.5 Scm^{-1}. Concerning heat transfer from the electrodes to the bipolar plates, the values of the GDL effective conductivity given in the literature show a large dispersion from 0.2 $Wm^{-1}K^{-1}$ for E-TEK materials [VK04] to 1.3 $Wm^{-1}K^{-1}$ for Ballard layers [BAL] (cf. Table 1.5). Experimental measurements of the temperature gradient between the interfaces of SGL backing layers (420 μm) subjected to a heat flux, performed by J. Ramousse in our laboratory revealed an effective thermal conductivity varying between 0.26 and 0.34 $Wm^{-1}K^{-1}$ at 20°C [RDLM08].

One of the main function of GDL is to facilitate the transport of gases and liquid water between the gas channels and the electrodes. On the one hand, the porous structure must allow the transport of the reactants and water, since the polymer electrolyte membrane needs to be hydrated for a good ionic conductivity (cf. section 1.5.1). On the other hand, a certain hydrophobicity is required to avoid saturating the pores with liquid water and impeding the gas transport and the electrochemical activity of the electrodes. That is the reason why polytetrafluoroethlene (PTFE) is added (through various methods) as hydrophobic agent and binder [LM04, WBB$^+$04, PW04b, LPS$^+$99]. However, PTFE is an electrical insulator and it reduces the layer's porosity, which results in higher oxygen transport losses [GAPP98]. Consequently, PTFE should be applied with care. As there exists no standard for the PTFE loading in backing layers, values from about 5 up to 60 *wt%* are reported in the literature [GFP$^+$06, LM04, SKVK09, KKL$^+$02].

One way to improve the removal of liquid water and to reduce the PTFE content in the GDL consists in inserting a thin hydrophobic *microporous layer* MPL at the interface with the active layer [WBB$^+$04, QK02a, QK02b, SCL01, LPS$^+$99] as shown in Figure 1.15. The MPL is made of the same material as the GDL, but it has a lower thickness (10 - 100 μm [GFI$^+$06, WBB$^+$04]) and a smaller mean pore size (0.1 - 1 μm [PWC05]). Furthermore, the MPL is usually more hydrophobic than the GDL, with PTFE contents between 20 and 35 % [LPS$^+$99, SCL01, QK02b]. The role of this hydrophobic sublayer is to enhance the water management (better humidification of the anode and enhanced water removal from the cathode) and to improve the electronic contact between the GDL and the catalyst layer [PWC05]. Several authors [PWC05] assume that the small MPL pores would improve the water back-flow through the membrane from the cathode to the anode by increasing the hydraulic pressure gradient. Thus, there is less water to evacuate through the cathode gas channel. According to others [QK02a, PW04a], the high hydrophobicity and the small pore sizes of the MPL would improve the liquid water evacuation from the catalyst layer to the gas channels, without any significant changes in the water flux through the membrane. Of course, both phenomena could occur simultaneously in practice.

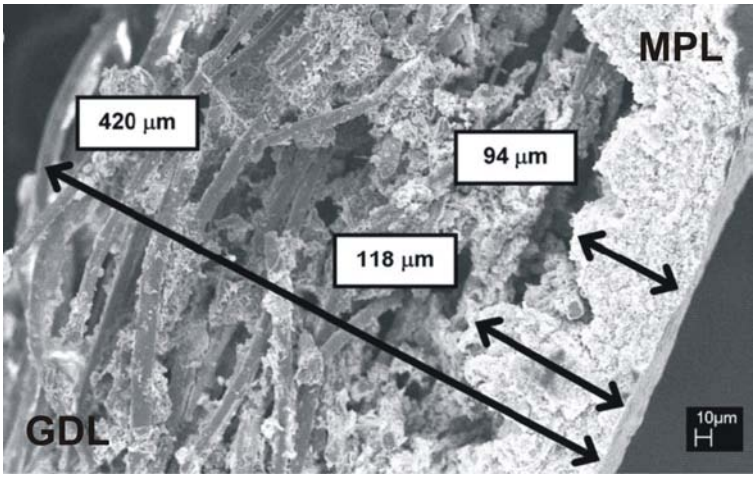


Figure 1.15: *SEM image of the cross-section of a SGL 10BB backing with a MPL (bright region on the right side) [GFI+06].*

1.6 Summary

In this chapter, a general introduction to fuel cells and their operation mode is given with a focus on PEM fuel cells. The chapter begins with a presentation of the basic principles of electrochemical reactions, which are the same for all kinds of fuel cells. However, the electrolyte as well as the nature of the exchanged ions and of the operating conditions differ, and an overview of the existing types of fuel cells is given.

Fuel cells convert chemical energy of a reactant/oxidant pair into electrical energy and heat. It is shown that the reversible *open circuit voltage* (OCV) can be derived from thermodynamics, which leads to the *Nernst equation*, a fundamental equation in electrochemistry. However, in real systems, especially when a net current is produced, the cell voltage is lower than the OCV. The different voltage drops and the typical shape of the resulting current-voltage curve (polarization curve) are thus exposed.

The *Membrane Electrode Assembly* MEA of PEMFC consists of different components that differ in their geometry and physical properties. Each of them (membrane, GDL, catalyst layers) has a well defined function that contributes to the operation of the cell. In order to optimize the efficiency, the MEA components have to fulfill certain conditions that are discussed in this chapter.

Starting from this presentation, the next chapter presents the main physical phenomena that govern the cell operation, according to the most widely accepted theoretical descriptions that can be found in the literature.

2 Main Physical Phenomena Governing the Operation of a PEM Fuel Cell

The different physical phenomena occurring in a fuel cell MEA are highly coupled. For instance, the kinetics of the electrochemical reactions depend on the gas concentration and thus on the mass transport through the diffusion layers (flow fields, GDL and active layers). In addition, the reaction kinetics and the mass transport depend on a variety of factors, such as the operating conditions, the geometry and the state of water. In order to make objective statements about mass transfer limitations in PEMFC diffusion media, it is necessary to understand the physical phenomena inside a porous electrode and the factors influencing them. This chapter describes the basic physical phenomena of charge and mass transport inside the electrodes of a PEMFC as well as some common representations of the porous structure of the active layers.

This is the first step toward impedance models that allow to discriminate between the different transfer processes and to identify the origin of the oxygen transport limitations.

2.1 Description of the Reaction Kinetics

After presenting the different steps of the half-reactions at the electrodes of a PEMFC, the fundamental *Butler-Volmer equation* is derived. This equation expresses the current density as a function of the activation overpotential and the reagent concentrations. It accounts thus indirectly for the influence of the electrode properties (roughness, catalytic activity, etc.) and the operating conditions (temperature, pressure, relative humidity, etc.) on the electric performance. For high current densities, one of the two half reactions can be neglected and the Butler-Volmer equation simplifies into a form known as *Tafel law*.

2.1.1 Electrochemical half-reactions

The oxygen reduction reaction (ORR) (1.3) at the cathode is significantly slower and more complex than the hydrogen oxidation reaction (HOR) (1.2) at the anode. Therefore, the performance losses due to the ORR are predominant and the studies of PEMFC performance focus most of the time on the cathode. Nevertheless, the reaction rate of the HOR is finite. The half-reactions at the anode and the cathode can be decomposed into five main stages presented schematically in Figure 2.1 (in the case of the HOR):

- Gas transport through the diffusion media to the reaction sites.
- Physical adsorption on the catalyst surface.
- Dissociation of the adsorbed molecule (chemisorption).

- Charge transfer between the adsorbed species and the catalyst surface.
- Recombination of the ionized atom with other reactants to form the product molecule.

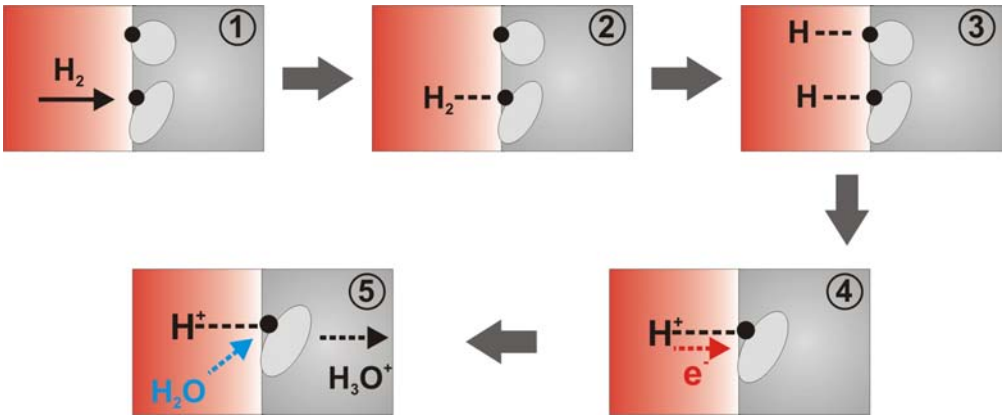


Figure 2.1: *Schematic representation of the main steps of H_2 oxidation: 1. Gas diffusion to the active sites; 2. Adsorption; 3. Molecule dissociation; 4. Electron transfer between atom and catalyst; 5. Recombination of the ionized atoms to form the product molecule.*

Hydrogen Oxidation Reaction

The hydrogen oxidation reaction (HOR) at the anode of a PEMFC and its inverse process, the hydrogen evolution reaction (HER) at the cathode of an electrolyzer, have been the focus of many studies because they are considered as archetypal processes in electrochemistry. They are generally described in the literature by a two step mechanism [CT02, MBK05]. However, electrochemical impedance studies performed by Meland *et al.* [MKB06, MK07] pointed out that the hydration of the hydrogen ions represents a third rate-determining step of the HOR.

The first step of the HOR on platinum consists in a dissociative adsorption of hydrogen at the catalyst surface, that can result from two reactions:

$$\text{Tafel reaction:} \quad H_2 \rightarrow 2H_{ads} \tag{2.1}$$

$$\text{Heyrovsky reaction:} \quad H_2 + H_2O \rightarrow H_{ads} + H_3O^+ + e^- \tag{2.2}$$

where H_{ads} stands for the hydrogen atoms adsorbed on the active catalyst sites. In the *Tafel reaction* (2.1), the adsorbed atoms H_{ads} result from regular dissociative chemisorption of the hydrogen molecules. In the *Heyrovsky reaction*, they result from dissociative ionization of the hydrogen molecules (2.2). The strength of the metal-H bond determines which one of both reactions is predominant, but this will be explained in more details below. There exist two widely accepted descriptions of the adsorption of H_2 as a function of the gas pressure P_{H_2}: the Langmuir isotherm, which considers the adsorption enthalpy of hydrogen on the metal surface ΔH_{ad} independent of the surface coverage and the Temkin isotherm which assumes a linear change of ΔH_{ad} with the surface coverage.

Results of electrochemical impedance measurements on hydrogen electrodes performed by Meland *et al.* [MBK05] indicate that the adsorption reaction appears in the carbon layer in front of

the catalyst surface which is the place of the charge transfer. They conclude that hydrogen adsorption takes place in combination with a subsequent surface diffusion of the adsorbed hydrogen molecules toward the active sites.

The adsorbed hydrogen atoms H_{ads} are then oxidized in a second step, the *Volmer reaction*:

$$H_{ads} + H_2O \rightarrow H_3O^+ + e^- \tag{2.3}$$

This leads to two possible oxidation processes, the *Tafel-Volmer mechanism* ((2.1) + (2.3)) or the *Heyrovsky-Volmer mechanism* ((2.2) + (2.3)), depending on the electrode material, or more precisely on the adsorption enthalpy ΔH_{ad} on the catalyst. A high metal-H bond enthalpy tends to weaken the H-H bond and to inactivate the adsorbed hydrogen atoms for further reactions at the expense of the Heyrovsky reaction (2.3).

The efficiency of a metal as a catalyst is thus determined by its activity with respect to the adsorption enthalpy of hydrogen. The exchange current density j_0 is an indicator of the electrochemical activity of a catalyst. Its evolution with the strength of the metal-H bond, *i.e.* in terms of the adsorption enthalpy ΔH_{ad} is shown on the *Volcano curve* (Figure 2.2).

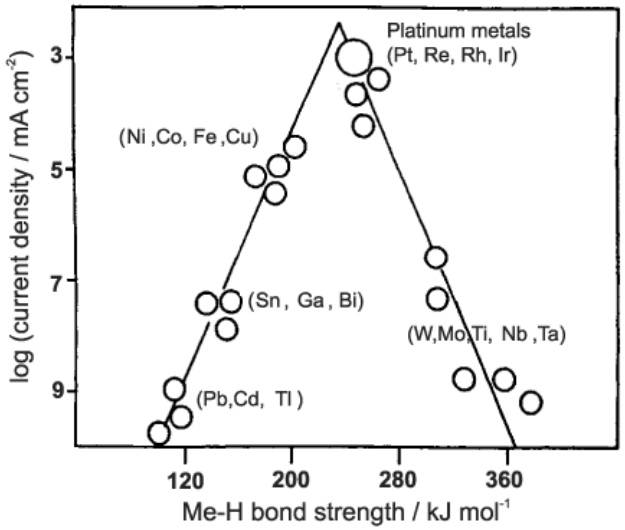


Figure 2.2: *Volcano curve: exchange current densities of the hydrogen oxidation (resp. the hydrogen evolution) reaction as functions of the adsorption enthalpy on different metals in aqueous $1N\ H_2SO_4$ solution at ambient temperature [WSONL05].*

The Volcano curve (Figure 2.2) shows clearly that platinum metals (catalytic noble metals: Pd, Pt, Rh, Ir, and Ru) are preferable because they present moderate adsorption enthalpies and yield therefore high exchange current densities. The highest exchange current densities are reached with platinum. In standard conditions, the values reported in the literature vary between 0.5 $mAcm_{Pt}^{-2}$ and 30 $mAcm_{Pt}^{-2}$ in acidic media [BR73, CT02, Boi05, WSONL05]. These data refer to the platinum surface A_{Pt}. In order to obtain the exchange current density referring to the electrode flat surface $A_{geom} = A_{Pt}/\gamma$ they have to be multiplied by the electrode roughness ($\gamma \approx 100$), which leads to values ranging from 0.05 Acm^{-2} to 3 Acm^{-2}. The exchange current densities of the HOR measured on an isolated electrode are of the same order of magnitude as the current densities in a working PEMFC. For comparison, the exchange current densities measured for the oxygen reduction reaction at PEMFC cathodes vary between $10^{-6}\ A\,cm_{Pt}^{-2}$ and $10^{-9}\ A\,cm_{Pt}^{-2}$

[Boi05, CR01, APBDSS+92, PSAM92, SPK05a, CR01]. Therefore, the HOR is usually considered as reversible and not limiting for the operation of the fuel cell.

Oxygen Reduction Reaction

According to the majority of the authors, the oxygen reduction reaction (ORR) is the limiting step in PEMFC [SZWG96, EK99, KLSC95]. The ORR has been the focus of many theoretical and experimental studies, but some details have still to be clarified [Boi05, ABD01, WSONL05]. Up to now, the Damjanovic mechanism [DB67, ABD01, SVD81, Adz98] is a widely accepted description of the ORR on platinum in acidic media.

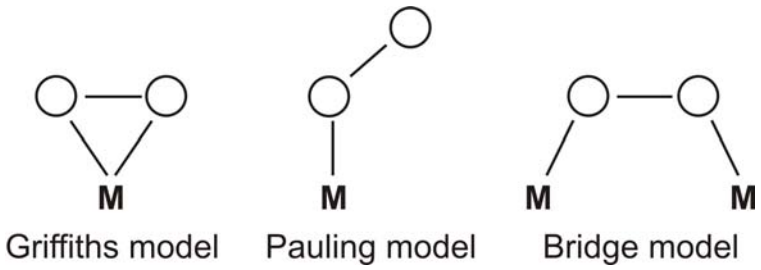


Figure 2.3: *Possible configurations for O_2 adsorption on catalyst sites [Adz98].*

The first step consists in a fast O_2 chemisorption on the catalyst surface. The subsequent reaction mechanism depends on the way oxygen is adsorbed at the metal surface [Adz98]. Some examples of O_2 adsorption configurations are shown in Figure 2.3. Dual adsorption sites (Griffiths model, bridge model) are likely to favor the direct reaction process (2.4), since the surface interaction is strong enough to substantially weaken the O-O bond. Single bond adsorption sites (Pauling model) do not weaken the O-O bond sufficiently and the indirect process is favored in this case.

Two reaction processes following the chemisorption are thus possible:

- A direct **four-electron transfer** mechanism that leads to water production according to:

$$(O_2)_{ads} + 4H^+ + 4e^- \rightarrow 2H_2O \tag{2.4}$$

  Antoine *et al.* [AD00] confirmed by studies on rotating ring-disc electrodes (RRDE) that this process is predominant in the O_2 reduction on platinum.

- An indirect reduction process with a **two-electron transfer** mechanism that can, for example, produce H_2O_2 as an intermediate species which is finally reduced to water in an additional step:

$$O_2 \quad +2H^+ + 2e^- \rightarrow H_2O_2 \tag{2.5}$$
$$H_2O_2 \quad +2H^+ + 2e^- \rightarrow 2H_2O \tag{2.6}$$

The two-electron reaction process can include many parallel and consecutive steps. The details of the reaction cannot be determined by stationary measurements. Using electrochemical impedance spectroscopy, Antoine *et al.* [ABD01] could validate an ECE mechanism (a first

Electrochemical step followed by a global **C**hemical step and a final **E**lectrochemical step) which is in agreement with Damjanovic's statement. Their investigations thus allowed to validate the Damjanovic mechanism which is widely accepted but had not been proved before. The ECE-mechanism can be summarized as follows [ABD01]:

After the O_2 chemisorption on the catalyst sites, there is a first electrochemical step, the protonation of the oxygen molecules, which is considered as the rate determining step (RDS):

$$(O_2)_{ads} + H^+ + e^- \rightarrow X_{ads} \tag{2.7}$$

X_{ads} represents the adsorbed intermediate species which are mainly O_{ads}, $(OH)_{ads}$ and $(O_2H)_{ads}$. Studies performed by Sepa *et al.* [SVD81] showed that O_{ads} may be the predominating intermediate species. The protonation of oxygen molecules is also the rate determining step in the direct reaction mechanism. At high potentials (low current densities), the surface concentration of the adsorbed intermediate species is mediate ($0.2-0.3$ [Boi05]) and varies linearly with the potential, the PH and the oxygen pressure according to a Temkin isotherm. At low potentials (high current densities), the surface coverage by the adsorbed intermediate species is very low (< 0.05 [Boi05]) and varies according to a Langmuir isotherm.

After this first electrochemical step, the ECE mechanism assumes a chemical step (2.8) followed by a final electrochemical step to produce water (2.9). For instance, assuming that $(O_2H)_{ads}$ are the adsorbed intermediate species produced by the first step (2.7), the chemical and the final electrochemical steps could be:

$$(O_2H)_{ads} \quad + H_2O \leftrightarrow 3\,(OH)_{ads} \tag{2.8}$$
$$(OH)_{ads} \quad + H^+ + e^- \rightarrow H_2O \tag{2.9}$$

The O_2 reduction reaction is a strongly restricted process that requires activation overpotentials of about 200 mV - 300 mV in acidic media on Pt surfaces [Mar04]. This can be explained by:

- A limited electrochemical activity of the adsorbed species at the reaction surface. With exchange current densities j_0 varying mostly between $10^{-6}\,A\,cm_{Pt}^{-2}$ and $10^{-9}\,A\,cm_{Pt}^{-2}$ [Boi05, CR01, APBDSS$^+$92, PSAM92, SPK05a, CR01, GCG$^+$98, ABDO98, RL01] the ORR is highly irreversible.
- A limited gas diffusivity in the GDL and catalyst layer, especially when the fuel cell is fed with air instead of pure O_2 [Des08].
- High mass transport losses and inactive reaction sites due to the flooding of the pores of the catalyst layer and of the GDL by the water produced by the ORR.

Several solutions exist to improve the ORR kinetics. Most of them focus on the increase of the electrode active area and catalyst activity. However, in order to realize these improvements, the origin of the different losses in the ORR have to be identified including those resulting from oxygen transport limitations.

2.1.2 Cell potential and reaction rate: Butler-Volmer law

The charge transfer is generally considered as the rate determining step in the oxygen reduction reaction [ABD01]. Its rate depends on various factors such as the operating conditions (pressure,

temperature, relative humidity), the catalytic activity, but also on the difference between the (internal) potentials[1] of the metal phase and of the electrolyte, $e = \Phi_m - \Phi_s$ being the driving force of the reaction. The oxidation half-reaction is favored for very positive values of e, whereas the reduction half-reaction rate increases when e decreases. Note that the potential difference e is only measurable with respect to a reference electrode (at the potential e_{ref}), that is to say $E = e - e_{ref}$. The equation relating the reaction rate (the faradaic current density j_f) to the electrode potential E is the *Butler-Volmer equation*, which is derived in the following.

Let us consider a general reversible electrochemical reaction between an oxidizing (Ox) and a reducing (Red) agent:

$$Ox + ne^- \longleftrightarrow Red \tag{2.10}$$

where n stands for the number of electrons exchanged during the reaction. In order to maintain the reaction, the species have to overcome a maximum of energy G_a^* which corresponds to the *activated state*. The difference between the energy of the reactants G^* and the activated state is denoted by ΔG^*. The reagent energy G^* is here the sum of the chemical (Gibbs) energy and of the electrical energy resulting from the potential difference between Φ_m and Φ_s. Figure 2.4 depicts schematically the energy profiles of a redox reaction of the form of equation 2.10 at equilibrium.

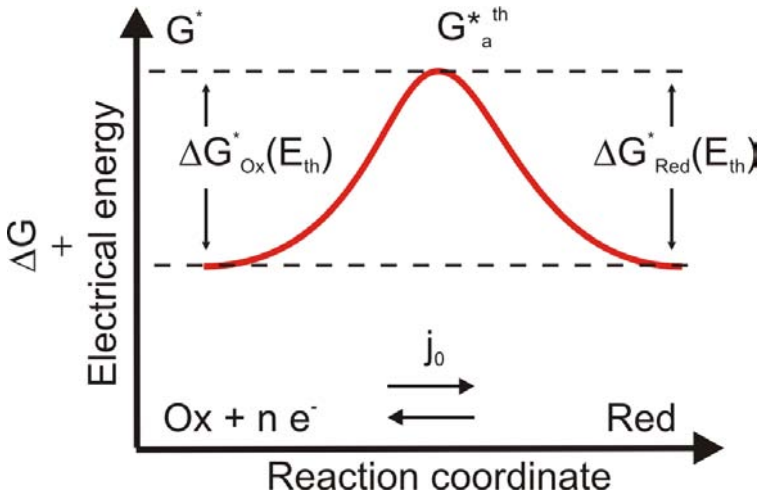


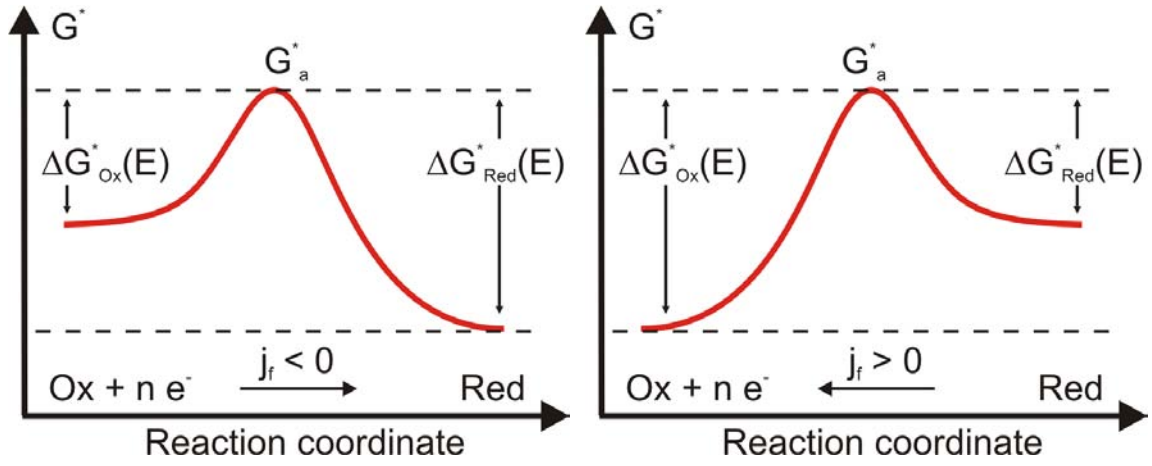
Figure 2.4: *Energy profile of a redox reaction $Ox + ne^- \leftrightarrow Red$ at equilibrium: $E = E_{th}$.*

In reversible conditions ($E = E_{th}$ as given by the Nernst equation (1.20)), the net current is null. In this case, the rates of reduction and oxidation are the same, as well as the activation energies of both species $\Delta G^*_{Ox/Red}$ (Figure 2.4):

$$\Delta G^*_{Ox}(E_{th}) = \Delta G^*_{Red}(E_{th}) = \Delta G^*_{eq} \tag{2.11}$$

Beyond equilibrium ($E \neq E_{th}$), the energy profile is unbalanced and the reaction rate is higher in one direction than in the other. If the electrode potential is lower than the equilibrium potential ($E < E_{th}$, Figure 2.5(a)), the activation energy of the reduction reaction is lower than that of the oxidation reaction ($\Delta G^*_{Ox} < \Delta G^*_{Red}$) and a negative net current is observed. If the cell potential is

[1] Potentials build by charge accumulation in the electrical double layer at the electrode/electrolyte interface, also known as *Galvani potentials*; cf. section 2.2.2



(a) At a cell potential: $E < E_{th}$ (b) At a cell potential: $E > E_{th}$

Figure 2.5: *Possible energy profiles of an electrochemical reaction of the type $Ox + ne^- \leftrightarrow Red$ beyond equilibrium $E \neq E_{th}$.*

higher than the equilibrium potential ($E > E_{th}$, Figure 2.5(b)), the oxidation reaction is predominant and the cell current is positive.

The reaction rates depend on the probability P_i^{act} of finding the reactant species $i = Ox, Red$ in the activated state:

$$P_i^{act} = \exp\left\{-\frac{\Delta G_i^*}{RT}\right\} \tag{2.12}$$

Hence, the rates v_i (in $mol\,m^{-2}s^{-1}$) of the half-reactions can be expressed as functions of the reagent concentrations at the electrode interface $c_i(0)$, the probability of finding them in the activated state P_i^{act} and the frequency at which they decay into products f_i [OCCP06]:

$$v_i = c_i(0) \times f_i \times P_i^{act} \tag{2.13}$$

The net reaction rate v is given by the difference between the partial reaction rates of reduction v_{Ox} and oxidation v_{Red}:

$$\begin{aligned} v &= v_{Ox} - v_{Red} \\ &= c_{Ox}(0) f_{Ox} e^{-\frac{\Delta G_{Ox}^*}{RT}} - c_{Red}(0) f_{Red} e^{-\frac{\Delta G_{Red}^*}{RT}} \end{aligned} \tag{2.14}$$

v_{Ox} and v_{Red} can be used to express the current densities of the partial reactions:

$$j_i = -nF v_i \tag{2.15}$$

that determine the net faradaic current density j_f in steady-state:

$$\begin{aligned} j_f &= j_{Ox} - j_{Red} \\ &= nF\left[c_{Red}(0) f_{Red} e^{-\frac{\Delta G^*_{Red}}{RT}} - c_{Ox}(0) f_{Ox} e^{-\frac{\Delta G^*_{Ox}}{RT}}\right] \end{aligned} \tag{2.16}$$

At thermodynamic equilibrium, the faradaic current density is null: the current densities of the forward and reverse reactions correspond to the exchange current density j_0 (Figure 2.4):

$$j_0 = nF c^*_{Ox} f_{Ox} e^{-\frac{\Delta G^*_{eq}}{RT}} = nF c^*_{Red} f_{Red} e^{-\frac{\Delta G^*_{eq}}{RT}} \tag{2.17}$$

In this case, the species concentrations at the electrode surface correspond to their bulk values c^*_i and the activation barriers of both partial reactions are equal to the equilibrium activation energy ΔG^*_{eq} (2.11).

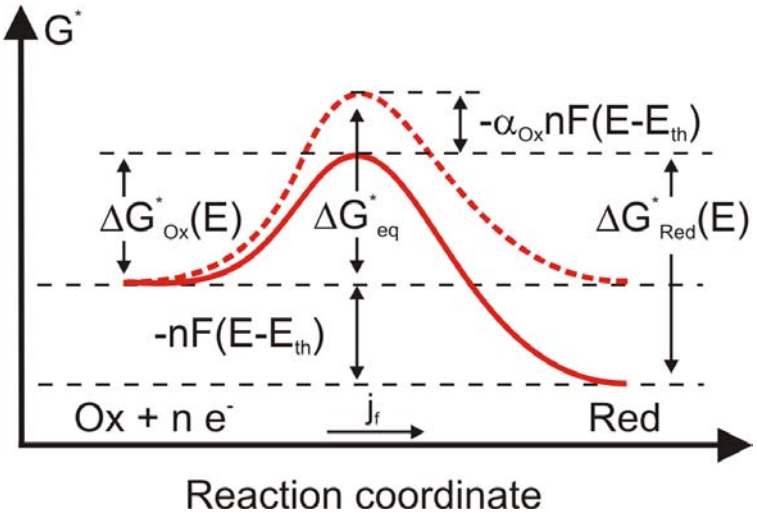


Figure 2.6: *By reducing the voltage by $E - E_{th}$ the energy profile is unbalanced in favor of the reduction reaction which results in a net current density j_f.*

In order to obtain a net faradaic current density j_f, one of the two activation barriers has to be smaller than the other. The example of Figure 2.6 shows that reducing the cell equilibrium voltage results in an increase of the rate of the reduction reaction, while reducing the rate of the oxidation reaction. The activation barriers in both reaction directions can be expressed in terms of the voltage E and of the *charge transfer coefficient* α. This latter is an indicator of the symmetry of the energy curve in the vicinity of the activated state, *i.e.* it is a measure of the preferred reaction direction. Its value varies between 0 and 1: $0 \leq \alpha \leq 1$. Note that a catalyst modifies the activation energy of the electrochemical reaction and has thus a direct influence on the charge transfer coefficient. An appropriate catalyst creates intermediate adsorption bonds between the reactants and the metal which increases the value of α in one direction and thus accelerates the reaction rate in this direction.

According to Figure 2.6, the activation barrier for the reduction reaction is reduced by a portion of the voltage difference, characterized by the charge transfer coefficient of the oxidizing agent α_{Ox}:

$$\Delta G^*_{Ox}(E) = \Delta G^*_{eq} + \alpha_{Ox} nF(E - E_{th}) \tag{2.18}$$

Whereas, the Gibbs free energy of the oxidation reaction $\Delta G^*_{Red}(E)$ is increased by:

$$\Delta G^*_{Red}(E) = \Delta G^*_{eq} - (1-\alpha_{Ox})\, nF(E-E_{th}) \tag{2.19}$$

Note that in this example $E < E_{th}$. Defining the charge transfer coefficient of the reducing agent α_{Red} by:

$$\alpha_{Red} = 1-\alpha_{Ox}, \tag{2.20}$$

equation (2.19) can be written:

$$\Delta G^*_{Red}(E) = \Delta G^*_{eq} - \alpha_{Red} nF(E-E_{th}) \tag{2.21}$$

This allows to express the current densities of the partial reactions (2.15) as functions of the exchange current density (2.17):

$$j_{Red} = j_0 \frac{c_{Red}(0)}{c^*_{Red}} e^{\frac{\alpha_{Red} nF(E-E_{th})}{RT}} \tag{2.22}$$

$$j_{Ox} = j_0 \frac{c_{Ox}(0)}{c^*_{Ox}} e^{-\frac{\alpha_{Ox} nF(E-E_{th})}{RT}} \tag{2.23}$$

In order to simplify the notations, the *activation overpotential* η_{act} is introduced:

$$\eta_{act} = E - E_{th} \tag{2.24}$$

The expression of the faradaic current density (2.16) as a function of η_{act} is called the *Butler-Volmer equation*:

$$j_f = j_0 \left[\frac{c_{Red}(0)}{c^*_{Red}} \exp\left\{ \frac{\alpha_{Red} nF}{RT} \eta_{act} \right\} - \frac{c_{Ox}(0)}{c^*_{Ox}} \exp\left\{ \frac{-\alpha_{Ox} nF}{RT} \eta_{act} \right\} \right] \tag{2.25}$$

In the absence of mass transport limitations ($c_{Ox/Red}(0) = c^*_{Ox/Red}$), the Butler-Volmer equation reduces to:

$$j_f = j_0 \left[\exp\left\{ \frac{\alpha_{Red} nF}{RT} \eta_{act} \right\} - \exp\left\{ \frac{-\alpha_{Ox} nF}{RT} \eta_{act} \right\} \right] \tag{2.26}$$

In a fuel cell, the activation overpotential $\eta_{act,a}$ of the HOR is counted positive, while the one of the ORR $\eta_{act,c}$ is negative. The reaction rate of the ORR at the cathode of a PEMFC is more limited than that of the HOR at the anode and $|\eta_{act,c}|$ is generally significantly higher than $|\eta_{act,a}|$. Since the extraction of a net cell current requires the same electron transfer at the anode than at the cathode, the absolute values of the faradaic current density in steady-state are the same at both electrodes, $\left|j_{f,a}\right| = \left|j_{f,c}\right|$.

Figure 2.7 shows a typical evolution of the faradaic current density (black lines) with the activation overpotential as predicted by the Butler-Volmer equation (2.25) for different values of α_{Red} [Boi05]. The graphs of the current densities of the partial reactions are plotted in gray. The curves are obtained by setting the species concentrations at the reaction interface to their bulk values. This assumption is not necessarily true, because the concentration at the reaction interface depends on the gas stoichiometry and on the mass transfer conditions in the backing layers, in the

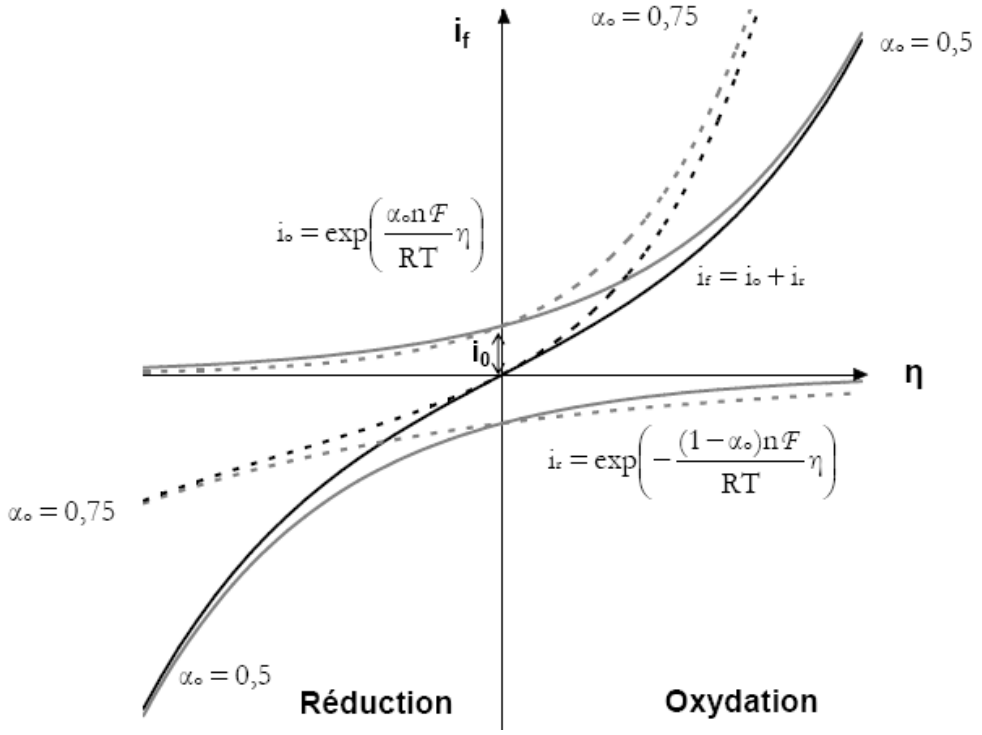


Figure 2.7: *Faradaic current density according to the Butler-Volmer law (black lines) and current densities of the partial reactions (gray lines) provided that the surface concentrations correspond to their bulk values. Solid line: $\alpha_{Red} = 0.5$. Dotted line: $\alpha_{Red} = 0.75$. [Boi05]*

active layers and in the flow field channels. The curves in Figure 2.7 show that at zero faradaic (net) current density, the current densities of the half-reactions (in gray) have the same absolute value corresponding to the exchange current density j_0. At a non zero net current density, a completely symmetric curve with reference to the overpotential η is observed for $\alpha_{Red} = \alpha_{Ox} = 0.5$. When $\alpha_{Red} \neq 0.5$, the current-voltage curve is unbalanced and one of the partial reactions proceeds faster than the other at a given overpotential.

The Butler-Volmer equation (2.25) can be simplified for high and low overpotentials (in absolute values):

At low values of $|\eta_{act}|$ (low current densities), the exponential can be approached by $e^x = 1 + x$. Assuming furthermore that in this case, the species concentrations at the reaction interface correspond to their bulk values $c_{Red/Ox}(0) = c^*_{Red/Ox}$, j_f can finally be approached by:

$$\begin{aligned} j_f &= j_0 \left(\frac{\alpha_{Red} nF}{RT} \eta_{act} + \frac{(1-\alpha_{Red})nF}{RT} \eta_{act} \right) \\ &= j_0 \frac{nF}{RT} \eta_{act} \end{aligned} \tag{2.27}$$

So that the overpotential can be written:

$$\eta_{act} = \frac{nF}{RT} \cdot \frac{j_f}{j_0} \tag{2.28}$$

At high values of $|\eta_{act}|$ one of the exponentials can be neglected with respect to the other. Depending on the sign of η_{act}, two cases have to be considered.

By convention, at the anode of a PEMFC ($Red = H_2$), the overpotential $\eta_{act,a}$ is positive and (2.25) becomes:

$$j_f = j_0 \frac{c_{H_2}(0)}{c^*_{H_2}} \exp\left\{\frac{\alpha_{H_2} nF}{RT}\eta_{act,a}\right\} \tag{2.29}$$

It is more usual to express the overpotential as a function of the current density so that equation (2.29) takes the form:

$$\eta_{act,a} = \frac{RT}{\alpha_{H_2} nF} \ln\left(\frac{j_f}{j_0 \frac{c_{H_2}(0)}{c^*_{H_2}}}\right) \tag{2.30}$$

At the cathode of a PEMFC ($Ox = O_2$) the activation overpotential as well as the faradaic current density are negative: $\eta_{act,c}, j_f < 0$. Thus, at high current densities, (2.25) reduces to:

$$j_f = -j_0 \frac{c_{O_2}(0)}{c^*_{O_2}} \exp\left\{\frac{-\alpha_{O_2} nF}{RT}\eta_{act,c}\right\} \tag{2.31}$$

or more commonly:

$$\eta_{act,c} = -\frac{RT}{\alpha_{O_2} nF} \ln\left(\frac{-j_f}{j_0 \frac{c_{O_2}(0)}{c^*_{O_2}}}\right) \tag{2.32}$$

By convenience, the absolute values of $\eta_{act,c}$ and j_f are generally used. Hence, (2.30) and (2.32) can be written under the same form, known as the *Tafel law*:

$$\eta_{act} = b \cdot \ln\left(j_f\right) + a \tag{2.33}$$

where a and b are parameters characterizing the reaction kinetics that can be used for the identification of α and j_0. b represents the *Tafel slope* for the oxygen reduction or the hydrogen oxidation reaction:

$$b_{H_2} = \frac{RT}{\alpha_{H_2} nF} \quad and \quad b_{O_2} = \frac{RT}{\alpha_{O_2} nF} \tag{2.34}$$

In the majority of the cases cited in the literature [Boi05, ABDO98, SPK05a], its values are situated around 60 $mVdec^{-1}$ at low current densities or 120 $mVdec^{-1}$ at high current densities. Nevertheless, values above 200 $mVdec^{-1}$ are also reported [BWJ+05, CR01]. In chapter 3, we present some results obtained by using global and locally resolved electrochemical impedance spectroscopy.

a depends on the reactant concentration, the Tafel slope and the exchange current density:

$$a_{H_2/O_2} = -b_{H_2/O_2} \ln\left(j_0 \frac{c_{H_2/O_2}(0)}{c^*_{H_2/O_2}}\right) \tag{2.35}$$

With equations (2.33)-(2.35), it is possible to compare the order of magnitude of the overpotentials at the anode and at the cathode. For this, let us suppose $\alpha_a = \alpha_c = 0.5$ and a gas supply so that $c_i(0) = 1/2c_i^*$. The exchange current density is set to $j_0^a = 3.2\,10^{-1}\ Acm^{-2}$ at the anode [Boi05] and to $j_0^c = 4\,10^{-5}\ Acm^{-2}$ at the cathode [BWJ+05]. The cathode and anode activation overpotentials (absolute values) for a PEMFC working at $j_f = 0.5\ Acm^{-2}$, at a temperature $T = 60°C$ are then expected to be:

$$\eta_{act,a} \backsimeq 0.03\ V \tag{2.36}$$
$$\eta_{act,c} \backsimeq 0.3\ V \tag{2.37}$$

Moreover, by supposing $\alpha_c = 0.75$, keeping the other parameters unchanged, it comes:

$$\eta_{act,c} \backsimeq 0.2\ V \tag{2.38}$$

As expected, a charge transfer coefficient $\alpha_c = 0.75$ shifts the activation energy barrier in favor of the reduction reaction at the cathode by decreasing $\eta_{act,c}$. However, the activation overpotential still remains significantly higher at the cathode than at the anode. Even if this example gives only rough estimates of the actual values, it illustrates well that the ORR remains the limiting factor in the energy conversion process of a PEMFC.

2.2 Electrical Double Layer and Double Layer Capacity

The electrode/electrolyte interface is the place of separation between ions and electrons. As the whole interfacial region is electrically neutral, every charge variation in the metal phase is compensated by an accumulation or loss of ions in the electrolyte. This results in the appearance of an electrical double layer at the electrode/electrolyte interface that behaves in a first approximation like a capacitor. Thus, in a dynamic regime, a part of the electrical current is due to the variation of the charge distribution at the reaction interface associated to a change in the potential difference between both phases. In other words, the global current density produced by a fuel cell can be written as the sum of a faradaic $j_f(t)$ and a capacitive current density $j_{dl}(t)$:

$$j(t) = j_f(t) + j_{dl}(t) \tag{2.39}$$

The ability of the interface to counterbalance charge variations, *i.e.* the charge and discharge rate of the double layer, is characterized by the *double layer capacity* C_{dl}. Supposing that the double layer capacity is independent of the cell voltage E gives [DLGM96]:

$$j_{dl}(t) = C_{dl} \frac{dE(t)}{dt} \tag{2.40}$$

The double layer capacity introduced in equation (2.40) is not necessarily a constant, but depends on the number of mobile charges at the electrode surface. As a consequence, C_{dl} varies with the cell voltage and the activation overpotential η_{act}. In the absence of a theory allowing to express

the variation of C_{dl} as a function of the cell potential when a net current is produced, the double layer capacity is generally considered as constant for modeling purpose. The following section will give an overview of the general (static) models of electrical double layers in the proximity of charged surfaces [Hun01, DLGM96], in order to allow estimating its order of magnitude at the electrodes of a PEMFC.

2.2.1 Electrical double layer in the vicinity of a charged surface

The term *electrical double layer* EDL describes a structure of two parallel layers of opposite charge that appears at the surface of a metal immersed in an electrolyte solution. A first layer is located at the surface of the metal plate. The charge of this first layer is compensated by a second layer of opposite sign which appears in the electrolyte solution to ensure the global electroneutrality of the system. The ions in the solution are not fixed in space but subjected to brownian motion. For this reason, the electrical double layer is also called *diffuse electrical double layer*. The electrolyte solution at the interface with the metal plate can be considered as a surface of constant potential Φ_m. For the sake of simplicity, the bulk potential of the electrolyte is generally set to zero, $\Phi_s = 0$.

The electric charge and potential distribution inside the EDL can be obtained by resolving the *Poisson-Boltzmann (PB) equation* (2.46), one of the most important equations in ionic electrochemistry. Its derivation is detailed in the framed box below.

NB: derivation of the Poisson-Boltzmann equation

Let us consider a charged metal/liquid interface in an electrolyte solution that is at a constant potential Φ_m. The bulk potential of the electrolyte is supposed to be null $\Phi_s = 0$. As a consequence of the continuity of the potential between the two phases, the local potential in the double layer Φ varies in the direction perpendicular to the metal section from Φ_m to Φ_s. The potential at any position in the EDL is determined by the *Poisson equation*:

$$\nabla.\vec{D} = \nabla.(\varepsilon\varepsilon_0\vec{E}) = q(\Phi) \tag{2.41}$$

$\vec{D} = \varepsilon\varepsilon_0\vec{E}$ is the dielectric displacement vector that accounts for the effect of free charges on the electric field $\vec{E}$ in a dielectric solution (*e.g.* water in polymer membranes). The ability of a medium to affect the electric field is expressed by its permittivity ε. $\varepsilon_0 = 8.8510^{-12}\ Fm^{-1}$ is the vacuum permittivity and $\varepsilon = \varepsilon_w/\varepsilon_0$ is the water relative permittivity, which is about 80. $q(\Phi)$ is the charge volume density (in Cm^{-3}) in the electrolyte, function of the potential Φ. In the absence of any magnetic field, $\vec{E}$ can be expressed as a function of the scalar potential Φ:

$$\nabla \times \vec{E} = 0 \ \Rightarrow\ \vec{E} = -\nabla\Phi \tag{2.42}$$

Assuming that the permittivities are constant and combining (2.41) and (2.42), the charge density q can be expressed by:

$$\nabla^2\Phi = -\frac{q}{\varepsilon\varepsilon_0} \tag{2.43}$$

Considering the ions in the solution as positive and negative point charges, the charge density can be written as:

$$q = \sum_i c_i(\Phi) z_i F \tag{2.44}$$

where c_i corresponds to the concentration of species i ($i = +, -$) in $mol\,m^{-3}$, z_i to the species valency and F to the Faraday constant. The species concentration is typically described by the *Boltzmann equation*:

$$c_i(\Phi) = c_i^0 e^{-\frac{W_{elec}(\Phi)}{RT}} \tag{2.45}$$

where $W_{elec} = z_i F(\Phi - \Phi_s) = z_i F \Phi$ is the electrical work necessary to move one mole of species i from the bulk solution ($\Phi_s = 0$) to a point in the double layer where the potential is Φ. The *Poisson-Boltzmann equation* is obtained by combining (2.43)- (2.45):

$$\nabla^2 \Phi = -\frac{1}{\varepsilon \varepsilon_0} \sum_i c_i^0 z_i F e^{-\frac{z_i F \Phi}{RT}} \tag{2.46}$$

In order to simplify the problem, it is supposed that the potential distribution inside the electrolyte is governed by ions of sign opposite to that of the metal surface, so that $z_+ = -z_- = z$. The PB equation (2.46) can thus be written:

$$\nabla^2 \Phi = \frac{2zFc^0}{\varepsilon \varepsilon_0} \sinh\left(\frac{zF\Phi}{RT}\right) \tag{2.47}$$

where $c^0 = c_+^0 = c_-^0$ is the bulk concentration, identical for positive and negative ions. The Poisson-Boltzmann equation can finally be expressed by:

$$\nabla^2 \overline{\Phi} = \kappa^2 \sinh\left(\overline{\Phi}\right) \tag{2.48}$$

with

$$\overline{\Phi} = \frac{zF\Phi}{RT} \tag{2.49}$$

and

$$\kappa^2 = \frac{1}{L_D^2} = \frac{2z^2F^2c^0}{RT\varepsilon\varepsilon_0} \tag{2.50}$$

L_D is the *Debye-Hückel length* or *Debye length*.

In order to obtain the potential distribution in the EDL in the case of point charges, the Poisson-Boltzmann equation is resolved with the following boundary conditions:

$$\begin{aligned} x = 0 : &\qquad \overline{\Phi} = \overline{\Phi}_m \\ x \to +\infty : &\qquad \overline{\Phi} = 0 \end{aligned}$$

Equation (2.48) is multiplied by $2d\overline{\Phi}/dx$:

$$2\frac{d\overline{\Phi}}{dx}\frac{d^2\overline{\Phi}}{dx^2} = 2\frac{d\overline{\Phi}}{dx}\kappa^2\sinh\left(\overline{\Phi}\right) \tag{2.51}$$

Integrating both sides from a point in the bulk where the electrostatic potential is null (and thus $d\overline{\Phi}/dx = 0$) to a point x in the EDL leads to:

$$\left[\left(\frac{d\overline{\Phi}}{dx}\right)^2\right]_{\infty}^{x} = 2\kappa^2\left[\cosh\left(\overline{\Phi}\right)\right]_{\infty}^{x}$$

$$\left(\frac{d\overline{\Phi}}{dx}\right)^2 = 2\kappa^2\left(\cosh\left(\overline{\Phi}\right)-1\right) = 4\kappa^2\sinh^2\left(\frac{\overline{\Phi}}{2}\right) \tag{2.52}$$

Or

$$\frac{d\overline{\Phi}}{dx} = -2\kappa\sinh\left(\frac{\overline{\Phi}}{2}\right) \tag{2.53}$$

The negative sign ensures that the potential is equal to zero in the bulk ($\frac{d\overline{\Phi}}{dx}$ is negative when $\overline{\Phi} > 0$ and positive when $\overline{\Phi} < 0$).

With the following substitutions:

$$t = \tanh\left(\frac{\overline{\Phi}}{4}\right)$$

$$\Rightarrow dt = \left(1-t^2\right)\frac{d\overline{\Phi}}{4} \qquad \text{and} \qquad \sinh\left(\frac{\overline{\Phi}}{2}\right) = \frac{2t}{1-t^2}$$

(2.53) becomes:

$$\frac{dt}{t} = -\kappa dx \tag{2.54}$$

The solution of the Poisson-Boltzmann equation is thus given by:

$$\tanh\left(\frac{\overline{\Phi}}{4}\right) = \tanh\left(\frac{\overline{\Phi}_m}{4}\right)e^{-\kappa x} \tag{2.55}$$

Figure 2.8 depicts the evolution of the electrostatic potential through the EDL according to equation (2.55), for a metal surface potential $\Phi_m = -0.05\ V$. This example points out that the EDL extends over a distance of about 3 times the Debye length L_D. Beyond this distance, the anion and cation concentrations are the same and equal to their bulk concentration c^0 and the local electrostatic potential reaches the electrolyte bulk potential $\Phi_s = 0$.

In order to estimate the capacitance of the double layer, the amount of excess charges in the double layer has to be expressed as a function of the local potential $\Phi(x)$. The charge density per unit area in the EDL is given by the global electroneutrality condition:

$$\sigma + \int_0^{\infty} q dx = 0 \tag{2.56}$$

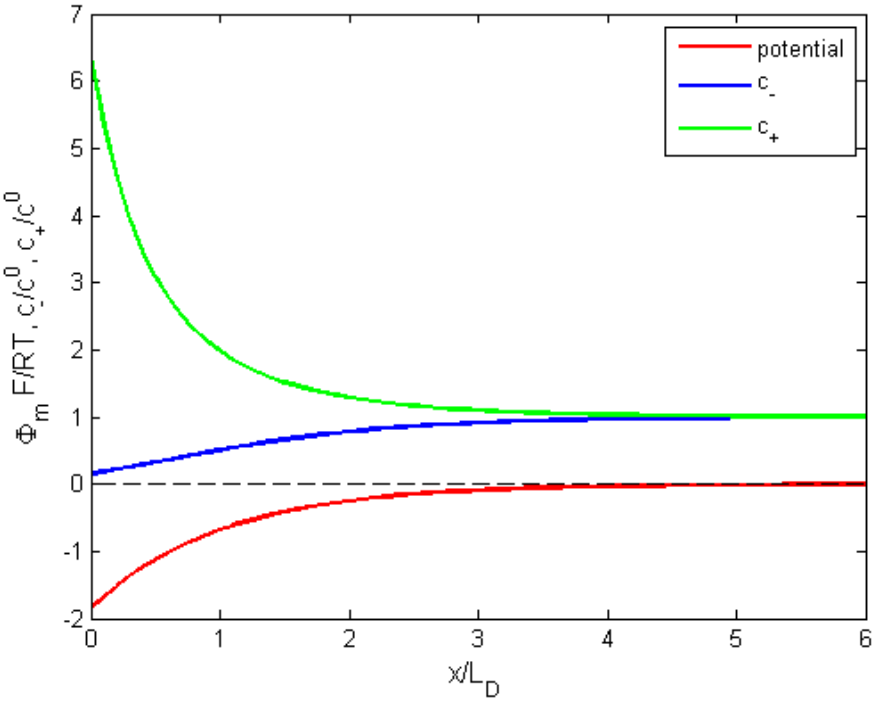


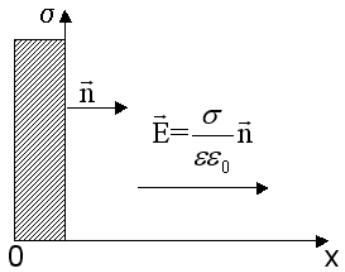
Figure 2.8: *Solution of the Poison-Boltzmann equation for an electrode potential $\Phi_m = -0.05\ V$. The bulk potential $\Phi_s = 0$ is reached beyond a distance of about 3 times the Debye length where the anion and cation concentrations are counterbalanced and equal to their bulk concentration $c_- = c_+ = c^0$.*

where σ is the charge density at the interface. Equation (2.56) can be expressed as a function of the local potential by (2.43), which leads to:

$$\sigma = \int_0^\infty \varepsilon\varepsilon_0 \frac{d^2\Phi}{dx^2} dx = -\varepsilon\varepsilon_0 \left.\frac{d\Phi}{dx}\right|_{x=0} \tag{2.57}$$

as $(d\Phi/dx)_{x\to\infty} = 0$.

NB: alternative way to obtain σ as a function of Φ



Note that there exists an alternative way to the global electroneutrality condition for obtaining equation (2.57). At the interface of a charged surface with the surface charge density σ which is immersed in a dielectric solution, the electric field vector is given by:

$$\vec{E} = \frac{\sigma}{\varepsilon\varepsilon_0}\vec{n} \tag{2.58}$$

where $\vec{n}$ is the normal to the solid surface. In the absence of any magnetic field, $\vec{E} = -\vec{\nabla}\Phi$ (2.42), which yields:

$$-\left.\frac{d\Phi}{dx}\right|_{x=0} = \frac{\sigma}{\varepsilon\varepsilon_0} \tag{2.59}$$

By combining (2.53) and (2.57), it comes:

$$\sigma = \frac{2\varepsilon\varepsilon_0 RT}{zF}\kappa \sinh\left(\frac{zF\Phi_m}{2RT}\right) \tag{2.60}$$

The derivation of the charge distribution in the electric double layer is valid in steady-state conditions. However, the double layer capacity of an electrochemical system is accessible only in AC conditions (by reference to a DC operating point):

$$\sigma(\Phi) = \sigma(\Phi_m) + \left.\frac{d\sigma}{d\Phi}\right|_{\Phi=\Phi_m}(\Phi - \Phi_m) + \ldots \tag{2.61}$$

The dynamic capacity C_{dl} (in Fm^{-2}) is then defined by:

$$\begin{aligned} C_{dl} = \left.\frac{d\sigma}{d\Phi}\right|_{\Phi=\Phi_m} &= \varepsilon\varepsilon_0\kappa\cosh\left(\frac{zF\Phi_m}{2RT}\right) \\ &= \sqrt{\frac{2z^2F^2\varepsilon\varepsilon_0 c^0}{RT}}\cosh\left(\frac{zF\Phi_m}{2RT}\right) \end{aligned} \tag{2.62}$$

The above derivation shows that the dynamic double layer capacitance depends on the charge and potential distribution in the EDL, as well as on the potential difference between the adjacent materials being at the origin of the double layer.

For very low potentials ($zF\Phi_m/2RT < 1$), the substitution $\sinh x \approx x$ simplifies the expression of the charge density (2.60):

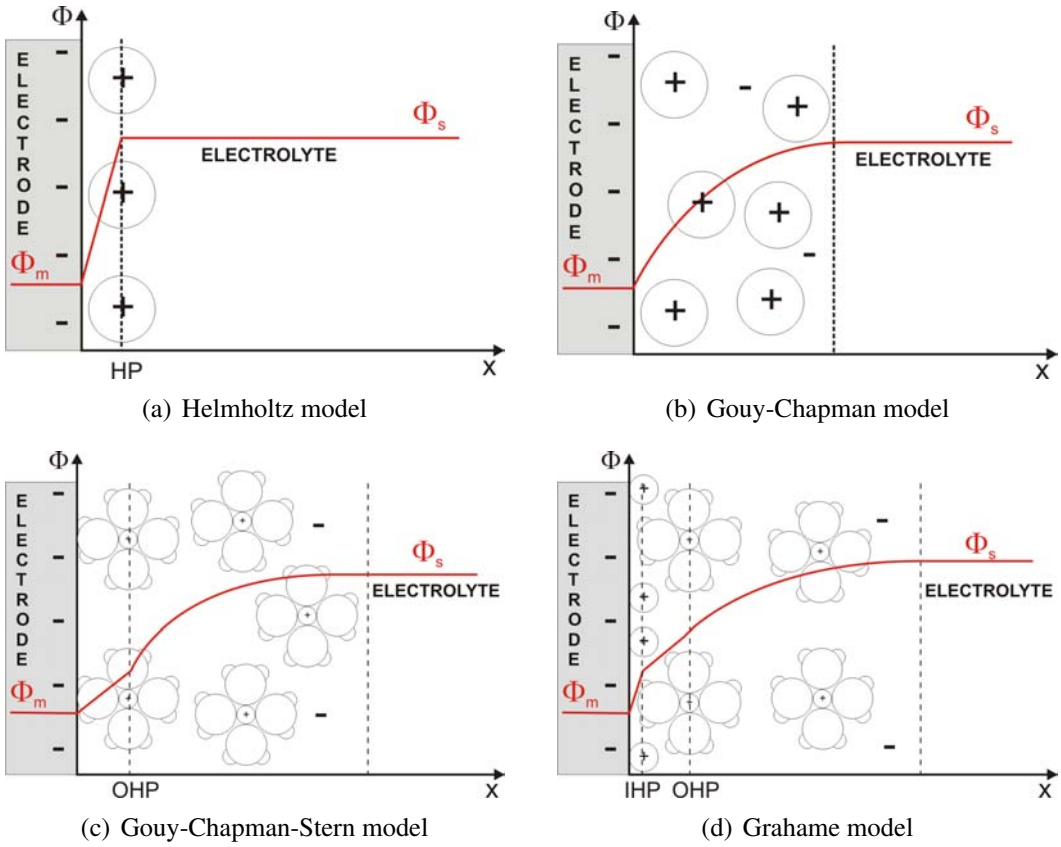
$$\sigma = \varepsilon\varepsilon_0\kappa\Phi_m \tag{2.63}$$

This yields:

$$C_{dl} = \varepsilon\varepsilon_0\kappa = \frac{\varepsilon\varepsilon_0}{L_D} \tag{2.64}$$

which confirms that for low potentials, the diffuse double layer behaves like a planar capacitor with an equivalent distance L_D between the two plates. Alternatively, the same result is obtained by setting $\Phi_m = 0$ in (2.62).

There exist different more or less sophisticated models for the EDL leading to different expressions of C_{dl}. The most common descriptions (according to Diard *et al.* [DLGM96]) are presented below:



(a) Helmholtz model

(b) Gouy-Chapman model

(c) Gouy-Chapman-Stern model

(d) Grahame model

Figure 2.9: *Different models of the electrical double layer and the corresponding potential distributions as described in the literature [DLGM96]. The examples are given for an electrode having an excess of negative charges on its surface.*

The Helmholtz model

The first model was proposed by Helmholtz (Figure 2.9(a)): the ions in the electrolyte, represented by spheres of radius d, form a mono-layer that is adsorbed on the electrode-metal interface to compensate the opposite charge at the metal surface. The rest of the electrolyte is supposed to be electrically neutral. The plane formed by the centers of the ions at $x = d$ is called the *Helmholtz plane*. Since there is no charge over the distance d, the electrostatic potential Φ varies linearly from the potential at the metal surface Φ_m $(x = 0)$ to that of the electrolyte bulk solution Φ_s $(x = d)$.

The EDL is thus equivalent to a capacitor with a dielectric thickness d and a capacitance:

$$C_{dl} = \frac{\varepsilon\varepsilon_0}{d}, \qquad \text{in } Fm^{-2} \tag{2.65}$$

Note that in this model, C_{dl} is independent of the potential difference. However, the experience shows that C_{dl} varies with the potential difference which does not allow to validate the Helmholtz model.

The Gouy-Chapman model

In an electric conductor, excess charges migrate on the surface. In an adjacent electrolyte solution, the excess charges are not fixed, but subjected to thermal motion. To take account of the motion of

the ions in the solution, Gouy and Chapman tried to explain the double layer capacity variation with the potential by the existence of a diffuse double layer (Figure 2.9(b)). In this model, the excess charges in the electrolyte are not present under the form of a mono-layer, but their concentration decreases from the interface to the bulk where it reaches its bulk value according to the Boltzmann distribution (2.45). The potential variation in the diffuse double layer is obtained by resolving the Poisson-Boltzmann equation (2.46). According to (2.62), in an $1:1$ electrolyte (where one anion at the interface is compensated by one cation inside the solution; $z=1$), the double layer capacity is expressed by:

$$C_{dl} = \sqrt{\frac{2F^2\varepsilon\varepsilon_0 c^0}{RT}}\cosh\left(\frac{zF(\Phi_m-\Phi_s)}{2RT}\right) \tag{2.66}$$

The main shortcoming of this approach is that C_{dl} tends to infinity for large values of the potential difference, which is not consistent with the experimental observations.

The Gouy-Chapman-Stern model

In the Gouy-Chapman model, the ions in the electrolyte are considered as point charges whose concentration can tend toward infinity near the metal/electrolyte interface. This is not a realistic assumption. Stern proposed therefore a combination of the Helmholtz and Gouy-Chapman models, where the ions have a finite size and cannot approach the interface at a distance lower than the radius of the solvated species (Figure 2.9(c)). The centers of the hydrated excess ions form a plane called the *Outer Helmholtz Plane* (OHP). The diffuse double layer appears beyond the OHP ($x > x_{OHP}$) and its potential variation is obtained by integrating the Poisson-Boltzmann equation (2.45) down to x_{OHP} (where the potential is Φ_{OHP}). Between the interface and the OHP, there are no charges and the potential varies linearly according to the Helmholtz model. The resulting double layer capacity for a $1:1$ electrolyte is given by:

$$\begin{aligned}\frac{1}{C_{dl}} &= \frac{x_{OHP}}{\varepsilon\varepsilon_0} + \frac{1}{\sqrt{\frac{2F^2\varepsilon\varepsilon_0 c^0}{RT}}\cosh\left(\frac{zF(\Phi_{OHP}-\Phi_s)}{2RT}\right)} \\ &= \frac{1}{C_1}+\frac{1}{C_2}\end{aligned} \tag{2.67}$$

As a consequence, C_{dl} behaves like a Helmholtz capacitor and a Gouy-Chapman capacitor connected in series. The maximum value of the global capacity is limited by the smallest of both.

The Grahame model

There exists a fourth model proposed by Grahame that takes into account the chemical nature of the adsorbed species in the electrolyte. In the Gouy-Chapman-Stern representation, the OHP consists only of solvated ions subjected to the electrostatic attraction of the excess charges at the metal/electrolyte interface. Grahame proposed a more detailed structure of the EDL by defining a third region delimited by the *Inner Helmholtz Plane* (IHP), which corresponds to the position of non-solvated ions that are adsorbed on the metal (Figure 2.9(d)). The IHP is followed by the OHP and finally by the diffusive double layer. This model allows to explain some experimental observations like the adsorption of anions at the electrode below the required adsorption poten-

tial, but it is too complex to derive an analytical expression of the double layer capacity [Fri03]. Nevertheless, it is worth mentioning the existence of this description, because the term of the IHP appears frequently in the literature.

2.2.2 Double layer capacity in a fuel cell

In this section, a description of the EDL at the membrane/electrode interfaces of a PEMFC is presented, which will allow to estimate the value of the cell double layer capacity. In order to facilitate the understanding, Figure 2.10 illustrates the different electrostatic potential and excess charge distributions appearing in the MEA.

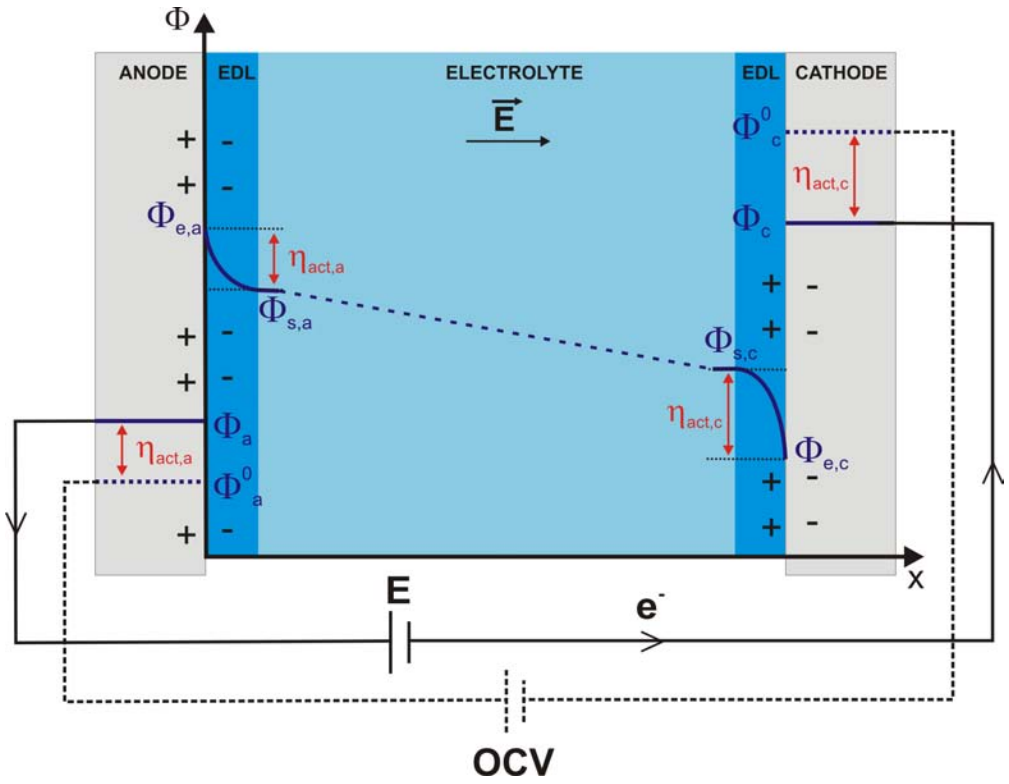


Figure 2.10: *Schematic representation of the potential profiles in a PEMFC membrane electrode assembly. The potential in the diffuse EDL varies from the electrode/electrolyte interface $\Phi_{e,a/c}$ to the bulk values in the electrolyte solution $\Phi_{s,a/c}$. This variation corresponds to the electrode activation overpotentials: $\left|\Phi_{e,a/c}-\Phi_{s,a/c}\right| = \left|\eta_{act,a/c}\right|$.*

Electrons are liberated by the HOR at the anode (at potential Φ_a) and flow through an external circuit to the cathode (at potential Φ_c). Since $\Phi_c > \Phi_a$, the metal at the anode is charged positively. This positive charge is compensated by a cation deficit in the electrolyte solution to maintain the global electroneutrality. The electrolyte potential at the anode/electrolyte interface is given by $\Phi_{e,a}$. Note that the value of $\Phi_{e,a}$ is not known, but by convention it is usually set equal to Φ_a. Hence, a double layer is formed at the anode/membrane interface which is extended inside the electrolyte until the local potential reaches the bulk potential $\Phi_{s,a}$. The potential difference of the anode double layer is usually set equal to the anode activation overpotential $\eta_{act,a}$: $\Phi_{e,a}-\Phi_{s,a} = \eta_{act,a} > 0$, since this potential difference is assumed to be at the origin of the excess charges. This corresponds to a representation of the electrode processes by a Randles equivalent circuit (charge transfer resistance

and a capacitor in parallel, cf. chapter 3.1.3) in which the capacity is not charged in the absence of an electrical current.

In the same way, an electrical double layer is created at the cathode/membrane interface. As the metal at the cathode is charged negatively, the charge distribution in the electrolyte of the cathode EDL is of the sign opposite to the anode. The respective potentials of the EDL are $\Phi_{e,c}$ and $\Phi_{s,c}$, with $\Phi_{e,c} - \Phi_{s,c} = \eta_{act,c} < 0$ (cf. Figure 2.10). The H^+ transport through the electrolyte being directed from the anode to the cathode, it can be concluded that $\Phi_{e,c} < \Phi_{e,a}$. The models describing the bulk potential profile through the ionomer between both electrodes are based on the estimation of the (local or space average) ionic resistance as a function of the membrane water content.

As the potentials $\Phi_{e,a}$ and $\Phi_{e,c}$ are not known, the potential differences between the two phases at the electrode/membrane interfaces, $\Delta\Phi_{a,e} = \Phi_a - \Phi_{e,a}$ and $\Delta\Phi_{c,e} = \Phi_c - \Phi_{e,c}$ are not measurable. It is only possible to measure the potential difference between the two electrodes corresponding to the cell voltage $\Phi_c - \Phi_a = E$.

In the following, the double layer capacity in a PEMFC is estimated using the Gouy-Chapman approach. Knowing that the electric field gradient in the metal phase is close to zero, the excess charge distribution in the electrolyte is created by the potential difference between the electrode/electrolyte interface $\Phi_{e,a/c}$ and the bulk potential Φ_s, assumed to be constant through the electrolyte and equal to zero $\Phi_s = 0$ [2]. In a PEMFC membrane, the positive charges being mobile protons and the negative charges being fixed sulfonate ions SO_3^-, the Poisson-Boltzmann equation (2.46) can be written as:

$$\frac{d^2\Phi}{dx^2} = \frac{F c_f}{\varepsilon\varepsilon_0}\left(1 - e^{-\frac{F\Phi}{RT}}\right), \tag{2.68}$$

where $c_f \approx 1200\ mol\,m^{-3}$ is the concentration of sulfonate end groups in the electrolyte. As a consequence of the electroneutrality, the bulk concentration of protons (or H^+ ions) has to be equal to that of SO_3^-. An alternative representation of equation (2.68) is:

$$\frac{d^2\overline{\Phi}}{dx^2} = \frac{\kappa^2}{2}\left(1 - e^{-\overline{\Phi}}\right) \tag{2.69}$$

with $\overline{\Phi} = F\Phi/RT$ and $L_D = \kappa^{-1} = \sqrt{\varepsilon\varepsilon_0 RT/2F^2 c_f}$. Resolving (2.69) with the boundary conditions

$$\begin{aligned} x = 0 \quad &: \qquad \Phi = \Phi_{e,a/c} \\ x \to \infty \quad &: \qquad \Phi = 0 \end{aligned}$$

and inserting the result in (2.57) leads to an analytic expression of the charge density in the EDL:

$$\sigma = -\frac{\varepsilon\varepsilon_0 RT}{F L_D}\sqrt{\overline{\Phi}_{e,a/c} + e^{-\overline{\Phi}_{e,a/c}} - 1} \tag{2.70}$$

Supposing that $\left|\overline{\Phi}_{e,a,c}\right| << 1$ and that the double layer capacity of the cell behaves in a first approach like a parallel plate capacitor allows to simplify equation (2.70) by $\sigma = -\frac{\varepsilon\varepsilon_0}{\sqrt{2}L_D}\Phi_{e,a/c}$ and to estimate the double-layer capacity by:

[2] Its variations due to the flow of protons are neglected

$$C_{dl}(Fm^{-2}) = \frac{\varepsilon\varepsilon_0\gamma}{L_D}, \qquad with \quad L_D = \sqrt{\varepsilon\varepsilon_0 RT/F^2 c_f} \tag{2.71}$$

$\gamma = 100$ [BWJ+05] is the roughness factor of the electrode expressing the ratio between the active and the geometrical area. In electrochemical impedance spectroscopy (EIS), the dynamic capacity C_{dl} is calculated according to (2.62), which leads to the same expression as equation (2.71). For a PEMFC working at $T = 320\ K$, equation (2.71) yields:

$$\begin{aligned} L_D &= 1.29\ \text{Å} \\ C_{dl} &= 0.055\ Fcm^{-2} \end{aligned}$$

These values of the double-layer capacity and the Debye length represent surprisingly good estimates of their actual values, even if the validity of the Gouy-Chapman description of the EDL in PEMFC can be discussed:

- In this model, the electrode is represented by a planar capacitor which corresponds to a one-dimensional representation of the EDL. PEMFC electrodes are made of porous composite materials (carbon and Pt particles) being in contrast to this approach. However, the reactions take place at the surface of Pt particles with a mean diameter $d_{Pt} \approx 5\ 10^{-9}\ m$, which is about 40 times larger than the estimated double layer thickness, $d_{Pt}/L_D \approx 40$. A 1D approach seems thus to be valid.

- Assuming that $\eta_{act} = \Phi_{e,a/c} - \Phi_{s,a/c}$, the potential at the membrane/electrode interface corresponds to the activation overpotential $\Phi_{e,a/c} = \eta_{act,a/c}$ (since $\Phi_{s,a/c} = 0$). According to the estimate in section 2.1.2, η_{act} is of about $0.1\ V$, which implies that $\overline{\Phi}_{e,a/c} = F\Phi_{e,a/c}/RT \approx 4$. It was shown that for an approach of the electrical double layer by a planar capacitor, $\overline{\Phi}_{e,a/c}$ has to be significantly lower than 1 (2.70), which is not the case here.

- The size of H^+ is not uniform since they are usually hydrated. This size distribution of the ions is not taken into account in the Gouy-Chapman approach, which can significantly change the value of their bulk concentration c_f.

- The most important shortcoming of this approximation is the low value of the double layer thickness $L_D = 1.29$ Å by comparison to the size of a water molecule ($d_{H_2O} \approx 2.75$ Å [ZX95]). The H^+ being hydrated, the double layer thickness has to exceed at least the size of a water molecule.

To conclude, even if the validity of the Gouy-Chapman approach can be discussed, it allows to understand the physical meaning of the electrical double layer and of the double layer capacity and gives a relatively good estimate of the double-layer characteristics (C_{dl}, L_D)[SZWG96]. Note however that the estimated Debye length is lower than the size of water molecules $d_{H_20} = 2.75$ Å [ZX95], which is not realistic.

2.3 Modeling of the Active Layer Structure

The catalyst layers are one of the major components determining the electrical performance of a fuel cell. In addition to charge separation, they are the place of various and coupled transport

phenomena (fluxes of protons, electrons, heat, reactants and products) that occur at different length scales. Thus, a well-adapted geometrical description of the electrode structure is necessary to allow the physico-chemical description of these phenomena; all the more so since the limiting layer(s) in term of oxygen diffusion has (have) not been clearly identified yet.

2.3.1 Modeling approaches of the active layer geometry

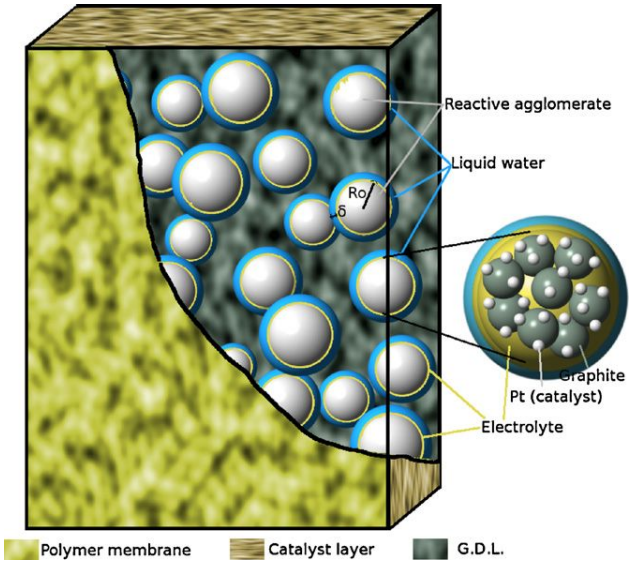
There exist different structural models of the electrodes in the literature depending on the scale of the considered phenomenon. The three most common catalyst layer models are the *macro-homogeneous* or *discrete-volume model* [GD97, GCG$^+$98, SWG93, SZWG96, RL01, EK99], the *agglomerate* or *Gas Diffusion Electrode (GDE) models* [GD97, GCG$^+$98, SR89, Rai90, BE97a, IJL$^+$02, SENVS03, SENVS04, JLW03, JL03, RDL$^+$05, BBO04, SPK05a, LHVN04, CCD$^+$10] and more simple approaches where the active layers are considered as interfaces which are referred to as the *ultra-thin layer models* (or *thin-film models*) [BD03, PW04b]. A detailed comparison between these three modeling approaches of the active layer geometry is given by Harvey *et al.* [HPK08].

The thin-film models are usually used for fluid dynamic investigations inside the GDL, the gas channels and the electrolyte, since they neglect the gas transport inside the catalyst layers and thus allow lower calculation times. However, they lead to an overestimation of the current density [SPK05a, HPK08].

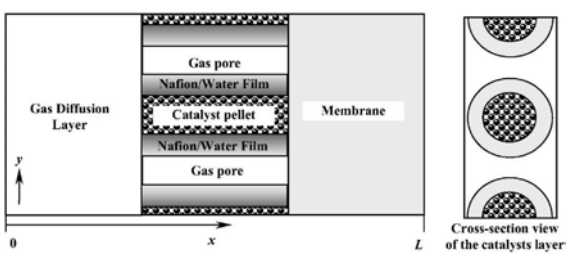
In the macro-homogeneous approaches, the catalyst layers are represented by one-dimensional layers consisting of a homogeneous mixture of catalyst particles, carbon, electrolyte solution and gas pores. In several representations of this model the gas pores are assumed to be filled with electrolyte or liquid water [GCG$^+$98, RL01] and gas transport is assumed to occur in dissolved form. According to Gloaguen *et al.* [GCG$^+$98], such an approach is suitable for ORR simulations on *rotating disc electrodes* (RDE) which is comparable to the mass transfer in completely flooded porous electrodes. However, for the simulation of the ORR on Gas Diffusion Electrodes (GDE) of a PEMFC, it leads to an overestimation of the mass transfer losses. They conclude that the presence of gas pores in the catalytic layer is essential for higher oxygen flow rates [GCG$^+$98].

The agglomerate models present the more detailed electrode description. In these models, the solid phase is represented by homogeneous assemblies (agglomerates) of catalyst (Pt) particles, carbon powder and (possibly) polymer electrolyte of a size of about 0.2 μm to 6 μm [BE97a, SPK05a, JLS02, IJL$^+$02, SENVS03, GCG$^+$98, LHVN04, CCD$^+$10] which are separated by a network of electrolyte-free macro-pores (not to confound with the electrolyte-filled micro-pores in the agglomerates, which are not considered) enabling the gas supply at relatively high flow rates. This approach is well adapted for the description of charge and mass transfer, especially in the gas phase where they lead to better results than a macro-homogeneous approach in which gas transport is assumed to occur only through the micro-pores [BE97a].

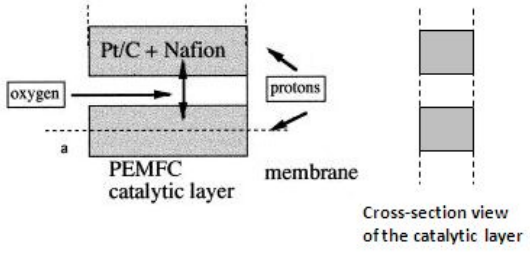
Figure 2.11 depicts the three main geometries of agglomerates that exist in the literature. Some authors [SPK05a, BE97a, IJL$^+$02, JLW03, JL03, LE08, CCD$^+$10] represent the agglomerates as spheres (Figure 2.11(a)) which is certainly the geometry approaching the real structure best. This representation is usually chosen to model transport of reactants and water through the catalyst layer. Other authors describe agglomerates by cylinders (Figure 2.11(b)) [RDL$^+$05, BBO04, SR89, Rai90, BWJ$^+$05, BE97a, SENVS04, SENVS03, LHVN04] or slabs (Figure 2.11(c)) [GCG$^+$98] that span over the whole active layer thickness. These representations are more likely to study the mass transport successively through the different phases of the active layers.



(a) Spherical geometry [CCD+10]



(b) Cylindrical geometry [LHVN04]



(c) Slab geometry according to [GCG+98]

Figure 2.11: *Shapes of the agglomerates as they can be found in the literature.*

The composition of the agglomerates varies according to the authors (Figure 2.12; assuming a cylindrical geometry):

- In the first case (left side in Figure 2.12), the solid phase consists of a homogeneous mixture of carbon, Pt and electrolyte [GD97, GCG+98, BBO04, BWJ+05, RDL+05].
- In the second case (right side in Figure 2.12) according to the works of Springer [SR89] and Raistrick [Rai90], the agglomerates are a mixture of carbon powder and catalyst particles; the electrolyte is assumed to cover the surface of the agglomerates only [LMM+98, SPK05a, LHVN04, JLS02, CCD+10, Eik06, LE08]. Actually, some ionomer is also present inside the agglomerates where it acts exclusively as a binder and not as a proton conductor. This approach assumes that the reaction sites are situated at the agglomerate/electrolyte interface. Before reaching the reaction sites, oxygen passes successively through the gas pores in the GDL and the catalyst layer, and finally (in dissolved form) through the thin electrolyte layer.

The agglomerate models are the most detailed electrode descriptions. They have contributed to advances in terms of understanding and modeling of the mass and charge transfer through the porous electrodes of fuel cells. In spite of being one-dimensional, they can be used for two-dimensional [SENVS03, SENVS04] and three-dimensional studies [UW04] of reaction and transport processes in fuel cells. However, it has to be mentioned that the conclusions obtained with

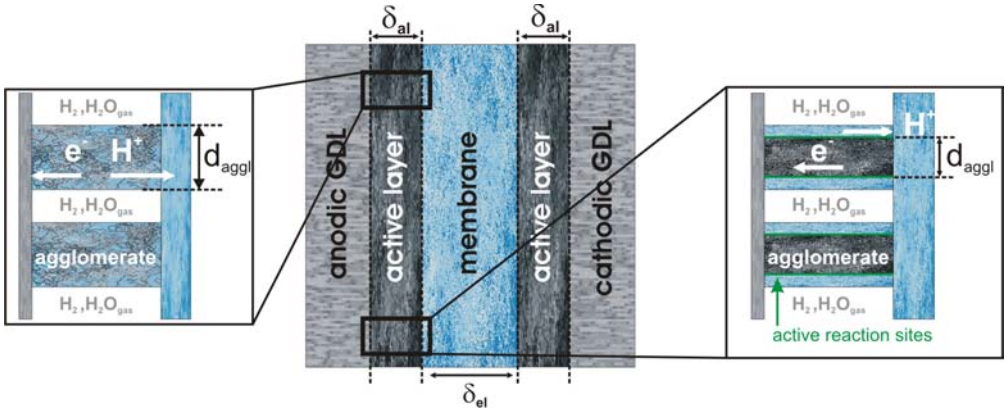
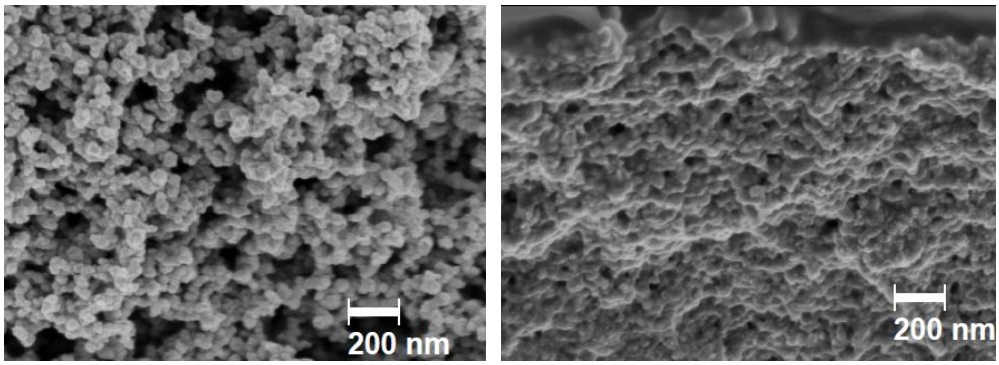


Figure 2.12: *Two representations of the agglomerates. Left side: homogeneous mixture of carbon black, catalyst particles and electrolyte solution [RDL+05, BWJ+05]. Right side: Electrolyte covers the surface of the agglomerates consisting of carbon powder and catalyst particles only [SR89, Rai90].*



(a) New cathode (b) Aged cathode

Figure 2.13: *SEM images showing the structure of a new (a) and an aged (b) PEMFC cathode [CGB+09]. Electrode thinning due to start-up/shut-down cycles or H_2 starvation entails a loss of the cathode porosity, which is not taken into account in the agglomerate models.*

theses models still remain limited for several reasons that can be understood by considering Figure 2.13 showing SEM images of new (Figure 2.13(a)) and aged (Figure 2.13(b)) C/Pt cathodes published by Carter *et al.* [CGB+09]: first, the agglomerate description is only a rough geometrical estimate of the electrode real structure and secondly, carbon corrosion modifies significantly its morphology during operation (Figure 2.13(b)), which is not considered through the theoretical approaches. As a consequence, it is obvious that the next challenging milestone will be the integration of real pore structures into the numerical models, as well as their evolution with time.

2.3.2 Parameters characterizing the electrode morphology

The morphology of the catalyst layer in an agglomerate model is characterized by several parameters, such as its thickness δ_{al}, its porosity ε_{al}, the agglomerate diameter d_{aggl}, the size of the gas pores d_{pore}, the electrolyte film thickness δ_{el} and the electrode roughness γ (Figure 2.14).

The porosity is defined by the ratio of the pore to the active layer volume [RDL+05, SENVS04]:

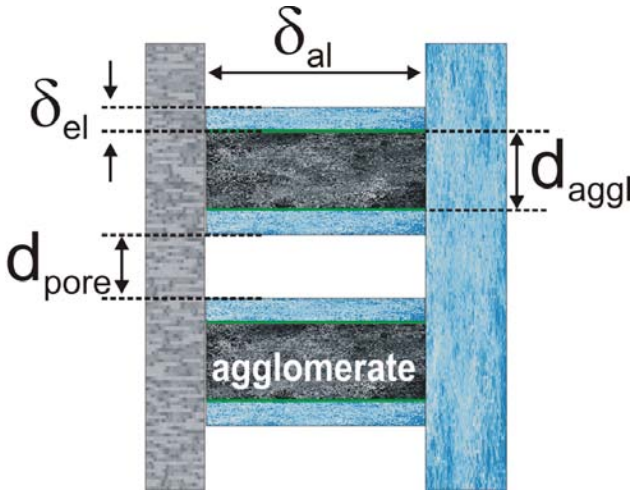


Figure 2.14: *Parameters characterizing the active layer structure in an agglomerate model.*

$$\varepsilon_{al} = \frac{V_{pore}}{V_{pore} + V_{aggl}} = \frac{S_{pore}}{S_{pore} + S_{aggl}} \tag{2.72}$$

where S_{pore} represents the pore section and S_{aggl} the agglomerate section. The porosity of electrodes prepared in a conventional way by hot-pressing or hot-spraying ranges generally between 0.2 and 0.35 [EAP98, FJW98, IJL$^+$02, SENVS04, RDL$^+$05]. When using an additional pore former, porosities up to $\varepsilon_{al} = 0.65$ can be reached [FJW98].

The pore equivalent diameter d_{pore} can be estimated with the layer porosity ε_{al} and the agglomerate mean diameter d_{aggl}:

$$d_{pore} = \frac{\varepsilon_{al}}{1 - \varepsilon_{al}} d_{aggl} \tag{2.73}$$

For modeling purpose, the agglomerate diameter d_{aggl} is often set to 1 μm [BE97a, GCG$^+$98, JLS02, BWJ$^+$05]. Assuming an active layer porosity $\varepsilon_{al} = 0.3$, the mean pore size according to (2.73) is $d_{pore} = 0.4\ \mu m$ which is of the same order of magnitude as the values given in the literature for the macro (or secondary)-pores: the majority of the authors [EAP98, GJL$^+$03, Eik06, LE08] report that their diameter d_{pore} varies mainly between 0.01 μm and 0.1 μm, whereas transmission electron microscope (TEM) studies performed by Siegel *et al.* [SENVS03] showed pores in the range of 1 μ to 10 μm.

By opposition to the macro-pores separating the agglomerates, the micro- (or primary) pores correspond to the space between the particles inside the agglomerates. As a consequence, their size is expected to range between the Pt particle size ($d_{Pt} : 2 - 3\ nm$ [EK99, SENVS03, SPK05a]) and the carbon particle size ($d_C : 10 - 100\ nm$ [Eik06, YW08]). Indeed, the values given in the literature are situated between 1 *nm* and 10 *nm* [Eik06, LE08]. Compared to the size of the macro-pores ($0.01 - 10\ \mu m$), it is evident that the agglomerate models allow higher gas flow rates than the macro-homogeneous models, which consider gas transport only through these micro-pores.

In the representation according to Springer and Raistrick [SR89, Rai90], the agglomerates are covered by a thin electrolyte layer (right side in Figure 2.14) whose thickness δ_{el} is typically set to 10 *nm* [LHVN04], 50 *nm* [CCD$^+$10] or 80 *nm* [SPK05a]. It is worth mentioning that TEM studies performed by Cheng *et al.* [CYH$^+$99] show that, in reality, the electrolyte does not cover

the solid phase homogeneously, but that its thickness varies between 10 *nm* and 100 *nm*. Their investigations show that in the case of a uniform coverage, the film thickness would not exceed 3 *nm*. However, higher values are observed, which confirms the non-uniform distribution. Lee *et al.* [LMM$^+$98] investigated the influence of the Nafion loading in the electrodes on the current-voltage characteristics of a PEMFC. Their fitting curves of the experimental data put forward that the electrolyte film thickness increases with the Nafion loading to reach a maximum value of $\delta_{el} = 80\ nm$ at $1.9\ mg_{Nafion}/cm^2$.

Since the active catalyst sites are at the interface between the agglomerates and the thin electrolyte layer, the active Pt area is higher than the MEA flat area. The electrode roughness γ is thus defined by:

$$\gamma = \frac{\text{active Pt area}}{\text{geometric area}} \tag{2.74}$$

For a perfectly flat electrode, the roughness is equal to 1. Depending on the electrode characteristics (platinum loading, Pt/C ratio...) and the preparation method, the roughness of PEMFC electrodes can vary between 100 and 1000 [Boi05]. The majority of the authors indicates that the electrode roughness in PEMFC is equal to 100 [BWJ$^+$05, CCD$^+$10, Des08] or 200 [GCG$^+$98, CR01].

δ_{al}	$[\mu m]$	$4-20$	[SWG93, BE97a, BE97b]
d_{aggl}	$[\mu m]$	$0.2-6$	[BE97a, SPK05a, JLS02, IJL$^+$02, SENVS03] [GCG$^+$98, LHVN04, CCD$^+$10]
ε_{al}	$[-]$	$0.2-0.35$	[EAP98, FJW98, IJL$^+$02, SENVS04, RDL$^+$05]
$d_{macro-pore}$	$[nm]$	$10-100$	[EAP98, GJL$^+$03, Eik06, LE08]
$d_{\mu-pore}$	$[nm]$	$1-10$	[Eik06, LE08]
δ_{el}	$[nm]$	$10-100$	[LMM$^+$98, CYH$^+$99, LHVN04, SPK05a, CCD$^+$10]
γ	$[-]$	$100-1000$	[Boi05, BWJ$^+$05, CCD$^+$10, Des08, GCG$^+$98, CR01]

Table 2.1: *Typical values of the main geometrical characteristics of PEMFC active layers.*

Typical values of the parameters characterizing the active layers are summarized in Table 2.1.

2.4 Oxygen Transport

Mass transport of one species in a mixture can occur by means of molecular motion (diffusion) due to a concentration gradient or by means of bulk motion of the fluid (convection). In the case of gas diffusion in porous media, the flow rate depends on the size of the gas pores and on the presence of liquid water, which has to be taken into account when modeling the species transport in the diffusion media of fuel cells (GDL, catalyst layers). This section presents the main formalisms of the description of monophasic mass transport through porous media and the simplifications that can be made in the case oxygen transport in the cathode of a PEMFC.

2.4.1 Mass fluxes

At steady-state, the mass flux densities N_i ($i = O_2, H_2$) in the direction perpendicular to the membrane are directly linked to the current density j.

By convention, the fluxes of consumed species are counted negative and those of produced species are counted positive. Note that the following definitions do not account for possible gas humidification.

At the anode, the hydrogen flux density N_{H_2} (consumed, negative sign) is expressed as a function of the current density, while the flux of water $N^a_{H_2O}$ corresponds to that passing through the membrane:

$$N_{H_2} = -\frac{j}{2F}, \qquad N^a_{H_2O} = N^m_{H_2O} \tag{2.75}$$

$F = 96485\ Cmol^{-1}$ stands for the *Faraday constant* giving the charge of one mole of electrons.

At the cathode, nitrogen being inert, its flux is null, while the fluxes of oxygen N_{O_2} (consumed, negative sign) and water $N^c_{H_2O}$ (produced, positive sign) can be expressed as functions of the current density again:

$$N_{O_2} = -\frac{j}{4F}, \qquad N^c_{H_2O} = \frac{j}{2F} + N^m_{H_2O}, \qquad N_{N_2} = 0 \tag{2.76}$$

The membrane is assumed to be impermeable for the reactant gases. The water transport phenomena through the membrane are not completely understood and are thus the focus of a multitude of studies [OXT96, Col08, LAC+09]. It is generally admitted that the net membrane water flux is the sum of electro-osmotic and diffusive fluxes:

$$N^m_{H_2O} = N^{osmotic}_{H_2O} + N^{diff}_{H_2O} \tag{2.77}$$

According to Okada *et al.* [OXT96], the electro-osmotic flux, which is always directed from the anode to the cathode, is a function of the proton flux and thus of the current density:

$$N^{osmotic}_{H_2O} = \tau \frac{j}{F} \quad \text{with} \quad \tau = \lambda \tau_0 \tag{2.78}$$

where τ stands for the number of water molecules dragged by a proton, τ_0 for the electro-osmotic drag coefficient and λ for the membrane water content.

The norm and the sign of the diffusive water flux depends linearly on the gradient of the water concentration:

$$N^{diff}_{H_2O} = -D_m \frac{dc_{H_2O}}{dx} \tag{2.79}$$

Inserting (2.78) and (2.79) in (2.77) yields a first order differential equation in λ which can be solved with an adequate transport model. Among the different models proposed in the literature, Lottin *et al.* [LAC+09] assumed a constant water diffusivity in the membrane $D_m = cte$ and expressed the membrane water flux by:

$$N^m_{H_2O} = \tau_0 \frac{j}{F} \left[\lambda_a + \frac{\lambda_c - \lambda_a}{1 - e^{k_m \delta_m}} \right] \quad \text{with} \quad k_m = \frac{EW \cdot \tau_0 \cdot j}{\rho_{dry} D_m F} \tag{2.80}$$

Generally, the membrane diffusivity depends on the water content $D_m(\lambda)$. T. Colinart [Col08] solved the differential equation for the membrane water flux (2.77) supposing $\tau = 1$ [ZDR+93] and $D_m = D_0 \cdot \lambda$ [FN92] and obtained:

$$N_{H_2O}^m = \frac{j}{F} - D_0 \frac{\rho_{dry}}{EW} \frac{\lambda_c^2 - \lambda_a^2}{2\delta_m} \tag{2.81}$$

λ_a and λ_c represent the water content at the electrolyte/anode and electrolyte/cathode interface, respectively. Supposing thermodynamical equilibrium between vapor in the GDL and liquid water in the membrane, λ_a and λ_c can be calculated with the sorption isotherms (cf. page 14 in chapter 1.5.1).

The variety of the expressions of $N_{H_2O}^m$ reflects that despite of numerous studies, many questions remain about water transport through the membrane. This uncertainty affects the validity of fuel cell numerical models.

Finally, it is worth mentioning that each reactant i is generally inserted in the fuel cell with a stoichiometric factor S_i different from 1. The molar flow rates at the gas channel inlet φ_i^{in} (in $mol\,s^{-1}$) are thus given by:

$$\begin{aligned} \varphi_{H_2}^{in} &= S_{H_2} \cdot \varphi_{H_2} \quad \rightarrow S_{H_2} = \frac{\varphi_{H_2}^{in}}{I/2F} \\ \varphi_{O_2}^{in} &= S_{O_2} \cdot \varphi_{O_2} \quad \rightarrow S_{O_2} = \frac{\varphi_{O_2}^{in}}{I/4F} \end{aligned} \tag{2.82}$$

where I (in A) stands for the current produced by the cell.

2.4.2 Mass transport mechanisms

Fick's law of binary diffusion

Molecular transport due to a concentration gradient of one species i in a mixture (gaseous, liquid or solid) with reference to the bulk velocity of the mixture $\vec{u}$ is known as *diffusion* (also *mass diffusion* or *concentration diffusion*). In the absence of any electrostatic or centrifugal force field, the diffusion of a species i in a binary solution of i and j is typically described by *Fick's law of diffusion* [BSL02, KW97]. At steady state, *Fick's 1st law* postulates that the molar flux $\vec{J}_i$ (in $mol\,m^{-2}s^{-1}$) is proportional to the concentration gradient ∇y_i, with $y_i = c_i/c$:

$$\vec{J}_i = -cD_{i,j}\vec{\nabla} y_i \tag{2.83}$$

where c_i stands for the molar concentration of species i and c for the molar density of the solution, with $c = \sum_{i=1}^{N} c_i$ and $\sum_{i=1}^{N} y_i = 1$. $D_{i,j}$ is the diffusivity of species i in j and is a function of temperature, pressure and composition.

Alternatively to the expression as a function of the concentration gradient, Fick's 1st law can also be written in terms of velocity:

$$\vec{J}_i = c_i(\vec{u}_i - \vec{u}) \tag{2.84}$$

where $\vec{u}_i$ is the molar average velocity of species i and $\vec{u}$ the mixture average velocity, defined by:

$$\vec{u} = \frac{\sum_{i=1}^{N} c_i \vec{u}_i}{\sum_{i=1}^{N} c_i} = \sum_{i=1}^{N} y_i \vec{u}_i \tag{2.85}$$

The diffusivity of gases at low pressure is almost independent of the concentration c_i, varies proportionally with the temperature T and inversely proportionally with the pressure P [BSL02]. Slattery and Bird [SB58] developed an analytical expression for the binary diffusivity of gas mixtures at low pressure:

$$D_{i,j} = \frac{a}{P}\left(\frac{T}{\sqrt{T_i^c T_j^c}}\right)^b \left(P_i^c P_j^c\right)^{1/3} \left(T_i^c T_j^c\right)^{5/12} \left(\frac{1}{M_i}+\frac{1}{M_j}\right)^{1/2} \tag{2.86}$$

In equation (2.86), $D_{i,j}$ is given in $cm^2 s^{-1}$, P in atm and T in K. For a nonpolar gas pair (excluding the mixture helium + hydrogen): $a = 2.745\ 10^{-4}$ and $b = 1.823$. In the case of a mixture of vapor and a nonpolar gas: $a = 3.64\ 10^{-4}$ and $b = 2.334$. The molar mass M_i, critical temperature T_i^c and critical pressure P_i^c of each species introduced in a H_2/air PEMFC are given in Table 2.2.

	$M\ [g\,mol^{-1}]$	$T^c\ [K]$	$P^c\ [atm]$
H_2	2.016	33.23	12.8
O_2	32	154.8	50.14
N_2	28.02	126.3	33.54
H_2O	18.016	647.4	12.8

Table 2.2: *Physical properties of H_2, O_2, N_2 and H_2O [ADP06].*

In gases at high pressure, liquids and solids, the diffusivity is strongly concentration dependent and increases significantly with the temperature. The behavior of $D_{i,j}$ is more complicated than for gases at low pressure and there exist only tentative analytical expressions which are based on data of a few substances (Ar, Kr, Xe and CH_4) [BSL02]. In a general way, it can be shown that $D_{i,j} = D_{j,i}$, so that only one diffusivity is needed to describe the diffusion in a binary mixture. However, for concentration-dependent diffusion coefficients, it is possible that the diffusivity of a dilute solution of i in j differs numerically from that of a dilute solution of j in i, so that $D_{i,j} = D_{j,i}$ is verified only for different concentration ratios.

It might be reminded that the molar fluxes $\vec{J}_i$ and $\vec{J}_j$ are measured with respect to the motion of the center of mass of the mixture. It follows from this definition that:

$$\vec{J}_i + \vec{J}_j = 0 \tag{2.87}$$

The expressions (2.83) and (2.84) of Fick's 1st law are all in molar units, which is convenient when dealing with chemical reactions. Nevertheless, in fluid dynamics, mass units are usually preferable. In this case, Fick's law (2.83) is expressed in terms of mass concentration ρ_i (in $kg\,m^{-3}$), mass fraction $w_i = \rho_i/\rho$ and mass flux n_i (in $kg\,m^{-2}s^{-1}$).

For a one-dimensional diffusion in z-direction, equation (2.83) takes the form:

$$J_i = -cD_{i,j}\frac{dy_i}{dz} \tag{2.88}$$

Fick's law of diffusion is valid for any binary solid, liquid or gas solution and consequently for the diffusion of hydrogen in vapor at the anode of a PEMFC. However, in a cell fed with H_2 and air, the oxygen transport takes place in a ternary gas mixture of O_2, N_2 and H_2O and it has to be described by a diffusion law in a multicomponent system: the *Maxwell-Stefan equations* (2.92).

Convecto-diffusive mass transport

In addition to molecular motion, mass may also be transported by the bulk motion of the fluid, *i.e.* by convection. The convective flux $\vec{N}_i^{conv}$ of a species i is defined with respect to the fixed coordinate system by:

$$\vec{N}_i^{conv} = c_i \vec{u} \tag{2.89}$$

As a consequence, the convecto-diffusive flux of i is given by:

$$\begin{aligned} \vec{N}_i &= \vec{J}_i + \vec{N_i^{conv}} \\ &= \vec{J}_i + y_i \vec{N_{tot}} \end{aligned} \tag{2.90}$$

where $\vec{N_{tot}} = \sum_{i=1}^{N} \vec{N}_i = c\vec{u}$.

Equation (2.90) shows that the mass transport can be described by Fick's law (2.83) only in binary systems where the global molar flux is null or negligible and $\vec{N}_i$ reduces to $\vec{J}_i$. In the other cases, the mass flux obeys the convecto-diffusive equation:

$$\vec{N}_i = -cD_{i,j}\vec{\nabla} y_i + cy_i\vec{u} \tag{2.91}$$

Multicomponent diffusion in gases at low density: the Maxwell-Stefan equations

Fick's law can also be used to describe the diffusion of a dilute species i in a multicomponent mixture. However, Krishna and Wesselingh [KW97] discuss the various limitations of the utilization of the Fick's law and argue that the *Maxwell-Stefan equations* (initially derived for a binary mixture) are a more convenient and general approach for describing mass transport in a multicomponent system. For multicomponent diffusion in gases at low density, the most common expression of the Maxwell-Stefan equations is [BSL02]:

$$\vec{\nabla} y_i = -\sum_{j=1}^{N} \frac{1}{cD_{i,j}} (y_j \vec{N}_i - y_i \vec{N}_j) \tag{2.92}$$

An important difference between binary diffusion (described by Fick's law) and multicomponent diffusion (described by the Maxwell-Stefan equations) is the fact that in the first case, the movement of species i is always proportional to the negative of its concentration gradient. In the case of multicomponent diffusion other phenomena can be observed [BSL02]:

- Reverse diffusion: a species moves against its concentration gradient.
- Osmotic diffusion: a species moves even without any concentration gradient.
- Diffusion barrier: a species remains immobile even though its concentration gradient is not zero.

To take account of this difference, the Maxwell-Stefan equations are expressed as functions of the convecto-diffusive flux density $\vec{N}_i$, whereas the Fick's law is expressed as a function of the diffusive flux desnity $\vec{J}_i$ only.

In the case of a one-dimensional diffusion in z-direction, (2.92) simplifies to:

$$\frac{dy_i}{dz} = -\sum_{j=1}^{N} \frac{1}{cD_{i,j}}(y_j N_i - y_i N_j) \tag{2.93}$$

According to the previous hypotheses, the mass transport of oxygen through the pores of the diffusion media in a PEMFC cathode fed with air should be described by the Maxwell-Stefan equations. Analytical solutions can be found for example in the Ph.D thesis of T. Colinart [Col08] or in [LAC+09]. However, as shown in chapter 3.2.2, the transport equations have to be solved in a dynamic regime for the derivation of a mass transport impedance expression. Though, there exists no analytic solution of the Maxwell-Stefan equations in the dynamic regime. As a consequence, the diffusion equations are usually simplified for modeling mass transport in PEMFC cathodes.

Simplification of the diffusion equations in air fed PEMFC cathodes

An air fed cathode is a ternary system (O_2, N_2, H_2O) and consequently, oxygen diffusion through this electrode should be described by the Maxwell-Stefan equations. However, the binary diffusivities of O_2/N_2 and O_2/H_2O being close to each other, it is possible to consider using Ficks law.

Let us write the Maxwell-Stefan equations (2.92) for a species i in a multicomponent gas system of N species and factorize each summand by the binary diffusivity $D_{i,j}$:

$$\begin{aligned}
\vec{\nabla} y_i &= -\frac{1}{c}\left[\frac{1}{D_{i,1}}(y_1\vec{N}_i - y_i\vec{N}_1) + \ldots + \frac{1}{D_{i,j}}(y_j\vec{N}_i - y_i\vec{N}_j) + \ldots + \frac{1}{D_{i,N}}(y_N\vec{N}_i - y_i\vec{N}_N)\right] \\
&= -\frac{1}{cD_{i,j}}\left[\frac{D_{i,j}}{D_{i,1}}(y_1\vec{N}_i - y_i\vec{N}_1) + \ldots + (y_j\vec{N}_i - y_i\vec{N}_j) + \ldots + \frac{D_{i,j}}{D_{i,N}}(y_N\vec{N}_i - y_i\vec{N}_N)\right] \\
&= -\frac{1}{cD_{i,j}}\left[\left(\frac{D_{i,j}}{D_{i,1}}y_1 + \ldots + y_j + \ldots + \frac{D_{i,j}}{D_{i,N}}y_N\right)\vec{N}_i \right. \\
&\qquad \left. - \left(\frac{D_{i,j}}{D_{i,1}}\vec{N}_1 + \ldots + \vec{N}_j + \ldots + \frac{D_{i,j}}{D_{i,N}}\vec{N}_N\right)y_i\right]
\end{aligned} \tag{2.94}$$

If the binary diffusion coefficients are close to each other, they can be written as:

$$\forall k : D_{i,k} = D_{i,j} + \Delta D_k, \text{ with } \Delta D_k << D_{i,j} \tag{2.95}$$

and the ratios of the diffusivities can thus be approached by:

$$\frac{D_{i,j}}{D_{i,k}} \approx 1 + \delta_k, \text{ with } |\delta_k| << 1 \tag{2.96}$$

By inserting (2.96) in (2.94), the Maxwell-Stefan equations take the form:

$$\begin{aligned}
\vec{\nabla} y_i &= -\frac{1}{cD_{i,j}}\left[\left(\sum_{k\neq i,j}(1+\delta_k)y_k + y_j\right)\vec{N}_i - \left(\sum_{k\neq i,j}(1+\delta_k)\vec{N}_k + \vec{N}_j\right)y_i\right] \\
&= -\frac{1}{cD_{i,j}}\left[\sum_{k\neq i} y_k\,\vec{N}_i - \sum_{k\neq i}\vec{N}_k\,y_i + \sum_{k\neq i,j}\delta_k(y_k\vec{N}_i - \vec{N}_k y_i)\right]
\end{aligned} \tag{2.97}$$

The convecto-diffusive molar flux densities $\vec{N}_i$ in (2.97) can be written as the sum of the diffusive $\vec{J}_i$ and convective flux densities $\vec{N}_i^{conv} = y_i c\vec{u}$ (2.90):

$$\begin{aligned}\vec{\nabla} y_i &= -\frac{1}{cD_{i,j}}\left[\sum_{k\neq i} y_k \vec{J}_i - \sum_{k\neq i}\vec{J}_k y_i + \left(\sum_{k\neq i} y_k y_i - \sum_{k\neq i} y_k y_i\right) c\vec{u} + \sum_{k\neq i,j}\delta_k\left(y_k(\vec{J}_i + y_i c\vec{u}) - (\vec{J}_k + y_k c\vec{u})y_i\right)\right] \\ &= -\frac{1}{cD_{i,j}}\left[\sum_{k\neq i} y_k \vec{J}_i - \sum_{k\neq i}\vec{J}_k y_i + \sum_{k\neq i,j}\delta_k\left(y_k\vec{J}_i - \vec{J}_k y_i\right)\right] \end{aligned} \tag{2.98}$$

The total mass flux density $\vec{N_{tot}}$ being $\sum_{i=1}^{N}\vec{N}_i = c\vec{u}$, it follows that the sum of all diffusive flux densities is null: $\sum_i \vec{J}_i = 0$ and equation (2.98) gives:

$$\begin{aligned}\vec{\nabla} y_i &= -\frac{1}{cD_{i,j}}\left[(1-y_i)\vec{J}_i + \vec{J}_i y_i + \sum_{k\neq i,j}\delta_k\left(y_k\vec{J}_i - \vec{J}_k y_i\right)\right] \\ &= -\frac{1}{cD_{i,j}}\left[\vec{J}_i + f(\delta_1,\ldots,\delta_{i-1},\delta_{i+1},\ldots,\delta_{j-1},\delta_{j+1},\ldots,\delta_N)\right] \end{aligned} \tag{2.99}$$

If $\delta_k \to 0\ \forall k$, the function $f(\delta_1,\ldots,\delta_{i-1},\delta_{i+1},\ldots,\delta_{j-1},\delta_{j+1},\ldots,\delta_N)$ tends to zero and equation (2.99) reduces to Fick's 1st law (2.83). If the diffusion is considered as one-dimensional, equation (2.99) can be further simplified. In the case of oxygen diffusion in an air fed cathode, it comes:

$$\frac{dy_{O_2}}{dx} = -\frac{1}{cD_{O_2,H_2O}}\left[J_{O_2} + \delta_{N_2}(y_{N_2}J_{O_2} - y_{O_2}J_{N_2})\right] \tag{2.100}$$

which reduces to:

$$\frac{dy_{O_2}}{dx} = -\frac{1}{cD_{O_2,H_2O}} J_{O_2}\left[1 + \delta_{N_2} y_{N_2}\right] \tag{2.101}$$

since $J_{N_2} = 0$.

It is thus possible to estimate the error made by using Fick's law for the description of the oxygen diffusion in a PEMFC cathode instead of the Maxwell-Stefan equations. Let us consider a PEMFC working under typical conditions: $P = 1\ atm$, $T = 333\ K$ and $RH = 0.7$. The mole fraction of each species is expressed as a function of the relative humidity:

$$y_{H_2O} = \frac{P_{H_2O}}{P} = RH\frac{P_{sat}}{P} \tag{2.102}$$

$$y_{O_2} = 0.21(1 - y_{H_2O}) \tag{2.103}$$

$$y_{N_2} = 0.79(1 - y_{H_2O}) \tag{2.104}$$

The vapor saturation pressure P_{sat} is calculated with equation (1.33).

The binary diffusivities of oxygen in nitrogen and oxygen in vapor in these working conditions can be calculated with equation (2.86), which yields:

$$D_{O_2,H_2O}(T = 333\ K, P = 1\ atm) = 3.25\ 10^{-5}\ m^2 s^{-1} \quad (2.105)$$
$$D_{O_2,N_2}(T = 333\ K, P = 1\ atm) = 2.52\ 10^{-5}\ m^2 s^{-1} \quad (2.106)$$

Hence, δ_{N_2} according to (2.96) is:

$$\begin{aligned} \frac{D_{O_2,H_2O}}{D_{O_2,N_2}} &= 1.29 = 1 + \delta_{N_2} \\ \Rightarrow \delta_{N_2} &= 0.29 \end{aligned} \quad (2.107)$$

According to (2.104), the nitrogen mole fraction at $RH = 0.7$ is: $y_{N_2} = 0.68$. Inserting y_{N_2} and δ_{N_2} (2.107) in the reduced form of the Maxwell-Stefan equations (2.101) yields the error made by modeling oxygen diffusion with Fick's law:

$$\frac{dy_{O_2}}{dx} = -\frac{1}{cD_{O_2,H_2O}} N_{O_2} [1 + 0.2] \quad (2.108)$$

According to this estimation, an error of about 20% is made by using Fick's law instead of the Maxwell-Stefan equations (in these working conditions), which is an important difference. On the top of that, note that for the estimation of the maximum error made by approaching the oxygen transport by Fick's law, the influence of convection has to be considered as well: this will be done in chapter 4.1 via impedance studies.

In conclusion, Fick's law allows to describe qualitatively the oxygen transport in PEMFC air cathodes. However, even in the absence of any convective flow, the difference between the binary diffusivities of O_2/H_2O and O_2/N_2 entails an error of about 20% in typical operating conditions when approaching the oxygen transport by this binary diffusion law.

Effective diffusivity in porous media

In fuel cell diffusion media (GDL, active layers), it is necessary to use an effective diffusion coefficient $D_{i,j}^{eff}$ taking account of the impact of their porous structure on the diffusion [BSL02]. A multitude of expressions have been developed, functions of geometrical characteristics like the porosity ε, the tortuosity τ and the pore size.

The path through a porous medium being tortuous (Figure 2.15), the distance traveled along x' is higher than that along the x direction. The mole flux density N_i' relative to the pore section can be expressed in terms of x by introducing the layer's tortuosity $\tau = x'/x$ in the Fick's 1st law (2.88):

$$N_i' = -c\frac{D_{i,j}}{\tau}\frac{dy_i}{dx} \quad (2.109)$$

The molar flux density relative to the total cross section N_i of the porous medium, can be expressed as a function of the porosity ε. Supposing a random pore distribution, the average cross section is proportional to ε, which yields:

$$N_i = \varepsilon N_i' = -c\frac{\varepsilon D_{i,j}}{\tau}\frac{dy_i}{dx} \quad (2.110)$$

This expression can be written in a form analogous to the 1st Fick's law (2.88):

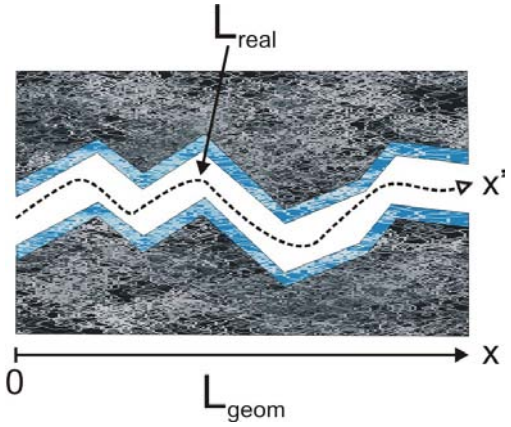


Figure 2.15: *Modeling of the tortuous pore structure*

$$N_i = -cD_{i,j}^{eff}\frac{dy_i}{dx} \tag{2.111}$$

where $D_{i,j}^{eff}$ stands for the effective diffusion coefficient taking account of the porosity and tortuosity of the medium:

$$D_{i,j}^{eff} = \frac{\varepsilon}{\tau}D_{i,j} \tag{2.112}$$

Although models exist for estimating the tortuosity [JS65], τ is generally determined experimentally. As a consequence, most of the models express the effective diffusivity only in terms of the porosity. In most of the cases, the expressions obey Archie's law [Arc42, Tor02]:

$$D_{i,j}^{eff} = \varepsilon^m D_{i,j} \tag{2.113}$$

where m is an exponent varying between 1.5 and 4. In the case of a 3D medium, there is a wide consensus (without strong justification) for using $m = 3/2$, which corresponds to the differential effective medium approximation introduced by Bruggeman [Tor02, Bru35]. $m = 3/2$ is probably appropriate for active layers, in which the orientation of the solid phase does not follow a preferred direction (although this is not true in numerical models based on a cylindrical description of the agglomerates [Ram05]). In the backing layers however, the solid phase can be considered as two-dimensional since the carbon fibers are mainly parallel to the electrodes. In this case, the result of the differential effective medium theory is $m = 2$ [Tor02].

In a liquid, the diffusion is governed by collisions between molecules and $D_{i,j}$ corresponds to the molecular diffusion coefficient $D_{i,j}^{mol}$, which can be calculated with equation (2.86). In a gas, two cases have to be distinguished depending on the values of the pore size and of the molecule's mean free path λ [BSL02, ADP06]:

$$\lambda = \frac{RT}{\sqrt{2}PN_A\sigma} \tag{2.114}$$

where N_A is the Avogadro number and $\sigma = \pi d_i^2$ the mean collision cross-section of species i with a molecule diameter d_i. The mean free path λ represents the average distance traveled by a molecule between two successive inter-molecular collisions. If the mean free path is much smaller than the pore size ($\lambda << d_{pore}$) inter-molecular collisions govern the diffusion process and

$D_{i,j} = D_{i,j}^{mol}$. However, if the pore size is much lower than the mean free path ($\lambda >> d_{pore}$), the gas flux is governed by molecule collisions with the pore wall and the molecule interactions are not significant. This diffusion regime is called the *Knudsen diffusion* and $D_{i,j}$ is replaced by the *Knudsen diffusivity* $D_{i,j}^{K}$, which can be approached by [BSL02, Boi05]:

$$D_{i,j}^{K} = \frac{1}{3} d_{pore} \sqrt{\frac{8RT}{\pi M_i}} \tag{2.115}$$

where M_i is the molar mass of species i in $kgmol^{-1}$.

A third diffusion regime is possible, known as the *flip-flow regime*, in which the mean free path is of the same range as the pore size ($\lambda \approx d_{pore}$). In this case, there exist various more or less sophisticated expressions combining $D_{i,j}^{K}$ and $D_{i,j}^{mol}$ for estimating the binary diffusivity $D_{i,j}$. One of the most simple relations is the *Bosanquet equation* [ZRI04, Boi05]:

$$\frac{1}{D_{i,j}} = \frac{1}{D_{i,j}^{mol}} + \frac{1}{D_{i,j}^{K}} \tag{2.116}$$

The Bosanquet equation shows that the smaller of both coefficients governs the diffusion process.

Effective diffusivity in the porous cathode of a PEMFC

In this section, we try to estimate the effective diffusivities of oxygen in the different layers of a fuel cell cathode. The mean pore size in the GDL and the catalyst layer comes from the literature and the equations introduced above. We consider only the case of purely gaseous oxygen diffusion.

At typical working conditions ($T = 333\ K$; $P = 1\ bar$), the mean free path of oxygen molecules can be estimated with equation (2.114), which yields:

$$\lambda_{O_2} \approx 80\ nm \tag{2.117}$$

Comparing λ_{O_2} to the mean pore size of the diffusion media determines the mass transport regime, *i.e.* molecular or Knudsen diffusion. For this estimation, the mean pore size in the GDL and in the active layer (micro and macro pores) is fixed at:

$$\overline{d}_{GDL} = 50\ \mu m >> \lambda_{O_2} \quad [\text{AST99, PWC05}] \tag{2.118}$$

$$\overline{d}_{M,AL} = 50\ nm \approx \lambda_{O_2} \quad [\text{EAP98, GJL}^{+}\text{03, Eik06, LE08}] \tag{2.119}$$

$$\overline{d}_{\mu,AL} = 5\ nm << \lambda_{O_2} \quad [\text{Eik06, LE08}] \tag{2.120}$$

The mean pore size in the GDL being significantly larger than λ_{O_2}, oxygen transport is assumed to be governed only by molecular diffusion. In this case, the binary diffusivity of oxygen in vapor D_{O_2,H_2O}^{GDL} can be determined with equation (2.86), which leads to:

$$D_{O_2,H_2O}^{GDL} = 3.25\ 10^{-5}\ m^2 s^{-1} \tag{2.121}$$

The pore diameters in the active layer being of the same order of magnitude as the mean free path, molecule-pore wall collisions become significant and the Knudsen diffusion has to be taken into account. The Knudsen diffusivity in the macro- and micro-pores can be determined with equation (2.115):

$$\text{M-pores:} \quad D^{K}_{O_2,M} = 7.82\ 10^{-6}\ m^2 s^{-1} \tag{2.122}$$

$$\mu\text{-pores:} \quad D^{K}_{O_2,\mu} = 7.82\ 10^{-7}\ m^2 s^{-1} \tag{2.123}$$

The micro-pores being significantly smaller than the mean free path, oxygen transport is governed exclusively by molecule-pore wall collisions and $D^{AL,\mu}_{O_2,H_2O} = D^{K}_{O_2,\mu}$. In the macro-pores, mass transfer occurs in the flip-flow regime and the binary diffusivity can be determined with the Bosanquet equation (2.116):

$$D^{AL,M}_{O_2,H_2O} = 6.3\ 10^{-6}\ m^2 s^{-1} \tag{2.124}$$

Comparing the binary diffusivity in the primary pores (2.123) to that in the secondary pores (2.124) shows that the difference in the pore size affects the mass flow velocity by a factor 10.

The porous structure of the layers is taken into account *via* the porosity ε using Archie's law (2.113). According to Springer *et al.* [SZWG96], the GDL porosity is set to $\varepsilon_{GDL} = 0.4$ and thus:

$$D^{eff}_{GDL} = 0.4^2 \cdot 3.25\ 10^{-5} = 5.2\ 10^{-6}\ m^2 s^{-1} \tag{2.125}$$

According to the work of Eikerling [Eik06], the porosity of the agglomerates (due to the micro-pores) is defined by a parameter $\chi = \varepsilon_M / \varepsilon_\mu$, which is generally set to 2. Setting the volume fraction of the macro-pores to a typical value of PEMFC active layers $\varepsilon_M = 0.3$ [SENVS04, RDL$^+$05] gives: $\varepsilon_\mu = 0.15$. The effective diffusivity in the pores inside and between the agglomerates is finally obtained by inserting the binary diffusivity of the micro- (2.122) and macro-pores (2.124) in Archie's law (2.113):

$$\text{M-pores:} \quad D^{eff}_{AL,M} = 0.3^{3/2} \cdot 6.3\ 10^{-6}\ m^2 s^{-1} = 1.04\ 10^{-6}\ m^2 s^{-1} \tag{2.126}$$

$$\mu\text{-pores:} \quad D^{eff}_{AL,\mu} = 0.1.5^{3/2} \cdot 7.6\ 10^{-7}\ m^2 s^{-1} = 4.42\ 10^{-8}\ m^2 s^{-1} \tag{2.127}$$

In this example, the effective diffusivity in the secondary pores (2.126) is about 26 times higher than that in the primary pores (2.127). Noting furthermore that the micro-pores are usually either filed with electrolyte or with water, their contribution to the effective diffusivity is generally neglected in mass transfer modeling [Eik06, LE08]. The effective diffusivity of oxygen is about 5 times larger in the GDL than in the macro-pores of the active layer.

Finally, according to our description of the agglomerates, oxygen has to dissolve and diffuse through a thin electrolyte layer to reach the reaction sites. The diffusion in the electrolyte occurs in liquid phase and is thus governed by collisions between the particles. Gode *et al.* [GLS02] estimated the diffusivity of oxygen in Nafion at $T = 333\ K$ and $P = 1\ atm$ for a relative humidity of 75% and found:

$$D_{O_2,Nafion} = 1.7\ 10^{-10}\ m^2 s^{-1} \tag{2.128}$$

Comparing (2.128) with (2.126) and (2.125), it can be seen that the diffusivity of oxygen in the ionomer is several orders of magnitude lower than those of a gas diffusion in the pores of the diffusion media. The low value of the diffusion coefficient leading to the expectation of high mass transport limitations in the ionomer film is counterbalanced by a very low layer thickness (10 - 100 *nm* [CYH$^+$99]).

2.4.3 Modeling the presence of liquid water

Another important role of PEMFC electrodes is the management of liquid water. Water is produced at the cathode by the ORR and is crucial for enabling a satisfying proton conduction through the ionomer. However, an accumulation of liquid water in the gas pores limits the reagent transport and can hinder the access to the reaction sites. The understanding of wetting properties of the GDL and catalyst layers as functions of the operating conditions and of the layer structure is of great importance for the enhancement of the cell performance. Different modeling approaches can be found in the literature which try to take into account the influence of liquid water accumulation on the transport processes and on the cell electric performance.

Siegel *et al.* [SENVS03] assume in their agglomerate model that water exists in dissolved form in the polymer membrane and in the polymer phase in the catalyst layer, where it is transported by diffusion or electro-osmotic drag. The authors assume furthermore that water is produced in liquid phase at the reaction sites and vaporized instantly to be evacuated in vapor form. Consequently, oxygen transport is considered to occur only by diffusion in gaseous phase.

Others take account of the liquid water content by a saturation factor S_r [Eik06, LE08]. In this approach, three hydration states are described

- In the "dry" state ($S_r \approx 0$), the whole porous structure is water-free.
- In the "optimal wetting" state ($0 < S_r < 1$), the primary pores are completely filled with water, while the secondary pores are water free.
- In the "fully flooded" state ($S_r = 1$), all pores of the active layer are filled with water.

Since the diffusion coefficients in liquid phase are significantly lower than those in gas phase, the authors assume that the macroscopic oxygen transport occurs only in vapor phase. The "fully flooded" state represents the limiting case since diffusion through pores filled with water or ionomer does not contribute to the mass transport. Liu *et al.* [LE08] used this approach to evaluate how gas composition, pore size distribution and wetting properties impact the cell performance. Their results confirm that the cell performance in the "fully flooded" state is significantly lower than in the "optimal wetting" state. However, a limiting current due to flooding of the gas pores only could not be observed. They explain the appearance of a limiting current by diffusion of dissolved oxygen through the ionomer film covering the agglomerates. Furthermore, they analyzed the current-voltage characteristics when passing from the ideally wetted to the saturated state by means of a diffusivity depending on the water saturation S_r. They found out that the transition between the two regimes can be monotonous or involve bistabilities.

Chupin *et al.* [CCD+10] use another approach or the consideration of liquid water accumulation in the catalyst layer (Figure 2.16). They assume that water forms a thin liquid layer covering the agglomerates. Oxygen has thus to diffuse successively through the liquid water layer and the thin ionomer layer in order to reach the reaction sites. Since the oxygen diffusivity in Nafion is close to that in water, the oxygen diffusion is considered to occur in an equivalent layer of thickness δ equal to the sum of the water layer δ_w and of the electrolyte layer thickness δ_n: $\delta = \delta_w + \delta_n$.

Notwithstanding the variety of the models that include the liquid water content, the oxygen transport is generally assumed to occur in form of gas diffusion. This is a realistic assumption since the diffusivity in vapor is significantly higher than in liquid water. The approach chosen in this work is similar to the descriptions using a saturation coefficient. This coefficient is a measure for the decrease of the available pore volume and the enhancement of the tortuosity and thus for

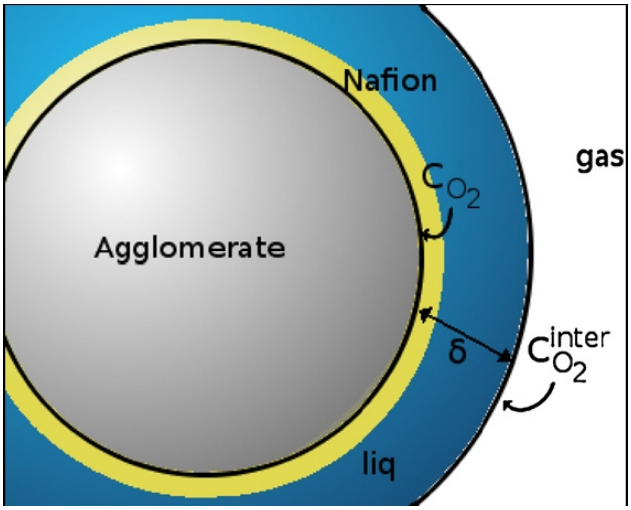


Figure 2.16: *Modeling approach for liquid water accumulation according to Chupin et al. [CCD+10]: liquid layer covering the agglomerates of the active layer.*

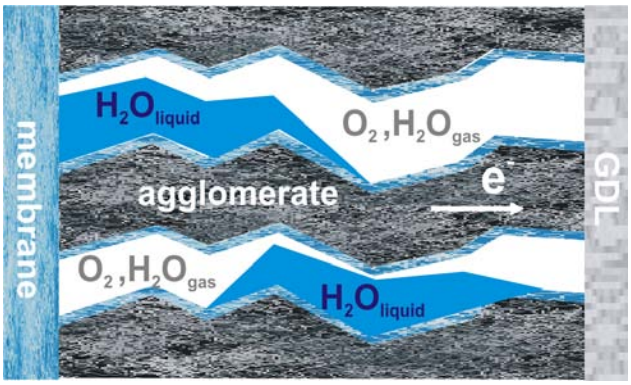


Figure 2.17: *Liquid water accumulation in the catalyst layer reduces the layer's porosity, while increasing the tortuosity.*

the related reduction of the effective diffusivity due to liquid water accumulation (Figure 2.17). Numerous expressions of the effective diffusivity as a function of the saturation coefficient can be found in the literature [Eik06, LE08, NK03]. The simplest consists in introducing a factor $(1-S_r)^m$ in the expression of the effective diffusivity (2.113):

$$D_{i,j}^{eff} = f(\varepsilon)(1-S_r)^m D_{i,j} \tag{2.129}$$

with $m = 2$ according to Nam *et al.* [NK03]. In order to limit the number of parameters, liquid water accumulation will be accounted for by a reduction of the layer porosity in this work.

2.5 Summary and Conclusions of the Chapter

This chapter is an introduction to the main physical phenomena of charge and mass transport occurring in the electrodes and diffusion media of a PEM fuel cell. More precisely, since the present work focuses on air fed cathodes, this chapter presents common simplifications that can be made in this case.

The chapter starts with a presentation of the different steps of the Hydrogen Oxidation Reaction (HOR) and the Oxygen Reduction Reaction (ORR). The charge transfer being considered as the rate determining step in the ORR [ABD01], the Butler-Volmer equation has been derived relating the reaction rate (cell current) to the electrode potential. In typical operating conditions, one of the two partial reactions (of oxidation or reduction) can be neglected, and in this case, the Butler-Volmer equation reduces to the Tafel law.

In a dynamic regime, a part of the current is produced by the variation of the charge distribution in the electrolyte and solid phase surrounding the reaction sites. In this context, the notion of the electrical double-layer (EDL) and of the double-layer capacity characterizing the ability of an interface to counterbalance the charge variations in the EDL are introduced. Starting from the classical description, the notion of the EDL is applied to the membrane/electrode interface in order to estimate the double-layer capacity of the cathode, which is an important parameter in the impedance analysis of fuel cells.

The electrodes are the place of various and coupled (charge, mass and heat) transport phenomena that occur at different length scales. Thus, in order to allow a physico-chemical description of these transport phenomena, a well adapted geometrical representation of the structure of the catalyst layer is necessary. In this context, common representations of the catalyst layer structure are presented, as well as the main parameters characterizing this porous layer.

The last part of this chapter deals with the main approaches used for the description of monophasic mass transport through porous media. It is shown, that an air fed cathode being a ternary system, the oxygen diffusion should be described by the Maxwell-Stefan equations. As there exists no analytical solution of these equations in a dynamic regime, a common simplification is derived which reduces the Maxwell-Stefan equations to Fick's law of binary diffusion. In addition, the presence of liquid water is taken into account in the description of the porous structure.

The understanding of these physico-chemical processes is the basis for the development of an impedance model that allows to discriminate between the different transport processes and to identify the origin of oxygen transport limitations.

3 Electrochemical Impedance Spectroscopy in PEM Fuel Cells

Applied to fuel cells, *Electrochemical Impedance Spectroscopy* (EIS) is a powerful diagnosis tool that can be used during operation with minimal perturbations [SZWG96, POT+98, OXT96]. The main advantage of this technique is that it allows to analyze in the frequency domain the different factors limiting the cell performance, *i.e.* ohmic, kinetic and mass transport losses. A common application of EIS is the identification of the origin of these different potential losses and their estimation [SR89, Rai90, SZWG96, ABD01, CR01, POT+98] with the focus to optimize the MEA design [Wag02] and to determine optimal working conditions [SZWG96, LMM+98]. Beside this, EIS is also used to determine the electrical properties of the fuel cell components, materials and interfaces [GCT+03], as well as their dependence on the operating conditions [FDN+06, POT+98, LCAH06] or on aging effects like electrode poisoning by carbon monoxide [LCAH06, WS03] or carbon corrosion of the bipolar plates [KMIY10]. EIS can also be used for the determination of the catalytic active surface [CR01], although other electrochemical techniques (*e.g.* cyclic voltammetry) are more appropriate. The water management and the MEA humidification playing an important role in the electrical efficiency of a fuel cell, numerous EIS studies focus on the detection of dry and flooded conditions and on their influence on the system operation [SZWG96, CR01].

PEMFC fed with air must be able to operate at high current densities with a satisfying efficiency. Under these conditions, slow oxygen diffusion to the active sites of the cathode has a direct influence on the oxygen reduction reaction (ORR) kinetics. A particular interest is put in this context on the expression of the diffusion impedance, allowing to achieve a better understanding of the mass transfer limitations at the cathode [BGA+02, BWJ+05, NNAO09, SKWS07, SFK+07, FMB91, Fre05]. Various works highlight the limiting role of the gas diffusion layer for oxygen diffusion [SZWG96, PSL+01, IML04], but the origin of the diffusion impedance in the impedance spectra is still not fully understood. Several authors attribute it to slow oxygen diffusion through the backing layers [SZWG96], back diffusion of water in the membrane [POT+98] or diffusion of water in the catalyst layer [WSML98]. Recently, experimental investigations performed by Schneider *et al.* [SKWS07, SFK+07] indicated that the low frequency loop - usually associated with mass transport losses - could be, at least to some extent, an artifact due to concentration oscillations generated by the AC signal that propagate along the air channel by convection and which affect the impedance locally (at a specific location along the cell) and globally (for the whole cell).

Furthermore, in conventional EIS, the measured impedance corresponds to a surface averaged value ascribable to the behavior of the whole MEA surface. However, in most of the cases the analyzed system does not show an ideal behavior: for example, electrodes exhibit usually certain surface heterogeneities or a gradient in oxygen concentration and/or humidity (for under-saturated conditions) can appear along the gas channel by reason of the finite gas flow rates. In order to overcome these difficulties, it is preferable to perform also locally resolved impedance spectroscopy [PBSM11, YWCSZ07, HWO+]. Therefore, we designed and built PEM fuel cells with a segmented cathode.

This chapter introduces the main tools and models that are required for the interpretation of global and local impedance spectra. Further generalities about EIS can be found in a review by D. Macdonald [Mac06] about the history of electrochemical impedance spectroscopy and more generally in a review of Wu *et al.* [WYW+08] about electrochemical techniques as diagnosis tools in PEMFC. A review about local EIS and some of the latest developments of this technique has been published recently by Huang *et al.* [HWO+]. A discussion about the interplay of model development, experimental observations and error analysis in EIS is presented by Orazem and Tribollet [OT08].

3.1 Principle of Electrochemical Impedance Spectroscopy

The main principle of EIS consists in applying a small sinusoidal perturbation (*e.g.* in current or potential) to a system and measuring the associated dynamic response, *i.e.* the resulting potential or current variation. This allows the determination of a transfer function, the cell impedance, which is interpreted in terms of system properties by means of an equivalent electrical circuit. Hence, it is possible to discriminate between the limiting processes occurring at different time scales.

Depending on the controlled variable, EIS is performed in **potentiostatic** or **galvanostatic** mode. In the potentiostatic mode, the voltage is varied and the current response is measured. In the galvanostatic mode, the current is controlled and the voltage response is measured. The experimental results shown in the present manuscript are all obtained in a galvanostatic mode.

EIS experiments can be carried out in the time or in the frequency domain. Measurements in the time domain require a transformation into the frequency domain which is generally done via Fourier transforms. In the second case, the impedance is directly measured as a function of frequency. This is the case of the impedance measurements presented in this work.

3.1.1 Definition of the impedance

The impedance of a system is defined as the transfer function allowing to predict the time-dependent outlet signal (response) as a function of the input signal (stimulus). A transfer function can only be defined for linear, stationary systems: the input and the output signals are connected to each other by a linear differential function which is independent of the applied signal. An alternative definition of a linear system is given by the principle of superposition: the response to multiple inputs is equal to the sum of the responses to each of them.

To perform EIS experiments, a small sinusoidal perturbation of the input signal, *e.g.* a perturbation of the current $\Delta I(t)$ is applied to the DC signal $\langle I \rangle_t$:

$$\Delta I(t) = I(t) - \langle I \rangle_t = \Delta \bar{I} e^{i\omega t} \tag{3.1}$$

where ω denotes the angular frequency (which is related to the frequency ν by $\omega = 2\pi\nu$) and i the imaginary unit defined by $i^2 = -1$. The resulting voltage response $\Delta E(t)$ (3.2) is:

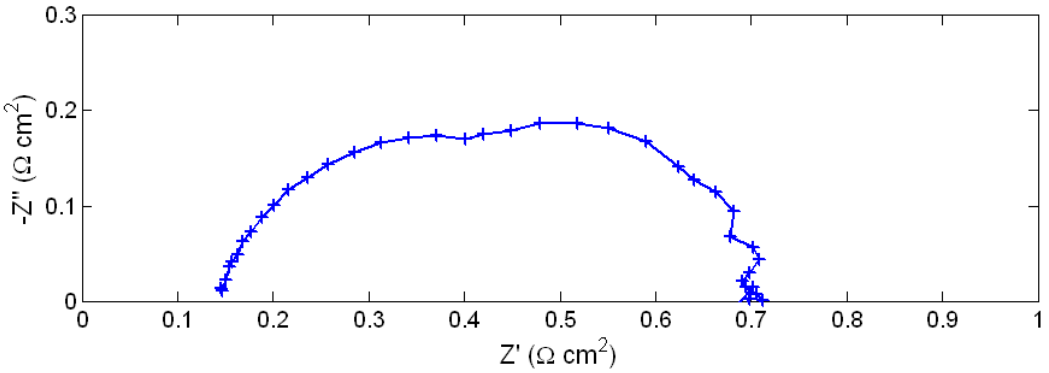
$$\Delta E(t) = E(t) - \langle E \rangle_t = \Delta \bar{E} e^{i(\omega t + \phi)} \tag{3.2}$$

where Φ stands for the phase shift between current and voltage. Note that this is equivalent to applying a voltage perturbation and measuring the corresponding current variation. This allows to

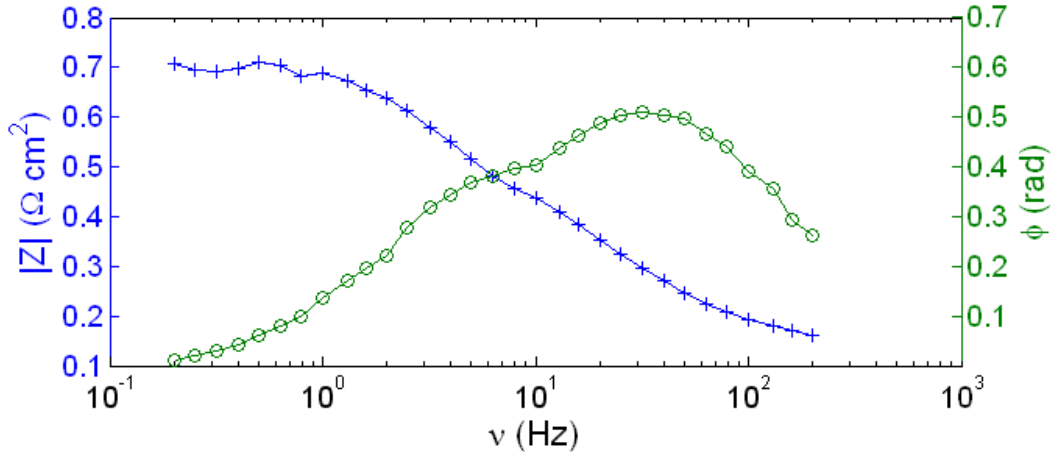
define the impedance Z as the ratio between the voltage and the current perturbation:

$$Z = \frac{\Delta E(t)}{\Delta I(t)} = \frac{\Delta \bar{E} e^{i(\omega t + \phi)}}{\Delta \bar{I} e^{i\omega t}} = \bar{Z} e^{i\phi} \tag{3.3}$$

The value of the phase shift depends on the analyzed electrical component. It is null only for a purely resistive system. In the case of a fuel cell, Φ varies as a function of the frequency.



(a) Nyquist plot: the imaginary part of the impedance $Z''(\omega)$ is represented as a function of the real part $Z'(\omega)$ over the whole frequency range.



(b) Bode plot: separate representation of the modulus $|Z| = \bar{Z}$ and argument ϕ as functions of the frequency $\nu = \omega/2\pi$ in a logarithmic scale.

Figure 3.1: *Experimental EIS spectra measured for a PEMFC fed with H_2/air in counter-flow ($S_{H_2} = 1.2/S_{air} = 2$) working at $\langle j_{cell} \rangle_t = 0.5\, A\, cm^{-2}$ at $T = 57°C$.*

In the case of fuel cells, the amplitude (modulus) and the phase shift (argument) of the impedance are measured over a wide range of frequencies (typically between 10 *mHz* and 10 *kHz*). The impedance being a complex number, there are two types of graphical representations (Figure 3.1):

- **Nyquist plot (Figure 3.1(a))**: Representation of the cell impedance as a function of the angular frequency ω in polar coordinates: $Z(\omega) = \bar{Z} e^{i\phi} = Z'(\omega) + iZ''(\omega)$. In order to obtain a representation in the positive quarter of the complex plan, the opposite of the imaginary part is plotted in general.

- **Bode plot (Figure 3.1(b))**: Separate representation of the modulus $\bar{Z} = |Z| = \sqrt{Z'^2 + Z''^2}$ and argument ϕ (where $\tan\phi = \frac{Z''}{Z'}$) as functions of the frequency $\nu = \omega/2\pi$ in a logarithmic scale.

A fuel cell is a highly non-linear and non-stationary system (consider the exponential relationship between voltage and current in the Butler-Volmer equation (2.25)). As a consequence, the measured voltage response $E(t)$ depends on several harmonics:

$$\Delta E(t) = E(t) - \langle E \rangle_t = \Delta\bar{E}e^{i(\omega t+\phi)} + \Delta\bar{E}e^{i(2\omega t+\phi)} + \Delta\bar{E}e^{i(3\omega t+\phi)} + \ldots \tag{3.4}$$

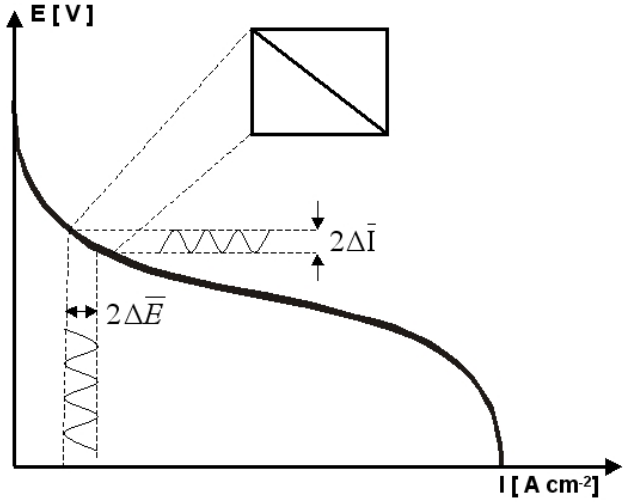


Figure 3.2: *Linearization of the fuel cell current-voltage characteristics by applying a small sinusoidal perturbation around a stationary DC operating point.*

However, when applying perturbations of small amplitude around an operating point one can assume that the cell behaves approximately like a linear system (Figure 3.2) and equation (3.4) can be approached by (3.2).

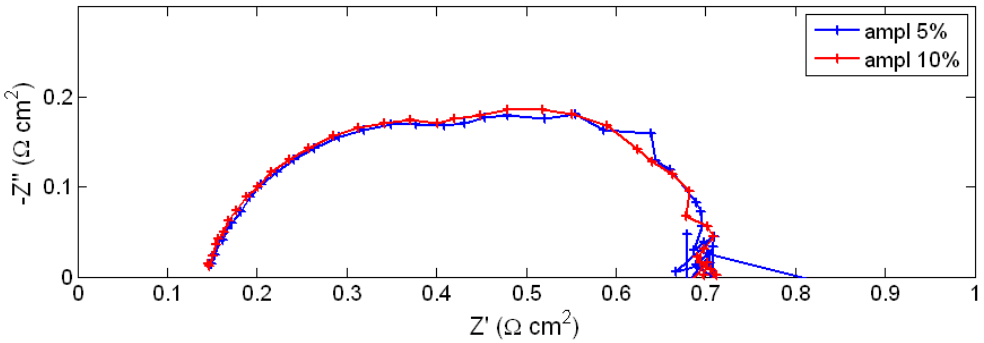


Figure 3.3: *Comparison of impedance spectra recorded with perturbation amplitudes of 5% and 10% of the DC signal. PEMFC operating at* $\langle j_{cell} \rangle_t = 0.5\ A\,cm^{-2}$ *and* $\langle E \rangle_t = 0.6\ V$ *at* $T = 56°C$*. The cell is fed with dry* H_2 *and humidified air* ($RH = 0.74$) *in counter-flow with* $S_{H_2} = 1.2$ *and* $S_{air} = 2$*.*

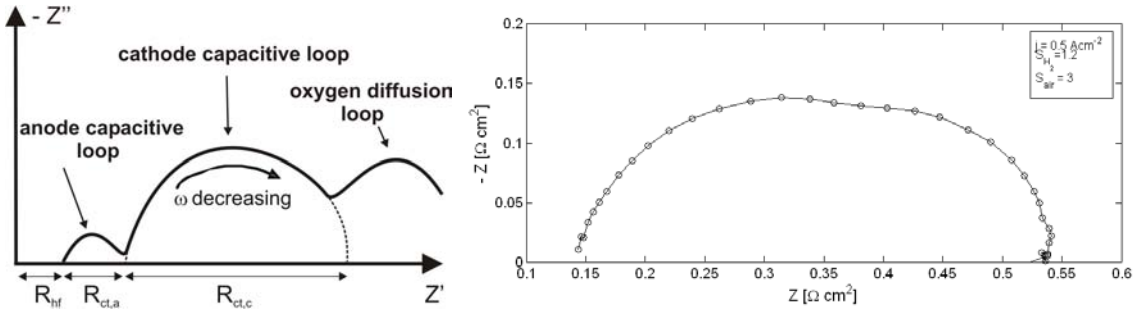
For EIS measurements, the AC signal amplitude must be sufficiently small in order to stay in the linear regime but large enough to obtain a satisfying signal resolution. According to statements in

the literature [Don02, RUKD08], this is the case provided that the voltage perturbation amplitude does not exceed the thermal voltage E_T:

$$\Delta\bar{E} < E_T = \frac{RT}{F} \approx 29\ mV \quad \text{at } T = 333\ K \tag{3.5}$$

In practice, the voltage variations applied to fuel cells are generally comprised between 1 mV and 20 mV [OCCP06]. Figure 3.3 depicts an example of EI spectra measured in typical operating conditions ($\langle j_{cell}\rangle_t = 0.5\ A\,cm^{-2}$ and $\langle E\rangle_t = 0.6\ V$, $T = 56°C$) for two different AC amplitudes: 5% and 10% of the DC signal. The spectra obtained in both cases do not differ significantly from each other, which indicates that the assumption of a linear behavior is valid. Note that perturbation amplitudes of 10% of the operation voltage ($\Delta\bar{E} = 60\ mV$) are above the thermal voltage ($E_T(T = 329\ K) \approx 28\ mV$). However, the spectra obtained with an amplitude of 5% are more scattered than those observed with larger signals. For oscillation amplitudes below 5%, the scattering of the impedance data does not allow to obtain reliable results. As a consequence, all our measurements are performed with AC amplitudes comprised between 5% and 10% of the DC signal.

3.1.2 General pattern of EI spectra



(a) Ideal EI spectrum (b) Experimental EI spectrum

Figure 3.4: *Ideal (a) and measured (b) EI spectra. The experimental spectrum is measured in a frequency range of* 0.025 Hz *to* 500 Hz.

Theoretically, the impedance spectrum of an ideal PEMFC should present three loops, as shown in Figure 3.4(a):

- Two loops at high frequencies due to capacitive and charge transfer processes characterizing the electrochemical half-reactions at the electrode/membrane interfaces: a first (and small) one associated with the HOR at the anode and a larger one associated with the slower ORR at the cathode.

  However, experimental impedance spectra are dominated by cathode potential losses [EK99, CW99], which is explained by the slow ORR kinetics at the cathode compared to the fast HOR rates at the anode. Therefore, the impedance linked to the anode reaction kinetics is usually negligible compared to the cathode loop on which most of the works [ABD01, Des08] focus.

- One loop at low frequencies, which is generally associated with oxygen diffusion at the cathode. We show in this work that this interpretation is not necessarily valid.

In practice, only two or sometimes only one loop are observed between 10^{-3} Hz and 10^{5} Hz [CR01, SZWG96, DLGM^{+}98] as shown by the experimental spectrum in Figure 3.4(b). This is probably due to a superposition of the characteristic times of the different phenomena.

Note that impedance spectra exhibit sometimes also inductive loops in the high frequency ($\nu >$ 1 kHz) [DLGM^{+}98, CR01, RO08] and/or in the low frequency domain ($\nu < 1$ Hz) [ABD01, CW99, SBWS08, MBZ^{+}08, RO08]. Whereas the high frequency inductive behavior is generally associated with experimental artifacts, the explanations of the low frequency inductive loop given in the literature are of various nature [ROT07, RO08, MBZ^{+}08, SBWS08]. Most frequently, this LF inductive loop is associated with the adsorption of reaction intermediates: according to experimental investigations of Roy *et al.* [ROT07], hydrogen peroxide (a surface intermediate of the ORR) could be at the origin of this behavior. They found furthermore that platinum dissolution and the associated deactivation of the catalytic sites could also explain this phenomenon. Schneider *et al.* [SBWS08] relate this phenomenon to water dynamics in the membrane under dry conditions, while Mathias *et al.* [MBZ^{+}08] consider slow kinetics of Pt oxidation at the cathode as a possible origin. Independently of the exact interpretation, the LF inductive behavior is generally related to physical or electrochemical processes occurring in the MEA and not to artifacts induced by the measuring method [RO08].

3.1.3 Interpretation of EI spectra by electrical analogues

Impedance spectra of fuel cells are interpreted, like in other branches of science, by means of models. These models fall in two classes:

- (Electrical) analogues, which are mainly *equivalent electrical circuits* (EEC).
- Physical models.

The difference between both approaches is that analogues aim to reproduce the electrical properties of the system (the impedance $Z(\omega)$), whereas physical models like the electrode models presented in chapter 2.3.1 rely on physical phenomena occurring in the components of the MEA.

Most of the EEC consist of an assembly of resistances R, capacitors C and possibly inductances L aiming to reproduce the spectra. By fitting experimental impedance spectra with an appropriate EEC - usually with a *nonlinear least-squares procedure* (NLSQ) [CR01] - the parameters characterizing the electrical components can be identified. These parameters being usually related to the physical phenomena occurring inside the MEA, their identification allows to obtain information about the kinetics of the electrochemical reactions, ionic and electronic conduction, or even mass transport processes.

Almost all experimental impedance spectra in the right side of the complex plane can be fitted with an equivalent circuit provided that it contains enough $R/C/L$ elements in parallel. As a consequence, a multitude of more or less sophisticated EEC can be found in the literature to describe all possible forms of impedance spectra. However, these EEC are not always consistent with the physics of the system. The aim being not to obtain the best fitting curve but to extract information about the physical processes, there does not exist *a unique equivalent electrical circuit* but many can represent the data equally well. As long as they allow to advance in the understanding of the physics, they have all their interest. In the following, some of the most common equivalent circuits are presented.

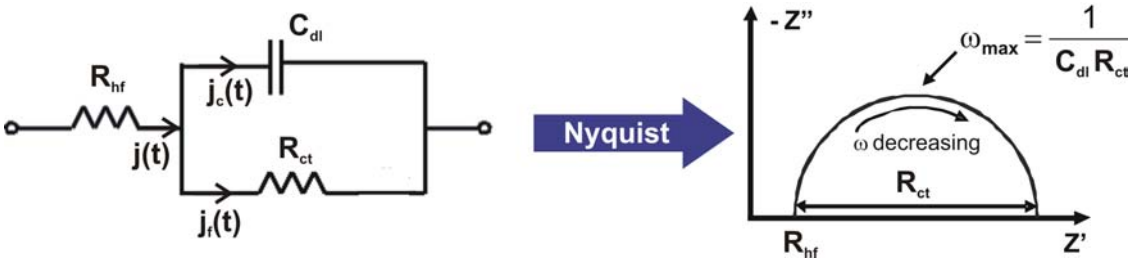


Figure 3.5: *Simple equivalent circuit of an electrode consisting of a charge transfer resistance R_{ct} and a double-layer capacity C_{dl} in parallel. The H^+ conduction in the electrolyte is accounted for by an ohmic resistance R_{hf} (high frequency limit of the spectra).*

The simplest EEC of an electrode is represented in Figure 3.5: it consists of a resistance R_{ct} and a capacity C_{dl} in parallel characterizing the interface where the electrochemical reaction occurs in series with a resistance R_{hf} (high frequency resistance) accounting for the membrane ionic resistance, as well as for the ionic and electronic resistances of the various MEA components (catalyst layer, GDL, bipolar plates) and the interfaces between them. The charge transfer resistance R_{ct} characterizes the rate of the electrochemical reaction. The double-layer capacity C_{dl} (introduced in chapter 2.2) is an indicator of the electrode ability to separate the positive and negative charges. It depends on its geometrical structure and on the platinum and electrolyte loading.

For a purely resistive behavior, the phase shift between a sinusoidal current and voltage is zero, and the impedance of a resistance is given by:

$$Z_R(\omega) = \frac{\Delta\bar{E}e^{i\omega t}}{\Delta\bar{I}e^{i\omega t}} = R \tag{3.6}$$

The impedance of a capacitor is purely imaginary with the following expression relating current and voltage (cf. equation (2.40) in chapter 2.2):

$$\Delta I(t) = C_{dl}\frac{d\Delta E(t)}{dt} \tag{3.7}$$

For a sinusoidal voltage perturbation $\Delta E(t) = \Delta\bar{E}e^{i\omega t}$, equation (3.7) becomes:

$$\Delta I(t) = i\omega C_{dl}\Delta\bar{E}e^{i\omega t} = \omega C_{dl}\Delta\bar{E}e^{i(\omega t+\pi/2)} \tag{3.8}$$

One can see that for a capacitor, the phase shift between the current and the voltage is $\phi = \pi/2$:

$$Z_C(\omega) = \frac{\Delta E(t)}{\Delta I(t)} = \frac{\Delta\bar{E}e^{i\omega t}}{i\omega C_{dl}\Delta\bar{E}e^{i\omega t}} = \frac{1}{i\omega C_{dl}} \tag{3.9}$$

Hence, with equations (3.6) and (3.9) the impedance of the electrical circuit of Figure 3.5 is expressed by:

$$Z(\omega) = R_{hf} + \frac{1}{1/R_{ct} + i\omega C_{dl}} \tag{3.10}$$

The resulting spectrum in the Nyquist plot is depicted in Figure 3.5. It consists of a semicircle of diameter R_{ct} with a maximum at $\omega_{max} = \frac{1}{C_{dl}R_{ct}}$. Its intersection with the real axis in the high frequency domain is at $Z' = R_{hf}$. However, this relatively simple equivalent circuit is not sufficient to fit actual spectra (Figure 3.4), because it does not take into account mass or proton

transport limitations or intermediate steps in the reaction kinetics which could have an impact on the impedance pattern.

The simplest way for representing mass transport limitations in the low frequency range would be to include a capacitance in parallel with a resistance in the basic equivalent circuit [CR01]. However, this assembly of electrical components is not based on a physical description of mass transport. One of the most common expressions of the mass transport impedance in fuel cell equivalent circuits is the finite Warburg element [War99] because it yields results in good agreement with the experimental data, at least qualitatively. It is based on simple assumptions: Fickian diffusion, surface reaction, and a constant gas concentration at the interface with the gas channel. The detailed derivation of the finite Warburg element Z_W is given in section 3.2.2. Note that this impedance depends on two parameters, a characteristic diffusion time τ_d and a diffusion resistance R_d^{1D}.

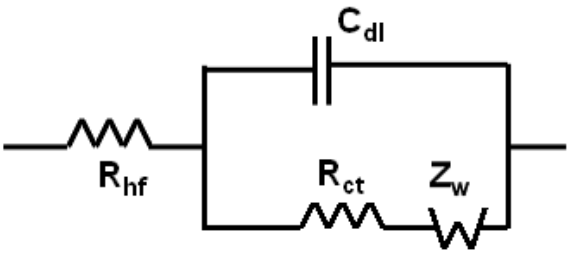


Figure 3.6: *Randles equivalent circuit [Ran47] consisting of a charge transfer resistance R_{ct} and a double-layer capacity C_{dl} in parallel occurring in series with a high frequency resistance R_{hf}. Diffusion limitations are accounted for by a finite Warburg element Z_W [War99].*

Thus, the most common equivalent circuit accounting for mass transport limitations is the Randles EEC (Figure 3.6) which has been introduced by Randles in 1947 [Ran47]. It consists of a (high frequency) resistance R_{hf}, a charge transfer resistance R_{ct}, a double-layer capacity C_{dl} and a finite Warburg element $Z_W(\tau_d, R_d^{1D})$. These 5 parameters can be determined by fitting the experimental impedance spectra using a NLSQ procedure which provides information about charge transfer, reaction and oxygen diffusion kinetics. This relatively simple equivalent circuit yields surprisingly good fitting curves and has the advantage that its components can be related to physical and electrochemical processes that are clearly identified. Furthermore, it is shown in section 3.3 that the 5 parameters are mathematically independent provided that the frequency range is well chosen. These are the reasons why this equivalent circuit is generally chosen as a first basis for investigations on mass transport.

In the recent years, it has been put forward that proton transport in the catalyst layer has an impact on the impedance of fuel cells and should be integrated in the models [SZWG96, EK99, BGA$^+$02, MMB05]. Therefore, the *transmission line models* (TLM) have been developed [EK99, BGA$^+$02, MMB05] for considering the 3D structure of the active layer. The principle of TLM consists in discretizing this layer into a finite number of segments, each of them being represented by an elementary EEC. An example of such an EEC [EK99] is depicted in Figure 3.7. It shows a discretized transmission line with m elementary equivalent circuits representing the electrochemical processes in each segment in the direction perpendicular to the electrode surface. Each elementary circuit consists of two resistances, one related to the electron transport through the carbon particles R_{el} and another to the ion transport through the electrolyte phase in the catalyst layer R_p. They are connected to each other by a double-layer capacitance C_{dl} in parallel with a

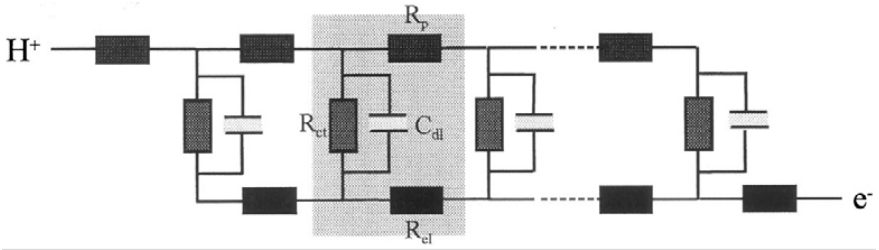


Figure 3.7: *One-dimensional transmission line model (TLM) representing the impedance of the catalyst layer in the direction perpendicular to the electrode surface. In order to account for phenomena in the depth of the electrode, the impedance is discretized into m elementary equivalent circuits. In this representation by Eikerling and Kornyshev [EK99], one elementary unit contains: a protonic R_p and an electronic resistance R_{el} connected by a double-layer capacity C_{dl} and a charge transfer resistance R_{ct} in parallel.*

charge transfer resistance R_{ct}.

Usually, there exists no analytical expression of the whole EEC impedance. The impedance of each segment can be obtained with an iterative procedure for adjusting the boundary conditions (calculating the characteristics of the adjacent segments). The impedance of the complete active layer is given by the limiting case when $m \longrightarrow \infty$.

The impact of phenomena occurring in the bulk of the catalyst layer on the impedance of the electrode is discussed with more details in section 4.2. Notwithstanding the fact that these phenomena are not negligible when analyzing the impedance response of an isolated electrode, this model does not seem fully appropriate for the identification of oxygen transport parameters due to its complexity. There are probably inter-correlations between the different parameters, which risk to lead to misinterpretations. However, a numerical analysis of this impedance model is presented in section 4.2.

Other frequently used elements in fuel cell EEC

Constant Phase Elements (CPE)

Fuel cell impedance spectra are often depressed semicircles and the quality of the fitting curves obtained with equivalent circuits containing capacities is not always satisfying. Therefore, *Constant Phase Elements* (CPE) are often used instead of capacities to better fit the depressed semicircles in Nyquist plots and to avoid frequency depending phase shifts between the cell voltage and current [CR01, MKB06, JOPT06, RO09]. Different expressions of the impedance of a constant phase element Z_{CPE} can be found in the literature [JOPT06]. In most of the cases, Z_{CPE} is written under the form:

$$Z_{CPE} = \frac{1}{CPE\,(i\omega)^{\alpha}} \tag{3.11}$$

where $\alpha \leq 1$. This impedance is purely resistive for $\alpha = 0$, purely capacitive for $\alpha = 1$ and inductive for $\alpha = -1$; generally $\alpha \in [0.5, 1]$.

The majority of the authors consider that CPE result from a distribution of the capacitance in the catalyst layer that is - in most of the cases - explained by its geometrical structure: surface irregularities due to the roughness of the active area and the electrode porosity [CR01, Las99, HL01] causing a heterogeneous current and potential distribution [JOPT06] that leads to a deviation from

an ideal capacitive behavior. Another explanation of CPE is linked to surface inhomogeneities associated with the electrode fractal geometry [NP85, KPK03]. Kim *et al.* [KPK03] compared the evolution of the values of α determined from electrochemical impedance measurements with the amount of edge planes (estimated qualitatively from *X-ray photoelectron spectroscopy* (XPS) analyses): their results showed that α decreases with an increasing number of edge planes. They conclude from these results that the contribution of surface inhomogeneities is higher than that of surface irregularities to the capacitance dispersion (CPE behavior) of the fractal electrode.

CPE are used for various kinds of investigations in equivalent electrical circuits: Ciureanu and Wang [CW99] studied the oxidation of hydrogen and hydrogen-CO mixtures on Pt-based gas diffusion electrodes via EIS and used circuits containing CPE to better fit their data. Meland *et al.* [MKB06] analyzed the effect of water on the HOR at the anode of a PEMFC by impedance spectroscopy and used CPE elements in their equivalent circuit and Roy *et al.* [RO09] evaluate the influence of the design and of the operating conditions on the interfacial capacitance by using equivalent circuits containing CPE. However, the various different expressions of the CPE impedance in addition with the sometimes conflicting physical interpretations underline that the physical meaning of this element is not clear: the main reason for the implementation of CPE in equivalent circuits is to obtain better fitting curves. Thus, the use of CPE is not necessarily recommended, especially if the impedance spectra exhibit an ideal capacitive behavior [Mac06].

Anode equivalent circuits

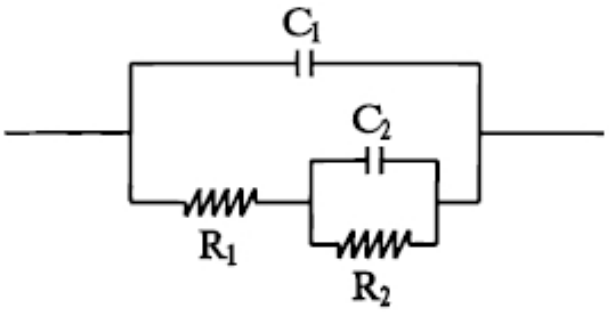


Figure 3.8: *Equivalent circuit used by Ciureanu and Wang [CW99] to model the HOR at the anode of a PEMFC. C_1 and R_1 represent the charge transfer step and C_2 and R_2 the dissociative chemisorption of hydrogen at the electrode surface.*

Impedance spectra measured at the anode of a PEMFC (by feeding both electrodes with hydrogen) exhibit two loops. The high frequency arc is associated with charge transfer processes, while Ciureanu and Wang [CW99] explain the low frequency arc by the dissociative chemisorption of hydrogen ($H_2 \rightarrow 2H_{ads}$; cf. chapter 2.1.1). According to them, slow hydrogen diffusion cannot be at the origin of this loop, since its shape is insensitive to the gas flow rates. They model the hydrogen adsorption by a resistance R_2 in parallel with a capacitance C_2 (Figure 3.8). The reaction kinetics are described in a classical way by a parallel circuit of a resistance R_1 and a capacity C_1. When their measured spectra showed depressed semicircles, they replaced the capacitances (C_1, C_2) by constant phase elements.

Meland *et al.* [MBK05, MKB06] explain the origin of the low frequency (LF) loop in anode impedance spectra by dissociative chemisorption of hydrogen, which takes place in two well separated steps. They conclud that constant phase elements are not sufficient to describe the ex-

perimental data. They fitted the LF loop with a *Gerischer element* (initially used mainly for solid oxide fuel cells) with two possible expressions of the impedance:

$$Z_{ad} = \frac{RT}{2F^2 c^a_{H_2,eq}\sqrt{2D^a_{H_2}k^d_{H_2}(1+i\omega\tau_{ad})}} \tag{3.12}$$

and

$$Z_{ad-2} = \frac{RT}{F^2 c^a_{H,eq}\sqrt{2D^a_H k^d_H c^a_{H,eq}(1+i\omega\tau_{ad})}} \tag{3.13}$$

depending whether hydrogen is adsorbed in molecular (3.12) or in atomic form (3.13). D^a, k^d and c^a represent the surface diffusivity, the reaction rate coefficient and the equilibrium concentration, respectively. The good quality of the fitting curves obtained with the Gerischer element confirms their assumptions: hydrogen adsorption occurs at the surface of carbon particles before a surface diffusion of the adsorbed species and finally the charge transfer step at the catalyst surface. Further studies of Meland *et al.* [MKB06] revealed the existence of a third rate-limiting step: proton hydration, which modifies the impedance of the charge transfer step. The arcs of these two processes are usually superimposed at higher temperatures, but can be separated at $30°C$. The anode equivalent circuit that follows from their investigations is depicted in Figure 3.9.

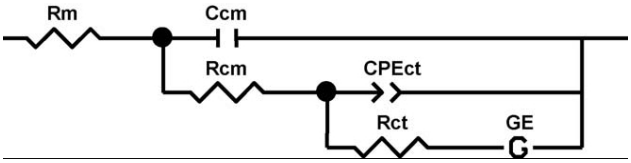


Figure 3.9: *Equivalent circuit derived by Meland et al. [MKB06] for the three rate-limiting steps at the anode of a PEMFC. The charge transfer step is represented by R_{ct} in parallel with the constant phase element CPE_{ct}. The consecutive adsorption-diffusion of hydrogen is accounted for by the Gerischer element GE, while the step corresponding to proton hydration is represented by R_{cm} in parallel with the capacitance C_{cm}. The ionic resistance of the membrane is denoted R_m.*

3.2 Analytical Expression of the Faradaic Impedance

This section presents the basic components of fuel cell electrical equivalent circuits. The attention is turned to the cathode and to the common Randles equivalent circuit (cf. Figure 3.6).

3.2.1 Definition of the faradaic impedance

The half-reactions at the electrodes of a PEMFC are of the form: $Ox + ne^- \leftrightarrow Red$. As shown in chapter 2.1.2, the reaction rate is generally described by the Butler-Volmer equation:

$$j_f = j_0\left(\frac{c_{Red}(0)}{c^*_{Red}}e^{\frac{\alpha nF}{RT}\eta_{act}} - \frac{c_{Ox}(0)}{c^*_{Ox}}e^{\frac{-(1-\alpha)nF}{RT}\eta_{act}}\right) \tag{3.14}$$

where $c_k(0)$ stands for the agent concentration at the reaction interface ($k = Red, Ox$) and c^*_k for the bulk concentration.

In AC conditions, the faradaic current density j_f and the activation overpotential η_{act} vary around their steady-state values, which allows to define the *faradaic impedance* Z_f by:

$$Z_f = \frac{\Delta\eta_{act}(t)}{\Delta j_f(t)} \tag{3.15}$$

According to the Butler-Volmer law (3.14), j_f depends on the activation overpotential, as well as on the concentrations of the reductant and oxidant at the reaction interface ($x = 0$, assuming a one-dimensional model as represented in Figure 3.10). The linearization of the faradaic current density yields:

$$\Delta j_f(t) = \frac{\partial j_f}{\partial \eta_{act}}\Delta\eta_{act}(t) + \left.\frac{\partial j_f}{\partial c_{Ox}}\right|_{x=0}\Delta c_{Ox}(0,t) + \left.\frac{\partial j_f}{\partial c_{Red}}\right|_{x=0}\Delta c_{Red}(0,t) \tag{3.16}$$

and the faradaic impedance (3.15) takes the form:

$$Z_f = \frac{\partial \eta_{act}}{\partial j_f} - \frac{\partial \eta_{act}}{\partial j_f}\left.\frac{\partial j_f}{\partial c_{Ox}}\right|_{x=0}\frac{\Delta c_{Ox}(0,t)}{\Delta j_f(t)} - \frac{\partial \eta_{act}}{\partial j_f}\left.\frac{\partial j_f}{\partial c_{Red}}\right|_{x=0}\frac{\Delta c_{Red}(0,t)}{\Delta j_f(t)} \tag{3.17}$$

The first term in (3.17) is the *charge transfer resistance* R_{ct}:

$$R_{ct} = \frac{\partial \eta_{act}}{\partial j_f} \tag{3.18}$$

This resistance is an indicator of the rate of charge separation during the reaction. Its general expression is obtained by derivation of the Butler-Volmer equation (3.14):

$$R_{ct}^{-1} = j_0\frac{nF}{RT}\left[\alpha_{Red}\frac{c_{Red}(0)}{c_{Red}^*}\exp\left\{\frac{\alpha_{red}nF}{RT}\eta_{act}\right\} + \alpha_{Ox}\frac{c_{Ox}(0)}{c_{Ox}^*}\exp\left\{\frac{-\alpha_{Ox}nF}{RT}\eta_{act}\right\}\right] \tag{3.19}$$

where $\alpha_{Ox} = 1 - \alpha_{Red}$. (3.19) can be simplified for low and high overpotentials:

- At low overpotentials (cf. equation (2.27)):

$$R_{ct} = \frac{RT}{nF\,j_0} \tag{3.20}$$

- At high overpotentials, the reaction kinetics are described by a Tafel law (2.33), which leads to:

$$R_{ct} = \frac{b}{j_f}, \quad \text{with } b = \frac{RT}{\alpha nF} \tag{3.21}$$

  R_{ct} decreases with increasing current density and depends on the interfacial reactant concentrations via j_f.

The other terms stand for the *mass transport impedances* Z_{c_k} functions of the species concentrations ($k = Ox, Red$) and indirectly of the reaction kinetics through R_{ct}:

$$Z_{c_k} = -R_{ct}\left.\frac{\partial j_f}{\partial c_k}\right|_{x=0}\frac{\Delta c_k(0,t)}{\Delta j_f(t)} \tag{3.22}$$

The first two factors of equation (3.22) - R_{ct} and $\left.\frac{\partial j_f}{\partial c_k}\right|_{x=0}$ - can be derived directly from the Butler-Volmer equation (3.14). In order to obtain an explicit expression of the last term $\frac{\Delta c_k(0,t)}{\Delta j_f(t)}$, an appropriate mass transport model is necessary to express the species concentrations as functions of the faradaic current density.

3.2.2 1D cathode mass transfer impedance: the finite Warburg element

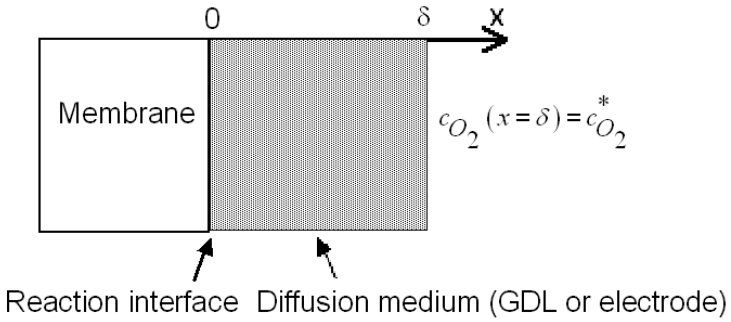


Figure 3.10: *1D geometry corresponding to the finite Warburg element: oxygen diffusion in x-direction, constant oxygen concentration at the diffusion medium boundary ($x=\delta$) and surface reaction at $x=0$. The geometric structure of the diffusion medium is taken into account through the effective diffusion coefficient D^{eff}.*

The infinite and finite Warburg elements have been expressed for the first time by Warburg in 1899 [War99]. They represent impedances relative to gas transport via diffusion in homogeneous media. The former arises from the one-dimensional solution of the Fick equations in an infinite medium. The finite Warburg element is usually chosen to describe gas diffusion through a homogeneous medium of a finite thickness δ (Figure 3.10).

Applied to the description of oxygen transport at the cathode of a PEMFC, the main hypotheses of this model are [BBO04, RDL$^+$05]:

- The cathode is isothermal and isobaric.
- The cathode being the place of water production, the ionomer is assumed to be well-hydrated. Consequently, ohmic drops in the active layer can be neglected due to its high electronic and ionic conductivity.
- Water diffusion through the solid phase of the active layer is not considered.
- Mass transport of H_2O and O_2 is assumed to occur only by monophasic diffusion through a porous medium. Consequently, oxygen transport through the pores of the diffusion media can be described using the Fick equations:

$$1^{st}\text{Fick's law:} \qquad N_k = -D_{k,l}^{eff} \left.\frac{\partial c_k}{\partial x}\right|_{x=0} \tag{3.23}$$

$$2^{nd}\text{Fick's law:} \qquad \frac{\partial c_k}{\partial t} = D_{k,l}^{eff} \frac{\partial^2 c_k}{\partial x^2} \tag{3.24}$$

with $k = O_2$ and $l = H_2O$. The molar flux densities of oxygen and water vapor in equation (3.23) can be expressed as functions of the faradaic current density: $N_{O_2} = -j_f/4F$ (2.76). According to the scheme in Figure 3.10, the molar fluxes are counted positive in the x-direction (from the anode to the cathode).

Strictly speaking, when the cell is fed with air instead of pure oxygen, the gas transport is described by Maxwell-Stefan equations. However, since the binary diffusion coefficients of O_2/H_2O and O_2/N_2 [BSL02] are close to each other, it is shown in section 2.4.2 that the error made by approaching the Maxwell-Stefan equations by the Fick equations is of about 20% in typical operating conditions. This is not negligible, but the Fick equations allow to derive an analytical expression of the oxygen diffusion impedance, which is not the case with the Maxwell-Stefan equations.

The assumption of a purely diffusive mass transport implies that the net molar flux density in the GDL $N_{O_2} + N_{H_2O}^{GDL}$ is null (cf. section 2.4.2). The flux density of water produced at the cathode being $\left|N_{H_2O}^{prod} = j_f/2F\right|$, it is thus assumed that only the half is evacuated through the cathode GDL in order to compensate the oxygen flux. However, this assumption is not necessarily valid and an additional convective flux in the x-direction can be present in practice. A detailed discussion about the impact of a convective flux on the cell impedance is made in section 4.1 where a 1D convecto-diffusive model is derived. Some experimental results obtained with this oxygen transport impedance are given in section 6.1.

- The Warburg approach assumes the presence of a reaction interface ($x = 0$) in order to express the reagent flux as a function of the faradaic current density in the first Fick law (3.23) (Figure 3.10). This description neglects the fact that the electrode is a composite medium with two phases for the charge transport (electrolyte for the proton transport and carbon for the electron transport) where the reaction sites are dispersed through its thickness. This approach does not allow to account for proton conduction and gas consumption inside the electrode. The impact of these two effects on the impedance response is discussed in section 4.2.

  Note that the assumption of a reaction interface does not mean that the catalyst layer is considered as an interface. Oxygen diffusion through the pores of the catalyst layer and of the GDL is characterized by an effective diffusion coefficient which accounts for the porosity and the pore size of each medium.

- Time variations of the concentration are assumed to be confined to the diffusive media: the concentration at the GDL/channel interface ($x = \delta$) is constant in time, $c_k(\delta, t) = c_k^*$ (Figure 3.10).

  Note that this assumption plus the fact that this model is based on a one-dimensional description of the mass transport neglects any influence of phenomena occurring in the direction parallel to the electrode surface, *i.e.* gas consumption along the channel length and the

propagation of the concentration oscillations. The impact of these two phenomena on the mass transport impedance is investigated via the pseudo-2D models developed in chapter 5.

Diffusion impedance of a reversible reaction

In the following, the expression of the finite Warburg element is derived in the case of quasi-reversible charge transfer reactions of the form:

$$\mathrm{n_{Ox}Ox} + \mathrm{ne^-} \underset{\mathrm{j_{f>0}}}{\overset{\mathrm{j_{f<0}}}{\rightleftharpoons}} \mathrm{n_{Red}Red} \tag{3.25}$$

Supposing that the reaction follows a Butler-Volmer law (3.14), the current density is counted positive in the direction of oxidation and negative in the direction of reduction.

The small sinusoidal perturbation of the current density $\Delta j_f(t)$ provokes an oscillation with the same frequency of the overpotential $\Delta\eta_{act}(t)$ and of the reagent concentrations $\Delta c_k(x,t)$ (with $k = Ox/Red$). In an established periodic regime (harmonic oscillations of small amplitude), the oscillations obey the following expressions:

$$\Delta\eta_{act}(t) = \eta_{act}(t) - \langle\eta_{act}\rangle_t = \Delta\bar{\eta}_{act}\exp(i\omega t) \tag{3.26}$$
$$\Delta j_f(t) = j_f(t) - \langle j_f\rangle_t = \Delta\bar{j}_f\exp(i\omega t) \tag{3.27}$$
$$\Delta c_k(x,t) = c_k(x,t) - \langle c_k(x)\rangle_t = \Delta\bar{c}_k(x)\exp(i\omega t) \tag{3.28}$$

The time-averaged value of the reactant concentrations $\langle c_k(x)\rangle_t$ corresponds to the steady-state solution of the Fick diffusion equations (3.23) and (3.24) in the boundary conditions of the one-dimensional diffusion model (Figure 3.10):

$$\text{At } x=\delta: \quad \langle c_k(x=\delta)\rangle_t = c_k^* \tag{3.29}$$
$$\text{At } x=0: \quad N_k = \mp\frac{\langle j_f\rangle_t}{\frac{n}{n_{Red}}F} = -D_k^{eff}\left.\frac{\partial\langle c_k\rangle_t}{\partial x}\right|_{x=0} \tag{3.30}$$

Remember that a purely diffusive mass transport implies that: $N_{Red} = -N_{Ox}$. The sign of the flux depends on if the concerned species is produced or consumed. Assuming that $j_f > 0$ and $\eta_{act} > 0$ (oxidation reaction), the reductant is consumed ($N_{Red} < 0$) and the oxidant is produced ($N_{Red} > 0$). The sign corresponding to the oxidation reaction is noted on the upper side and that of the reduction reaction on the lower side in the derivation of the mass transport impedance which is presented in the following.

Hence, the concentration in steady-state is given by:

$$\langle c_k(x)\rangle_t = c_k^* \mp \frac{\langle j_f\rangle_t}{\frac{n}{n_{Red}}F}\frac{\delta - x}{D_k^{eff}} \tag{3.31}$$

In order to determine the concentration variations $\Delta c_k(x,t)$, the two Fick equations (3.23) and (3.24) have to be solved in AC conditions. The boundary conditions take the form:

$$\text{At } x=\delta: \quad \Delta\bar{c}_k(x=\delta)=0 \tag{3.32}$$

$$\text{At } x=0: \quad \mp\frac{\Delta\bar{j}_f}{\frac{n}{n_{Red}}F}=-D_k^{eff}\left.\frac{\partial\Delta\bar{c}_k}{\partial x}\right|_{x=0} \tag{3.33}$$

The species concentration is then given by:

$$\begin{aligned} c_k(x,t) &= \Delta c_k(x,t)+\langle c_k(x)\rangle_t \\ &= \mp\frac{\Delta\bar{j}_f}{\frac{n}{n_{Red}}F\sqrt{i\omega D_k^{eff}}}\frac{\sinh\left(\sqrt{\frac{i\omega(\delta-x)^2}{D_k^{eff}}}\right)}{\cosh\left(\sqrt{\frac{i\omega\delta^2}{D_k^{eff}}}\right)}e^{i\omega t}+\langle c_k(x)\rangle_t \end{aligned} \tag{3.34}$$

The detailed derivation of the expressions of the reactant concentration is given in appendix A. With the expression of the concentration (3.34), the diffusion impedance of species k defined by equation (3.22) takes the form:

$$Z_{c_k}=R_{ct}\frac{j_0\exp\left(\pm\frac{\alpha_k nF}{RT}\langle\eta_{act}\rangle_t\right)}{c_k^*}\frac{\tanh\left(\sqrt{\frac{i\omega\delta^2}{D_k^{eff}}}\right)}{\frac{n}{n_{Red}}F\sqrt{i\omega D_k^{eff}}} \tag{3.35}$$

The charge transfer resistance R_{ct} in reversible conditions is given by equation (3.19), where the values of the overpotential and the species concentrations correspond to their steady-state values $\langle\eta_{act}\rangle_t$ and $\langle c_k(0)\rangle_t$.

The sum of the reductant and of the oxidant diffusion impedances represents the mass transport impedance and is called the *finite Warburg impedance* Z_W:

$$Z_W=R_{ct}\frac{j_0}{\frac{n}{n_{Red}}F\sqrt{i\omega}}\left[\frac{\exp\left(\frac{\alpha_{Red}nF}{RT}\langle\eta_{act}\rangle_t\right)}{c_{Red}^*\sqrt{D_{Red}^{eff}}}\tanh\left(\sqrt{\frac{i\omega\delta^2}{D_{Red}^{eff}}}\right)+\frac{\exp\left(-\frac{\alpha_{Ox}nF}{RT}\langle\eta_{act}\rangle_t\right)}{c_{Ox}^*\sqrt{D_{Ox}^{eff}}}\tanh\left(\sqrt{\frac{i\omega\delta^2}{D_{Ox}^{eff}}}\right)\right] \tag{3.36}$$

Cathode diffusion impedance

At the cathode of a PEM fuel cell $Red=H_2O$, $Ox=O_2$ and $n_{O_2}=1/2$. For sufficiently high values of the current density, the reductant contribution in the Butler-Volmer law (3.14) can be neglected and the cathode activation overpotential follows a Tafel law of the form:

$$\eta_{act}=-b\ln\left(\frac{-j_f}{j_0\frac{c_{O_2}(0)}{c_{O_2}^*}}\right) \quad \text{, with } b=\frac{RT}{\alpha_{O_2}nF} \tag{3.37}$$

By convention, the activation overpotential and the current density are negative at this electrode.

However, for convenience, the absolute values of η_{act} and j_f are considered in the following.

As the reaction is described by a Tafel law (3.37), the different terms of the faradaic impedance can be simplified: the charge transfer resistance takes the form of equation (3.21) and the finite Warburg impedance (3.36) reduces to:

$$Z_W = R_d^{1D} \frac{\tanh\sqrt{i\omega\tau_d}}{\sqrt{i\omega\tau_d}} \tag{3.38}$$

where R_d^{1D} is a constant resistance corresponding to the low-frequency limit of Z_w:

$$R_d^{1D} = \lim_{\omega\to 0} Z_W = \frac{b\delta}{4FD^{eff}\left\langle c_{O_2}(0)\right\rangle_t} \tag{3.39}$$

The mean oxygen concentration at the reaction interface is obtained with (3.31), leading to:

$$\left\langle c_{02}(0)\right\rangle_t = c_{02}^* - \frac{\left\langle j_f\right\rangle_t \delta}{4FD^{eff}} \tag{3.40}$$

τ_d is a time constant depending on the diffusion medium thickness δ and on D^{eff}:

$$\tau_d = \frac{\delta^2}{D^{eff}} \tag{3.41}$$

Since it is assumed that water is present in vapor form, the effective diffusivity D^{eff} is actually the one of oxygen in water vapor $D^{eff}_{O_2,H_2O}$ (cf. section 2.4.2).

For low frequencies ($\tau_d << 3/\omega$), the finite Warburg element can be approached by R_d^{1D} in parallel with a capacity $C_d^0 = \delta^2/\left(3D^{eff}R_d^{1D}\right)$. For high frequencies ($\tau_d >> 3/\omega$), this impedance behaves like an *infinite Warburg element* describing the diffusion over an infinite length [Don02]:

$$Z_{W\infty} = \frac{R_d^{1D}}{\delta}\frac{(1-i)}{\sqrt{2\omega/D^{eff}}} \tag{3.42}$$

It is worth mentioning that the hydrogen diffusion impedance at the anode is obtained in an analogous way, by inserting $Red = H_2$, $Ox = H_3O^+$ and $n_{H_2} = 1$ in the general expression of the finite Warburg impedance (3.36).

3.3 Sensitivity Analysis

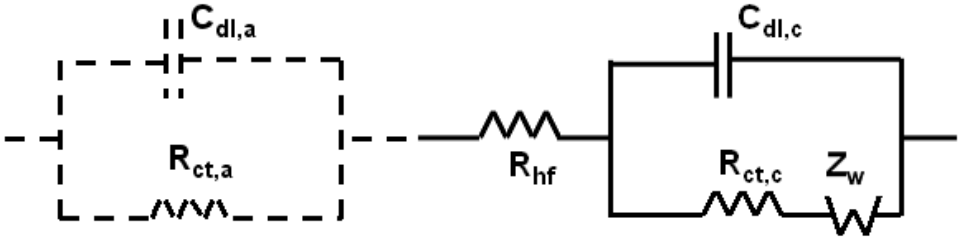


Figure 3.11: *MEA equivalent electrical circuit(s). Dashed lines: anode equivalent circuit used only for sensitivity analysis. Plain lines: Randles equivalent circuit [Ran47] of the cathode and the electrolyte used for parameter estimation.*

Our impedance studies are performed with a PEMFC fed with pure hydrogen and air. In a first step, we chose to represent the cathode by a Randles equivalent electrical circuit (Figure 3.11, plain lines) [Ran47]. It consists of a resistance R_{hf}, a charge transfer resistance $R_{ct,c}$, a double-layer capacity $C_{dl,c}$ and a finite Warburg element Z_W [War99] depending on two parameters, the characteristic diffusion time τ_d and the diffusion resistance R_d^{1D}.

On the anode side (Figure 3.11, dashed lines), the equivalent circuit is simpler, containing only a charge transfer resistance $R_{ct,a}$ in parallel with a double layer capacity $C_{dl,a}$. When working with pure hydrogen, mass transport is not rate-limiting [CW99] and the use of a diffusion impedance in series with $R_{ct,a}$ is not necessary. The anode equivalent circuit is taken into account only in order to estimate its influence on the identification of the cathode impedance parameters with the focus to justify its neglect in the following.

The cell impedance corresponding to the MEA equivalent circuit in Figure 3.11 is expressed by:

$$\begin{aligned} Z_{cell} &= Z_{anode} + R_{hf} + Z_{cathode} \\ &= \left(\frac{1}{R_{ct,a}} + i\omega C_{dl,a}\right)^{-1} + R_{hf} + \left(\frac{1}{R_{ct,c} + Z_W} + i\omega C_{dl,c}\right)^{-1} \end{aligned} \tag{3.43}$$

The impedance parameters are determined by fitting experimental spectra with the expression of equation (3.43) using a complex nonlinear least square method. In practice, we use the Matlab function *fminsearch* that determines the minimum of the function ΔZ being defined as the square of the difference between the experimental Z_{exp} and the theoretical impedance Z_{cell} (3.43) - $\Delta Z = (Z_{exp} - Z_{cell})^2$ - starting from an initial set of model parameters (R_{hf}, $R_{ct,c}$, $C_{dl,c}$, R_d^{1D}, τ, $R_{ct,a}$, $C_{dl,a}$). *fminsearch* uses the Nelder-Mead simplex algorithm of Lagarias *et al.* [LRWW99]. x being the vector containing the model fitting parameters. If n is the dimension of x, the corresponding simplex is characterized by $n+1$ distinct vectors that are its vertices (if $n = 2$ the simplex is a triangle and if $n = 3$ it is a pyramid). At each step of the search, a new point in or near the current simplex is generated. The function value at the new point is compared with its values at the vertices of the simplex and if the new point reduces the diameter of the simplex, one of the vertices is replaced by the new point. This step is repeated until the diameter of the simplex is less than the predefined tolerance.

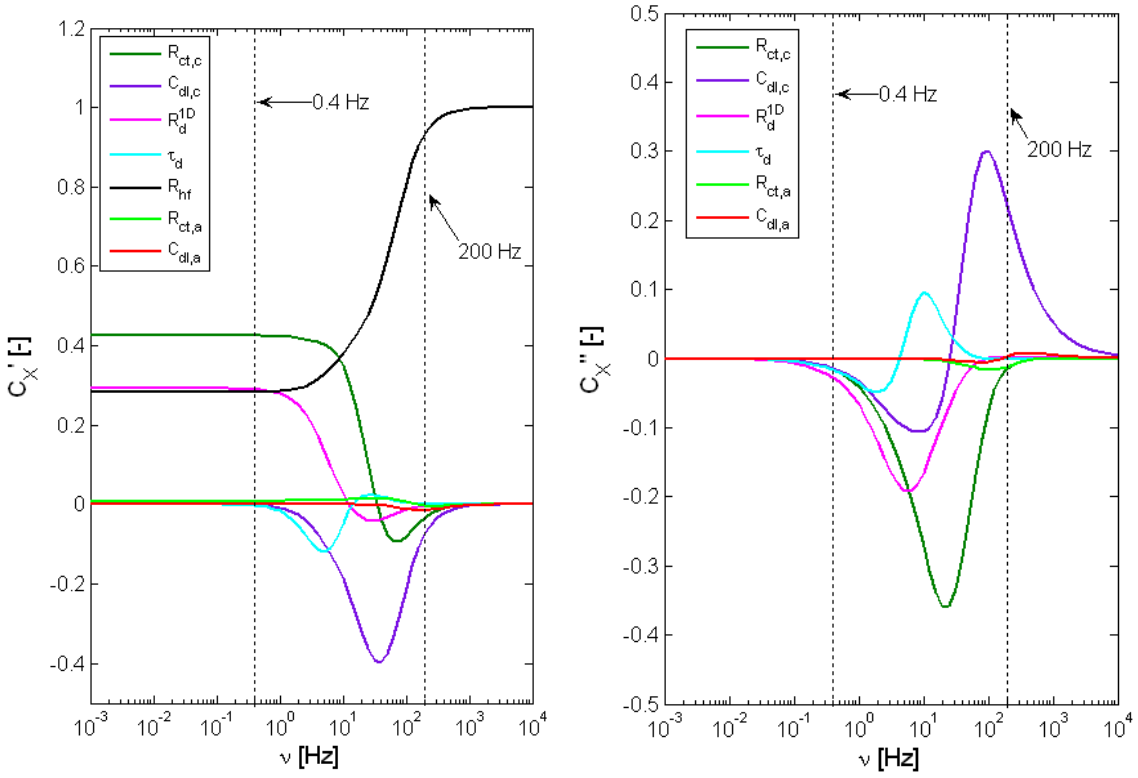
In order to check the validity of the equivalent circuit of Figure 3.11 a sensitivity analysis relative to the impedance parameters is carried out. The aim of this study is:

- To ensure that the impedance model parameters are not correlated.
- To check the influence of the anode on the estimation of the cathode parameters.

For clarity, all sensitivity coefficients C_X are normalized as follows:

$$C_X = \frac{X}{\|Z_{cell}\|}\frac{dZ_{cell}}{dX} \tag{3.44}$$

with $X = R_{hf}$, $R_{ct,c}$, $C_{dl,c}$, R_d^{1D}, τ_d, $R_{ct,a}$, $C_{dl,a}$ and Z_{cell} standing for the global impedance of the MEA, as defined by equation (3.43). C_X is an indicator of the sensitivity of the cell impedance with respect to the parameter X. In other words, the higher the absolute value of C_X, the more important is the influence of X on the value of the cell impedance Z_{cell}.



(a) (b)

Figure 3.12: *Real (a) and imaginary part (b) of the sensitivity coefficients of the MEA impedance C_X with respect to the EEC parameters $X = R_{hf}, R_{ct,c}, C_{dl,c}, R_d^{1D}, \tau_d, R_{ct,a}, C_{dl,a}$ as functions of the frequency ν.*

The sensitivity coefficients being complex numbers, Figure 3.12(a) and 3.12(b) show the evolution of the real and imaginary parts of C_X as functions of the applied frequency ν ranging between 1 mHz and 10 kHz. The sensitivity coefficients depending on the values of the model parameters, the values chosen for this example are those obtained by fitting experimental impedance spectra measured with a mono-channel single cell (experimental setup presented in section 3.5) in typical operating conditions ($\langle j_f \rangle_t = 0.5\ Acm^{-2}$, $S_{H_2} = 1.2$, $S_{air} = 3$, $RH_{air} = 75\%$). The impedance paramters are given in Table 3.1 (p. 90). Even if the absolute values of C_X may vary for other operating conditions, the curves in Figure 3.12 reflect well the relative influence of the different model parameters on the global cell impedance.

It can be seen that the sensitivities of the cathode parameters (Randles EEC) are significant in the frequency range 0.1 Hz - 1 kHz. For frequencies above or below this interval, the values of C_X are either negligibly small or constant for several parameters indicating a correlation between them. This leads to the conclusion that measurements performed with frequencies beyond this interval would not contribute to a better precision.

The sensitivity coefficient relative to the high frequency resistance $C_{R_{hf}}$ (black line in Figure 3.12(a)) is a real number. It is the parameter which has the highest influence on the value of the cell impedance for frequencies above 10 Hz.

The real and the imaginary part of the sensitivity coefficients relative to $C_{R_{ct,c}}$ (green lines) and $C_{C_{dl,c}}$ (purple lines) reach their maximum (absolute) values between 10 Hz and 1 kHz. The sensitivities with respect to the diffusion impedance parameters - $C_{R_d^{1d}}$ (pink lines) and C_{τ_d} (blue

lines) - are generally lower, but they reach significant (absolute) values for frequencies comprised between 0.1 Hz and 100 Hz. $\left\|C_{R_d^{1d}}\right\|$ and $\|C_{\tau_d}\|$ reach their maximum value below 10 Hz. This confirms that the time-scales of the mass transport and of the charge separation and transfer are well separated in this EEC. However, the curves in Figure 3.12 show that correlations exist between $R_{ct,c}$ and R_d^{1D} at intermediate frequencies. In order to obtain independent parameter estimations, the impedance spectra have to be fitted over a frequency range exceeding at least these correlations.

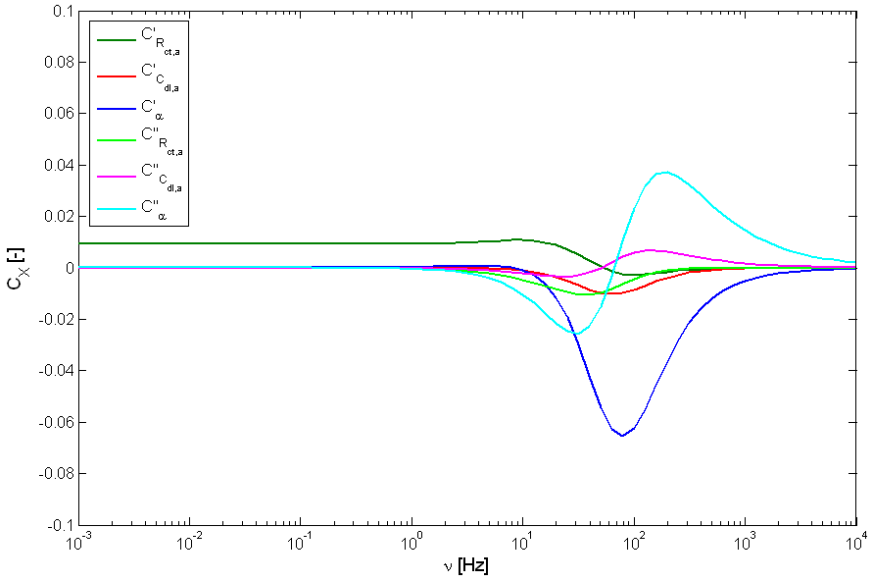


Figure 3.13: *Real and imaginary parts of the sensitivity coefficients relative to the anode impedance parameters as functions of the frequency.*

Figure 3.12 shows furthermore that the anode coefficients are significantly lower than those of the cathode, *i.e.* the phenomena at the anode have a lower influence on the cell impedance than those occurring at the cathode. For the sake of clarity, Figure 3.13 shows the anode sensitivity coefficients as functions of the signal frequency. Similarly to the cathode, $\left\|C_{C_{dl,a}}\right\|$ (red and pink lines) and $\|R_{ct,a}\|$ (dark and light green lines) reach their maximum (absolute) values at frequencies between 10 Hz and 1 kHz, but at slightly higher frequencies than the corresponding cathode components. However, the absolute values of the anode sensitivities do not exceed 0.02, whereas the corresponding coefficients at the cathode have maximum absolute values of about 0.4. The sensitivity of the cell impedance to the anode being about 20 times smaller than that of the cathode, it can be neglected for our investigations, which is in good agreement with previous references in the literature [ABD01, CR01, FDN$^+$06, RUKD08, Des08].

In addition, the impact of a CPE (3.11) in the anode equivalent circuit is analyzed in Figure 3.13. C_α (purple and blue lines) not only governs the anode impedance over the whole frequency range, but has a similar behavior as $C_{C_{dl,a}}$, indicating a possible correlation between both parameters. This leads to the conclusion that the simultaneous estimation of the model parameters would not be feasible with a CPE in this EEC.

The absence of cross-correlations between the cathode parameters in the experimental frequency range can be checked by plotting their sensitivity coefficients as functions of each other. The graphs in Figure 3.14 clearly show that there is no cross-correlation between the cathode parameters when analyzing the spectra over the whole frequency range ($\nu \in [0.01\ Hz; 200\ Hz]$). However, it has to

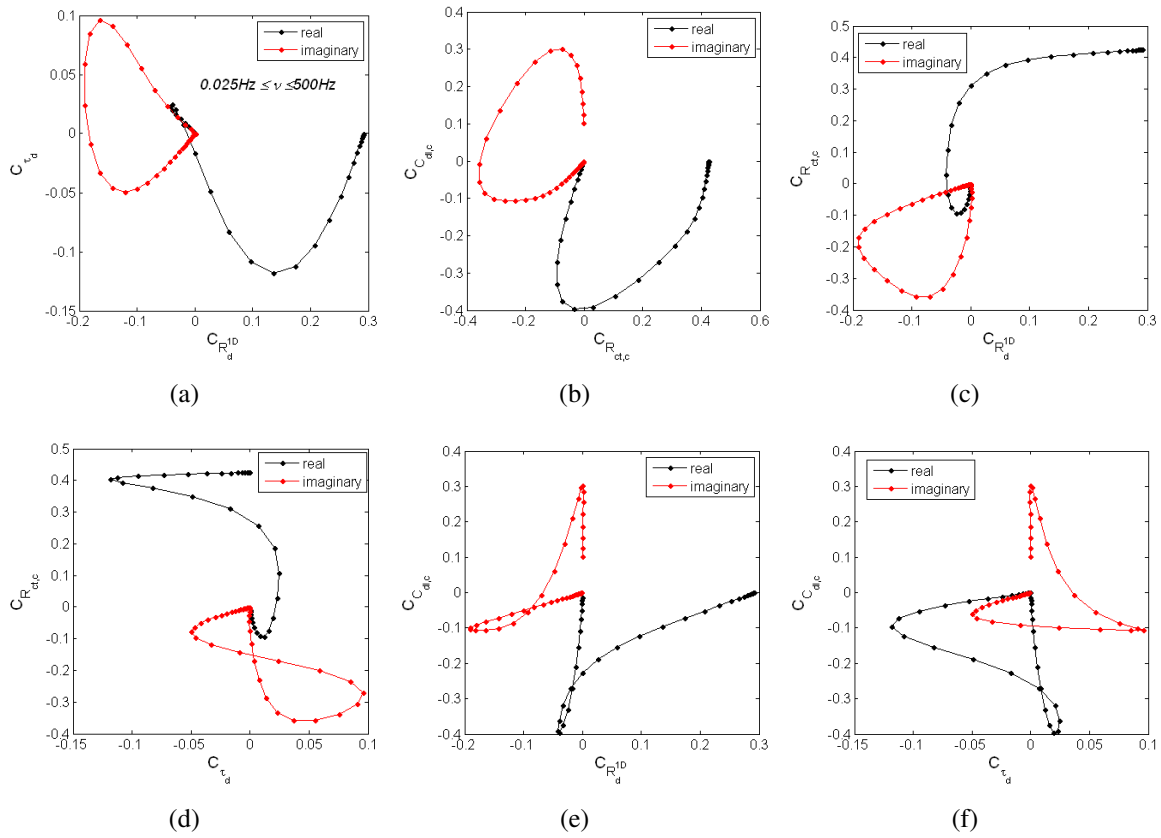


Figure 3.14: *Interdependency analysis of the cathode impedance parameters for frequencies ranging from* 0.01 Hz *to* 200 Hz*: (a)* C_{τ_d} *vs.* $C_{R_d^{1D}}$*; (b)* $C_{C_{dl,c}}$ *vs.* $C_{R_{ct,c}}$*; (c)* $C_{R_{ct,c}}$ *vs.* $C_{R_d^{1D}}$*; (d)* $C_{R_{ct,c}}$ *vs.* C_{τ_d}*; (e)* $C_{C_{dl,c}}$ *vs.* $C_{R_d^{1D}}$*; (f)* $C_{C_{dl,c}}$ *vs.* C_{τ_d}*.*

be pointed out that the curves in Figure 3.14 exhibit some linear sections in which the impedance parameters seem to be correlated: the spectra have thus to be fitted over a frequency range exceeding these linear sections in order to make the simultaneous estimation possible.

The conclusions of this sensitivity analysis can be confirmed by fitting experimental spectra with the equivalent circuit of Figure 3.11. Figure 3.15 shows a mean EI spectrum (average values and standard deviation) resulting from a series of 5 spectra measured under identical conditions (in the same operating conditions as the sensitivity analysis). For frequencies below 0.4 Hz, the data exhibit an important scattering. One of the possible explanations of this phenomenon could be the evacuation of liquid water droplets through the air channel which affects the impedance measurements at low frequencies. Therefore, impedance data obtained at frequencies below 0.4 Hz are not retained for the parameter identification. This avoids subsequent complications resulting from possible inductive features observed sometimes at low frequencies [ABD01, CW99, SBWS08, MBZ$^+$08, RO08]. The experimental spectra exhibit sometimes also an inductive loop at high frequencies, which is in agreement with observations from the literature [DLGM$^+$98, CR01, RO08]. Since our analyses show that the highest values of the sensitivity coefficients are reached in a frequency range 0.4 Hz - 200 Hz (Figure 3.12) and that in addition, the model parameters are not correlated in this domain (Figure 3.14), the investigations are limited to this interval.

[1]Fit results obtained by Meland *et al.* [MKB06] on a cell fed with hydrogen at both electrodes at $T = 50°C$ and

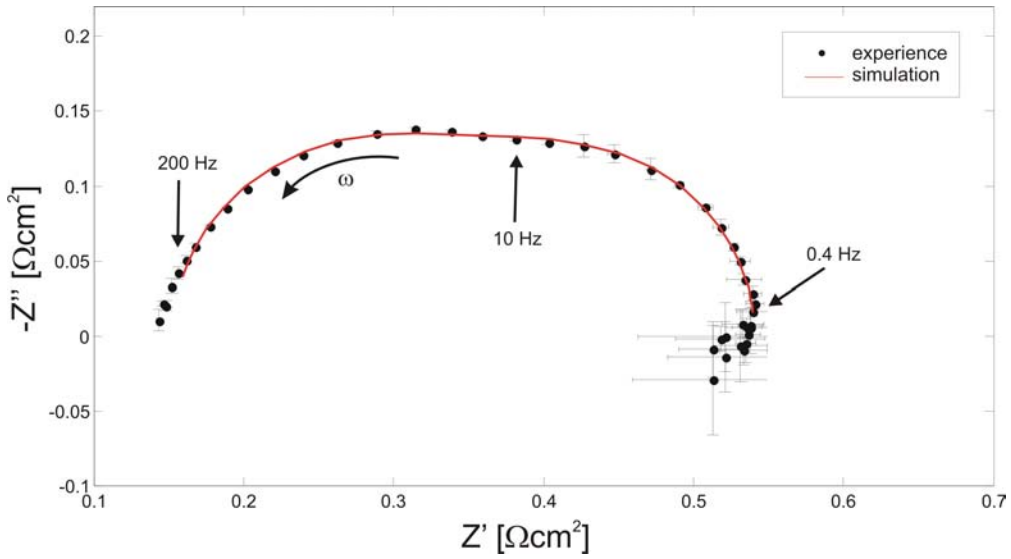


Figure 3.15: *Experimental mean spectrum resulting from a series of 5 measurements under identical conditions and theoretical spectrum simulated after identification of the model parameters.*

R_{hf} $[\Omega cm^2]$	$R_{ct,c}$ $[\Omega cm^2]$	$C_{dl,c}$ $[F\,cm^{-2}]$	R_d^{1D} $[\Omega cm^2]$	τ_d $[s]$	$R_{ct,a}$ $[\Omega cm^2]$	$C_{dl,a}$ $[F\,cm^{-2}]$	α $[-]$
$0.153 \pm 2\%$	$0.23 \pm 0.8\%$	$0.02 \pm 0.5\%$	$0.158 \pm 2\%$	$0.066 \pm 3\%$	-	-	-
$0.148 \pm 0.06\%$	$0.23 \pm 0.8\%$	$0.02 \pm 0.1\%$	$0.157 \pm 1\%$	$0.066 \pm 3\%$	$0.005 \pm 20\%$	$0.2 \pm 50\%$	1
-	-	-	-	-	0.007^1	0.75^1	0.97^1

Table 3.1: *Mean cathode and anode impedances and standard deviations estimated from a series of 5 impedance spectra (Figure 3.15). In spite of a large dispersion, the anode parameters are in good agreement with values from the literature [MKB06] (third row), but have no influence on the estimation of the cathode model parameters.*

Table 3.1 shows the mean cathode and anode impedance parameters estimated from a series of 5 experimental spectra with their expected standard deviations. The first row shows the cathode parameters obtained by using only the Randles EEC (cf. Figure 3.11). The corresponding standard deviations do not exceed 3%. The second row of Table 3.1 shows the estimated paramters obtained by fitting the spectra with the anode and cathode EEC together (Figure 3.11). Actually, the estimation of the 8 parameters is not possible directly with the fminsearch function of Matlab because of the cross-correlations between them. Therefore, the following method was employed:

1. Estimation of the cathode parameters while keeping constant the anode parameters.
2. Keeping constant the former estimated cathode parameters and estimating the anode parameters.
3. Keeping constant again the anode parameters for a re-estimation of the cathode parameters.

The values of the cathode parameters do not change between steps 1 and 3. Estimating the anode parameters has thus no significant influence on the values of the cathode parameters. Actually, the only difference lies in the value of R_{hf}: the value obtained when considering the cathode only

[1] $P = 1\ atm$.

corresponds to the sum of the high frequency resistance and of the anode charge transfer resistance $R_{ct,a}$ when considering both electrodes.

Finally, note that the experimental values of $R_{ct,a}$ and $C_{dl,a}$ are in good agreement with those encountered in the literature for similar operating conditions [MKB06], although the scattering reaches 50% (in our case). A parameter estimation is not possible when using a CPE in the anode equivalent circuit, since the parameters strongly depend on the initial value of α. This confirms the results of the sensitivity analysis indicating a correlation between the impedance parameters of Z_{CPE} and those of the other EEC components.

These results are also validated by sensitivity analyses performed in other operating conditions, starting from experimental data, as well as with series of 1000 numerically simulated and noised spectra.

3.4 Estimation of Electrode Kinetic Parameters

As shown in the literature, EIS can be used as a method alternative to the polarization curve for the determination of the Tafel slope b [APBDSS$^+$92, Boi05]. Comparing the values of b obtained by the identification of the impedance parameters with values from the literature would be an additional test of validity of the Randles EEC for impedance analyses on PEMFC.

The usual method for the determination of the Tafel slope stems from the estimation of the cathode overpotential (where $j_{cell} = j_f$) with the Tafel law (introduced in section 2.1.2):

$$j_{cell} = j_0 \frac{c_{O_2}}{c^*_{O_2}} \exp\left\{-\frac{\eta_{act}}{b}\right\} \tag{3.45}$$

Plotting the overpotential η_{act} as a function of the common logarithm of the current density $\log j_{cell}$ yields a straight line (with the slope b_{10}) expressed in $V\,dec^{-1}$ and a y-intercept at $-b_{10} \log\left(j_0 c_{O_2}/c^*_{O_2}\right)$. The relation between b in equation (3.45) and b_{10} is given by: $b_{10} = \ln 10 \times b = 2.3 \times b$.

Two different Tafel slope regimes are usually reported in the literature for the oxygen reduction reaction with MEA consisting of Pt/C electrodes and Nafion membranes [GD97, ABDO98, ABD01, PMS91, APBDSS$^+$92, PSAM92]:

$$\text{For low current densities } (E > 0.8\ V) \longrightarrow b_{10} \approx 60\ mV\,dec^{-1}$$
$$\text{For high current densities } (E < 0.8\ V) \longrightarrow b_{10} \approx 120\ mV\,dec^{-1}$$

The change in the Tafel slope is generally explained by a shift in the oxygen reduction mechanism from a reduction on a Pt-oxide covered surface (at low current densities) to a reduction on an oxide free surface (at high current densities) being characterized by different adsorption isotherms (Langmuir, Temkin) [PMS91, PSAM92].

It has to be noted that these values are only orders of magnitude and the results reported in the literature vary usually in a range of about 20 $mV\,dec^{-1}$ depending on temperature, gas pressure, oxidant gas (pure O_2 or air) and investigated system, *i.e.* if the identification is made on a single electrode or on a cell [Boi05, ABDO98, GD97, APBDSS$^+$92, PSAM92, CR01]. For instance, by fitting the Tafel plots of a PEMFC operated at $25°C$ with H_2 and air at $P = 1\ atm$, Ciureanu *et al.* [CR01] observed a doubling of the Tafel slope from about 130 $mV\,dec^{-1}$ to 270 $mV\,dec^{-1}$.

Regardless of the exact values of b_{10}, all studies in the literature report consistently an increase (doubling) of the Tafel slope from the low to the high current density (high η_{act}) regime.

A good agreement between the Tafel slope obtained by the steady-state method and by EIS is reported in the literature [APBDSS$^+$92, Boi05]. When using EIS, b is usually determined either by plotting E_{cell} vs. $\left[-\log(R_{ct}+R_{hf})\right]$ [APBDSS$^+$92] or by plotting R_{ct} as a function of $1/j_f$ [Boi05] which leads again to one (respectively two) averaged slope(s).

The ORR being irreversible at the usual current densities (Tafel behavior of the reaction) the charge transfer resistance is defined by (cf. section 3.2.1):

$$R_{ct} = \frac{b}{j_f} \tag{3.46}$$

This expression makes it possible to determine the Tafel slope (at a given current density) through j_f and R_{ct} via EIS.

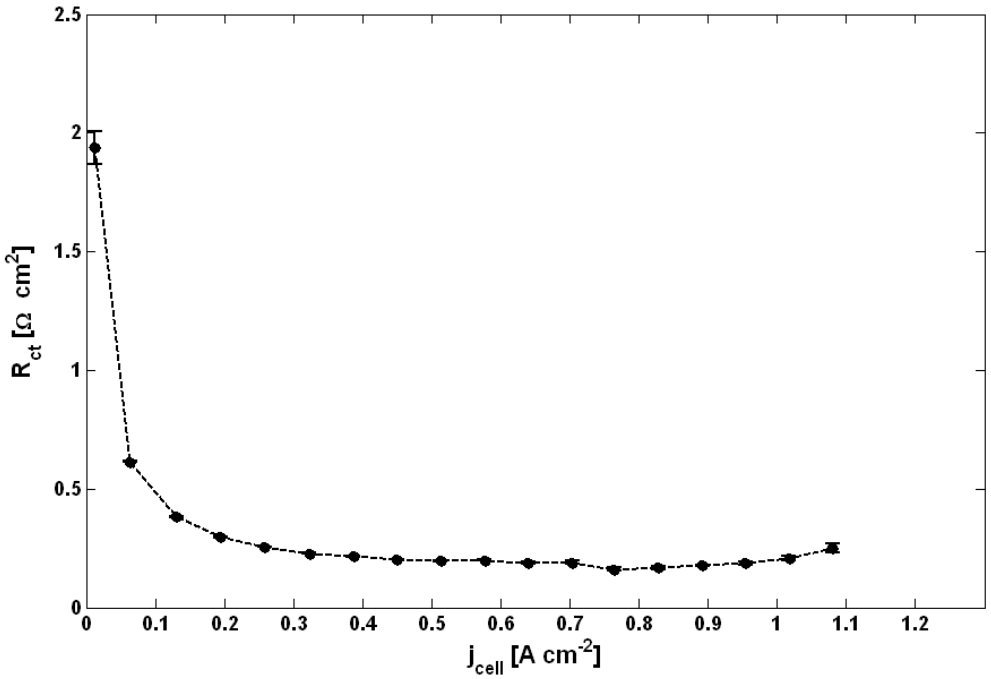


Figure 3.16: *R_{ct} from identification of EI spectra with the Randles equivalent circuit vs. the cell current density j_{cell}.*

Figure 3.16 depicts the mean charge transfer resistance at different current densities identified by fitting experimental spectra measured with a mono-channel PEMFC (cf. section 3.5.1). The cell was operated with dry hydrogen and humidified air ($RH_{air} \approx 78\%$) in counter-flow at $T = 56°C$ and $P_{H_2/air} = 1\ atm$, between $jcell = 0.013\ Acm^{-2}$ and $jcell = 1.1\ Acm^{-2}$.

R_{ct} remains rather constant over the whole current density range. However, it increases steeply at low current densities ($j_{cell} \leq 0.1\ Acm^{-2}$). This behavior could be explained with the definition of R_{ct} at very low overpotentials which is derived in section 3.2.1:

$$R_{ct} = \frac{RT}{nF\,j_0} \tag{3.47}$$

In theory, the identification of R_{ct} at the open circuit voltage could thus be used for the determination of the exchange current density j_0 [APBDSS$^+$92]. However, in the literature, the exchange

current densities determined by fitting the Tafel plot show a large dispersion, all the more so since it is not always clear whether the values are related to the geometrical area A_{geom} or to the electrochemically active area γA_{geom} (γ being the electrode roughness). In addition, j_0 varies with the temperature [CR01, PSAM92] and impedance measurements at OCV are not easy to perform. To cite some examples for H_2/air PEMFC:

- Parthasarathy *et al.* [PSAM92] find at $80°C$:
  - Low slope regime: $3.85\,10^{-8}\ Acm^{-2}$
  - Low slope regime: $1.5\,10^{-6}\ Acm^{-2}$
- Antoine *et al.* [ABDO98] find at $25°C$:
  - Low slope regime: $6.985\,10^{-11}\ Acm^{-2}$
  - Low slope regime: $1.5\,10^{-7}\ Acm^{-2}$
- Ciureanu *et al.* [CR01] find for the high slope regime:
  - For $31°C \leq T \leq 60°C$: $1.34\,10^{-9}\ Acm^{-2} \leq j_0 \leq 4.06\,10^{-9}\ Acm^{-2}$
- Bultel *et al.* [BWJ$^+$05] find for the high slope regime:
  - $T = 60°C$: $0.4\,10^{-4}\ Acm^{-2}$
  - $T = 80°C$: $0.42\,10^{-4}\ Acm^{-2}$

The orders of magnitude of the exchange current densities typically given in the literature for PEMFC [ABDO98, BWJ$^+$05, Boi05, CR01, APBDSS$^+$92, PSAM92, SPK05a] are summarized in Table 3.2.

Slope regime	$j_0\ [Acm_{Pt}^{-2}]$
Low slope ($b_{10} \approx 60\ mV\,dec^{-1}$)	$10^{-8} - 10^{-9}$
High slope ($b_{10} \approx 120\ mV\,dec^{-1}$)	$10^{-6} - 10^{-7}$

Table 3.2: *Ranges of values of the exchange current density of PEMFC as they can be found in the literature [Boi05, CR01, APBDSS$^+$92, PSAM92, SPK05a].*

These values can be used for the estimation of R_{ct} that is expected for the data shown in Figure 3.16 when approaching the OCV. In our example, the charge transfer resistance is given in Ωcm^2 referred to the geometrical area ($A = 7.87\ cm^2$). Supposing an electrode roughness $\gamma = 200$ the exchange current densities found in the literature (Table 3.2) are between $10^{-7}\ A\,cm^{-2}$ and $10^{-4}\ A\,cm^{-2}$. Inserting these values in equation (3.47) yields:

$$j_0 = 10^{-4}\ A\,cm^{-2} \rightarrow R_{ct}(OCV) = 71\ \Omega cm^2 \tag{3.48}$$

$$j_0 = 10^{-7}\ A\,cm^{-2} \rightarrow R_{ct}(OCV) = 7.1\,10^4\ \Omega cm^2 \tag{3.49}$$

This example confirms the experimental observation that the charge transfer resistance is be several orders of magnitude higher at low current densities than its values at usual current densities. Depending on the value of j_0, R_{ct} exhibits an important dispersion at low current densities. For a better precision, the values of R_{ct} at the lowest experimental current densities ($j_{cell} \leq$

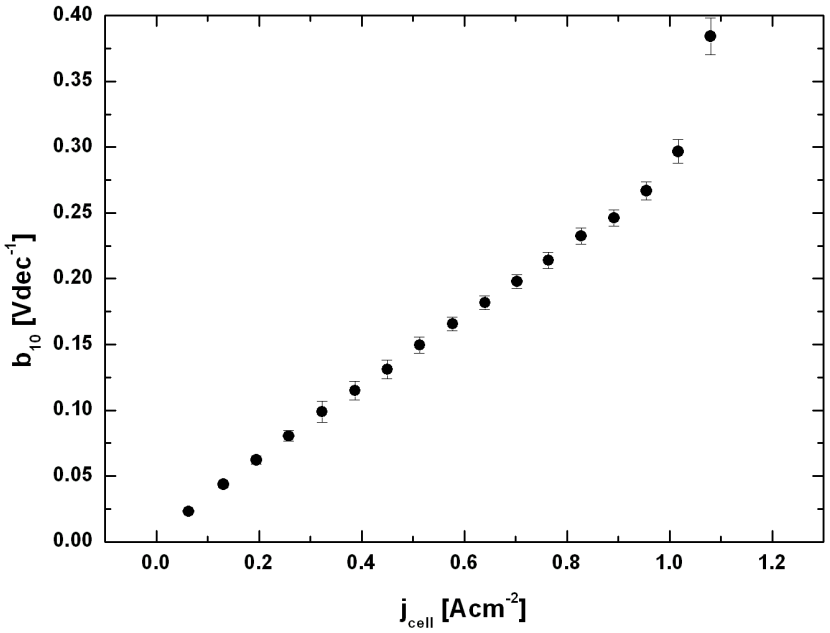


Figure 3.17: *b_{10} derived from the charge transfer resistance of Figure 3.16 vs. j_{cell}.*

$0.013\ A\,cm^{-2}$) will not be taken into account for the determination of the electrode kinetic parameters - the Tafel slope b and the charge transfer coefficient α - with equation (3.46).

According to (3.46), the Tafel slope can be determined by multiplying $R_{ct}(j_{cell})$ by the corresponding current density. Figure 3.17 depicts the Tafel slope (in $mV\,dec^{-1}$) derived from the charge transfer resistances in Figure 3.16 as a function of the current density. b_{10} increases continuously from 23 $mV dec^{-1}$ at $j_{cell} = 0.063\ A\,cm^{-2}$ up to 384 $mV dec^{-1}$ at $j_{cell} = 1.08\ A\,cm^{-2}$.

The values of b_{10} as well as their increase with the current density are in good agreement with previous results from the literature [GD97, ABDO98, ABD01, PMS91, APBDSS$^+$92, PSAM92]. However, instead of the two slope regimes that are reported in the literature, b_{10} increases continuously. Note that there is a correlation at intermediate frequencies between the Tafel slope (or the charge transfer resistance) and the diffusion impedance, which can be put forward by using models alternative to the classical Warburg approach (cf. section 6.2). However, although the choice of the diffusion impedance impacts slightly the values of b_{10} and R_{ct}, it is shown in section 6.3.2 that the significant and continuous increase of $b10$ with the current density is observed in all cases.

The Tafel slope is related to the (cathode) charge transfer coefficient α_c by:

$$b = \frac{RT}{\alpha_c 2F} \tag{3.50}$$

The charge transfer coefficient is an important parameter characterizing the electrochemical activity of an electrode. The conventional approach consists in estimating this parameter from the current-voltage curve (like the Tafel slope). The values reported in the literature (cf. Table 3.3) show a large dispersion [PSAM92, SPK05b, DT10, CCD$^+$10], all the more so since the charge transfer coefficient in the high slope regime depends on the temperature [PSAM92].

In the majority of the cases, this parameter varies between 1 and 0.4. For modeling purpose, the charge transfer coefficient is often set to $\alpha_a = \alpha_c = 0.5$ which corresponds to symmetrical reactions. However, its actual value depends strongly on the operating conditions. Measurements

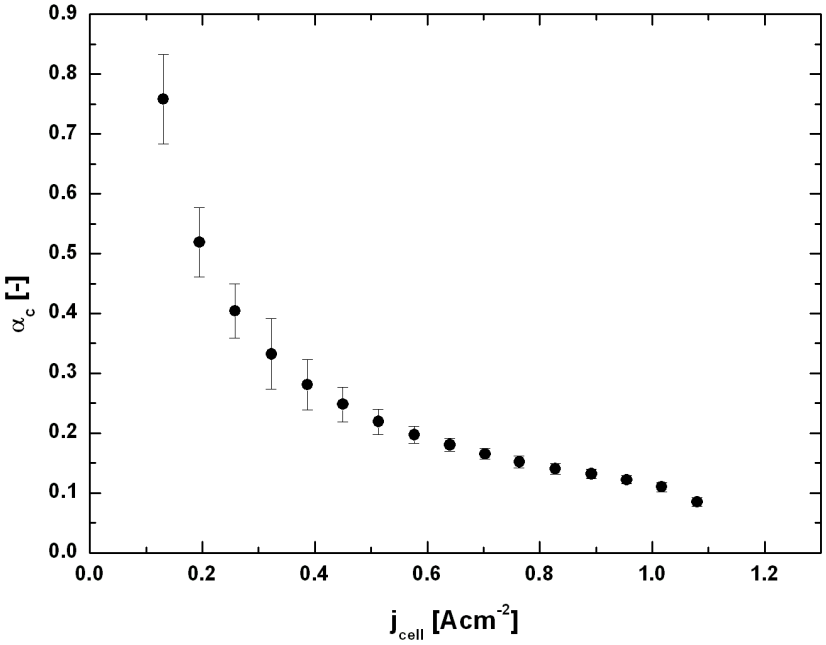


Figure 3.18: *Plot of α_c obtained from EIS measurements vs. the cell current density j_{cell}.*

T [°C]	slope regime	α_c	Ref.
70	low slope	0.95	[PSAM92]
	high slope	0.60	
70	low slope	0.89	[DT10]
	high slope	0.43	
80	low slope	1	[SPK05a]
	high slope	0.61	

Table 3.3: *Typical values of the cathode charge transfer coefficient α_c as they can be found in the literature.*

performed by Parthasarathy *et al.* [PSAM92] show a decrease of α_c from 1 (low Tafel slope regime) to 0.5 (high Tafel slope regime). Danilov *et al.* [DT10] identify 3 different charge transfer coefficients for low, intermediate and high current densities: their results show a decrease of α_c with the current density. Figure 3.18 depicts the variation of α_c (deduced from the charge transfer resistance in Figure 3.16) with the cell current density j_{cell}. α_c approaches 1 for low current densities and decreases with increasing cell current, which is in good agreement with the predictions from the literature. Contrary to classical steady-state methods (*e.g.* Tafel plot), EIS is not limited to 2 or 3 values of α_c. Furthermore, the determination of b and α_c from the Tafel plot requires the measurement of a whole current-voltage curve, whereas when using EIS the interpretation of one impedance spectrum is sufficient for the determination of these parameters at a given operating point, which reduces drastically the measuring time.

These results show that EIS can be used as an alternative technique for the determination of the parameters characterizing the reaction kinetics (b, j_0, α) in PEMFC.

3.5 Experimental Setup

3.5.1 Fuel cells

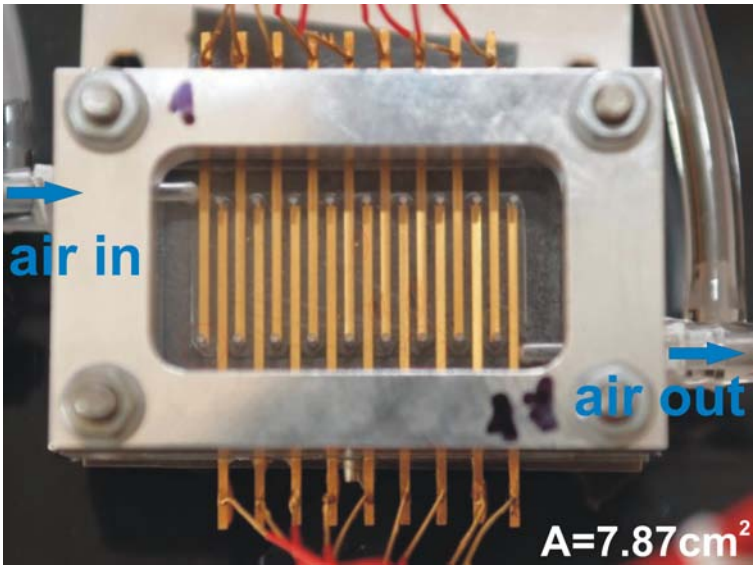


Figure 3.19: *Mono-channel single cell with a geometrical area $A = 7.87\ Acm^{-2}$. The current collectors build the serpentine flow field.*

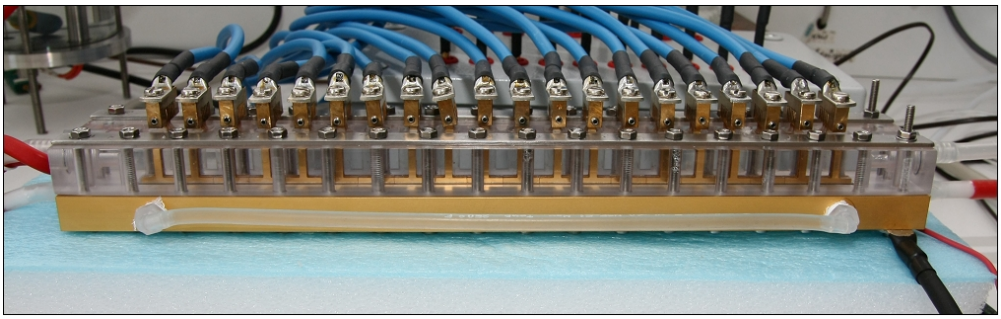
Global impedance studies (applied to the whole cell) yield only information about processes occurring over the whole MEA surface and effects of possible local variations in the operating conditions (temperature, humidity, concentration, current density ...) on the impedance response cannot be assessed. In order to perform impedance measurements with a spatial resolution over the electrode, PEMFC with a segmented current collection at the cathode have been designed and built in our group. The experimental results presented in this work are carried out with two different cells which differ in the number and shape of their gas channels and in their active area.

Figure 3.19 shows the "mono-channel" single cell where the current collection is segmented at the cathode thanks to a set of 18 gold plated brass stripes placed at intervals of 1 mm. The current collectors are embedded in a PMMA plate and delimit the serpentine flow field (of a $0.7x1.0\ mm^2$ section and 33 cm length). Furthermore, the transparency of the PMMA allows to observe the appearance and the removal of water droplets in the air flow. The hydrogen channel is machined in an aluminum plate and is symmetric to the air channel. The active area of this cell is $A = 7.87\ cm^2$.

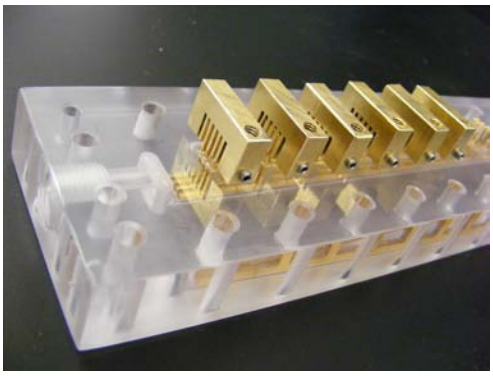
The "2D" PEMFC with an active area $A = 27\ cm^2$ is represented in Figure 3.20. Each segment consists of a set of 4 current collector stripes (gold plated brass) so that the local current I_{loc} is actually the average of the values measured by the 4 collectors. These collector stripes delimit the 5 parallel air channels (with a $0.7x1.0\ mm^2$ section and 30 cm length). Like for the mono-channel cell, the hydrogen channels (machined in an aluminum plate) are symmetric to the air channels.

For convenience, the "mono-channel" PEMFC is referred to as cell 1 and the "2D" PEMFC as cell 2 in the following.

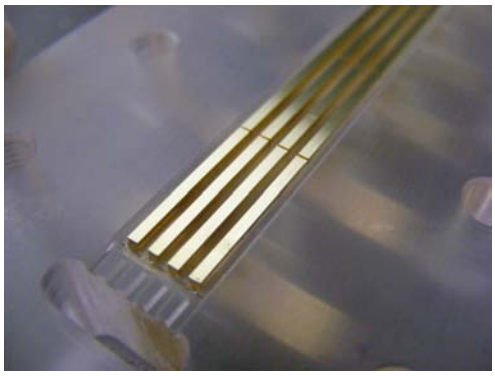
Identical MEA (Johnson Matthey) are used in both cells, the only difference being the active area. The GDL is a 190 μm thick carbon fiber paper (Toray^{TM} TGP-H-060) with a porosity (without compression) $\varepsilon = 0.78$ [TI]. The MEA consists of a PFSA (Gore) polymer membrane of



(a) Side view



(b) j_{loc} of one segment: mean value over 4 collector stripes.



(c) 5 parallel channels separated by the collector stripes.

Figure 3.20: *"2D"PEMFC with* 20 *segments along the cathode (active area* $A = 27\ cm^2$*).*

thickness $\delta_m = 30\ \mu m$ and catalytic (active) layers ($\delta_{al} \approx 10\ \mu m$) with an average Pt loading of $0.406\ mg_{Pt}cm^{-2}$ at the anode and $0.385\ mg_{Pt}cm^{-2}$ at the cathode.

In reference conditions, the fuel cell is fed in counter-flow (at $1\ atm$) with dry hydrogen with a stoichiometry $S_{H_2} = 1.2$ and with humidified air with a stoichiometry $S_{air} = 3$. The air is humidified up to about 80% *RH* thanks to a bubbler. The cell temperature is controlled ($T_{cell} = 56 \pm 1°C$) thanks to an electric heating system fixed to the anode bipolar plate. Nevertheless, thermal gradients exist probably within the cell because of the thermal resistances of the various components and of the interfaces between them [TMD+11].

3.5.2 Impedance measurements

All impedance measurements are performed in a galvanostatic mode at frequencies ranging logarithmically from $0.025\ Hz$ to $500\ Hz$ with a resolution of 10 points per decade and a peak-to-peak sinusoidal perturbation of 5% of the cell current (at $\langle j_{cell} \rangle_t = 0.5\ Acm^{-2}$, $\Delta j_{cell} = 0.25\ mAcm^{-2}$ and $\Delta V \leq 30\ mV$). For low current densities, the measured data obtained with a perturbation amplitude of 5% exhibit sometimes large scattering. In this case, the perturbation amplitude is increased up to 10% whereas it is verified that the signal oscillations do not influence the measured impedance (cf. section 3.1.1).

Global and local impedance measurements are performed using a data acquisition and processing system depicted in Figure 3.21. Since the cell impedance is almost entirely determined by the cathode, the membrane and some contact resistances, it is possible to use the anode as a reference

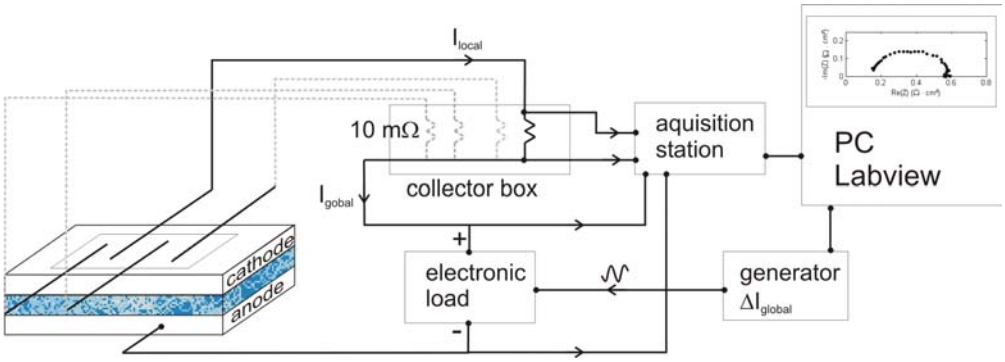


Figure 3.21: *Data acquisition and processing setup for the impedance measurements.*

electrode [CR01]. In order to measure the current intensities with the least possible perturbations, a passive electronic circuit is used: each of the current collectors is connected to a 10 $m\Omega$ shunt resistance. An acquisition station (*SCXI National Instruments*) measures the potential difference between the terminals of the shunts and thus determines the local current intensities. A particular attention is given to this circuit in order to reduce and to homogenize as much as possible all parasitic (contact and connection) resistances, so that the cathode gas diffusion layer can be considered as isopotential. The measured contact resistances due to the current collectors are:

$$\text{Cell 1:} \quad R_{elec} = \frac{R_{segment} * A_{contact}}{18} = \frac{62\ m\Omega * 7.87 cm^2}{18} = 27\ m\Omega cm^2$$

$$\text{Cell 2:} \quad R_{elec} = \frac{R_{segment} * A_{contact}}{20} = \frac{9\ m\Omega * 27 cm^2}{20} = 12\ m\Omega cm^2$$

which is of a factor 10 smaller than the impedances of the processes occurring in the MEA (order of magnitude of about 100 $m\Omega cm^2$). The current collectors are connected together to an electronic load (*Amrel FEL-60-1*) which is driven by a signal generator. The whole experimental setup is controlled by a *Labview* program developed by J. Dillet (LEMTA, Nancy).

3.6 Local EI Analyses Using the Classical 1D Warburg Approach

EIS deals with phenomena taking place at different length and time scales. The impedance parameters identified by fitting the experimental data with an appropriate EEC are assumed to be related to physical and electrochemical phenomena occurring over a depth of about 1 *mm* perpendicular to the electrode (Figure 3.22). Global EIS allows to identify the values of the parameters that characterize these phenomena averaged over the whole MEA surface. However, the operating conditions (RH, T, c_{H_2/O_2}, j_f ...) as well as the electrode geometrical structure are prone to vary along the gas channels and to impact the local reaction and transport kinetics. By performing locally resolved EIS (lEIS) it is possible to obtain a spatial resolution of the cell impedance [HWO^+]. The length scales analyzed by lEIS with the segmented cells developed in our group (cf. section 3.5.1) are represented schematically in Figure 3.22. The gas channels are divided into segments, which allows a spatial resolution of the order of magnitude of about 1 *cm* (cell 1: $33/18 = 1.8$ *cm*; cell 2:

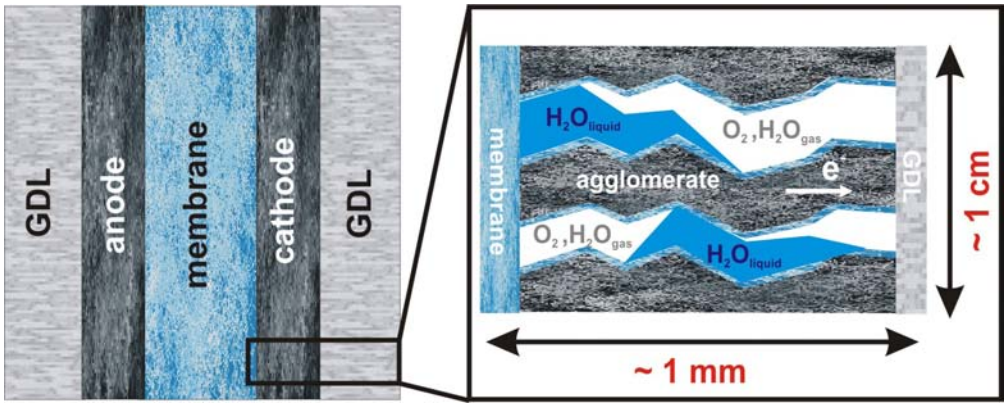


Figure 3.22: *Characteristic length of locally resolved EIS with the segmented cells presented in the previous section.*

$30/20 = 1.5\ cm$).

This section presents some results of lEIS obtained with the two segmented PEMFC. The data are all obtained in similar conditions:

- $\langle j_{cell} \rangle_t = 0.5\ Acm^{-2}$
- $S_{H_2} = 1.2$, $S_{air} = 3$
- $T_{cell1} = 56°C$, $T_{cell2} = 50°C$
- Cell 1: $RH_{H_2} = 0\%/RH_{air} = 78\%$
  Cell 2: $RH_{H_2} = 60\%/RH_{air} = 60\%$

Cell 1 is operated in co- and in counter-flow. Fuel cells are usually fed in counter-flow because local variations of the MEA water content are expected to be less pronounced than in co-flow, which leads to a higher electrical efficiency. However, measuring the local impedances in co-flow is expected to accentuate the non-uniformities, which can be of interest for the interpretation of the experimental results. Cell 2 is operated only in counter-flow.

All the spectra are interpreted with the one-dimensional Warburg diffusion impedance (3.38) with the intention to test the limits of a one-dimensional description of oxygen diffusion in the cathode.

3.6.1 Local impedance parameter profiles

Figure 3.23 shows the global impedance spectra measured with the two cells. The data of cell 1 are mean values of 5 experiments with their standard deviations, those of cell 2 correspond to one single series. The impedance spectra exhibit a low and a high frequency loop. Slight inductive behaviors can be observed at the highest and the lowest frequencies. Furthermore, at the highest frequencies, the spectrum of cell 1 in co-flow describes a straight line at 45°, which is most probably due to proton conduction in the catalyst layer as shown with a bulk electrode impedance model derived in section 4.2.2. This is consistent with results from the literature [EK99, BGA+02, SZWG96]. As inductive processes and ion transport in the electrode bulk are not taken into account in the Randles EEC, the low and the high frequency limits of the spectra are excluded from the identification of the impedance parameters (Table 3.4).

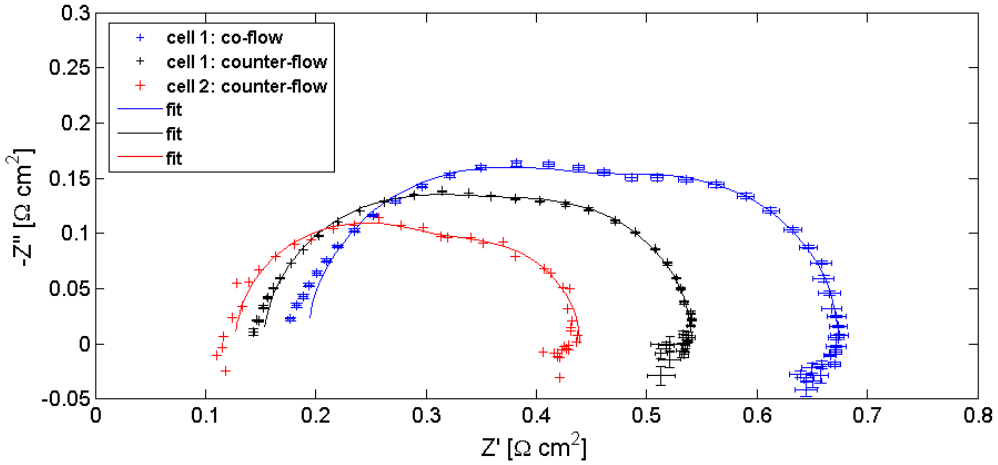


Figure 3.23: *Global impedance spectra measured with cell 1 (mono-channel cell with serpentine flow field) in co- and counter flow and with cell 2 ("2D" PEMFC with 5 parallel flow fields) in counter-flow at* $\langle j_{cell} \rangle_t = 0.5\ A cm^{-2}$, $S_{H_2} = 1.2$ *and* $S_{air} = 3$ *and their respective fitting curves.*

Cell	Flow geometry	R_{hf} $[\Omega cm^2]$	R_{ct} $[\Omega cm^2]$	C_{dl} $[F\,cm^{-2}]$	R_d^{1D} $[\Omega cm^2]$	τ_d $[s]$
1	co-flow	$0.193 \pm 3\%$	$0.277 \pm 3\%$	$0.013 \pm 3\%$	$0.21 \pm 5\%$	$0.068 \pm 2\%$
1	counter-flow	$0.153 \pm 0.2\%$	$0.23 \pm 1\%$	$0.02 \pm 0.5\%$	$0.158 \pm 2\%$	$0.066 \pm 3\%$
2	counter-flow	0.124	0.195	0.025	0.118	0.086

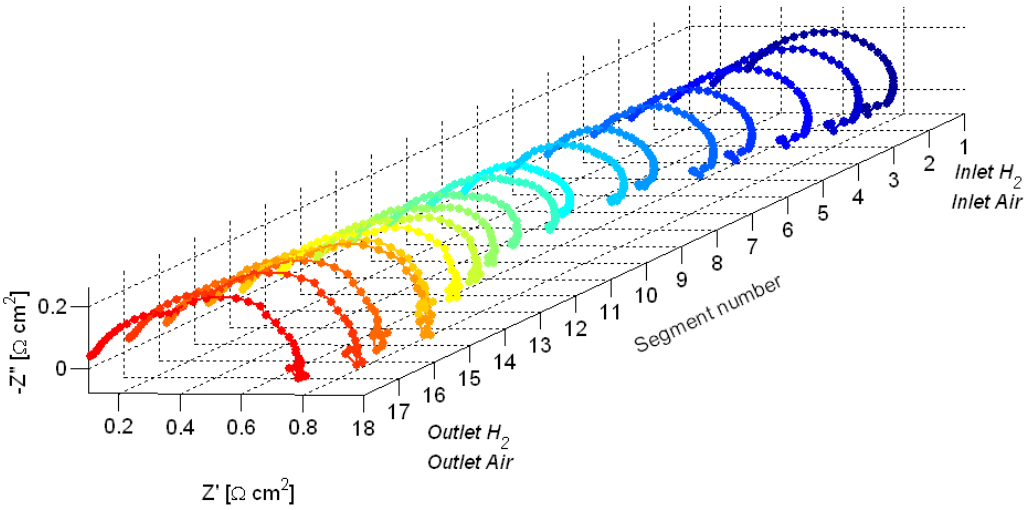
Table 3.4: *Impedance parameters identified by fitting the global impedance spectra of Figure 3.23.*

The impedance spectrum of cell 2 is significantly smaller than those of the cell 1. A possible explanation of this observation can be a better humidification of the membrane, since both gases (H_2 and air) are humidified, whereas only air is humidified in cell 1. A more homogeneous humidification could also explain the lower impedance of cell 1 in counter-flow than in co-flow. The high frequency resistance R_{hf} can be considered as an indicator of the membrane water content, because among other (ionic, electronic and contact) resistances, it accounts for the finite proton conduction of the membrane. Indeed, a comparison of R_{hf} (Table 3.4) confirms this interpretation in term of water content. The difference in the contact resistances of both cells (about 15 $m\Omega cm^2$; cf. section 3.5.2) has only a very low impact on R_{hf} and is neglected.

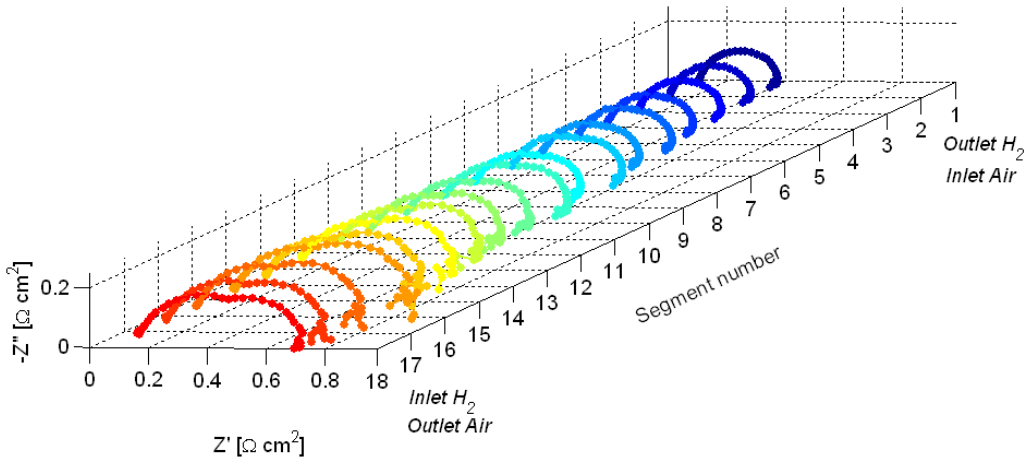
The differences between the parameters related to charge separation and transfer (R_{ct}, C_{dl}) are less important than those of the high frequency resistance, but they show the same tendency. However, these global impedance spectra do not allow to conclude whether these observations are only related to humidification or whether the difference in the channel geometry affects the spectra, too.

The interpretation of the Warburg diffusion parameters (R_d^{1D}, τ_d) is even more delicate: The diffusion resistance R_d^{1D} in cell 1 is the highest when the cell is working in co-flow. When both cells are operated in counter-flow, a lower value of R_d^{1D} is obtained for cell 2. However, the characteristic diffusion time is the highest in cell 2 (counter-flow) and the lowest in cell 1 for a gas supply in counter-flow. The only conclusion that can be drawn from these impedance parameters is that a gas supply in counter-flow seems to create less mass transport losses than in co-flow.

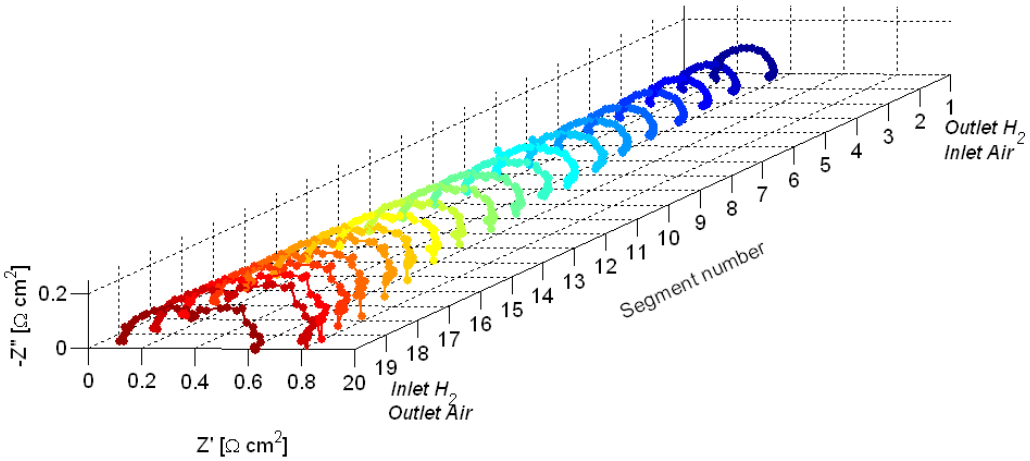
An interpretation in term of water content inside the MEA remains the most obvious and perhaps the only possible analysis of the impedance spectra. However, these first conclusions are preliminary and need to be verified. The analysis of the local impedance spectra is expected to



(a) Cell 1: co-flow



(b) Cell 1: counter-flow



(c) Cell 2: counter-flow

Figure 3.24: *Local impedance spectra of cell 1 and 2 corresponding to the global spectra shown in Figure 3.23.*

yield more detailed information about the origin of the different impedances. The profiles of the local impedance spectra of cell 1 and 2 are depicted in Figure 3.24. They are measured simultaneously to the global impedance spectra. In both cases, segment number 1 designates the air inlet. The local spectra of cell 2 are smaller than those obtained with cell 1 which is consistent with the tendencies observed with the global impedance spectra. For a gas supply in counter-flow (Figure 3.24(b) and 3.24(c)), the spectra increase from the air inlet to the outlet. In co-flow (Figure 3.24(a)), they exhibit a large high frequency loop at the air inlet indicating lower reaction rates. In general, the local impedance spectra are the largest in co-flow which is in good agreement with the observations of the global spectra.

Independently of the gas supply and of the geometry, the local EI spectra at the air inlet exhibit only one high frequency loop. The low frequency loop can be observed only when approaching the outlet. According to the 1D Warburg model, this can be explained by an increasing oxygen diffusion resistance along the cathode.

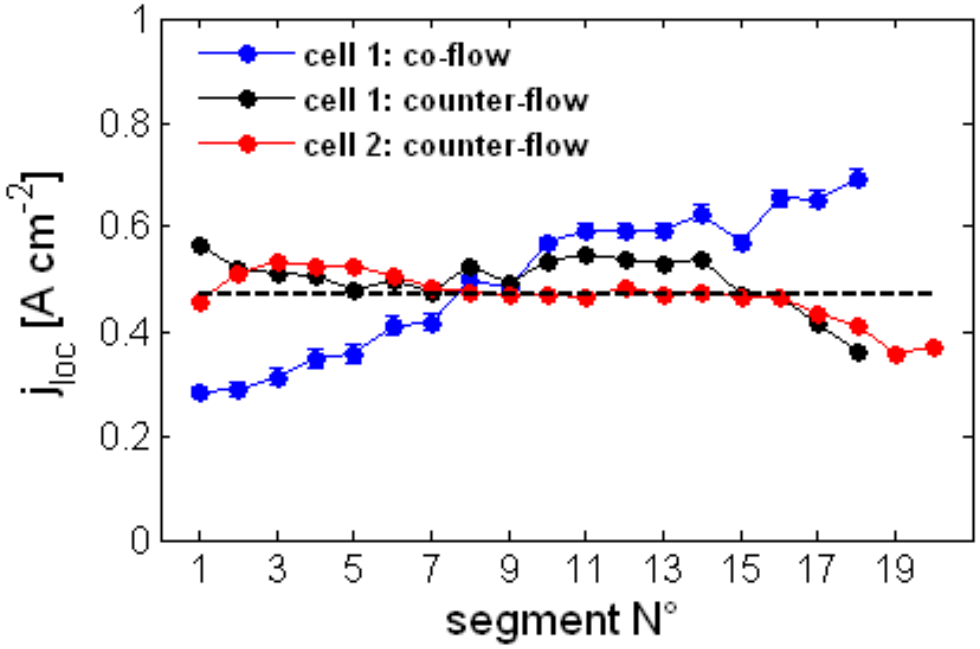


Figure 3.25: *Local current densities of cell 1 and cell 2 in co- and in counter-flow;* $j_{cell} = 0.5\ Acm^{-2}$, $S_{H_2} = 1.2$ *and* $S_{air} = 3$.

The variations in shape and size of the local impedance spectra with increasing segment number are more pronounced in co-flow than in counter-flow. This is consistent with the profiles of the local current densities depicted in Figure 3.25: the profile of j_{loc} in co-flow exhibits significant variations along the cathode, whereas it is rather flat in counter-flow. This confirms that the local cell operation is more uniform in counter-flow than in co-flow. However, an identification of the local impedance parameters is necessary to obtain more precise information.

The profiles of the local impedance parameters obtained by fitting each local spectrum with the Randles equivalent circuit are presented in Figure 3.26. The values measured in counter-flow with both cells are similar and show almost the same behavior along the cathode surface. This leads to the conclusion that the impedance parameters seem to depend mostly on the MEA composition and not on its geometry. Remember that in cell 1 the MEA has an area of 7.87 cm^2 and 27 cm^2 in cell 2. These results show the good reproducibility of the impedance measurements, as well as the

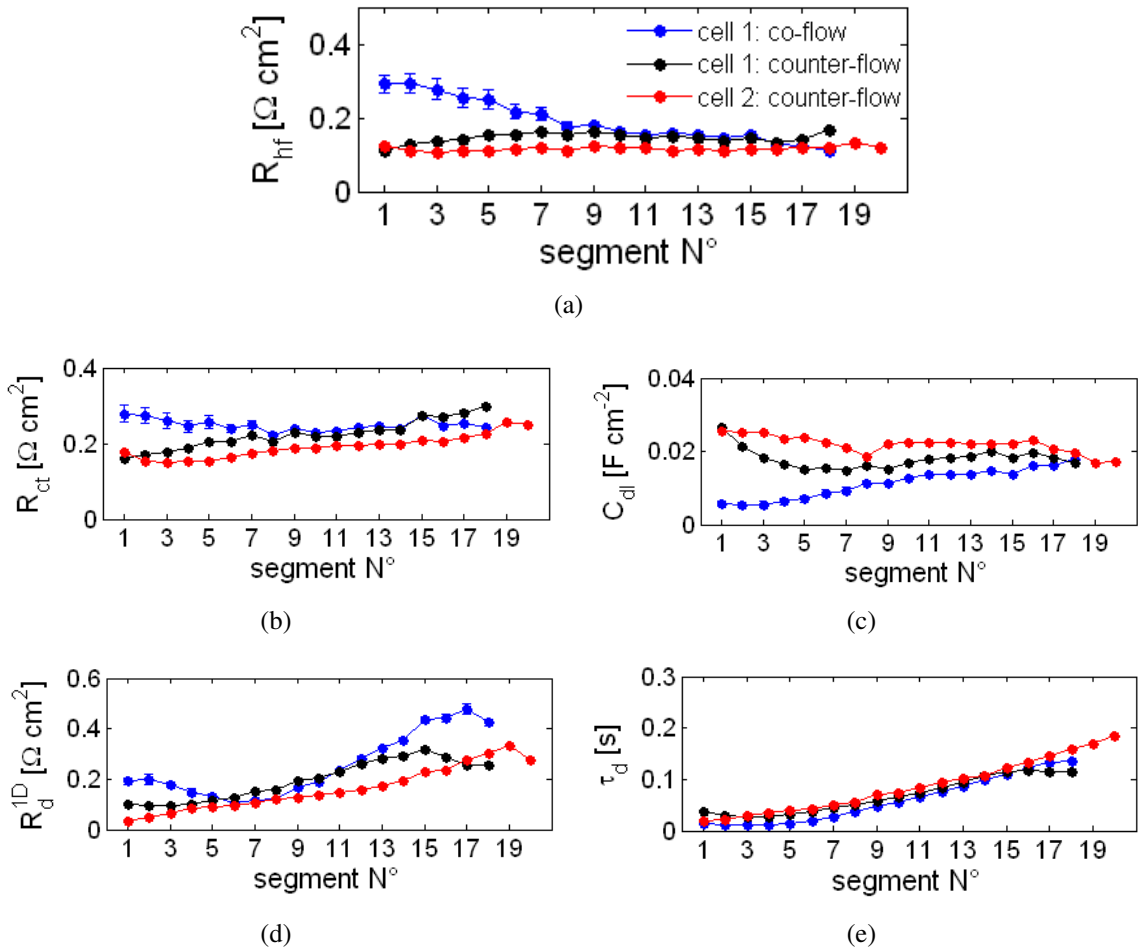


Figure 3.26: *Local impedance parameters identified by fitting the local EI spectra of Figure 3.24 using the Randles EEC.*

low scattering of the data.

The profile of R_{hf} (Figure 3.26(a)) is rather flat in counter-flow which is consistent with the hypothesis of a more uniform hydration along the cathode. The evolution of R_{hf} along the channel in co-flow fits well to this interpretation: it is the highest at the air and hydrogen inlet. The progressive humidification of the membrane explains most probably the decrease of R_{hf} over the segments 1 to 9. The data obtained with cell 1 in counter-flow show a slight increase of R_{hf} at the air outlet which could be explained by a local drying of the membrane facing the inlet of dry hydrogen. Hydrogen being humidified in cell 2, this phenomenon is not observed.

The profile of the charge transfer resistance (Figure 3.26(b)) in co-flow shows a similar behavior as that of R_{hf}: it decreases over the segments 1 to 9 indicating that an insufficient humidification results in a decrease of the reaction rate, which is consistent with former results in the literature [SZWG96]. The variation of R_{ct} in counter-flow is less pronounced, but a slight increase from the air inlet to the outlet can be observed for both cells. Gases being humidified at both electrodes, this increase is less pronounced in cell 2. The charge transfer resistance of cell 1 at the air outlet is higher in counter-flow than in co-flow, which is consistent with the hypothesis of local drying when the air outlet faces the dry hydrogen inlet. A slight increase of R_{ct} can be observed at the air outlet in cell 2. Both gases being humidified in this cell, this increase could be explained by local

flooding hindering the oxygen to access the reaction sites and decreasing thus indirectly the rate of oxygen reduction.

The double-layer capacity C_{dl} (Figure 3.26(c)) being an indicator of the ability of the electrode to separate charges. Beside others, it depends on the water content of the catalyst layer via the proton conductivity of the electrolyte [SZWG96]. Starting from this hypothesis, it is not surprising that the double-layer capacity increases over the first segments of cell 1 in co-flow. In counter-flow, the variation of C_{dl} is less pronounced, since the humidification is more uniform over the MEA surface.

The diffusion impedance parameters R_d^{1D} (Figure 3.26(d)) and τ_d (Figure 3.26(e)) increase with the segment number independently of the air and hydrogen flow direction. Their values are slightly lower for cell 1 than for cell 2. This can probably be explained by a better liquid water removal in cell 1 due to a higher gas pressure since the cell has only one serpentine flow channel. Cell 2 having a flow field consisting of 5 straight parallel channels, the gas pressure is lower and the evacuation of liquid water is less efficient. The diffusion impedance of cell 1 decrease slightly at the air outlet when the cell is operated in counter-flow. Again, this can most probably be explained by a local drying near the inlet of the dry hydrogen.

These interpretations of the impedance parameter profiles give only first conclusions and have to be completed by further local EIS measurements performed in other conditions. Nevertheless, it can be shown that local EIS provides more precise information about the phenomena influencing the cell performance as global EIS. By comparing the profiles in co- and in counter-flow, some preliminary interpretations in term of hydration can be proposed.

In the following, the profiles of the impedance parameters of the Randles EEC are used to obtain information about the physical processes of charge and mass transfer along the cathode, by analyzing the profiles of the impedance parameters linked to the reaction rate (b, α) and to the gas transport (D^{eff}, δ).

3.6.2 Physical interpretation of the local electrode kinetic parameters

Similarly to global EIS, the local impedance parameters can be used to determine the Tafel slope b and the charge transfer coefficient α_c. This allows to obtain information about the ORR kinetics with a spatial resolution along the cathode.

The Tafel slope b profiles are deduced with those of the charge transfer resistance R_{ct} (Figure 3.26(b)) and in combination with the local current densities j_{loc} (Figure 3.25):

$$b = R_{ct}\, j_{loc} \tag{3.51}$$

The profiles of the Tafel slope b_{10} ($b_{10} = 2.3 \times b$) are presented in Figure 3.27, in $V\,dec^{-1}$ in order to be consistent with the notations in the literature. The local values of b_{10} are in the same range as those measured over the whole cell (Table 3.5), but the local Tafel slope is generally lower than the global value, except near the air outlet: b_{10} depends on the local current density and on the local charge transfer resistance, and thus on the local conditions (humidification, temperature, concentration).

As expected, the profile of b_{10} is more homogeneous in counter-flow. However, the values obtained with cell 1 first increase with the segment number and then decrease near the air outlet, whereas the profile obtained with cell 2 remains flat. Furthermore, the values of cell 1 are systematically higher than those of cell 2. The current density profiles being almost identical in the two

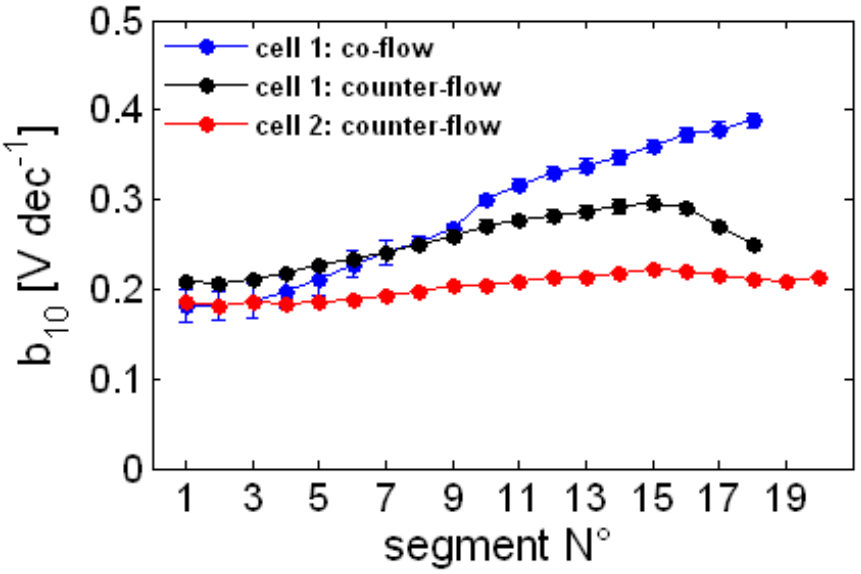


Figure 3.27: *Tafel slope profiles calculated with the local charge transfer resistances (Figure 3.26(b)) and with the local current densities (Figure 3.25);* $\langle j_{cell} \rangle_t = 0.5\ Acm^{-2}$. *The global values of* b_{10} *are reminded in Table 3.5.*

Cell	Flow geometry	b_{10} $[mV\ dec^{-1}]$	α_c $[-]$
1	co-flow	$318 \pm 3\%$	$0.103 \pm 3\%$
1	counter-flow	$265 \pm 1\%$	$0.123 \pm 1\%$
2	counter-flow	212	0.151

Table 3.5: *Tafel slope and charge transfer coefficient deduced from the global impedance parameters of Table 3.4.*

cells, this behavior is possibly due to the differences observed in the profiles of the charge transfer resistance (Figure 3.26(b)). The global values of b_{10} measured with the two cells show the same tendency (Table 3.5).

However, the difference between the profiles of cell 1 in co- and in counter-flow is an indication that the water content is not the only parameter influencing the ORR rate: at the air inlet, the values of b_{10} are almost identical, although the profiles of R_{ct} make us expect higher values in co-flow. Furthermore, b_{10} increases with the segment number in co-flow, which is not consistent with the expected humidification profile.

As reported on page 88, there is a correlation at intermediate frequencies between the Tafel slope (*i.e.* the charge transfer resistance R_{ct}) and the diffusion resistance R_d^{1D}. Actually, it is shown in section 6.2 that the increase of b_{10} along the channel length is most probably an artifact induced by the finite Warburg impedance. When estimating the local Tafel slope with the pseudo-2D convecto-diffusive impedance (accounting for concentration oscillations along the air channel), the profiles of b_{10} are flat. Nevertheless, the values obtained using the Warburg impedance are in the ranges reported. Averaged over the whole channel length the Tafel slope is higher in co- than in counter-flow, which is consistent with the global values (Table 3.5).

The profiles of the charge transfer coefficient α_c (Figure 3.28) show the same tendency as those of the Tafel slope, which is not surprising since both parameters are linked by equation (3.50). The

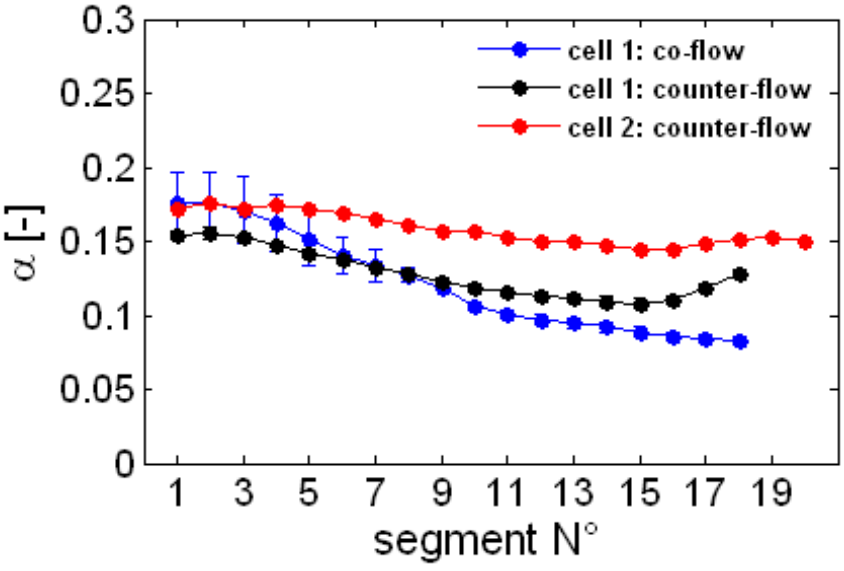


Figure 3.28: *Charge transfer coefficient profiles calculated with the local Tafel slopes (Figure 3.27);* $\langle j_{cell} \rangle_t = 0.5\ Acm^{-2}$.

local values are generally slightly higher than the corresponding global values (Table 3.5).

In conclusion, the profiles of b_{10} and α_c are indicators of the evolution of the ORR along the MEA surface. The reaction rate depending on the humidification [FDN$^+$06, RSD$^+$10], these parameters depend on the local water content. However, being also functions of the local current density, the effect of other parameters are reflected in their profiles. These first results aim to illustrate the interest of performing local analyses of the electrode kinetics, but more detailed studies are necessary to gather supplementary information about the parameters influencing the local operation of the electrodes.

3.6.3 Analysis of the local diffusion impedance parameters

The diffusion resistance R_d^{1D} (3.39) and the characteristic diffusion time τ_d (3.41) depend both on the diffusion layer thickness δ, on the effective diffusion coefficient D^{eff} and therefore indirectly on the porosity ε. Thus, these parameters can be identified from experimental impedance spectra provided that the 1D diffusion model leading to the expression of Z_W is correct. Identifying the diffusion parameters starting from the local impedance data allows to detect possible non-uniformities of the oxygen transport along the air channel. Furthermore, by comparison of the calculated parameters with characteristic values (given in the literature), information can be obtained about the media in which O_2 diffuses (GDL, active layers, electrolyte film).

The expressions of the impedance parameters related to the oxygen transport are recalled below:

$$R_d^{1D} = \frac{b\delta}{4FD^{eff}c_{02}^* - \langle j_f \rangle_t \delta} \tag{3.52}$$

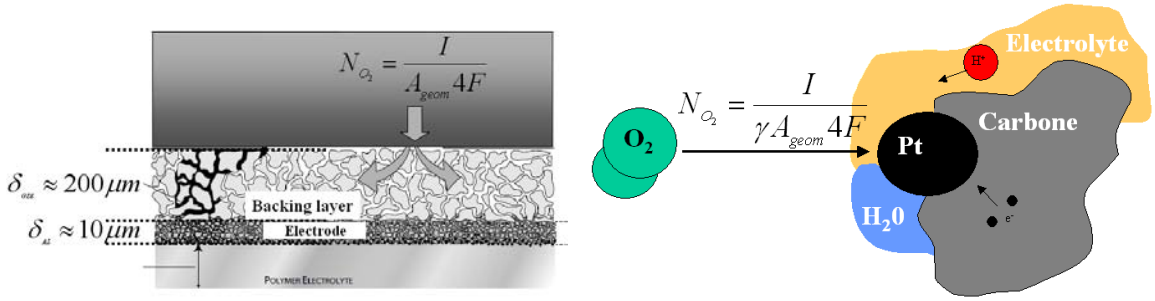
$$\tau_d = \frac{\delta^2}{D^{eff}} \tag{3.53}$$

$$R_{ct} = \frac{b}{\langle j_f \rangle_t} \tag{3.54}$$

Combining these expressions allows to determine the diffusion medium thickness δ:

$$\delta = \frac{\tau_d \langle j_f \rangle_t}{4Fc_{O_2}^*} \left(\frac{R_{ct}}{R_d^{1D}} + 1 \right) \tag{3.55}$$

In the case of lEIS, the time-averaged value of the faradaic current density $\langle j_f \rangle_t$ of a segment corresponds to the mean current density measured at this location j_{loc}. The effective diffusivity D^{eff} can be determined from equation (3.53) and the porosity ε from Archie's law (2.113): $D^{eff} = \varepsilon^m D_{i,j}$, with $m = 3/2$ for the catalyst layer and $m = 2$ for the GDL (cf. section 2.4.2).



(a) Macroscopic mass flux (scheme adapted from [Reu08])

(b) Microscopic mass flux

Figure 3.29: *Oxygen flux at different length scales: the macroscopic scale (a) is relative to the MEA flat surface, whereas the microscopic scale (b) corresponds to the surface of the gas pores of the catalyst layer.*

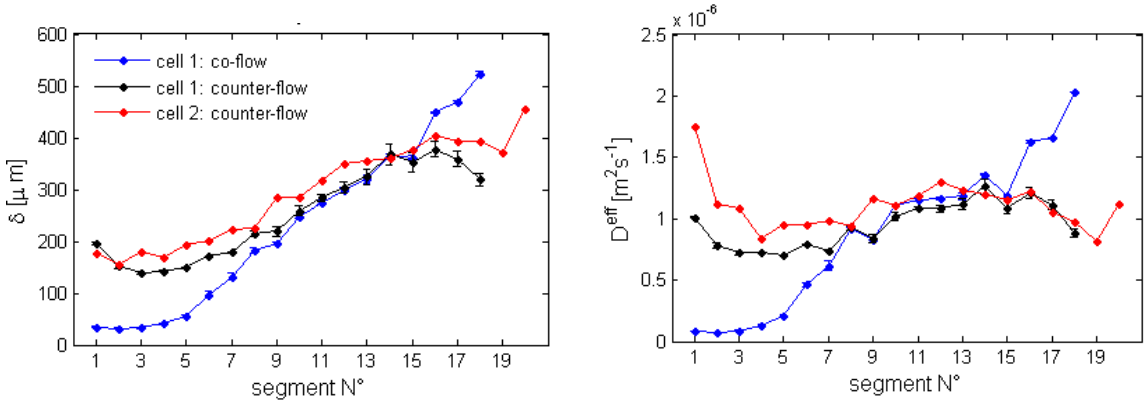
For the parameter estimation, it is necessary to define on which length scale (micro, macro) the oxygen transport is considered. The characteristic lengths of the microscopic and macroscopic scales are represented schematically in Figure 3.29. Regarding oxygen diffusion with a macroscopic point of view (Figure 3.29(a)) means to analyze the oxygen flux perpendicularly to the MEA flat surface A_{geom}, through the pores of the GDL and of the active layer. The oxygen flux is expressed by:

$$N_{O_2}^{macro} = \frac{I}{A_{geom}4F} = \frac{\langle j_f \rangle_t}{4F} \tag{3.56}$$

Note that the faradaic current density $\langle j_f \rangle_t$ is defined by reference to the MEA flat surface. At a microscopic scale (Figure 3.29(b)), oxygen transport is considered by reference to the surface of the pores of the catalyst layer, which is assumed to be the active area $A_{Pt} = \gamma A_{geom}$. This means to consider the oxygen flux in liquid phase, either in an electrolyte layer or in a liquid water layer covering the pores of the active layer. The microscopic flux is given by:

$$N_{O_2}^{micro} = \frac{\langle j_f \rangle_t}{\gamma 4F} \tag{3.57}$$

In practice, both cases are considered for the determination of the transport parameters: the current density in equation (3.55) corresponds either to the local faradaic current density $\langle j_f \rangle_t$ or to $\langle j_f \rangle_t / \gamma$. A comparison of the estimated parameters with the values expected for the different layers (GDL, active layer, electrolyte layer) could allow to obtain information about the layer limiting the oxygen transport and about the state of water in the electrode.



(a) (b)

Figure 3.30: *Diffusion parameters δ (a) and D^{eff} (b) identified using the 1D Warburg impedance perpendicular to the MEA flat surface A_{geom} (macroscopic approach).*

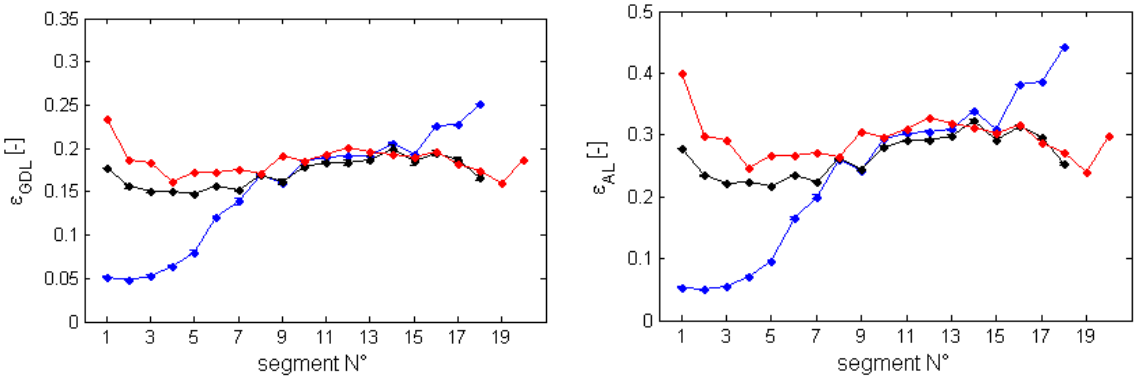
Layer	Phase	δ $[\mu m]$	$D^{eff} = \varepsilon^m$ $[m^2 s^{-1}]$	ε $[-]$
GDL	vapor	190	$3.2\ 10^{-5} \times \varepsilon_{GDL}^2$ [BSL02]	$0.2 - 0.6$ [SZWG96]
	liquid		$1.2\ 10^{-10} \times \varepsilon_{GDL}^2$ [BSL02]	
Active layers	vapor	≈ 10	$6.9\ 10^{-6} \times \varepsilon_{AL}^{3/2}$ (2.116)	$0.2 - 0.35$ [FJW98]
	liquid		$1.2\ 10^{-10} \times \varepsilon_{AL}^{3/2}$ [BSL02]	
Nafion®	liquid	≤ 0.1 [CYH+99]	$1.7\ 10^{-10}$ [GLS02]	-

Table 3.6: *Diffusion layer characteristics as found in the literature.*

The results of the macroscopic approach are given in Figure 3.30. The profiles obtained with both cells in counter-flow fit well to each other and it seems that the gas channel geometry or the MEA size do not have a significant influence on the diffusion behavior.

The estimated values of δ (Figure 3.30(a)) are in the range of the GDL thickness (cf. Table 3.6). The values of δ increase from the channel inlet to the outlet independently of the gas flow direction. The simplest and perhaps the only possible interpretation of their profiles along the channel is in terms of water content. On a macroscopic scale, increasing the liquid water content leads to higher values of the tortuosity of the gas pores and consequently to higher values of the diffusion length. Consequently, the observed increase of δ in Figure 3.30(a) indicates an increase of the water content along the channel. According to these curves, this phenomenon is more important in co-flow than in counter-flow, which is consistent with the expectations.

The profiles of the effective diffusivity are shown in Figure 3.30(b). The values of D^{eff} are in the range expected for (macroscopic) gas diffusion through the GDL and through the active layer (cf. Table 3.6). A continuous increase of D^{eff} is observed in co-flow, **which is not consistent with an increase of the liquid water content**: liquid water blocking the pores for the gas flow, the layer porosity and thus the effective diffusivity are expected to decrease with an accumulation of liquid water. Either this behavior results from another phenomenon occurring in the GDL or it is an artifact due to the simple assumptions of the 1D Warburg model. This is discussed in more details in section 6.2. The profiles of D^{eff} observed in counter-flow show less variations along the cathode indicating a more uniform humidification. A decrease is observed at the channel inlet (segment 1) of cell 2, which could be explained by vapor condensation when the humidified gases enter the gas channels.



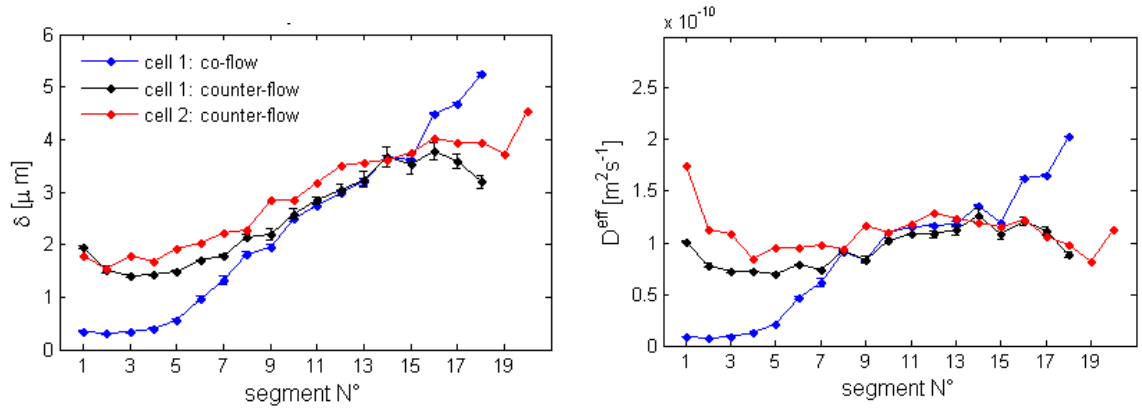
(a) (b)

Figure 3.31: *Local porosities obtained from the profiles of D^{eff} by supposing either the GDL (a) or the active layer (b) limiting for the oxygen diffusion using the macroscopic approach relative to the MEA flat surface A_{geom}.*

Regardless of the local variations, the values of the diffusivities are in ranges expected for gas diffusion through the backing and active layers. However, with these values, it is not possible to determine whether the diffusion limitations are due exclusively to the GDL or to the GDL and the active layer together.

For more detailed information, the profiles of the porosities are determined starting from those of D^{eff} assuming that the GDL (Figure 3.31(a)) or the active layer (Figure 3.31(b)) is the limiting layer for oxygen diffusion. The values are obtained by supposing the diffusion to take place in pure gas phase according to the macroscopic description of the oxygen flux. Diffusion in liquid phase is neglected and an increase in the liquid water content is assumed to result in a decrease of ε. The porosities (Figure 3.31) are in ranges expected for both layers (Table 3.6) which confirms that the 1D Warburg model is valid from a qualitative point of view.

The profiles of the diffusion thickness δ and of the diffusivity D^{eff} obtained when using a microscopic point of view (fluxes perpendicular to the active area γA_{geom}) are shown in Figure 3.32. The only difference between both approaches is the order of magnitude of the results (the reference surface is larger than in the macroscopic approach): the values of the diffusion thickness have to be divided by γ and those of the diffusivity by γ^2. Setting the electrode roughness to $\gamma = 100$, the values of δ (Figure 3.32(a)) vary between 1 μm and 6 μm which is in the range of the active layer thickness (Table 3.6). The values of D^{eff} are in typical ranges of oxygen diffusion



(a) (b)

Figure 3.32: *Profiles of δ (a) and D^{eff} (b) assuming 1D oxygen diffusion perpendicular to the total active area γA_{geom} (microscopic approach).*

in liquid phase, *i.e.* either in water or in electrolyte which is in agreement with the hypotheses of the microscopic approach. The values of the diffusion thickness being significantly higher than the thickness of the electrolyte film covering the pores of the catalyst layer (0.01 μm - 0.1 μm [CYH$^+$99]). At this stage, these results lead to the conclusion that this film alone is not limiting: liquid water has to be present in the catalyst layer. The increase of the values of δ over the MEA surface is consistent with this hypothesis: the liquid water content is expected to increase along the channel due to the ORR which results in an increase of the diffusion thickness in liquid phase. In co-flow, the humidification is expected to be less uniform than in counter-flow, which can explain the steeper increase of δ. The increase of D^{eff} in co-flow goes along with a progressive humidification of the electrolyte resulting in an improvement of the diffusion rate.

Despite the relative simplicity of the one-dimensional Warburg description, the identified parameters are in ranges expected for diffusion in the GDL and in the active layer. A significant difference is observed for the values obtained with a macroscopic and a microscopic approach: by choosing a macroscopic approach, the estimated parameters (δ, D^{eff}, ε) are in ranges typical for diffusion in gas phase. The results are in good agreement with the characteristics expected for the GDL, but diffusion limitations due to the GDL and the active layer together cannot be excluded. However, the interpretation of the profiles of D^{eff} with a macroscopic point of view are not consistent with an increase of the water content in the pores of the diffusion media along the channel. By choosing a microscopic point of view, oxygen diffusion is considered in liquid phase and the results indicate a transport limitation due to liquid water accumulation in the active layer. The profiles of δ and D^{eff} are consistent with this interpretation.

The 1D Warburg impedance allows to make qualitative statements about oxygen diffusion in PEMFC porous media, but a clear identification of the limiting layer and of the phase in which oxygen diffuses is not possible. A more detailed mass transport model is thus needed to elucidate the origin of the low frequency loop in the local (and consequently global) impedance spectra.

3.6.4 Conclusion about the interpretation of local EI spectra with the 1D Warburg diffusion model

Some preliminary results are presented in this section about the interpretation of local impedance spectra, which are measured with the segmented PEMFC developed in our group. The spectra are fitted with a Randles equivalent circuit. This should allow to identify the origin of the different performance losses and to conclude about the physical processes occurring in the cell. The oxygen transport is accounted for by a classical one-dimensional Warburg diffusion impedance with the aim to test the limits of validity of this approach. The main results of this study are:

- The profiles of the 5 impedance parameters (R_{hf}, R_{ct}, C_{dl}, R_d^{1D}, τ_d) along the air channel can be identified for the two cells fed in co- and in counter-flow. These profiles allow to access the local variations of these parameters, which is not possible when performing only global impedance measurements.

- Comparing the profiles of the impedance parameters of both cells in counter-flow leads to the conclusion that they are almost independent of the cell surface or of the gas channel geometry, at least with this type of MEA (Johnson Matthey in both cases).

- The impedance spectra are used to identify the parameters characterizing the electrode kinetics (b, α_c) and oxygen diffusion (δ, D^{eff}, ε), which provides information about the physical processes in the cathode layers. An interpretation of their profiles in term of water content is the most obvious and perhaps the only possible explanation at this stage.

- The local values of b and α are generally higher than their global values, which shows that the latter are not equal to the average value of the formers over the electrode length. Their profiles seem to indicate that the reaction kinetics depend on the electrode humidification, which is consistent with former results in the literature [SZWG96, FDN$^+$06, RSD$^+$10]. However, note that the more elaborate models of oxygen transport used in chapter 6 lead to more uniform profiles of b and α.

- The oxygen transport parameters are interpreted with reference to two length scales: a macroscopic approach referring to the MEA flat surface A_{geom}, *i.e.* oxygen transport is considered through the pores of the GDL and the active layer; a microscopic approach referring to the catalytic active area γA_{geom}, which consists in considering oxygen transport in an electrolyte or liquid water film covering the agglomerates in the active layer. The conclusions obtained with both approaches show significant differences:
  - Using the macroscopic approach, the values of δ and D^{eff} are in ranges typical of a diffusion in gas phase. In this case, the results indicate that the GDL is probably limiting. However, it cannot be excluded that the active layer contributes to the oxygen transport limitations.
  - The values obtained with a microscopic point of view are in ranges typical of diffusion in liquid phase: the oxygen transport limiting layer is probably an electrolyte and/or a liquid water film covering the agglomerates.

  Note that optimally, none of the MEA components should be more limiting than the other for oxygen diffusion/transport: this may be the reason why we have difficulty in determining the main origin of the oxygen transport impedance.

- The values of δ and D^{eff} increase over the MEA surface (this tendency being more pronounced in co-flow). The interpretation of their profiles depends also on the considered length scale:
  - The macroscopic description considers oxygen transport in gas phase, the profiles of δ can be interpreted by an increase of the liquid water content over the channel length, which is consistent with the expectations: an accumulation of liquid water in the gas pores leads to an increase of the tortuosity and thus to an increase of the diffusion thickness. **Simultaneously, the diffusion coefficient is expected to decrease, which is not the case for the profiles of D^{eff} obtained with the finite Warburg element.**
  - In a microscopic point of view, the increase of the diffusion parameters can be interpreted by an increase of the liquid water content, which improves the diffusion through the electrolyte. In addition, this increase of the liquid water content could lead to a higher diffusion thickness.

These uncertain and sometimes conflicting interpretations of the diffusion parameter profiles leads to the conclusion that the 1D Warburg impedance is not fully appropriate for modeling local and thus global impedance spectra. More detailed oxygen transport models seem to be necessary to obtain a reliable interpretation of the low frequency loop in fuel cell impedance spectra. The Warburg approach being based on simple assumptions (one-dimensional, mass transport only by diffusion, presence of a reaction interface...), several other phenomena could influence the mass transport:

- The Warburg model accounts only for oxygen transport by diffusion. Possible effects of convection perpendicular to the electrode are neglected.
- The Warburg approach is based on the assumption of a reaction interface, which means to neglect phenomena in the bulk of the active layer. However, it has been shown that proton transport limitations and oxygen consumption in the catalyst layer have a significant impact on the impedance spectra and should not be neglected in the impedance modeling of fuel cells [SZWG96, EK99, BGA$^+$02, MMB05].
- The Warburg model is one-dimensional, which means that possible effects of phenomena occurring in the channel direction are completely neglected. Thus, by fitting the local impedance spectra with the 1D Warburg model, any decrease of the oxygen concentration along the channel as a consequence of a finite gas flow rate is neglected [MMD$^+$10a]. Furthermore, experimental studies of Schneider *et al.* [SFK$^+$07, SKWS07] show that the low frequency loop seems to be, at least to some extent, an artifact resulting from concentration oscillations induced by the measuring signal and propagating along the channel by convection.

All these phenomena are not taken into account by the Warburg diffusion impedance, which risks to lead to misinterpretations of the diffusion parameter profiles. Therefore, different mass transport impedance models are developed in the next chapters with the focus to analyze the influence of each of these phenomena on the size and the shape of the impedance spectra and finally on the diffusion parameter profiles.

4 Alternative Expressions to the Warburg Impedance: 1D Approaches

First results of the identification of the local diffusion parameters (δ, D^{eff}) have been presented in the previous chapter. However, the values of these parameters, which are intrinsic to the materials, depend actually on the model used for their estimation. They have been deduced by fitting experimental impedance spectra with an equivalent electrical circuit in which the mass transport impedance is represented by a finite Warburg element. Despite of the simplicity of the oxygen transport description, the identified values of δ and D^{eff} are in the typical ranges usually specified in the literature for GDL and active layers. However, their profiles identified based on local impedance spectra (measured with a segmented cell, especially for a gas supply in co-flow) are conflicting. It seems that the mass transport impedance depends on phenomena that are neglected in the classical Warburg approach. Indeed, the impedance expression of the latter is based on simple assumptions:

- One-dimensional purely diffusive flux.
- Constant concentration at the GDL/channel interface along the entire electrode length.
- Existence of a reaction interface.
- Ohmic drops in the catalyst and backing layers are neglected due to high protonic and electronic conductivities.

In order to derive a more appropriate mass transport impedance, several improvements have to be brought to the model. In this context, this chapter presents one-dimensional oxygen transport impedance expressions that allow to analyze the influence of phenomena occurring in the direction perpendicular to the electrode that are not considered in the classical Warburg approach. A first model makes it possible to study the influence of a convective flux entailed by vapor evacuation, and in a second step, oxygen consumption and the finite proton conduction in the catalyst layer are considered using a model close to work developed by Eikerling and Kornyshev [EK99].

4.1 Influence of a Convective Flux on the Diffusion Impedance

The oxygen transport is still considered as one-dimensional and the model hypotheses are represented in Figure 4.1.

The model hypotheses are the same as for the finite Warburg element (cf. chapter 3.2.2) except for the presence of a non-zero convective mass flux N^{conv} that depends on the net gas velocity V:

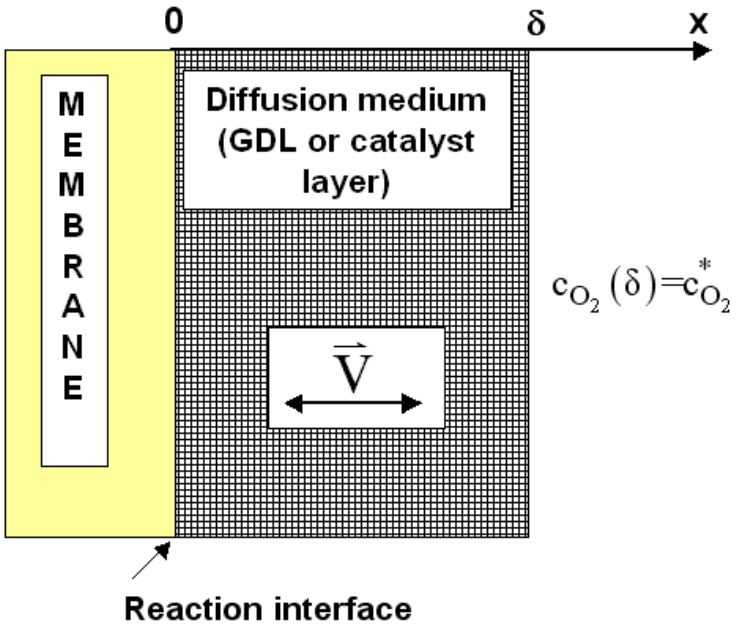


Figure 4.1: *One-dimensional convecto-diffusive mass transport impedance model. The active sites are assumed to be situated at the electrode/membrane interface at* $x = 0$.

$$N^{conv} = N^{conv}_{O_2} + N^{GDL}_{H_2O} = cV \quad \text{with} \quad c = c_{O_2} + c_{H_2O} \tag{4.1}$$

Note that all water is assumed to be evacuated in vapor phase: $N^{GDL}_{H_2O}$ denotes the vapor flux through the cathode backing layer which can be in the direction of the channel or of the membrane. By convention, the fluxes are considered positive in the x-direction. The oxygen flux density is the sum of a diffusive contribution J_{O_2} and of a convective contribution $N^{conv}_{O_2}$ (cf. (2.90) in chapter 2.4.2):

$$\begin{aligned} N_{O_2} &= J_{O_2} + N^{conv}_{O_2} \\ &= -D^{eff}_{O_2} \frac{dc_{O_2}}{dx} + c_{O_2} V \end{aligned} \tag{4.2}$$

with $N_{O_2} = -j_f/4F$. The oxygen flux is thus described by the following system of equations:

$$\frac{\partial c_{O_2}}{\partial t}(x,t) + V \frac{\partial c_{O_2}}{\partial x}(x,t) = D^{eff} \frac{\partial^2 c_{O_2}}{\partial x^2}(x,t) \tag{4.3}$$

$$-D^{eff} \left.\frac{\partial c_{O_2}}{\partial x}\right|_{x=0,t} + c_{O_2}(0,t)V = -\frac{j_f(t)}{4F} \tag{4.4}$$

Neglecting 2D effects like oxygen consumption along the air channel, the concentration at the diffusion medium inlet ($x = \delta$) is set equal to the equilibrium concentration:

$$c_{O_2}(\delta,t) = c^*_{O_2} \tag{4.5}$$

The convective flux through the backing layers is assumed constant (the possible condensation and evaporation of water is neglected). It can be expressed by the water transport coefficient α which is defined as the ratio of the vapor flux through the GDL $N_{H_2O}^{GDL}$ to that of the produced water $N_{H_2O}^{prod} = j_f/2F$:

$$\alpha = \frac{N_{H_2O}^{GDL}}{N_{H_2O}^{prod}} \tag{4.6}$$

The convective flux N^{conv} is null for $\alpha = 0.5$, *i.e.* when each mole of oxygen consumed by the fuel cell is replaced in the air channel by a mole of water vapor. This corresponds to a purely diffusive oxygen transport which is described by the classical Warburg approach. Assuming that water flows in the GDL in vapor form and that the gases are ideal gases, V can be expressed as a function of α and the faradaic current density j_f:

$$\begin{aligned} V &= \left(\alpha N_{H_2O}^{prod} + J_{O_2}\right)\frac{1}{c} \\ &= (2\alpha - 1)\,\frac{j_f}{4F}\frac{RT}{P} \end{aligned} \tag{4.7}$$

4.1.1 DC solution

The local oxygen concentration $c_{O_2}(x)$ is obtained by solving equation (4.3) in steady-state (4.8):

$$D^{eff}\frac{\partial^2 c_{O_2}}{\partial x^2} - V\frac{\partial c_{O_2}}{\partial x} = 0 \tag{4.8}$$

which leads to the general solution:

$$c_{O_2}(x) = A\exp\left(\frac{V}{D^{eff}}x\right) + B \tag{4.9}$$

The boundary condition at the membrane/electrode interface ($x = 0$) (4.4) allows the determination of B:

$$B = -\frac{j_f}{4FV} \tag{4.10}$$

And A can be deduced from the boundary condition at the gas channel/GDL interface ($x = \delta$) (4.5):

$$\begin{aligned} c_{O_2}(\delta) = c_{O_2}^* &= A\exp\left(\frac{V}{D^{eff}}\delta\right) - \frac{j_f}{4FV} \\ \Rightarrow A &= \left(c_{O_2}^* + \frac{j_f}{4FV}\right)\exp\left(-\frac{V}{D^{eff}}\delta\right) \end{aligned} \tag{4.11}$$

Inserting (4.10) and (4.11) in the general expression of $c_{O_2}(x)$ (4.9) yields finally:

$$c_{O_2}(x) = c_{O_2}^*\exp\left(-\frac{V\delta}{D^{eff}}\right) - \frac{j_f}{4FV}\left[1 - \exp\left(\frac{V}{D^{eff}}(x-\delta)\right)\right] \tag{4.12}$$

The oxygen concentration at the membrane/electrode interface in steady-state is thus given by:

$$c_{O_2}(0) = c^*_{O_2} \exp\left(-\frac{V\delta}{D^{eff}}\right) - \frac{j_f}{4FV}\left[1 - \exp\left(-\frac{V\delta}{D^{eff}}\right)\right] \tag{4.13}$$

Impact of a convective flux on the oxygen concentration at the GDL/membrane interface

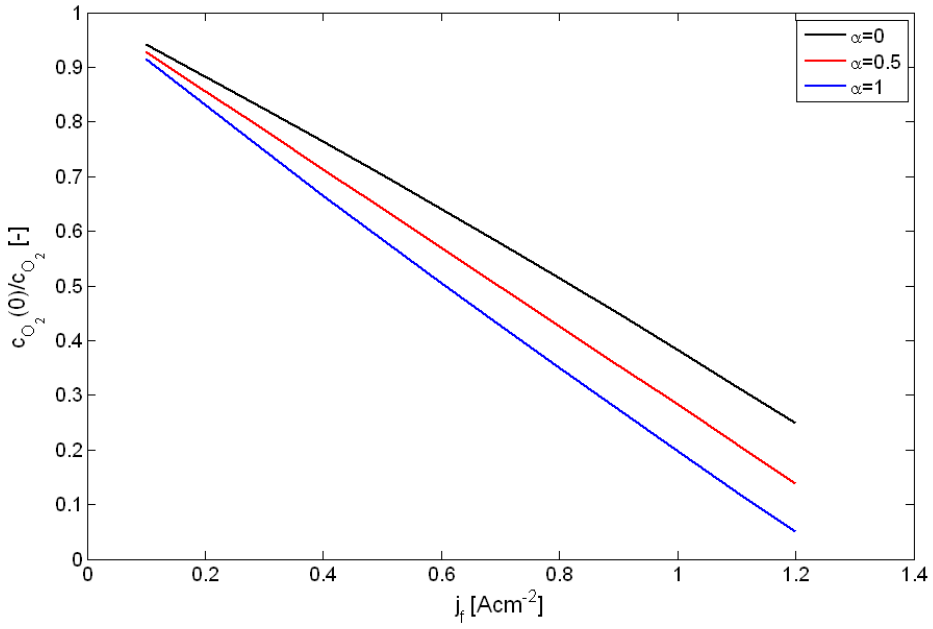
Figure 4.2(a) shows the evolution of the oxygen concentration at the reaction interface ($x = 0$) normalized relative to the inlet concentration $c_{O_2}(0)/c^*_{O_2}$ as a function of j_f in typical operating conditions ($T = 333\ K$ and $P = 1\ bar$). The diffusion layer characteristics are $\delta = 200\ \mu m$ and $D^{eff} = 10^{-6}\ m^2 s^{-1}$. Three different cases are treated:

- $\alpha = 0$: all water flows through the membrane and the convective flux is oriented in the same direction as the diffusive one.
- $\alpha = 0.5$: only half of the water is evacuated through the cathode GDL. The convective flux is null and the oxygen transport occurs only by diffusion (assumption leading to the expression of the Warburg diffusion impedance).
- $\alpha = 1$: all water is evacuated through the cathode GDL and the convective flux is directed opposite to the diffusive one.

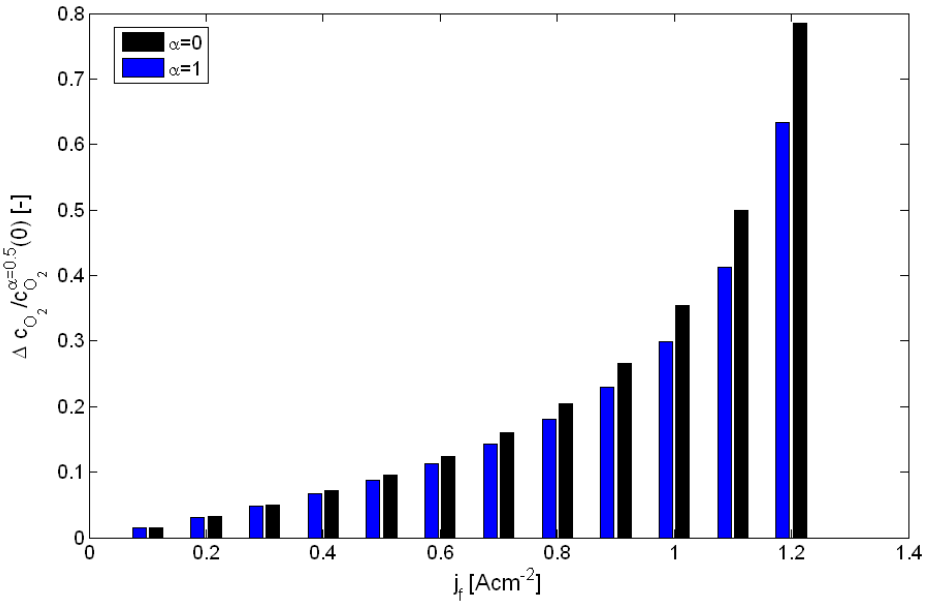
According to the curves in Figure 4.2, the convection has no significant influence on the concentration at the electrode at low current densities. With increasing values of j_f, a water transport coefficient $\alpha = 0$ makes the oxygen concentration increasing compared to a purely diffusive mass transport because the convection is oriented in the same direction as the diffusion. For $\alpha = 1$, the convection is directed opposite to the diffusion and the opposite is observed. The deviation from the purely diffusive case increases with increasing current density.

In Figure 4.2(b), it can be seen that up to a current density $j_f = 0.5\ Acm^{-2}$, the relative error defined by $\Delta c^{\alpha}_{O_2}(0)/c^{\alpha=0.5}_{O_2}(0) = \left|c^{\alpha=0.5}_{O_2}(0) - c^{\alpha}_{O_2}(0)\right| / c^{\alpha=0.5}_{O_2}(0)$ does not exceed 10%. However, with increasing current densities, the relative error increases steeply and reaches almost 80% for $j_f = 1.2\ Acm^{-2}$ and $\alpha = 0$. It can be noticed that the relative error is more important for a convective flux oriented in the direction of the diffusion ($\alpha = 0$) than for a convective flux in the opposite direction ($\alpha = 1$).

It is thus possible to define a criterion indicating whether the influence of convection on $c_{O_2}(0)$ can be neglected or not according to the water transport coefficient (for example if the relative error is below 10 %). Note that in the majority of cases, the value of the water transport coefficient in PEMFC is around 0.5 [CCD+09].



(a) Normalized oxygen concentration at the membrane/GDL interface $(x = 0)$ for a purely diffusive flux (in red), or with an additional convective flux in the same direction (in black) and in the opposite direction (in blue).



(b) Normalized discrepancy between the oxygen concentration at the reaction interface of a purely diffusive flux ($\alpha = 0.5$) and that of the two limit cases ($\alpha = 0, 1$): $\Delta c^{\alpha}_{O_2}(0) = \left| c^{\alpha=0.5}_{O_2}(0) - c^{\alpha}_{O_2}(0) \right|$.

Figure 4.2: *Application example of the steady-state solution* (4.13) *for a PEMFC working at* $T = 333$ *K and* $P = 1$ *bar. The diffusion medium characteristics are* $\delta = 200$ μm *and* $D^{eff} = 10^{-6}$ $m^2 s^{-1}$.

4.1.2 AC solution

In order to analyze the influence of a convective flux in the x-direction on the impedance of a PEMFC, the convecto-diffusive equation (4.3) has to be considered in transient regime. The current density $j_f(t)$, the activation overpotential $\eta_{act}(t)$ and the oxygen concentration $c_{O_2}(x,t)$ are expressed in the same way as for a purely diffusive mass transport (3.26) – (3.28). In the case of small amplitude harmonic oscillations, the equations describing the oxygen transport take the form:

$$i\omega\Delta\bar{c}_{O_2}(x)+V\frac{\partial\Delta\bar{c}_{O_2}(x)}{\partial x}=D^{eff}\frac{\partial^2\Delta\bar{c}_{O_2}(x)}{\partial x^2} \tag{4.14}$$

$$-D^{eff}\left.\frac{\partial\Delta\bar{c}_{O_2}}{\partial x}\right|_{x=0}+V\Delta\bar{c}_{O_2}(0)=-\frac{\Delta\bar{j}_f}{4F} \tag{4.15}$$

The general solution of (4.14) is:

$$\Delta\bar{c}_{O_2}(x)=A\exp(r_1x)+B\exp(r_2x) \tag{4.16}$$

with

$$r_1=\frac{V}{2D^{eff}}+\sqrt{\left(\frac{V}{2D^{eff}}\right)^2+\frac{i\omega}{D^{eff}}} \tag{4.17}$$

$$r_2=\frac{V}{2D^{eff}}-\sqrt{\left(\frac{V}{2D^{eff}}\right)^2+\frac{i\omega}{D^{eff}}} \tag{4.18}$$

The boundary condition at the reaction interface ($x=0$) is given by (4.15). The amplitude of concentration variations at the GDL/channel interface is assumed constant $\Delta\bar{c}_{O_2}(\delta)$. The coefficients A and B can thus be determined with these two boundary conditions:

$$x=0: \qquad r_1A+r_2B-\frac{V}{D^{eff}}(A+B)=\frac{\Delta\bar{j}_f}{4FD^{eff}} \tag{4.19}$$

$$x=\delta: \qquad A\exp(r_1\delta)+B\exp(r_2\delta)=\Delta\bar{c}_{O_2}(\delta) \tag{4.20}$$

$$\Rightarrow A=\frac{\left(r_2-\frac{V}{D^{eff}}\right)\Delta\bar{c}_{O_2}(\delta)-\frac{\Delta\bar{j}_f}{4FD^{eff}}\exp(r_2\delta)}{\left(r_2-\frac{V}{D^{eff}}\right)\exp(r_1\delta)-\left(r_1-\frac{V}{D^{eff}}\right)\exp(r_2\delta)} \tag{4.21}$$

$$B=\frac{\left(r_1-\frac{V}{D^{eff}}\right)\Delta\bar{c}_{O_2}(\delta)-\frac{\Delta\bar{j}_f}{4FD^{eff}}\exp(r_1\delta)}{\left(r_1-\frac{V}{D^{eff}}\right)\exp(r_2\delta)-\left(r_2-\frac{V}{D^{eff}}\right)\exp(r_1\delta)} \tag{4.22}$$

Inserting (4.21) and (4.22) in (4.16) yields the explicit expression of the oxygen concentration variation along the x-direction:

$$\Delta\bar{c}_{O_2}(x) = \frac{\left(r_1 - \frac{V}{D^{eff}}\right)\exp(r_2 x) - \left(r_2 - \frac{V}{D^{eff}}\right)\exp(r_1 x)}{\left(r_1 - \frac{V}{D^{eff}}\right)\exp(r_2\delta) - \left(r_2 - \frac{V}{D^{eff}}\right)\exp(r_1\delta)}\,\Delta\bar{c}_{O_2}(\delta) - \frac{\exp(r_1\delta + r_2 x) - \exp(r_2\delta + r_1 x)}{\left(r_1 - \frac{V}{D^{eff}}\right)\exp(r_2\delta) - \left(r_2 - \frac{V}{D^{eff}}\right)\exp(r_1\delta)}\,\frac{\Delta\bar{j}_f}{4FD^{eff}} \tag{4.23}$$

Assuming that the oxygen concentration in the channel is constant ($\Delta\bar{c}_{O_2}(\delta) = 0$), the oxygen concentration at the reaction interface ($x = 0$) takes the form:

$$\Delta\bar{c}_{O_2}(0) = -\frac{\exp(r_1\delta) - \exp(r_2\delta)}{\left(r_1 - \frac{V}{D^{eff}}\right)\exp(r_2\delta) - \left(r_2 - \frac{V}{D^{eff}}\right)\exp(r_1\delta)}\,\frac{\Delta\bar{j}_f}{4FD^{eff}} \tag{4.24}$$

Replacing r_1 and r_2 by their explicit expressions ((4.17) and (4.18)), it comes:

$$\Delta\bar{c}_{O_2}(0) = -\frac{1}{\frac{\sqrt{\left(\frac{V}{2D^{eff}}\right)^2 + \frac{i\omega}{D^{eff}}}}{\tanh\left(\sqrt{\left(\frac{V}{2D^{eff}}\right)^2 + \frac{i\omega}{D^{eff}}}\,\delta\right)} + \frac{V}{2D^{eff}}}\,\frac{\Delta\bar{j}_f}{4FD^{eff}} \tag{4.25}$$

When the convective flux velocity tends to zero, (4.25) tends to the classical expression of $\Delta\bar{c}_{O_2}(0)$ corresponding to the finite Warburg impedance:

$$\lim_{V\to 0}\Delta\bar{c}_{O_2}(0) = -\frac{\tanh\left(\sqrt{\frac{i\omega}{D^{eff}}}\,\delta\right)}{\sqrt{\frac{i\omega}{D^{eff}}}}\,\frac{\Delta\bar{j}_f}{4FD^{eff}} \tag{4.26}$$

The mass transport impedance $Z_{c_{O_2}} = -\frac{\partial\eta_{act}}{\partial j_f}\,\frac{\partial j_f}{\partial c_{O_2}}\Big|_{x=0}\,\frac{\Delta\bar{c}_{O_2}(0)}{\Delta\bar{j}_f}$ (3.22) corresponding to this convecto-diffusive model is finally given by:

$$Z^{1D}_{conv,diff} = \frac{b}{4FD^{eff}\left\langle c_{O_2}(0)\right\rangle_t}\,\frac{1}{\frac{\sqrt{\left(\frac{V}{2D^{eff}}\right)^2 + \frac{i\omega}{D^{eff}}}}{\tanh\left(\sqrt{\left(\frac{V}{2D^{eff}}\right)^2 + \frac{i\omega}{D^{eff}}}\,\delta\right)} + \frac{V}{2D^{eff}}} \tag{4.27}$$

where $\left\langle c_{O_2}(0)\right\rangle_t$ is the steady-state value of the oxygen concentration (4.13).

Impact of a convective flux on the impedance spectra of PEMFC

In the following, a discussion will be made about the impact of convection perpendicularly to the electrode starting from numerical simulations of PEMFC impedance spectra under typical operating conditions (cf. Table 4.1).

For this, the finite Warburg impedance in the Randles equivalent circuit is replaced by $Z^{1D}_{conv,diff}$ (4.27) which leads to the following expression of the cell impedance:

Working conditions:	T_{cell}	$[^{\circ}C]$	60
	P	$[bar]$	1
	j_f	$[Acm^{-2}]$	0.5
Mass transport characteristics:	δ	$[\mu m]$	200
	D^{eff}	$[m^2 s^{-1}]$	10^{-6}
Impedance parameters:	R_{hf}	$[\Omega cm^2]$	0.13
	R_{ct}	$[\Omega cm^2]$	0.19
	C_{dl}	$[Fcm^{-2}]$	0.02

Table 4.1: *Reference values used for the impedance analysis.*

$$Z_{cell} = R_{hf} + \left(\frac{1}{R_{ct} + Z^{1D}_{conv,diff}} + i\omega C_{dl} \right)^{-1} \tag{4.28}$$

The main parameters used for the simulations are given in Table 4.1. The high frequency parameters are set to typical values measured with the mono-channel cell at $j_{cell} = 0.5\ Acm^{-2}$, *i.e.* $R_{hf} = 0.13\ \Omega cm^2$, $R_{ct} = 0.19\ \Omega cm^2$ and $C_{dl} = 0.02\ Fcm^{-2}$. They do not vary significantly with the current density and can therefore be considered as constant for this study. The effective diffusion coefficient in the reference case is set to $D^{eff} = 10^{-6}\ m^2 s^{-1}$ (Table 4.1), which is in the range of gas diffusion in the GDL. The impedance spectra are simulated for frequencies ranging between $10^{-3}\ Hz$ and $10^{5}\ Hz$ with a resolution of 10 points per decade. In order to test the effect of convection, three limit cases are considered depending on the water transport coefficient: $\alpha = 0$, 0.5 and 1.

In order to probe the validity of this convecto-diffusive impedance expression, impedance spectra have been simulated for different values of C_{dl} (Figure 4.3(a)) and R_{ct} (Figure 4.3(b)), while keeping the other parameters unchanged. For the highest values ($C_{dl} = 0.2\ Fcm^{-2}$ and $R_{ct} = 0.19\ \Omega cm^2$), it seems that the low frequency loop disappears and that the spectra exhibit only one loop. This is actually due to the large size of the high frequency loop (compared to the low frequency loop), which dominates the whole spectrum, all the more so since the diffusion limitations are low in this example ($D^{eff} = 10^{-6}\ m^2 s^{-1}$). The low frequency arc associated with mass transport limitations can be visualized by reducing significantly the values of R_{ct} and C_{dl}, which shifts the capacitive loop to higher frequencies. This is in good agreement with previous observations in the literature [BWJ+05], which confirms the validity of this approach.

The curves in Figure 4.3 confirm that the presence of a convective flux perpendicular to the electrode affects the impedance spectra only in the low frequency range: a convective flux oriented in the direction opposite to the diffusive flux ($\alpha = 1$) widens the LF loop, while a convective flux in the same direction ($\alpha = 0$) reduces its size. These curves show furthermore that the impact of α on the impedance pattern does not depend on the values of R_{ct} or C_{dl}. The impact of convection on the cell impedance depends on the ratio of convection (expressed by the mean gas velocity V) to diffusion (characterized by the diffusive velocity defined by: $V_{diff} = D^{eff}/\delta$). The convective flux velocity can be determined with equation (4.7). In the reference conditions of Table 4.1, we obtain $|V| = 3.5 \times 10^{-4}\ ms^{-1}$ in both limit cases ($\alpha = 0$ and 1) and $V_{diff} = 5 \times 10^{-3}\ ms^{-1}$. V_{diff} is about 10 times higher than V in these conditions and the oxygen transport is governed consequently by diffusion.

However, for lower values of the diffusive flux velocity, when the convective flux remains un-

changed, the impact of convection on the impedance spectra is more pronounced. This is reflected by the curves in Figure 4.4 showing the impedance spectra that are simulated with different values of D^{eff} (Figure 4.4(a)) and δ (Figure 4.4(b)) respectively: with increasing diffusion limitations (decreasing D^{eff} or increasing δ), the discrepancy between the low frequency loops obtained with different values of α increases. The impact of convection on the cell impedance can be quantified by the intercept of the spectra with the real axis R_{lf}. In this context, we define the quantity ΔR_{lf} giving the difference between the low frequency limits of the limit cases R_{lf}^{α} ($\alpha = 0,1$) and that obtained for a purely diffusive behavior $R_{lf}^{\alpha=0.5}$ normalized with reference to $R_{lf}^{\alpha=0.5}$:

$$\Delta R_{lf} = \left| \frac{R_{lf}^{\alpha=0.5} - R_{lf}^{\alpha}}{R_{lf}^{\alpha=0.5}} \right| \tag{4.29}$$

In the reference case ($D^{eff} = 10^{-6} m^2 s^{-1}$, $\delta = 200 \mu m$), we obtain:

$$\begin{aligned} &\text{For } \alpha = 0: \qquad \Delta R_{lf} = 1.2\% \\ &\text{For } \alpha = 1: \qquad \Delta R_{lf} = 1.7\% \end{aligned}$$

When the diffusive flow velocity is divided by 2 ($V_{diff}/2 \leftrightarrow D^{eff} = 5 \times 10^{-7}\ m^2 s^{-1}$ or $\delta = 400\ \mu m$), it comes:

$$\begin{aligned} &\text{For } \alpha = 0: \qquad \Delta R_{lf} = 10.6\% \\ &\text{For } \alpha = 1: \qquad \Delta R_{lf} = 15.9\% \end{aligned}$$

This example shows that the impact of convection on the cell impedance depends strongly on the value of the diffusive flux. Moreover, the impact of a convective flux on the cell impedance is more important for convection in the direction opposite to the diffusion than in the same direction.

Limiting current density

According to this model, there is a critical value of $V_{diff}^{crit}(\delta, j_f, \alpha)$ below which no oxygen reaches the reaction sites anymore and the oxygen concentration at the reaction interface becomes zero: $c_{O_2}(x = 0) = 0$. As a consequence, the cell impedance tends toward infinity when the diffusion velocity approaches V_{diff}^{crit}. For $\alpha \neq 0.5$, the expression of the critical flow velocity can be deduced from (4.13). If $\alpha = 0.5$, the critical value is obtained with the expression of the oxygen concentration in the case of a purely diffusive flow (3.40). It comes:

$$\alpha \neq 0.5: \quad V_{diff}^{crit} = \frac{D_{crit}^{eff}}{\delta_{crit}} = \frac{(2\alpha - 1) j_f RT}{4FP \ln(1 + 0.21(2\alpha - 1))} \tag{4.30}$$

$$\alpha = 0.5: \quad V_{diff}^{crit} = \frac{D_{crit}^{eff}}{\delta_{crit}} = \frac{j_f}{4F c_{O_2}^*} \tag{4.31}$$

The diffusion being characterized by the effective diffusivity and the diffusion layer thickness, it is possible to determine the critical values of one of these parameters as a function of the other. For the example of Figure 4.4, the critical values are given in Table 4.2.

α $[-]$	V_{diff}^{crit} $[ms^{-1}]$	D_{crit}^{eff} $[m^2s^{-1}]$	δ_{crit} $[\mu m]$
0	$4.63\,10^{-4}$	$3.04\,10^{-7}$	657
0.5	$5.84\,10^{-4}$	$3.42\,10^{-7}$	586
1	$7.07\,10^{-4}$	$3.76\,10^{-7}$	532

Table 4.2: *Critical values of the diffusion parameters for the curves in Figure 4.4 for which the oxygen concentration at the GDL/membrane interface becomes zero. The critical effective diffusivity is calculated with $\delta = 200\ \mu m$ and the critical diffusion layer thickness with $D^{eff} = 10^{-6}\ m^2s^{-1}$.*

As expected, a convective flux directed in the diffusion direction allows lower values of the diffusion velocity and of the effective diffusivity, or the use of a thicker diffusion layer than a convective flux in the opposite direction. Nevertheless, the critical values in the three cases are close to each other.

Equation (4.7) shows that V depends also on the electronic current density j_f: the convective flux increases with the current density and thus its impact on the impedance spectra. Figure 4.5 shows the impedance spectra simulated in the operating conditions of Table 4.1 for three different current densities: $j_f = 0.5\ Acm^{-2}$, $j_f = 1\ Acm^{-2}$ and $j_f = 1.3\ Acm^{-2}$: the impact of convection on the impedance spectra increases significantly with the current density. At $j_f = 1.3\ Acm^{-2}$, the mass transport loop dominates the spectrum when $\alpha = 1$. For a given diffusion flow velocity, it is possible to determine the critical current densities with (4.30) and (4.31). Assuming $D^{eff} = 10^{-6}\ m^2s^{-1}$ and $\delta = 200\ \mu m$, it comes:

$$\begin{aligned} j_{f,crit}(\alpha = 0) &= 1.64\ Acm^{-2} \rightarrow V = -1.2\,10^{-3}\ ms^{-1} \\ j_{f,crit}(\alpha = 0.5) &= 1.46\ Acm^{-2} \rightarrow V = 0\ ms^{-1} \\ j_{f,crit}(\alpha = 1) &= 1.33\ Acm^{-2} \rightarrow V = 1\,10^{-3}\ ms^{-1} \end{aligned}$$

Despite of the pronounced influence of the current density on the impedance spectra (Figure 4.5) in the presence of convection opposite to the diffusion, the critical current density does not vary a lot with α. Even in the case of a purely diffusive mass transport, it is not possible to apply current densities above $1.46\ Acm^{-2}$. This rough estimation of the critical current density and the shape of the impedance spectra in Figure 4.5 allow to understand the origin of a maximum of the current density in a fuel cell: at high current densities, mass transport losses become dominant for the cell performance and the diffusion is not sufficient to maintain the gas supply. Note that the curves in Figure 4.5 are obtained in the case of a weakly limited diffusion in pure gas phase ($D^{eff} = 10^{-6}\ m^2s^{-1}$). In the case of higher mass diffusion limitations (diffusion in liquid phase, decreasing porosity due to liquid water accumulation, ...), the impact of j_f on the impedance spectra would be even more significant.

Conclusions about the numerical investigations with the 1D convecto-diffusive impedance

These results lead to the conclusion that as long as the mass transport losses remain low compared to the other voltage drops, the influence of a possible convective flux due to the evacuation of vapor remains limited and can be neglected. However, for increasing diffusion limitations (*e.g.* with the appearance of liquid water in the diffusion media) and for current densities above 0.5 Acm^{-2}, convection along the x-direction affects significantly the low frequency loop of the impedance spectra. Consequently, in these conditions, convection should be taken into account in the oxygen transport model in order to avoid wrong conclusions about the origin of the transport limitations. Thus, convection should be included in the impedance models of automotive fuel cells, which work commonly at high current densities ($\geq 1\ Acm^{-2}$). The results obtained with the 1D convecto-diffusive model are in good agreement with experimental observations made by A. Thomas in our group at LEMTA (cf. chapter 6.1) confirming the validity of this approach.

Nevertheless, investigations of the water transport coefficient in PEMFC revealed that in typical operating conditions ($j_{cell} \approx 0.5\ Acm^{-2}$) the values of α are usually close to 0.5 [CCD$^+$09]: the description of oxygen transport perpendicular to the electrode by diffusion only is justified in these conditions.

4.2 Bulk Electrode Impedance Model

It has been pointed out that proton transport limitations in the catalyst layer have an impact on the size and shape of impedance spectra and should not be neglected in the impedance modeling of fuel cells [SZWG96, EK99, BGA$^+$02, MMB05]. There exist different modeling approaches in the literature which account for phenomena arising over the depth of the electrode [SZWG96, EK99, BGA$^+$02]. The model used in the following is adapted from the works of Eikerling and Kornyshev [EK99]. It accounts for the finite proton conductivity in the liquid or electrolyte phase of the active layer, as well as for oxygen consumption in the electrode bulk. The aim of this study is to point out that a bulk description of the catalyst layer can explain several features of impedance spectra in particular in the high frequency domain. Furthermore, the results obtained with this model may help to distinguish between voltage drops due to proton transport limitations in the active layer and those caused by other cell components and physical phenomena.

This impedance model treats only the catalyst layer, considered as a one-dimensional and homogeneous medium (Figure 4.6). The model hypotheses are the following:

- The catalyst layer is isothermal.
- Ohmic losses in the electronic conducting phase are neglected: the cell potential of the carbon phase is uniform over the electrode thickness.
- The protonic conductivity σ_p (in $S\,cm^{-1}$) is uniform in the catalyst layer.
- Strictly speaking, the differential double-layer capacitance is a function of the local potential drop across the carbon/electrolyte interface. However, its variations with the cell potential are neglected.
- Oxygen transport through the pores of the catalyst layer is assumed to occur only by gas diffusion.

The reaction kinetics are described by a Tafel law:

$$\eta_{act} = b \ln \left(\frac{j_f(x,t) c^*_{O_2}}{j_0 c_{O_2}(x,t)} \right) \tag{4.32}$$

where η_{act} is the activation overpotential which is defined in this context by the potential difference between the solid phase (equipotential) and the electrolyte solution.[1] Note that the electronic current densities j_f and j_0 are given in Am^{-3} in this approach. The proton conduction in the electrode is described by Ohm's law:

$$\frac{\partial \eta_{act}}{\partial x} = -\rho_p j_p(x,t) \tag{4.33}$$

where $\rho_p \propto \frac{1}{\sigma_p}$ (in Ωm) stands for the protonic resistivity of the electrode and $j_p(x,t)$ for the protonic current density expressed in Am^{-2}. The protonic resistivity can be estimated roughly as a function of the proton conductivity of Nafion σ_p by:

$$\rho_p = \frac{1}{\sigma_p \varepsilon \chi_N} \tag{4.34}$$

where ε stands for the electrode porosity and χ_N for the Nafion loading (portion of pores filled with electrolyte) of the electrode. The proton flux can be expressed as a function of the faradaic and capacitive current densities:

$$\frac{\partial j_p(x,t)}{\partial x} = -j_f(x,t) - C^v_{dl} \frac{\partial \eta_{act}}{\partial t} \tag{4.35}$$

Note that in this approach, C^v_{dl} is expressed in Fm^{-3}. As the protons pass through the ionomer present in the electrode to reach the polymer membrane, it follows that:

At the electrode/membrane interface:	$j_p(x=0,t) = j_{cell}(t)$	(4.36)
At the GDL/electrode interface:	$j_p(x=\delta,t) = 0$	(4.37)

The oxygen transport is described by Fick's law. Oxygen consumption along the pore walls is taken into account by a source term - $-\frac{j_f(x,t)}{4F}$ - and the 2nd Fick's law takes the from:

$$\frac{\partial c_{O_2}(x,t)}{\partial t} = D^{eff} \frac{\partial^2 c_{O_2}(x,t)}{\partial x^2} - \frac{j_f(x,t)}{4F} \tag{4.38}$$

The pores of the catalyst layer are of the same order of magnitude as the mean free path of the oxygen molecules. As a consequence, the oxygen diffusion is a mixture of molecular and Knudsen diffusion, which is taken into account by the effective diffusivity D^{eff} (cf. section 2.4.2).

In the following, the equations will be solved in two cases: in a first approach, the faradaic current density is null, which is possible because the description accounts for charge variations in the electrical double-layer in a dynamic regime. This leads to an analytical expression of the electrode impedance that allows to predict the cell impedance in the absence of any reactant gas

[1] In the classical approach, η_{act} is defined as the potential difference between the cell potential and the Nernst potential. Both definitions coincide if the carbon and the electrolyte at the electrode/membrane interface ($x = 0$) are at the same potential (cf. chapter 2.2.2).

(*e.g.* when the cell is fed with nitrogen at both electrodes). In a second approach, the complete system of equations is solved. In this case, there exists no analytical solution. A numerical solution of the problem is possible by discretizing the electrode into slices and by determining the model parameters between two successive slices by an iterative procedure.

4.2.1 Impedance response in the absence of oxygen $(j_f(x,t) = 0)$

When there is no reactant gas in the electrodes, the faradaic current density is null $(j_f(x,t) = 0)$ and the system is described by equations (4.33) and (4.35). In this case, the proton flux density depends only on the capacitive current density and equation (4.35) simplifies to:

$$\frac{\partial j_p(x,t)}{\partial x} = -C_{dl}^v \frac{\partial \eta_{act}}{\partial t} \tag{4.39}$$

In steady-state, the protonic current density $j_p(x)$ is zero and it follows from equation (4.33) that the electrode potential (overpotential) is constant over the electrode depth:

$$\eta_{act}(x) = \eta_{act}(0) \tag{4.40}$$

In a dynamic regime, the parameter variations are defined in a classical way (cf. equations (3.26) - (3.28)). Thus, the equations describing the processes in the catalyst layer take the form:

$$-\frac{1}{\rho_p}\frac{\partial \Delta\bar{\eta}_{act}(x)}{\partial x} = \Delta\bar{j}_p(x) \tag{4.41}$$

$$\frac{\partial^2 \Delta\bar{\eta}_{act}(x)}{\partial x^2} - i\omega\rho_p C_{dl}^v \Delta\bar{\eta}_{act}(x) = 0 \tag{4.42}$$

The general solution of (4.42) is given by:

$$\Delta\bar{\eta}_{act}(x) = \Delta\bar{\eta}_{act}(x=0)\cosh(\kappa x) + B\sinh(\kappa x), \text{ with } \kappa = \sqrt{i\omega\rho_p C_{dl}^v} \tag{4.43}$$

Assuming that the potential variations are confined to the active layer, it comes:

$$\frac{\partial \Delta\bar{\eta}_{act}(x=\delta)}{\partial x} = \Delta\bar{\eta}_{act}(0)\kappa\sinh(\kappa\delta) + B\kappa\cosh(\kappa\delta) = 0 \tag{4.44}$$

$$\Rightarrow B = -\Delta\bar{\eta}_{act}(0)\tanh(\kappa\delta) \tag{4.45}$$

The potential variation is thus expressed by:

$$\Delta\bar{\eta}_{act}(x) = \Delta\bar{\eta}_{act}(0)\left[\cosh\left(\sqrt{i\omega\rho_p C_{dl}^v}x\right) - \tanh\left(\sqrt{i\omega\rho_p C_{dl}^v}\delta\right)\sinh\left(\sqrt{i\omega\rho_p C_{dl}^v}x\right)\right] \tag{4.46}$$

The electrode impedance is then given by:

$$Z_{j_f=0}(\omega) = \frac{\Delta\bar{\eta}_{act}(0)}{\Delta\bar{j}_p(0)} \tag{4.47}$$

The potential variation at the electrode/membrane interface can be obtained with (4.41), which

yields:

$$Z_{j_f=0}(\omega) = \frac{\rho_p}{\sqrt{i\omega\rho_p C_{dl}^v}\tanh\left(\sqrt{i\omega\rho_p C_{dl}^v}\delta\right)} \tag{4.48}$$

According to (4.48), the impedance is proportional to $(i\omega)^{-1/2}$ at high frequencies and resembles thus to a Warburg behavior. Note that in a representation of the electrode by a fractal geometry, this high frequency behavior could be attributed to a constant phase element (CPE) [Boi05]. The capacitive behavior $\left|Z_{j_f=0}\right| \propto 1/i\omega$ appears only for low frequencies. This is illustrated by the impedance spectrum of an electrode of thickness $\delta = 10\ \mu m$ (Figure 4.7). The frequency range spans from $10^{-3}\ Hz$ to $10^4\ Hz$. $T = 60°C$, the proton resistivity is $\rho_p = 3.33\ \Omega m$ and the double layer capacity $C_{dl}^v = 0.02\,10^4/\delta Fm^{-3}$. The electrode impedance tends toward infinity in the low frequency regime, whereas it exhibits a straight line at 45° ($\propto (i\omega)^{-1/2}$) in the high frequency regime, which is usually characteristic for diffusion losses. However, the model does not take into account mass transport losses and the behavior at high frequencies is exclusively controlled by proton conduction and charge variations in the EDL through the active layer.

4.2.2 Solution of the complete impedance model

At non zero current density, the system is described by the set of equations (4.33) – (4.38). Neither in the stationary, nor in the dynamic regime, it is possible to obtain analytical solutions, except for certain limiting cases where one or more processes are negligible compared to the others. In order to obtain a numerical solution, the electrode is discretized into n slices of thickness Δx, as represented in Figure 4.8. With appropriate boundary conditions ($\eta_{act}(0) = \eta_{act_0}$, $c_{O_2}(\delta) = c_{O_2}^*$), it is possible to determine the model parameters (η_i, c_i) at the boundary of each slice i by an iterative procedure. The equations are solved with the electrode characteristics and operating conditions of Table 4.3. The parameters with reference to the proton conduction (σ_p, ε and χ_N) are chosen in a way that in the reference case, the protonic resistivity is $\rho_p = 3.33\ \Omega m$ according to equation (4.34).

δ	$[\mu m]$	10
b_{10}	$[mV dec^{-1}]$	120
C_{dl}^v	$[Fm^{-3}]$	$0.02\,10^4/\delta = 2\,10^7$
j_0	$[Am^{-3}]$	200
P	$[bar]$	1
T	$[K]$	333
$c_{O_2}^*$	$[molm^{-3}]$	$0.21\frac{P}{RT}$
η_0	$[V]$	0.9
D^{eff}	$[m^2 s^{-1}]$	10^{-7}
σ_p	$[Sm^{-1}]$	10
ε	$[-]$	0.3
χ_N	$[-]$	0.1

Table 4.3: *Main parameters used for the solution of the complete bulk electrode model.*

DC solution

Combining equations (4.33) (4.35) and (4.38) in steady-state, it comes:

$$\frac{\partial^2 \eta_{act}(x)}{\partial x^2} = \rho_p j_0 \frac{c_{O_2}(x)}{c^*_{O_2}} \exp\left(\frac{\eta_{act}(z)}{b}\right) \tag{4.49}$$

$$\frac{\partial^2 c_{O_2}(x)}{\partial x^2} = \frac{j_0}{4FD^{eff}c^*_{O_2}} c_{O_2}(x) \exp\left(\frac{\eta_{act}(x)}{b}\right) \tag{4.50}$$

These equations can be solved with the assumption that the GDL is not limiting neither for oxygen transport processes nor for electronic conduction:

$$\frac{\partial \eta_{act}(\delta)}{\partial x} = \frac{\partial c_{O_2}(\delta)}{\partial x} = 0 \tag{4.51}$$

Equations (4.49) and (4.50) are discretized according to Figure 4.8 using a finite-difference method:

$$\eta_{i+1} + \eta_{i-1} - 2\eta_i = \frac{\rho_p j_0 \Delta x^2}{c^*_{O_2}} c_i \exp\left(\frac{\eta_i}{b}\right) \tag{4.52}$$

$$c_{i+1} + c_{i-1} - c_i \left(2 + \frac{\Delta x^2 j_0}{4FD^{eff}c^*_{O_2}} \exp\left(\frac{\eta_i}{b}\right)\right) = 0 \tag{4.53}$$

Equations (4.52) and (4.53) form a set of $2n$ equations with $2n$ unknowns that can be solved by an iterative procedure and known boundary conditions. At the membrane/electrode interface ($\eta = \eta_0$; left side in Figure 4.8) the equations become:

$$\frac{3}{2}\eta_2 - \frac{9}{2}\eta_1 + 3\eta_0 = \frac{\rho_p j_0 \Delta x^2}{c^*_{O_2}} c_1 \exp\left(\frac{\eta_i}{b}\right) \tag{4.54}$$

$$c_2 - c_1 \left(1 + \frac{\Delta x^2 j_0}{4FD^{eff}c^*_{O_2}} \exp\left(\frac{\eta_i}{b}\right)\right) = 0 \tag{4.55}$$

At the electrode/GDL interface ($c_{n+1} = c^*_{O_2}$; right side in Figure 4.8), it comes:

$$-\eta_n + \eta_{n-1} = \frac{\rho_p j_0 \Delta x^2}{c^*_{O_2}} c_n \exp\left(\frac{\eta_i}{b}\right) \tag{4.56}$$

$$3c_0 - \left(\frac{9}{2} + \frac{\Delta x^2 j_0}{4FD^{eff}c^*_{O_2}} \exp\left(\frac{\eta_i}{b}\right)\right) c_n + \frac{3}{2} c_{n-1} = 0 \tag{4.57}$$

Figure 4.9 depicts the profiles of the model parameters in the catalyst layer, *i.e.* c_{O_2} (Figure 4.9(a)), η_{act} (Figure 4.9(b)) and j_f (Figure 4.9(c)) - obtained by solving equations (4.52), (4.53) and (4.32) with the parameters of Table 4.3. The effect of diffusion limitations is studied by varying the oxygen diffusivity between 10^{-6} $m^2 s^{-1}$ and 10^{-9} $m^2 s^{-1}$.

For high diffusivities ($D^{eff} = 10^{-6} m^2 s^{-1}$), the concentration remains almost constant along the x direction and the overpotential increases exponentially from the GDL to the membrane. In this case, most of the electronic current j_f is produced close to the membrane. With a lower diffusion coefficient, the decrease of the concentration along the x direction becomes more pronounced and for important transport limitations ($D^{eff} = 10^{-9} m^2 s^{-1}$), there exists a penetration depth beyond which no oxygen reaches the active sites. Simultaneously, the profile of the overpotential flattens until being linear. In this case, almost all of the faradaic current is produced close to the GDL. The linear decrease of the potential from the membrane to the GDL can be explained by the finite proton conduction of the electrode that is expressed by $\sigma_p \propto 1/\rho_p$.

Note that for intermediate values of the diffusivity (in this example $D^{eff} = 10^{-8} m^2 s^{-1}$), the local faradaic current density (Am^{-3}) exhibits a minimum along the x direction. The variations of j_f in this case are significantly lower than in the other cases of very high or low diffusion coefficients. Therefore, the profile of j_f for $D^{eff} = 10^{-8} m^2 s^{-1}$ appears almost flat in Figure 4.9(c). The position of the minimum depends on the proton conductivity (not shown here), which indicates that the local operation of the electrode is governed by proton conduction and oxygen diffusion.

It is possible to estimate the macroscopic exchange current density with respect to the electrode active area (in Am^{-2}) with this electrode model. Some preliminary investigations on this subject indicate that there exists an ideal electrode thickness depending on the electrolyte content of the catalyst layer (proton conductivity), the local exchange current density (Pt loading) and the effective diffusivity. These results will be presented in a future document, because we focus here on electrochemical impedance spectroscopy.

AC solution

In an established dynamic regime, each variable X can be decomposed in its time-averaged value $\langle X \rangle_t$ and a small sinusoidal component of amplitude $\Delta\bar{X}$:

$$\Delta\eta_{act}(x,t) = \eta_{act}(x,t) - \langle \eta_{act}(x) \rangle_t = \Delta\bar{\eta}_{act}(x)\exp(i\omega t) \tag{4.58}$$

$$\Delta j_f(x,t) = j_f(x,t) - \left\langle j_f(x) \right\rangle_t = \Delta\bar{j}_f(x)\exp(i\omega t) \tag{4.59}$$

$$\Delta j_p(x,t) = j_p(x,t) - \left\langle j_p(x) \right\rangle_t = \Delta\bar{j}_p(x)\exp(i\omega t) \tag{4.60}$$

$$\Delta c_{O_2}(x,t) = c_{O_2}(x,t) - \langle c_{O_2}(x) \rangle_t = \Delta\bar{c}_{O_2}(x)\exp(i\omega t) \tag{4.61}$$

Inserting these expressions into the Tafel law (4.32) and the equation defining the proton flux (4.35), it comes:

$$\frac{1}{\rho_p}\frac{\partial^2 \Delta\bar{\eta}_{act}(x)}{\partial x^2} = \Delta\bar{j}_f(x) + i\omega C_{dl}^v \Delta\bar{\eta}_{act}(x) \tag{4.62}$$

$$\Delta\bar{j}_f(x) = \frac{j_0 \langle c_{O_2}(x) \rangle_t}{c_{O_2}^*} \exp\left(\frac{\langle \eta_{act}(x) \rangle_t}{b}\right)\left[\frac{\Delta\bar{\eta}_{act}(x)}{b} + \frac{\Delta\bar{c}_{O_2}(x)}{\langle c_{O_2}(x) \rangle_t}\right] \tag{4.63}$$

Combining (4.62) and (4.63) leads to an expression that allows to determine the local variations of the overpotential:

$$\frac{\partial^2 \Delta\bar{\eta}_{act}(x)}{\partial x^2} = \left[\frac{\rho_p j_0 \langle c_{O_2}(x) \rangle_t}{b c_{O_2}^*} \exp\left(\frac{\langle \eta_{act}(x) \rangle_t}{b}\right) + i\omega\rho_p C_{dl}^v\right]\Delta\bar{\eta}_{act}(x) + \frac{\rho_p j_0}{c_{O_2}^*}\exp\left(\frac{\langle \eta_{act}(x) \rangle_t}{b}\right)\Delta\bar{c}_{O_2}(x) \tag{4.64}$$

The expression that allows to determine the local variations of the concentration can be derived by combining (4.38) and (4.63):

$$\frac{\partial^2 \Delta\bar{c}_{O_2}(x)}{\partial x^2} = \left[\frac{i\omega}{D^{eff}} + \frac{j_0}{4FD^{eff}c_{O_2}^*}\exp\left(\frac{\langle \eta_{act}(x) \rangle_t}{b}\right)\right]\Delta\bar{c}_{O_2}(x) + \frac{j_0 \langle c_{O_2}(x) \rangle_t}{4Fbc_{O_2}^*}\exp\left(\frac{\langle \eta_{act}(x) \rangle_t}{b}\right)\Delta\bar{\eta}_{act}(x) \tag{4.65}$$

Again, it is assumed that the GDL is not limiting neither for electron conduction nor for oxygen diffusion processes and that the variations of the model parameters are confined to the catalyst layer:

$$\frac{\partial \Delta\bar{\eta}_{act}(\delta)}{\partial x} = \frac{\partial \Delta\bar{c}_{O_2}(\delta)}{\partial x} = 0 \tag{4.66}$$

Like in steady-state, there exists no analytical solution of equations (4.64) and (4.65) and they must be discretized for a numerical solution according to Figure 4.8:

$$\Delta\bar{\eta}_{i+1} + \Delta\bar{\eta}_{i-1} - \left[2 + \frac{\Delta x^2 \rho_p j_0 c_i}{b c^*_{O_2}} \exp\left(\frac{\eta_i}{b}\right) + i\Delta x^2 \omega \rho_p C_{dl}\right] \Delta\bar{\eta}_i = \frac{\Delta x^2 \rho_p j_0}{c^*_{O_2}} \exp\left(\frac{\eta_i}{b}\right) \Delta\bar{c}_i \tag{4.67}$$

$$\Delta\bar{c}_{i+1} + \Delta\bar{c}_{i-1} - \left[2 + \frac{i\omega\Delta x^2}{D^{eff}} + \frac{j_0 \Delta x^2}{4F D^{eff} c^*_{O_2}} \exp\left(\frac{\eta_i}{b}\right)\right] \Delta\bar{c}_i = \frac{j_0 c_i \Delta x^2}{4F b c^*_{O_2}} \exp\left(\frac{\eta_i}{b}\right) \Delta\bar{\eta}_i \tag{4.68}$$

At the membrane/electrode interface ($\eta = \eta_0$; left side of Figure 4.8) equations (4.67) and (4.68) take the form:

$$\frac{3}{2}\Delta\bar{\eta}_2 - \left[\frac{9}{2} + \frac{\Delta x^2 \rho_p j_0 c_1}{b c^*_{O_2}} \exp\left(\frac{\eta_1}{b}\right) + i\Delta x^2 \omega \rho_p C_{dl}\right] \Delta\bar{\eta}_1 + 3\Delta\bar{\eta}_0 = \frac{\Delta x^2 \rho_p j_0}{c^*_{O_2}} \exp\left(\frac{\eta_1}{b}\right) \Delta\bar{c}_1 \tag{4.69}$$

$$\Delta\bar{c}_2 - \left[1 + \frac{i\omega\Delta x^2}{D^{eff}} + \frac{j_0 \Delta x^2}{4F D^{eff} c^*_{O_2}} \exp\left(\frac{\eta_1}{b}\right)\right] \Delta\bar{c}_1 = \frac{j_0 c_1 \Delta x^2}{4F b c^*_{O_2}} \exp\left(\frac{\eta_1}{b}\right) \Delta\bar{\eta}_1 \tag{4.70}$$

At the electrode/GDL interface ($c_{n+1} = c^*_{O_2}$; right side of Figure 4.8) they are given by:

$$-\left[1 + \frac{\Delta x^2 \rho_p j_0 c_n}{b c^*_{O_2}} \exp\left(\frac{\eta_n}{b}\right) + i\Delta x^2 \omega \rho_p C_{dl}\right] \Delta\bar{\eta}_n + \Delta\bar{\eta}_{n-1} = \frac{\Delta x^2 \rho_p j_0}{c^*_{O_2}} \exp\left(\frac{\eta_n}{b}\right) \Delta\bar{c}_n \tag{4.71}$$

$$3\Delta\bar{c}_0 - \left[\frac{9}{2} + \frac{i\omega\Delta x^2}{D^{eff}} + \frac{j_0 \Delta x^2}{4F D^{eff} c^*_{O_2}} \exp\left(\frac{\eta_n}{b}\right)\right] \Delta\bar{c}_n + \frac{3}{2}\Delta\bar{c}_{n-1} = \frac{j_0 c_n \Delta x^2}{4F b c^*_{O_2}} \exp\left(\frac{\eta_n}{b}\right) \Delta\bar{\eta}_n \tag{4.72}$$

In terms of equivalent electrical circuits, this amounts to represent the catalyst layer by a transmission line (Figure 4.10). The elementary unit of one slice contains a protonic resistance R_p, an electronic resistance R_{el}, a charge transfer resistance R_{ct} and a double-layer capacity C_{dl} [EK99].

Numerical results

In the following, a discussion is made about the impact of diffusion losses and proton conduction on the cathode impedance spectra in the operating conditions of Table 4.3. Note that a typical value of the cathode overpotential would be $\eta_0 = 0.3\ V$ (cf. (2.37) in chapter 2.1.2). However, in this case, the spectra consist of only one loop. As the present study has a qualitative character, the value $\eta_0 = 0.9\ V$ is chosen in order to allow a clear distinction of the effects of the different parameters on the impedance.

Figure 4.11(a) depicts spectra obtained for values of the diffusivity D^{eff} ranging between $10^{-8}\ m^2 s^{-1}$ and $10^{-6}\ m^2 s^{-1}$. It can be seen that diffusion in the catalyst layer affects their size, but even for very low values of the diffusion coefficient ($D^{eff} = 10^{-8}\ m^2 s^{-1}$), no separate low frequency loop can be observed. According to these curves, diffusion through the active layer does not seem to generate a separate loop at low frequencies. As shown in Figure 4.11(b), the separation between the capacitive and diffusion loops is only visible for very low values of the double layer capacity ($C^v_{dl} = 2 \times 10^{-4}/\delta\ F cm^{-3}$), because decreasing the double layer capacity leads to a shift of the capacitive loop to higher frequencies [BGA+02]. The separation of these two loops allows to see that the diffusion impedance associated with the catalyst layer creates a loop at intermediate fre-

quencies rather than at low frequencies: up to frequencies of about 1600 Hz. This frequency is obtained with an overpotential $\eta_0 = 0.9\ V$. For more common values of the cathode overpotential ($\eta_0 = 0.3\ V$ for instance), no separation between the loops associated with diffusion and proton conduction can be obtained (not shown here). This does not mean that oxygen diffusion in the catalyst layer has no impact on the impedance, but that the effects of proton conduction and oxygen diffusion affect the impedance in the same frequency range. Oxygen diffusion through the catalyst layer seems thus not to be at the origin of a separate loop at low frequencies.

Nevertheless, experimental impedance spectra exhibit generally clearly a low frequency loop: our numerical results seem to show that this loop is not entailed by oxygen diffusion in vapor phase through the catalyst layer. Macroscopic oxygen diffusion in liquid phase does not seem either to be at the origin of the experimental low frequency loop: it was not observed numerically even for values of the diffusion coefficient of about $10^{-11}\ m^2 s^{-1}$ (neither for $\eta_0 = 0.9\ V$, nor for $\eta_0 = 0.3\ V$). This leads to three possible origins of the low frequency loop:

- Macroscopic gas diffusion through the pores of the GDL (cf. section 3.6.3).
- Microscopic diffusion through a liquid (water or electrolyte) film covering the pores of the catalyst layers (cf. sections 3.6.3 and 6.3.2).
- A measuring artifact caused by concentration oscillations propagating along the channel and influencing the impedance measurements downstream (cf. sections 5.2.2 and 6.3.2).

Indeed, in this numerical model, macroscopic diffusion is considered only through the thickness of the whole electrode ($\approx 10\ \mu m$) with reference to the MEA flat surface: none of the phenomena mentioned above are considered. However, oxygen diffusion affects significantly the size of the impedance spectra and their low frequency limit: in the example of Figure 4.11(a), decreasing the value of D^{eff} from $10^{-6}\ m^2 s^{-1}$ to $10^{-8}\ m^2 s^{-1}$ increases the low frequency resistance from $0.08\ \Omega cm^2$ to $0.41\ \Omega cm^2$, which is in the ranges commonly observed experimentally. Macroscopic oxygen diffusion through the pores of the catalyst layer affects significantly the cell impedance and should thus be included in fuel cell impedance modeling.

Furthermore, similarly to what is observed at zero current density (Figure 4.7), a straight line at 45° appears at high frequencies in all cases, independently of the value of the effective diffusivity (Figure 4.11(a)). This is consistent with the experimental results usually presented in the literature [EK99, BGA+02, SZWG96]. These conclusions are confirmed by the curves in Figure 4.12 reflecting the effect of the protonic resistance ρ_p. Different values of ρ_p (ranging between $0.37\ \Omega m$ and $3.33\ \Omega m$) can be obtained by varying the Nafion content (dimensionless number) in equation (4.34) between 0.1 and 0.9. The high frequency resistance does not depend on the proton conductivity; this is a property of the transmission line equivalent circuit in Figure 4.10: at high frequencies the capacities are short-circuited and no current passes through the protonic resistances (considering that the electronic resistance R_{el} is negligible). Actually, the occurrence of the straight line at 45° does not depend on the value of the model parameters, but only on the porous structure of the electrode. Nevertheless, the curves in Figure 4.12 show that the straight line at 45° extends to lower frequencies with increasing values of ρ_p, which is consistent with the results of Eikerling and Kornyshev [EK99]. In addition, these curves show that proton transport governs the impedance of the electrode at low frequencies: multiplying the protonic resistivity by 10 (from $0.37\ \Omega m$ to $3.33\ \Omega m$) increases the low frequency limit of the spectra by a factor of almost 2.5 (from $0.04\ \Omega cm^2$ to $0.11\ \Omega cm^2$ at $\eta_0 = 0.9\ V$).

As far as the estimation of the different model parameters is concerned, correlations between them (j_0, b, ρ_p, C_{dl}, D^{eff}) exist most probably. Whatever it is, the first goal of this study is to visualize qualitatively the impact of the porous structure of the electrode on the impedance. In this regard, two main conclusions can be drawn:

- Independently of the values of the parameters, the porous structure of the catalyst layer leads to the appearance of a straight line at 45°. The frequency range over which this line extends depends on the protonic resistance ρ_p: with increasing values of ρ_p, this line spans to lower frequencies. This is consistent with results from the literature [EK99, BGA$^+$02, SZWG96]. The high frequency resistance of the spectra is not affected by proton conduction in the electrode. On the other hand, the low frequency limit of the spectra depends highly on this parameter: the low frequency resistance increases by a factor 2.5 when ρ_p increases by a factor 10 (when $\eta_0 = 0.9\ V$).

- Macroscopic diffusion of oxygen at the scale of the thickness of the active layer ($\approx 10\ \mu m$) does not give rise to a separate loop at low frequencies but contributes to the loop at intermediate frequencies, which is usually attributed to the double-layer capacity and charge transfer kinetics. A separation of both effects is only possible for very low values of the double layer capacity [BGA$^+$02]. As a consequence, (i) macroscopic gas diffusion through the GDL (cf. section 3.6.3), (ii) microscopic diffusion through a liquid water or electrolyte film covering the pores of the active layer (cf. sections 3.6.3 and 6.3.2), or (iii) concentration oscillations induced by the AC measuring signal (cf. sections 5.2.2 and 6.3.2) are the only phenomena that can be at the origin of the separate loop observed at low frequencies. However, this does not mean that macroscopic oxygen transport through the catalyst layer in vapor or in liquid phase does not affect the impedance spectra: its effect can be significant, but at intermediate frequencies.

4.3 Conclusions about the One-Dimensional Mass Transport Models

Proton and mass transport in the direction perpendicular to the electrode is included in the models with the objective to estimate the error made by using a finite Warburg element.

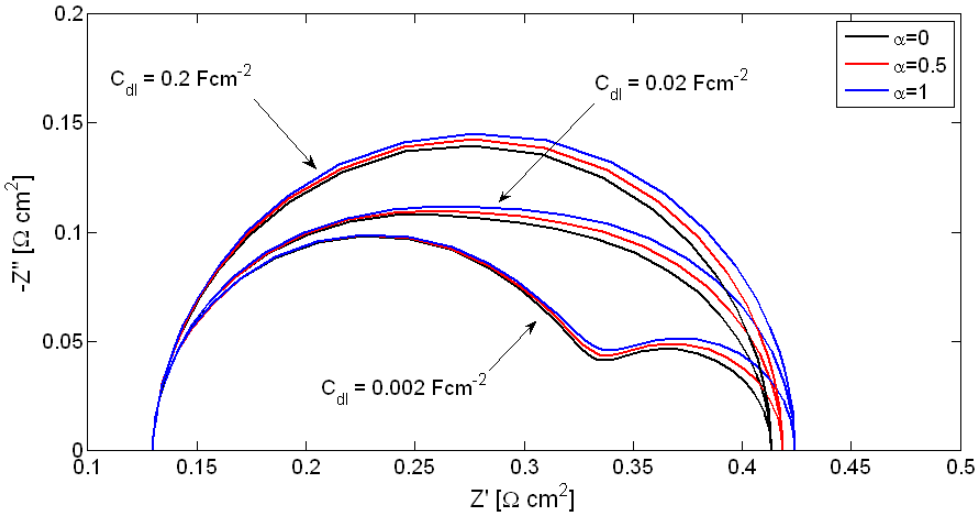
In the first part of this chapter, the influence of a convective flux caused by vapor evacuation (accounted for by means of the water transport coefficient α) on the cell impedance is analyzed. The usual description of oxygen transport leading to the Warburg impedance assumes a purely diffusive flux (and thus that $\alpha = 0.5$), which is not always verified. The numerical results point out that as long as diffusion losses are small compared to other cell voltage losses and for relatively low current densities ($j_{cell} \leq 0.5\ Acm^{-2}$), the convection can be neglected. However, for higher current densities and with the appearance of liquid water in the diffusion media, the contribution of convection to the cell impedance becomes significant and should be taken into account in order to avoid misleading conclusions about the oxygen transport processes. These results are confirmed by experimental investigations on a PEMFC performed by A. Thomas of our group at LEMTA that are presented in section 6.1.

In the second part of this chapter, the impact of the electrode porous structure on the cathode impedance is investigated according to a model developed starting from the works of Eikerling and Kornyshev [EK99]. This one-dimensional description accounts for the protonic resistance of

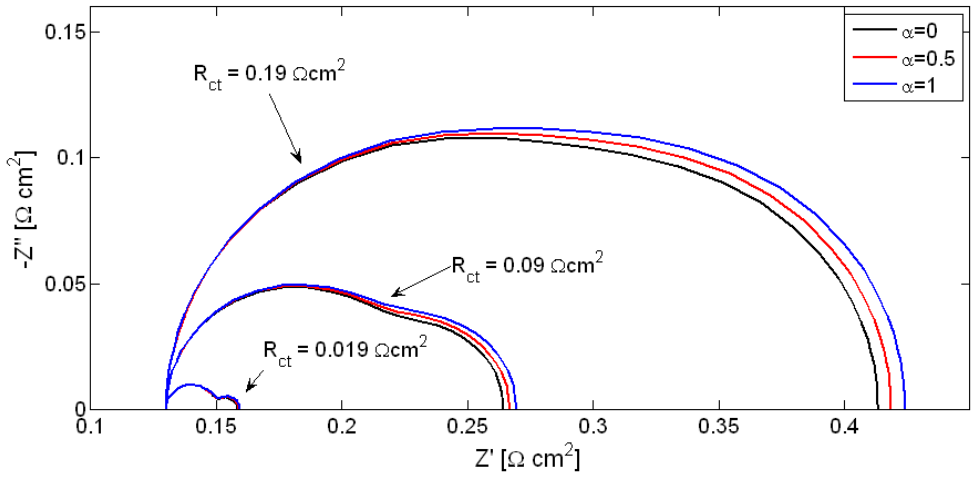
the electrolyte in the catalyst layer, as well as for oxygen consumption and diffusion along the gas pores. Two main conclusions can be drawn:

- The finite proton conduction in the catalyst layer has a significant influence on the cathode impedance. The model confirms that the high frequency behavior of the impedance spectra, *i.e.* the straight line at 45° is not caused by diffusion (Warburg behavior) but is related to the porous structure of the electrode. Its appearance does not depend on the values of the model parameters. However, with increasing values of the protonic resistance in the electrode ρ_p, this straight line is extended to lower frequencies. This parameter does not affect the high frequency resistance of the spectra, but has a significant impact on the size of the spectra at intermediate and low frequencies, and thus on the low frequency resistance.

- As far as the effects of oxygen diffusion in the catalyst layer are concerned, even for very low values of D^{eff}, only one loop can be observed. A separation of the capacitive and diffusion loops occurs only for very low values of the double-layer capacity ($C_{dl}^{v} = 2 \times 10^{-4} / \delta F cm^{-3}$) and even in this case, the loop associated with oxygen diffusion spans up to frequencies of about 1600 Hz (with an overpotential $\eta_0 = 0.9\ V$). This shows that diffusion and charge transport limitations in the catalyst layer occur in the same frequency range. The simulations made with $\eta_0 = 0.3\,V$, which is a more common value, did not allow a separation of the loops associated with the two processes. The low frequency loop observed usually in PEMFC impedance spectra (for frequencies $\leq 10\ Hz$) seems thus to be due to (i) macroscopic gas diffusion through the GDL (cf. section 3.6.3), to (ii) microscopic diffusion through a liquid water or electrolyte film covering the pores of the active layer (cf. sections 3.6.3 and 6.3.2), or to (iii) concentration oscillations induced by the AC measuring signal (cf. sections 5.2.2 and 6.3.2). It would be interesting to develop an impedance model allowing to identify simultaneously diffusion losses in the cathode active and backing layers, but the difficulty is that some parameters are correlated, which impedes their independent estimation.

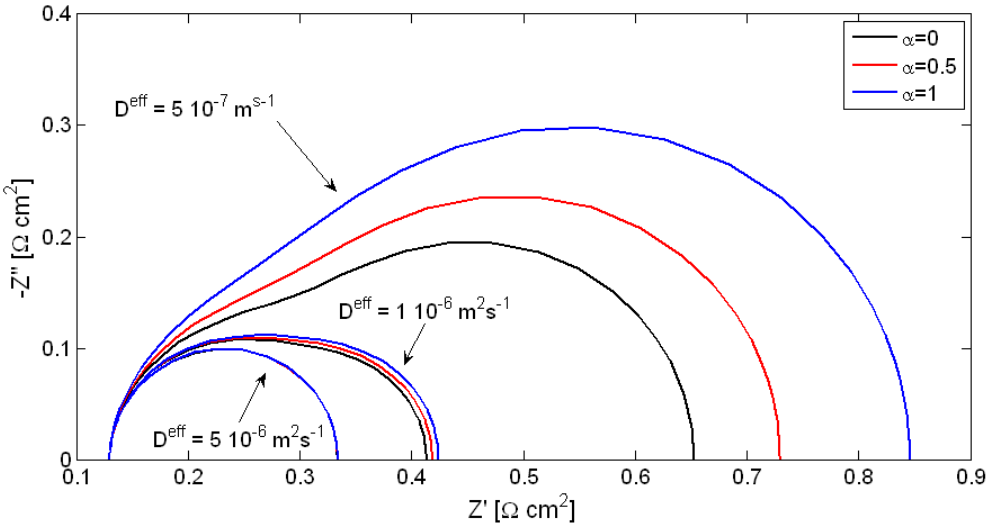


(a)

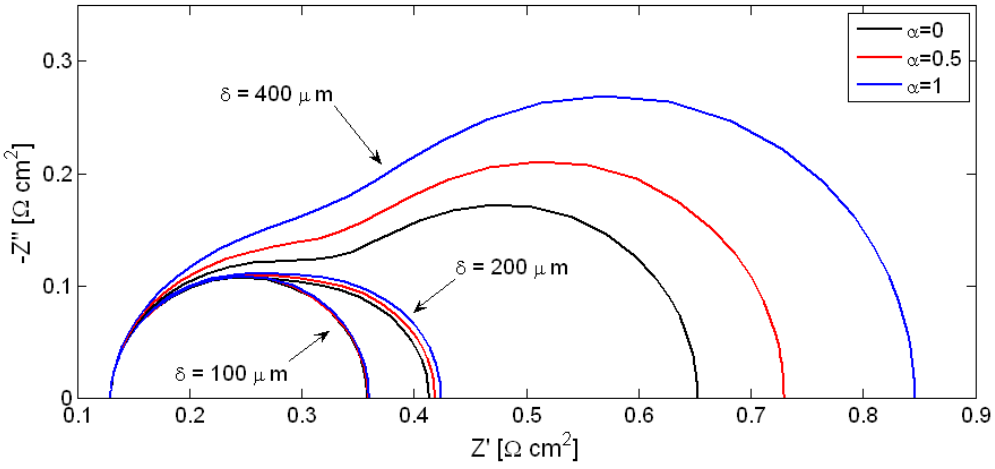


(b)

Figure 4.3: *Simulated impedance spectra in the conditions of Table 4.1 for different values of R_{ct} and C_{dl}: (a) influence of the double-layer capacity C_{dl}; (b) influence of the charge transfer resistance R_{ct}. As expected, the impact of the water transport coefficient on the impedance spectra is not affected by C_{dl} or R_{ct}.*



(a)



(b)

Figure 4.4: *Impedance spectra simulated in the conditions of Table 4.1 for different values of (a) the effective diffusivity D^{eff} and of (b) the diffusion layer thickness δ (b). The impact of the convection becomes more pronounced with increasing δ or decreasing D^{eff}.*

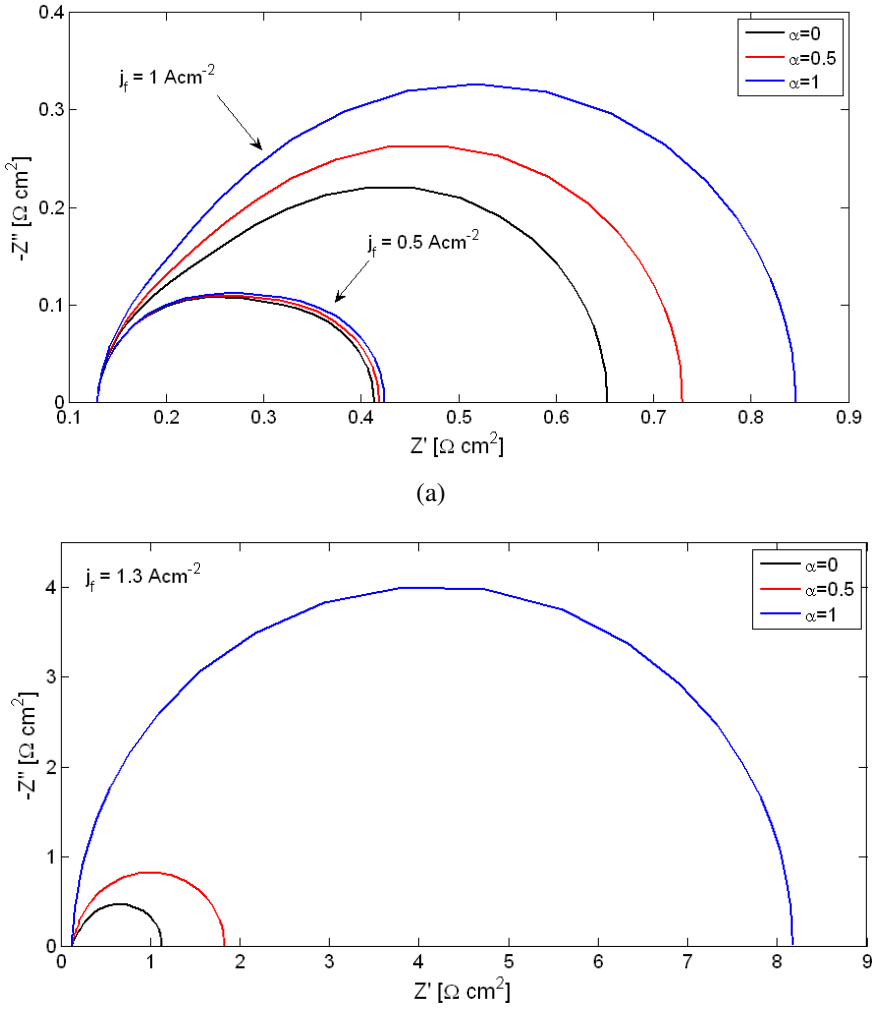


Figure 4.5: *Impedance spectra simulated in the conditions of Table 4.1 for different values of the current density: (a) results obtained at low current densities* $0.5\ Acm^{-2}$ *and* $1\ Acm^{-2}$*; (b) results obtained for a current density* $j_f = 1.3\ Acm^{-2}$*. With increasing current density, the effect of convection increases.*

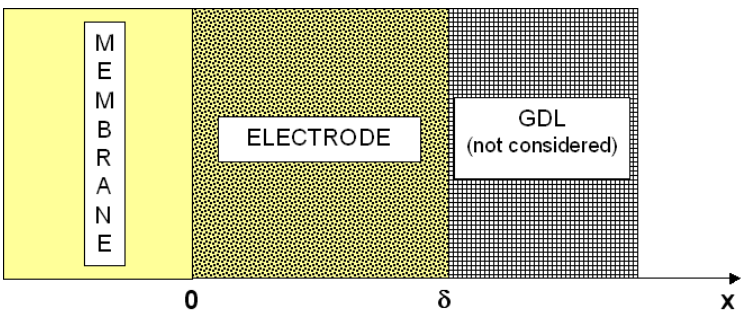


Figure 4.6: *One-dimensional bulk electrode impedance model according to Eikerling and Kornyshev [EK99] taking account of the finite proton conductivity in this layer. The active sites are distributed in the catalyst layer.*

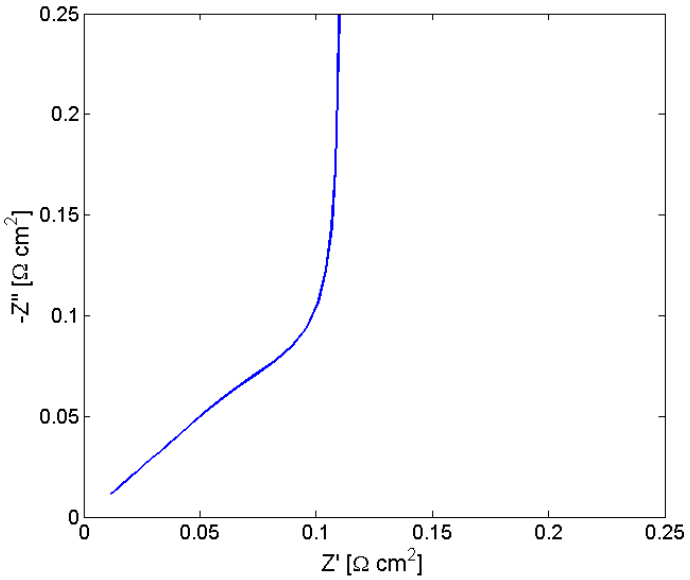


Figure 4.7: *Nyquist plot of an impedance spectrum for a zero faradaic current density determined with the 1D electrode model accounting for a finite proton conduction in the active layer. At high frequencies, the spectrum shows a straight line at* 45°*, which is usually characteristic of diffusion losses and described by a Warburg element.*

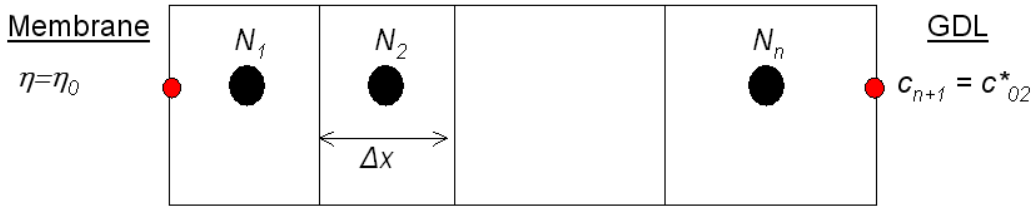


Figure 4.8: *Scheme for the resolution of the complete impedance model: the electrode is divided into n slices. Local model parameters (η_i, c_i) between two successive slices are determined by iteration. The boundary conditions are: at the electrode/membrane interface $\eta = \eta_0$ and at the electrode/GDL interface $c_{O_2} = c^*_{O_2}$.*

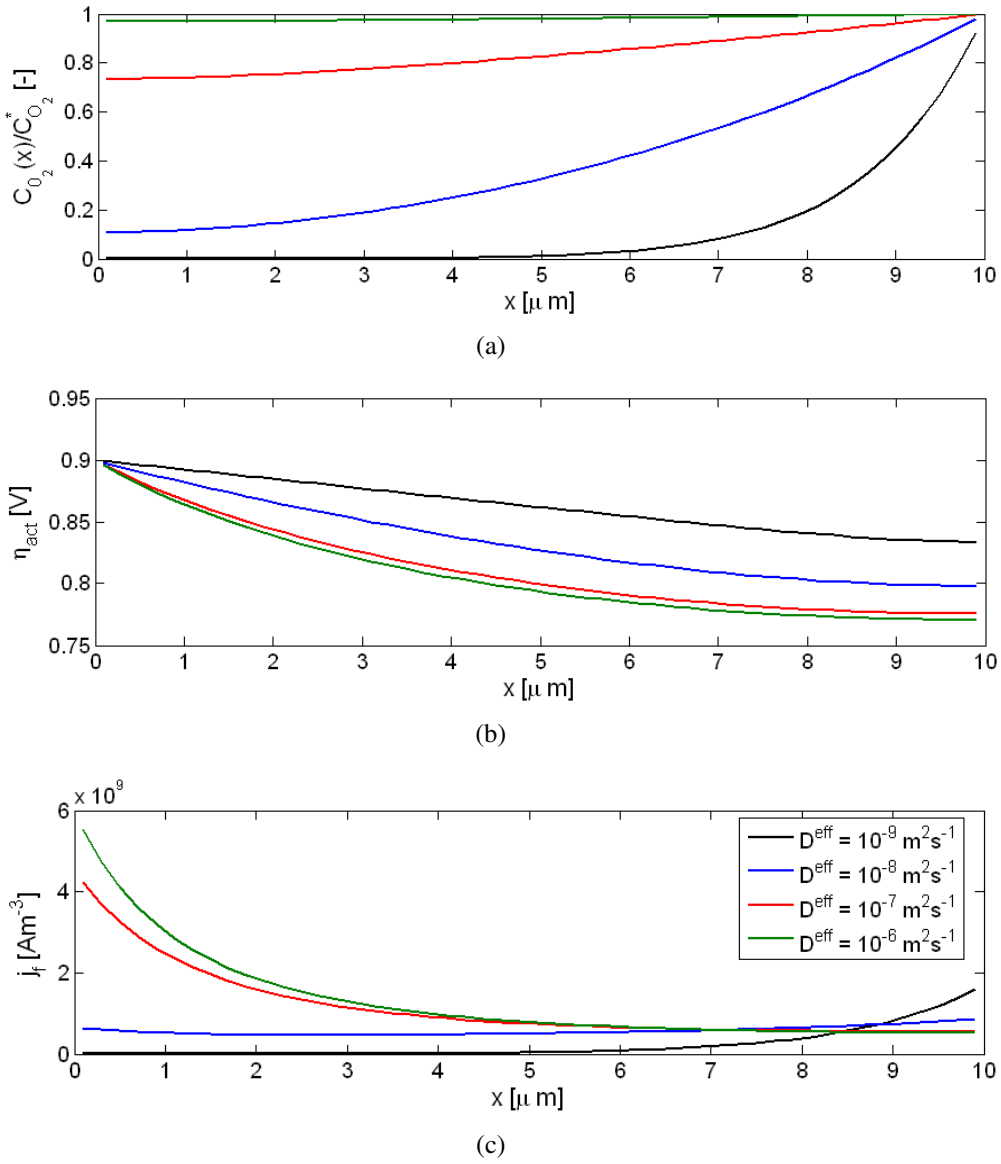


Figure 4.9: *Profiles of the model parameters (a) c_{O_2}, (b) η_{act} and (c) j_f) in the catalyst layer under stationary conditions obtained with the parameters of Table 4.3. The curves show the influence of a decreasing diffusivity D^{eff}.*

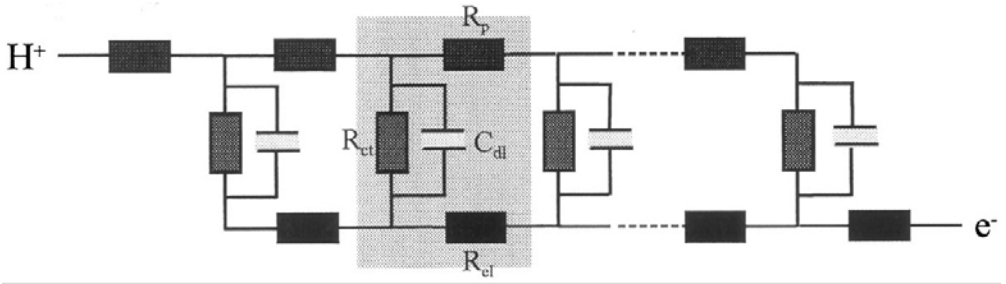
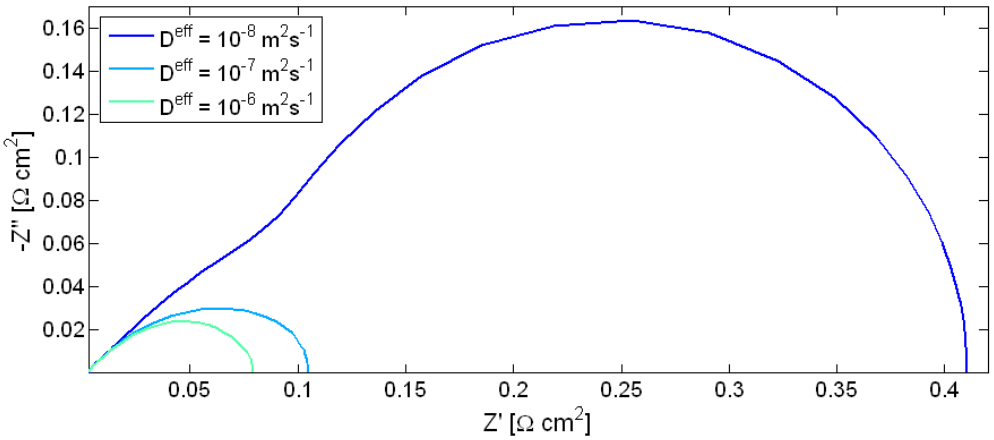
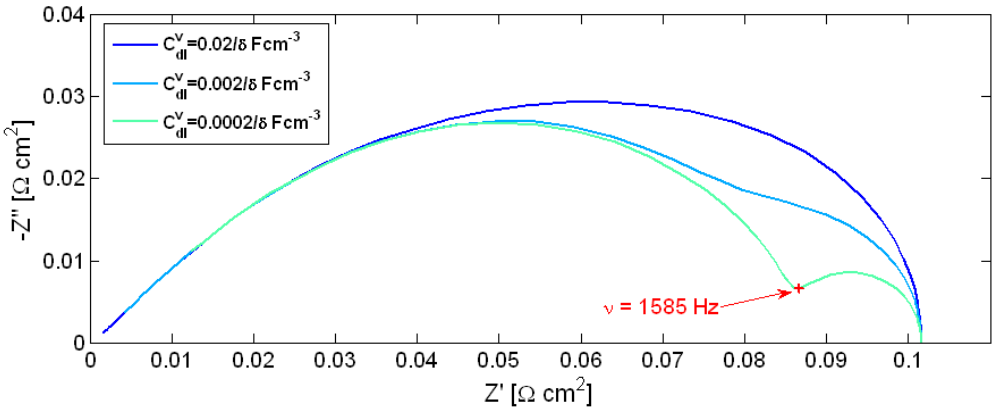


Figure 4.10: *The 1D transmission line equivalent circuit according to Eikerling and Kornyshev [EK99] used for the simulations of the complete impedance of the catalyst layer. The elementary unit of one slice contains a protonic resistance R_p, an electronic resistance R_{el}, a charge transfer resistance R_{ct} and a double-layer capacity C_{dl}. The impedance of O_2 diffusion does not appear in this circuit.*

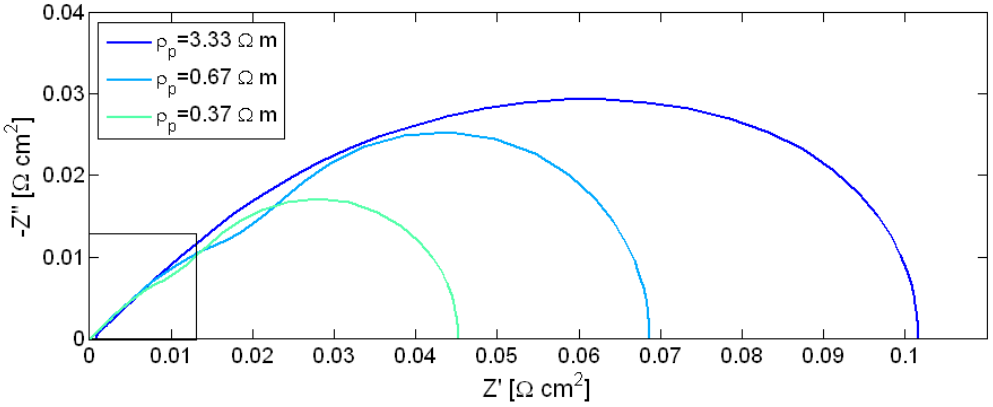


(a)

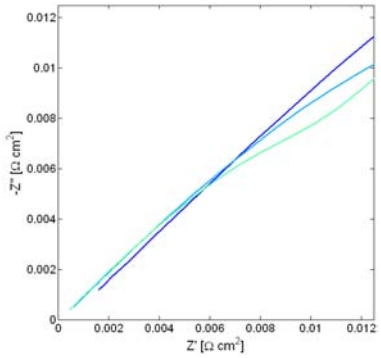


(b)

Figure 4.11: *Impedance spectra determined numerically with the finite-difference method in the operating conditions of Table 4.3: (a) for different values of the effective diffusivity; $C^{v}_{dl} = 0.02/\delta\ Fcm^{-3}$ and (b) for different values of the double-layer capacity; $D^{eff} = 10^{-7}\ m^2 s^{-1}$. Even for important diffusion losses ($D^{eff} = 10^{-8}\ m^2 s^{-1}$), there is no clear separation between the capacitive and diffusive loops, except for very low values of the double-layer capacity. However, this separation does only arise in the high frequency regime.*



(a)



(b)

Figure 4.12: *Impedance spectra simulated the conditions of Table 4.3 for different values of the protonic resistivity ρ_p obtained by varying the Nafion content in equation* (4.34) *between* 0.1 *and* 0.9*: (a) entire spectra, (b) zoom in the high frequency domain. The curves show that proton transport impacts the impedance response over the whole frequency domain. At high frequencies, it leads to the straight line at* 45° *which is extended to lower frequencies with increasing values of ρ_p [EK99]. The high frequency resistance is not affected by the protonic resistance.*

5 Pseudo-2D Impedance Models

In this chapter, all transport phenomena in the direction perpendicular to the electrode apart from diffusion are neglected and the influence of gas consumption and convection in the direction parallel to the electrode is assessed.

In a first approach, oxygen depletion in the gas channel is considered in terms of DC effects: this results in a simple alternative expression to the classical Warburg impedance that accounts for a decrease in the oxygen concentration along the gas channel as alternative boundary condition [MMD+10a].

In order to complete this model, the next step consists in the consideration of oxygen depletion along the air channel in terms of AC effects. The origin of this impedance model comes from on experimental observations of Schneider *et al.* [SFK+07, SKWS07] who put forward that the AC signal that is applied for the impedance measurements entails oxygen concentration oscillations propagating along the air channel and influencing significantly the impedance spectra downstream.

5.1 Effect of Oxygen Depletion along the Air Channel on the Warburg Impedance

5.1.1 Model development

The pseudo-2D model presented in this section considers only oxygen diffusion (*i.e.* the water transport coefficient is equal to 0.5) and the main hypotheses are the same as for the classical one-dimensional Warburg description (cf. chapter 3.2.2). However, three more hypotheses are made (Figure 5.1):

- The mass transfer resistance in the gas channel is neglected.
- Time variations of the oxygen concentration in the channel are neglected.
- The Tafel slope b is assumed uniform between the inlet and the outlet of the air channel.

At the cell inlet, the gases flow in the y-direction along the channel length L; the electrode flat surface is given by $L \times d$. With these assumptions, the model can be considered as pseudo two-dimensional, the first dimension (x-axis) being the direction of oxygen diffusion from the channel to the active layer, whereas the second dimension (y-axis) is the direction of the channel, with a decrease in the time-averaged oxygen concentration.

For sufficiently high current densities and in steady-state, the activation overpotential follows a Tafel law of the form:

$$\eta_{act} = b \ln \frac{j_f(y) c^*_{O_2}}{j_0 c_{O_2}(x=0,y)} \tag{5.1}$$

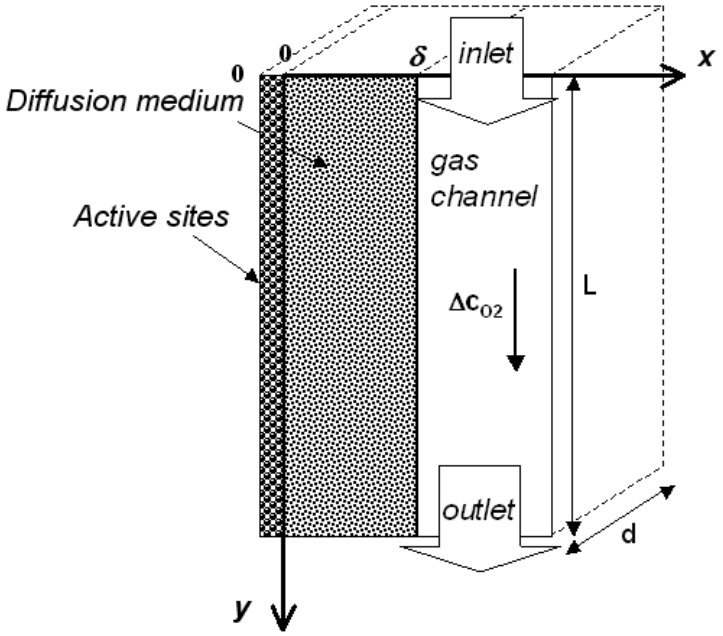


Figure 5.1: *Schematic representation of the pseudo-2D diffusion model that accounts for oxygen concentration depletion in the channel as boundary condition at the GDL/channel interface for the mass transport modeling.*

The faradaic current density $j_f(y)$ and the oxygen concentration $c_{O_2}(x,y)$ can vary along the gas channel, *i.e.* as functions of the y-coordinate (Figure 5.1). The cell-averaged current density j_{cell} is given by:

$$j_{cell} = \frac{I}{Ld} = \frac{1}{L}\int_0^L j_f(y')dy' \tag{5.2}$$

By convention, the activation overpotential and the faradaic current density at the cathode side are usually negative. As for the former approaches, we consider their absolute values: $j_f(y), \eta_{act} > 0$.

In the following, φ_{O_2} and φ_{H_2O} denote the fluxes in the y-direction (in the air channel, in *mol* s^{-1}), while N_{O_2} and N_{H_2O} denote the flux densities in the x-direction (in the gas diffusion layer, in *mol* $s^{-1}m^{-2}$). The molar fluxes of oxygen φ_{O_2} and water φ_{H_2O} in the channel depend also on their y-position: $\varphi_{O_2}(y)$ is equal to the molar fluxes of oxygen at the gas channel inlet $\varphi_{O_2}^{in}$ minus the amount consumed along the cathode:

$$\varphi_{O_2}(y) = \varphi_{O_2}^{in} - \frac{d\int_0^L j_f(y')dy'}{4F} \tag{5.3}$$

Mass transfer along the x-direction is assumed to occur only by diffusion, which means that the global molar flux density in this direction - $N_{O_2} + N_{H_2O}$ - has to be null. As discussed in the previous sections (cf. chapter 4.1), this is a particular case that happens only when half of the water produced at the cathode is evacuated toward the air channel ($N_{H_2O}^{GDL} = j_f(y)/4F$) to compensate for the oxygen flux $N_{O_2} = -j_f(y)/4F$ in the opposite direction. The other half of the water produced

by the cell, as well as the molecules flowing from the anode to the cathode under the effect of the electro-osmotic drag must diffuse through the membrane under the effect of a concentration gradient. As shown in chapter 4.1, a convective flux in the x-direction can have a significant influence on the impedance response and the validity of the Warburg diffusion impedance in PEM fuel cells is not fully confirmed yet. However, since the focus of this model is to study the influence of oxygen consumption on the impedance response, a contribution of a possible convective flux is not considered for the moment. Hence, the water flux along the gas channel φ_{H_2O} is a function of y, given by:

$$\varphi_{H_2O}(y) = \varphi^{in}_{H_2O} + \frac{d\int_0^L j_f(y')dy'}{4F} \tag{5.4}$$

The fuel cell being fed with air, the oxygen mole fraction along the GDL/gas channel interface is given by:

$$\begin{aligned} y_{O_2}(y) &= \frac{\varphi_{O_2}(y)}{\varphi_{O_2}(y)+\varphi_{N_2}+\varphi_{H_2O}(y)} \\ &= \frac{\varphi^{in}_{O_2} - \frac{d\int_0^y j_f(y')dy'}{4F}}{\varphi^{in}_{O_2} - \frac{d\int_0^y j_f(y')dy'}{4F} + \varphi_{N_2} + \varphi^{in}_{H_2O} + \frac{d\int_0^y j_f(y')dy'}{4F}} \end{aligned}$$

And since $\varphi_{N_2} = 4\varphi^{in}_{O_2}$, the above equation simplifies into:

$$y_{O_2} = \frac{S_{O_2} - \frac{d\int_0^y j_f(y')dy'}{I}}{5S_{O_2}(1+H)} \tag{5.5}$$

where $S_{O_2} = \frac{\varphi^{in}_{O_2}}{I/4F}$ stands for the oxygen stoichiometry and $H = \frac{\varphi^{in}_{H_2O}}{\varphi^{in}_{O_2}+\varphi_{N_2}}$ stands for the absolute humidity at the air inlet. Assuming that air is a mixture of ideal gases, the concentration along the air channel/GDL interface ($x = \delta$) can be expressed as:

$$\begin{aligned} c_{O_2}(x=\delta,y) &= \frac{P}{RT} y_{O_2}(y) \\ &= \frac{P}{RT} \frac{S_{O_2} - \frac{d\int_0^y j_f(y')dy'}{I}}{5S_{O_2}(1+H)} \end{aligned} \tag{5.6}$$

The inlet concentration of oxygen in dry air being $c^*_{O_2} = \frac{P}{5RT}$, (5.6) takes the form:

$$c_{O_2}(x=\delta,y) = c^*_{O_2} \frac{IS_{O_2} - d\int_0^y j_f(y')dy'}{IS_{O_2}(1+H)} \tag{5.7}$$

Oxygen diffusion is then described by the Fick equations ((3.23) and (3.24)).

DC solution

Using equation (5.7) as boundary condition at the GDL/channel interface, instead of $c_{O_2}(x=\delta) = c^*_{O_2}$ (3.29) gives:

$$c_{O_2}(x,y) = c^*_{O_2} \frac{IS_{O_2} - d\int_0^y j_f(y')dy'}{IS_{O_2}(1+H)} - \frac{j_f(y)\delta}{4FD^{eff}}\left(1-\frac{x}{\delta}\right) \tag{5.8}$$

For comparison, the oxygen concentration in the classical 1D model is expressed by (3.31):

$$c_{O_2}(x,y) = c^*_{O_2} - \frac{j_{cell}\delta}{4FD^{eff}}\left(1-\frac{x}{\delta}\right) \tag{5.9}$$

The difference between (5.8) and (5.9) lies mainly in the oxygen concentration at the gas channel boundary. In the one-dimensional model, it is constant over the electrode surface, whereas in the pseudo two-dimensional model it varies between the gas inlet and the outlet. Furthermore, the pseudo-2D model takes also account of the air stoichiometry S_{O_2} and of the gas humidification via the absolute humidity H at the fuel cell inlet.

AC solution

In an established dynamic regime, the expressions of the current density and the concentration obey the following conditions:

$$\Delta c_{O_2}(x,y,t) = c_{O_2}(x,y,t) - \langle c_{O_2}(x,y)\rangle_t = \Delta\bar{c}_{O_2}(x,y)\exp(i\omega t) \tag{5.10}$$

$$\Delta j_f(y,t) = j_f(y,t) - \langle j_f(y)\rangle_t = \Delta\bar{j}_f(y)\exp(i\omega t) \tag{5.11}$$

The time-averaged value of the oxygen concentration $\langle c_{O_2}(x,y)\rangle_t$ corresponds to the steady-state solution (5.8):

$$\langle c_{O_2}(x,y)\rangle = c^*_{O_2} \frac{IS_{O_2} - d\int_0^y \langle j_f(y')\rangle_t dy'}{IS_{O_2}(1+H)} - \frac{\langle j_f(y)\rangle_t \delta}{4FD^{eff}}\left(1-\frac{x}{\delta}\right) \tag{5.12}$$

The local concentration oscillation amplitude $\Delta\bar{c}_{O_2}(x,y)$ can be determined in a classical way by resolving Fick's 2nd law with the hypotheses of a surface reaction at $x=0$ (Fick's 1st law) and a confinement of the concentration oscillations to the backing layers ($\Delta\bar{c}_{O_2}(x=\delta,y)=0$), leading to:

$$\Delta\bar{c}_{O_2}(x=0,y,t) = -\frac{\Delta\bar{j}_f(y)}{4F\sqrt{i\omega D^{eff}}}\tanh\left(\sqrt{\frac{i\omega\delta^2}{D^{eff}}}\right)\exp(i\omega t) \tag{5.13}$$

The oxygen transport impedance $Z^{W,loc}(y)$ - general definition: $Z_{c_{O_2}} = -\frac{\partial\eta_{act}}{\partial j_f}\frac{\partial j_f}{\partial c_{O_2}}\frac{\Delta\bar{c}_{O_2}}{\Delta\bar{j}_f}\Big|_{x=0}$ - is thus given by:

$$Z^{W,loc}(y) = b\frac{\tanh\left(\sqrt{\frac{i\omega\delta^2}{D^{eff}}}\right)}{4F\left\langle c_{O_2}(x=0,y)\right\rangle_t\sqrt{i\omega D^{eff}}} \tag{5.14}$$

The oxygen concentration at $(x=0)$ can be determined with (5.12), so that the diffusion impedance (5.14) can also be written under the form:

$$Z^{W,loc}(y) = R_d^{2D}(y)\frac{\tanh\left(\sqrt{i\omega\tau_d}\right)}{\sqrt{i\omega\tau_d}} \tag{5.15}$$

with the low frequency limit $\lim_{\omega\to 0} Z^{2D}_{c_{O_2}}(y) = R_d^{2D}(y)$:

$$R_d^{2D}(y) = \frac{b\delta}{4FD^{eff}\left\langle c_{O_2}(x=0,y)\right\rangle_t}, \text{ in } \Omega cm^2 \tag{5.16}$$

and the characteristic diffusion time τ_d:

$$\tau_d = \frac{\delta^2}{D^{eff}} \tag{5.17}$$

The expression of the pseudo-2D diffusion impedance is close to that of the one-dimensional finite Warburg impedance (3.38):

$$Z_W = R_d^{1D}\frac{\tanh\sqrt{i\omega\tau_d}}{\sqrt{i\omega\tau_d}} \tag{5.18}$$

with

$$R_d^{1D} = \frac{b\delta}{4FD^{eff}\left\langle c_{O_2}(0)\right\rangle_t} \tag{5.19}$$

The characteristic diffusion time τ_d (5.17) is common to both cases. Actually, the difference between both expressions lies in the low frequency limit $R_d^{1D/2D}$: in the pseudo-2D model (5.16), the oxygen concentration $\left\langle c_{O_2}(x,y)\right\rangle_t$ depends on the y position, the gas stoichiometry S_{O_2} and the absolute humidity H, which should improve the precision of the parameter estimation starting from the global diffusion impedance as well as from its local values along the cell surface.

5.1.2 Comparison of the 1D and pseudo-2D approaches

This pseudo-2D model gives access to the global and local mass transfer parameters (δ, D^{eff}) under specified conditions. In the following, a discussion is made about its pertinence and interest. In order to be sure to make representative statements, typical data from the literature [BWJ+05, RUKD08] are used for this numerical analysis. Note that the impedance data identified with our experimental setup (cf. chapter 3 and 6) are of the same order of magnitude.

Local mass transfer

The first data that we are using have been published by Bultel *et al.* [BWJ+05] for a H_2/air PEMFC operating at $60°C$ with an inlet relative humidity RH of about 90%. The main parameters are summarized in Table 5.1.

T_{cell}	$[^\circ C]$	60
RH	$[-]$	0.9
H	$[-]$	0.2
P	$[bar]$	1
S_{O_2}	$[-]$[1]	2 (if not mentioned otherwise)
A	$[cm^2]$	0.5
L	$[cm]$[1]	1
d	$[cm]$[1]	0.5
δ_{GDL}	$[\mu m]$	500 (if not mentioned otherwise)
ε_{GDL}	$[-]$	0.2
D^{eff}	$[m^2 s^{-1}]$	$3.98\,10^{-5} \times \varepsilon_{GDL}^2$
b_{10}	$[V\,dec^{-1}]$	0.22
I	$[A]$	0.25

Table 5.1: *Main parameters used for the analysis of oxygen diffusion [BWJ+05].*

An explicit expression of the diffusion resistance $R_d^{2D}(y)$ can be obtained from (5.16) and (5.12):

$$R_d^{2D}(y) = \frac{b\delta}{4FD^{eff}\frac{IS_{O_2} - d\int_0^y \left\langle j_f(y')\right\rangle_t dy'}{IS_{O_2}(1+H)}c_{O_2}^* - \left\langle j_f(y)\right\rangle_t \delta} \tag{5.20}$$

Figure 5.2 depicts profiles of $R_d^{2D}(y)$ for different values of the air stoichiometry S_{O_2} that are determined with the hypothesis of a constant local current density $\left\langle j_f(y)\right\rangle_t = I/dL$. The influence of a non-uniform current density is analyzed in section 5.2.2. Large variations in the mass transfer resistance along the electrode surface can be observed for the curves in Figure 5.2. Furthermore, the profiles of $R_d^{2D}(y)$ are highly dependent on S_{O_2}.

In the same way as for the studies with the 1D convecto-diffusive model presented in the previous chapter, the local Warburg impedance $Z^{W,loc}$ (5.15) can be used to determine the limiting operating conditions for which no oxygen reaches the reaction interface. Contrarily to the one-dimensional models that give only access to the global parameters, this pseudo-2D description allows to estimate the limiting operating conditions with a spatial resolution along the air channel. In the following, the limiting air stoichiometry $S_{O_2}^{lim}(\delta)$ will be derived as a function of the diffusion layer thickness δ. Below $S_{O_2}^{lim}(\delta)$ no oxygen reaches the membrane/electrode interface near the gas channel outlet $c_{O_2}(x=0, y=L) = 0$. As a consequence, R_d^{2D} tends toward infinity for S_{O_2} approaching $S_{O_2}^{lim}(\delta)$. The expression of $S_{O_2}^{lim}(\delta)$ can be easily deduced from (5.8):

$$S_{O_2}^{lim} = \frac{c_{O_2}^*}{c_{O_2}^* - \frac{j_{cell}\delta}{4FD^{eff}}(1+H)} \tag{5.21}$$

In the example of Figure 5.2, the value of $S_{O_2}^{lim}(\delta = 500\ \mu m)$ is about 1.44 and for $S_{O_2} = 1$, there is no oxygen reaching the electrode/membrane interface beyond $y_{lim}/L = 0.69$. The analysis of the profiles makes it possible to determine in which conditions the diffusion impedance can be described by a one-dimensional model (when, for instance, the maximum relative variation over

[1] Hypothetical values added to complete the analysis.

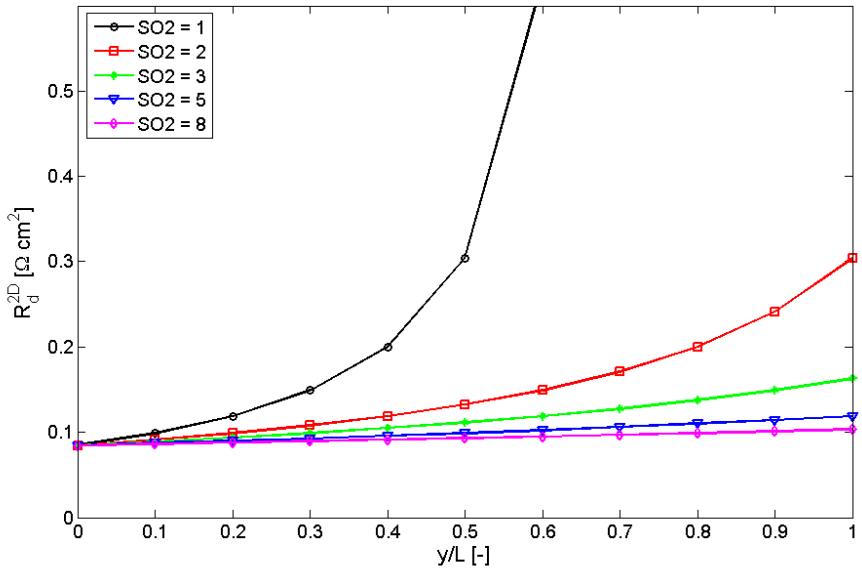


Figure 5.2: *Profiles of the diffusion resistance between the air inlet and outlet for air stoichiometries comprised between* 1 *and* 8 *obtained with* (5.20) *and the values of Table 5.1. In the considered operating conditions, the curves tend toward infinity for* $S_{O_2} < 1.44$ *according to* (5.21).

the electrode length $\Delta R_d^{2D}(L) = \left| \frac{R_d^{2D}(L) - R_d^{2D}(0)}{R_d^{2D}(0)} \right|$ is below 10%). In the conditions of Table 5.1, a one-dimensional behaviour would be achieved only for air stoichiometries S_{O_2} above 11.

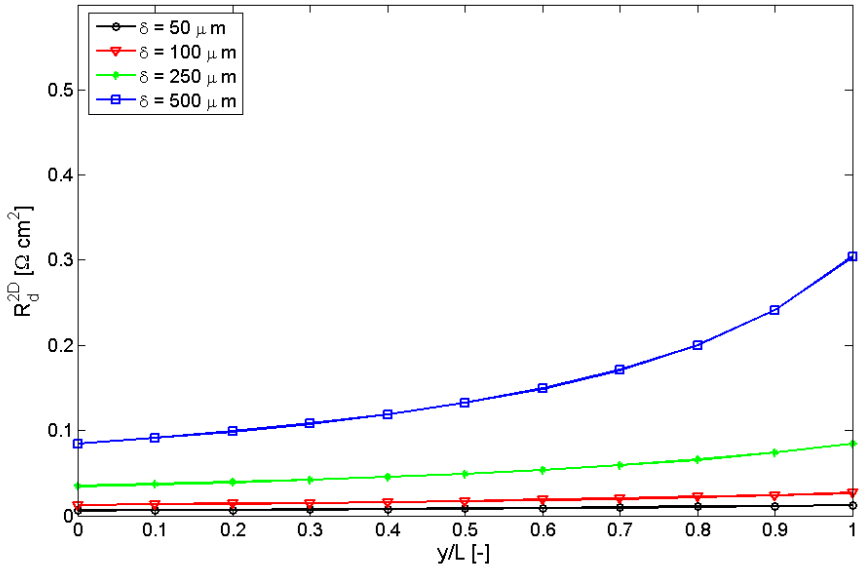


Figure 5.3: *Profiles of* $R_d^{2D}(y)$ *between the air inlet and outlet for different values of the diffusion layer thickness and for a fixed air stoichiometry* $S_{O_2} = 2$ *(starting from data of Bultel et al. [BWJ+05], Table 5.1).*

The curves in Figure 5.3 confirm that the thickness of the diffusion layer has a significant impact on the mass transport. When $S_{O_2} = 2$, reducing its initial value ($\delta = 500\ \mu m$) by one half decreases

significantly the mass transfer limitations: $\Delta R_d^{2D}(L)$ is reduced by a factor of 1.7. When $S_{O_2} = 4$, $\Delta R_d^{2D}(L)$ is still reduced by a factor of 1.3 when dividing the diffusion layer thickness by one half.

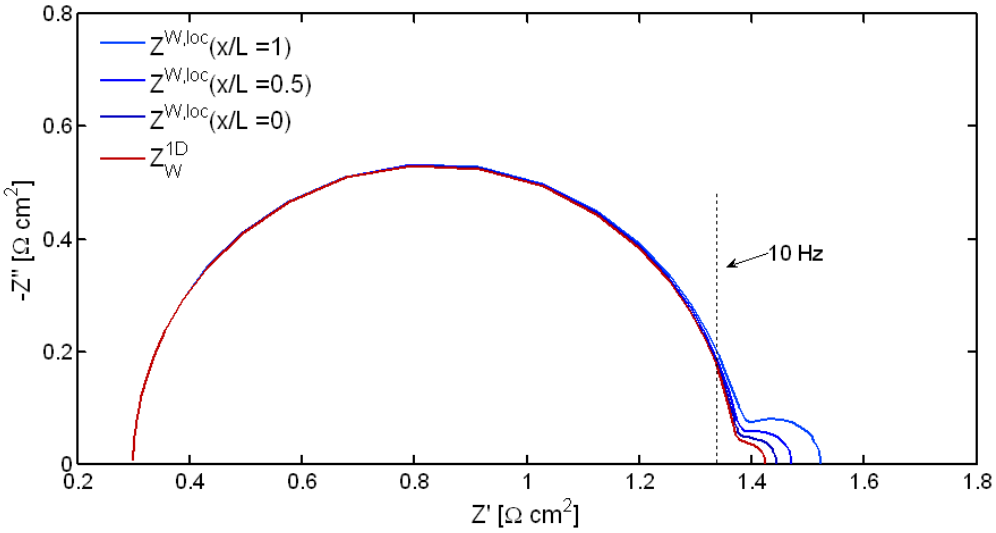


Figure 5.4: *Comparison between a PEMFC impedance spectra obtained using a classical finite Warburg element Z_W* (5.18) *and spectra obtained using the local Warburg impedance $Z^{W,loc}$ accounting for oxygen depletion* (5.15),(5.16) *and* (5.20). *The PEMFC is modeled using the Randles equivalent circuit (Figure 5.5). All the electrical parameters, except the diffusion impedance, are taken from experimental data measured by Rubio et al.* (5.20).

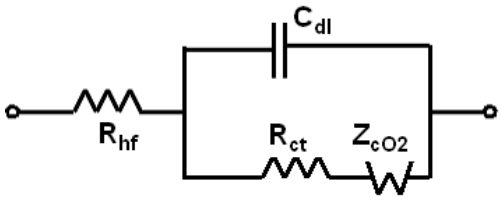


Figure 5.5: *MEA equivalent circuit used for the simulation of the impedance spectra in Figure 5.4.*

Another way to estimate the effect of oxygen depletion is to compare the impedance spectra obtained with a usual finite Warburg impedance Z_W (5.18)-(5.19) and those obtained with the expression of the local Warburg impedance $Z^{W,loc}$ derived above (5.15)-(5.16). Figure 5.4 shows the evolution of local impedance spectra simulated in the operating conditions of Table 5.1 with an air stoichiometry $S_{O_2} = 3$ by the use of a Randles equivalent circuit (Figure 5.5) in which the mass transport impedance $Z_{c_{O_2}}$ is expressed either by Z_W or by $Z^{W,loc}$. The values of the impedances in the equivalent circuit - except the diffusion resistance - are taken from experimental data of Rubio *et al.* [RUKD08] measured with a 100 cm^2 area single cell in similar working conditions. For modeling purpose, they are kept constant along the air channel in order to put forward the effects of variations in the value of $R_d^{2D}(y)$ on the cell impedance: $R_{hf} = 2.6\ m\Omega$, $R_{ct} = 10.6\ m\Omega$, $C_{dl} = 0.25\ F$ and $\tau_d = 0.751\ s$ [RUKD08]. The cell impedance is simulated for frequencies ranging from 1 mHz to 10 kHz.

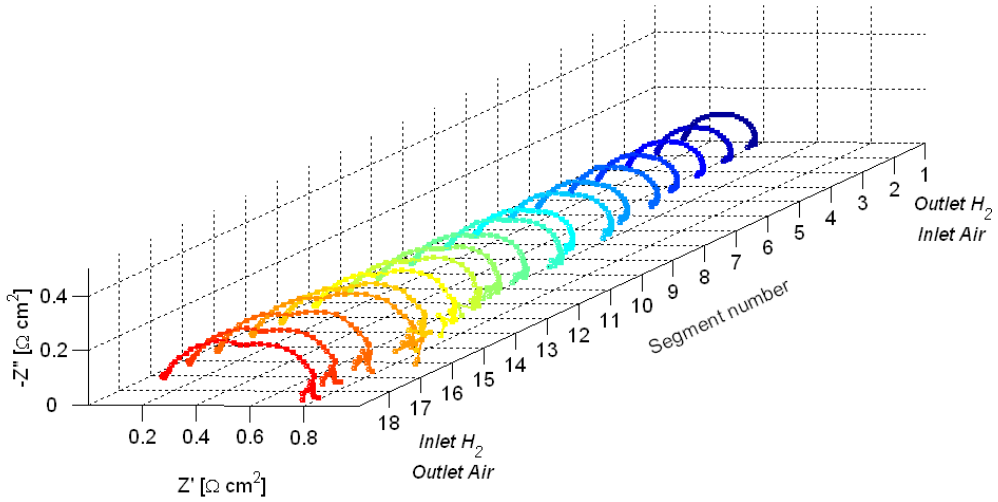
As expected, the impedance spectra do not depend on the mass transfer impedance at frequencies above 10 Hz [SZWG96]. In the low frequency range however ($< 10\ Hz$), the higher values of the mass transfer resistance $R_d^{2D}(y)$ close to the air channel outlet impact significantly the spectra. Note that the size of the low frequency loop corresponding to the 1D finite Warburg impedance with $c_{O_2}(x=\delta) = c^*_{O_2}$ (*i.e.* with dry air) is smaller than that obtained with $Z^{W,loc}$ at the channel inlet $Z^{2D}_{c_{O_2}}(y/L=0)$ because the latter accounts for the air humidification ($c_{O_2}(x=\delta, y=0) = c^*_{O_2}/(1+H) = 0.83\, c^*_{O_2}$ - Table 5.1).

An experimental validation of these numerical predictions is beyond the scope of this chapter and will be presented in chapter 6.2. Nevertheless, a first qualitative experimental validation of the conclusions of Figure 5.4 is given in Figure 5.6 showing experimental impedance spectra measured along the air channel of cell 1 (mono-channel single PEMFC). The fuel cell was fed in counter-flow with dry hydrogen ($S_{H_2} = 1.2$) and humidified air ($S_{air} = 3$, $RH_{air} = 0.78$) and operated at a mean current density $\langle j_{cell} \rangle_t = 0.5\ Acm^{-2}$ [MMD$^+$10b].

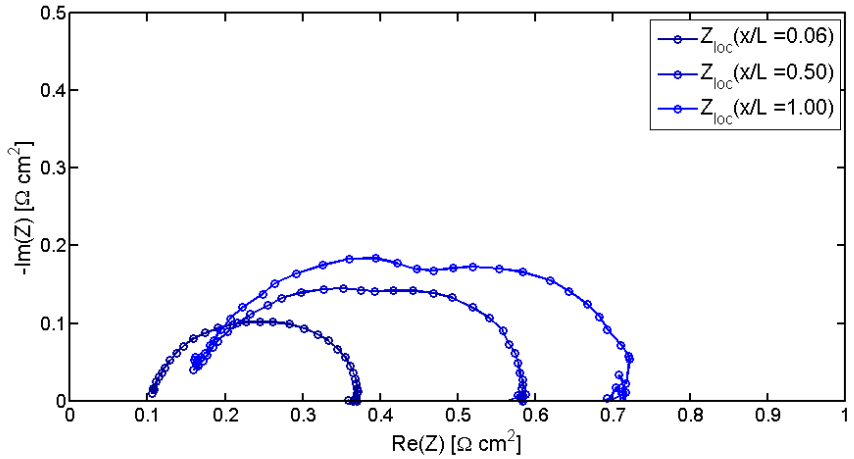
The experimental data in Figure 5.6(a) show the appearance and enlargement of a separate low frequency loop along the air channel, which is consistent with the expectations of increasing oxygen transport limitations from the inlet to the outlet of the channel. The low frequency loop cannot be distinguished in the impedance spectra of the first segments (Figures 5.6(a) and 5.6(b)), probably because of the relatively large high frequency impedance compared to the (low frequency) mass transfer impedance at these locations. With increasing segment number, the LF loop increases in size and reaches its maximum at the air channel outlet. This could probably be explained by a liquid water accumulation in the flow field which is the highest at the cathode outlet where the water is evacuated.

In order to assess these hypotheses, the experimental and numerical data have to be compared to each other: starting from expressions (5.15)-(5.16), the identification of the local mass transfer parameters [MMD$^+$10b] yields values that are in a typical range expected for gas diffusion in PEMFC backing layers layers. However, the results also show that for quantitatively reliable results, AC effects like those recently put forward by Schneider *et al.* [SFK$^+$07, SKWS07] have to be included in the oxygen transport model. Furthermore, the possible accumulation of liquid water near the air channel outlet (which should affect also the characteristic diffusion time τ_d) is not considered in this description. In this context, the following chapter presents a pseudo-2D convecto-diffusive impedance model that accounts for AC effects on the impedance spectra.

In conclusion, the simple modifications of the hypotheses that lead to the expression of the classical Warburg impedance show that in usual conditions, oxygen consumption along the channel has a quite significant impact on the low frequency loop of fuel cell impedance spectra: the usual 1D approach is satisfying only for large values of the air stoichiometry which do not correspond to usual operating conditions. The local Warburg impedance accounting for oxygen depletion in terms of DC effects (consumption) presents a more realistic description. However, as oxygen concentration oscillations induced by alternative currents seem to impact the impedance spectra downstream along the air channel, this phenomenon should be included in the mass transport impedance model.



(a)



(b)

Figure 5.6: *Experimental impedance spectra measured along the cathode of a segmented PEMFC fed with dry hydrogen ($S_{H_2} = 1.2$) and humidified air ($S_{air} = 3$, $RH_{air} = 0.78$) in counter-flow with a mean current density $\langle j_{cell} \rangle_t = 0.5\ Acm^{-2}$ [MMD+10b]. (a) 3-D plot of the local impedance spectra. (b) 2-D plot of the local experimental impedance spectra of segments 1 ($y/L = 0.06$), 9 ($y/L = 0.5$) and 18 ($y/L = 1$). The results show clearly the appearance and enlargement of the separate low frequency loop along the air channel.*

5.2 2D Diffusion Impedance Model Accounting for Convection along the Channel Direction

The usual expression of the Warburg impedance derives from a 1D description of the oxygen diffusion through the cathode that assumes a constant and uniform oxygen concentration in the channel. Actually, the validity of this hypothesis ifs not justified for several reasons: first of all, we showed in the previous section that the (time-averaged) concentration is not uniform along the channel length due to oxygen consumption by the fuel cell, which has significant effects on the local impedance spectra [MMD+10a]. Furthermore, Schneider et al. [SFK+07, SKWS07] recently pointed out experimentally that the low frequency loop seems to be - at least to some extent - due to the propagation of oxygen concentration oscillations resulting from the current variations ΔI that are used to perform the impedance measurements.

In the following, a pseudo 2D convecto-diffusive impedance model is described which accounts for the propagation of concentration oscillations by convection and presents thus a theoretical approach to complement the experimental results of Schneider *et al.* [SFK+07, SKWS07]. With this impedance description, it is possible to discriminate between the contributions of diffusion losses and of the propagation of oxygen concentration oscillations along the gas channel to the low frequency loop in PEMFC impedance spectra. It results from this approach that under usual working conditions, the concentration oscillations seem to be the main phenomenon being at the origin of the low frequency loop. In this context, a non-dimensional number is proposed to check if this "convection" effect is negligible or not, as a function of the operating conditions and over the whole frequency range.

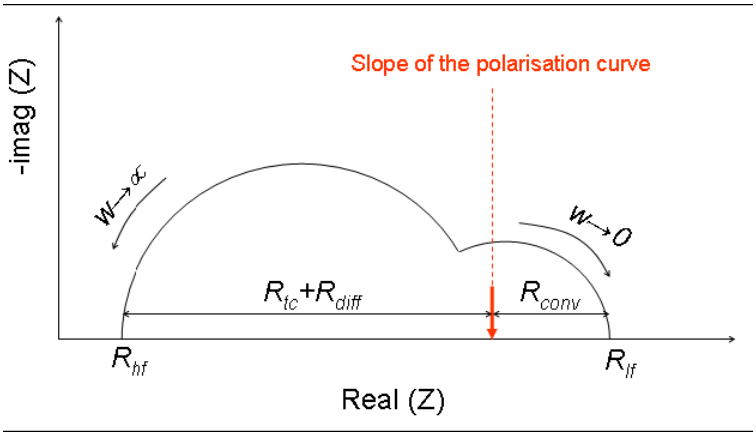


Figure 5.7: *Commonly observed discrepancy between the low frequency limit of the impedance spectra of a PEMFC fed with air and the steady-state resistance derived from the slope of the polarization curve.*

Furthermore, this 2D convecto-diffusive impedance model yields a possible explanation of a commonly mentioned shortcoming in EIS: the discrepancy between the low frequency impedance and the steady-state resistance calculated starting from the slope of the polarization curve [RO07]. As shown in Figure 5.7, the low frequency impedance is always higher than the slope of the polarization curve. This hypothesis is assessed experimentally in chapter 6.4.

5.2.1 Development of the pseudo-2D (or $1+1D$) model

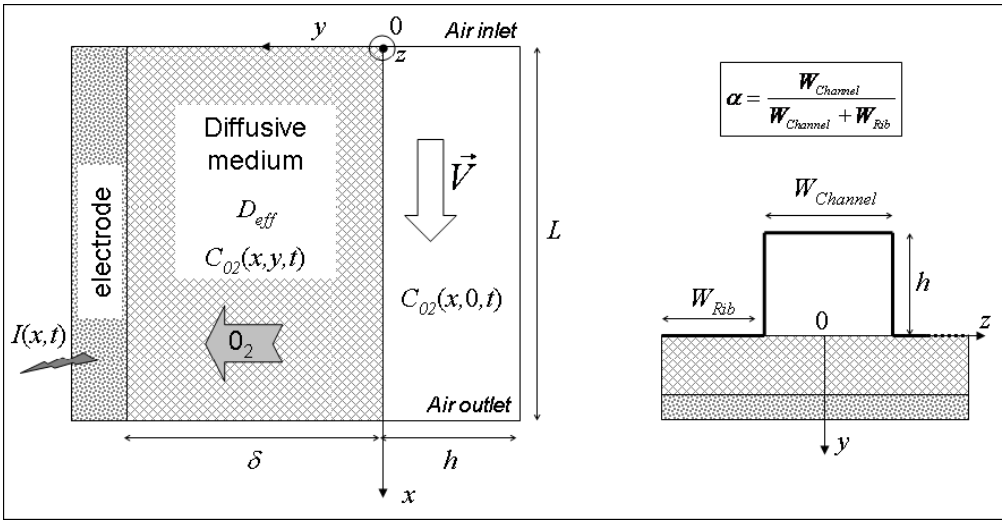


Figure 5.8: *Geometry of the pseudo-2D convecto-diffusive impedance model: the x-axis is directed along the channel length and the y-axis in the direction perpendicular to the cell plane. α is the channel to active surface ratio, h the channel depth, L the channel length and V the flow velocity depending on the air stoichiometry.*

The 2D geometry is represented in Figure 5.8. The MEA is represented by a surface electrode separated from the air channel by a diffusive medium. Note that in the most general form of the model, no assumption is made about the main resistance for oxygen diffusion: the diffusive medium can be a carbon cloth, as well as a water or an electrolyte layer coating the platinum particles. In the first case, the current density is calculated by reference to the MEA flat surface whereas the second case corresponds to a microscopic approach where the reference surface is that of the active sites: consequently, the current density must be divided by the electrode roughness factor γ.

The main model hypotheses are:

- The anode is neglected.
- The cell voltage E is assumed uniform.
- The flow velocity V is constant along the channel length. As long as the air is not saturated, we assume that each mole of oxygen consumed by the fuel cell is replaced by one mole of vapor (whereas one mole of liquid water passes through the membrane from the cathode to the anode) [CCD+09]. When the air is saturated, the gentle decrease in the flow velocity due to oxygen consumption is neglected (cf. appendix B.1.2).
- The diffusion of O_2 is Fickian.
- The diffusion of O_2 along the channel direction $(0x)$ is neglected compared to the convective transport. Therefore, this model is called "pseudo-2D".
- Under the effect of the air flow, the oxygen concentration is assumed to be uniform over the channel depth (in y-direction).

- For the sake of simplicity, the high frequency resistance R_{hf}, the Tafel slope b, the diffusion medium thickness δ, the oxygen effective diffusivity D^{eff} and the double layer capacity of the cathode C_{dl} are considered as uniform. Actually, the numerical method for solving the equation system is unchanged if their values are constant over each (numerical) segment of the fuel cell. This assumption is also useful if the model is used for the estimation of the profiles of these (local) parameters along the electrode by using a segmented cell [MLC+08, MMD+10a, PBSM11].

From a local point of view, the equations governing the cathode potential and current density are those describing the Randles equivalent circuit (Figure 5.5):

$$E(t) = E_0 - R_{hf}\, j(x,t) - \eta_{act}(x,t) \tag{5.22}$$

$$\eta_{act}(x,t) = b \ln\left[\frac{j_f(x,t) c^*_{O_2}}{j_0 c_{O_2}(x, y=\delta, t)}\right] \tag{5.23}$$

$$j(x,t) = j_f(x,t) + C_{dl}\frac{\partial \eta_{act}(x,t)}{\partial t} \tag{5.24}$$

Where $j(x,t)$ is the local current density (which can be measured using a segmented cell [MLC+08, MMD+10c, DLM+10]), $j_f(x,t)$ the faradic current density and $\eta_{act}(x,t)$ the voltage loss resulting from oxygen depletion and reaction kinetics, derived from a Tafel law. The local current density $j(x,t)$ is the sum of the faradic current density $j_f(x,t)$ and the capacitive current density $j_c(x,t)$, expressed as: $j_c(x,t) = C_{dl}\frac{\partial \eta_{act}}{\partial t}$.

The equation governing the oxygen concentration inside the diffusion layer is the 2nd Fick law which takes the form:

$$\frac{\partial c_{O_2}(x,y,t)}{\partial t} = D^{eff}\frac{\partial^2 c_{O_2}(x,y,t)}{\partial y^2} \tag{5.25}$$

with two boundary conditions:

1. At the channel interface $(y = 0)$:

$$\left.\frac{\partial c_{O_2}}{\partial t}\right|_{y=0} + V \left.\frac{\partial c_{O_2}}{\partial x}\right|_{y=0} = \frac{D^{eff}}{\alpha h}\left.\frac{\partial c_{O_2}}{\partial y}\right|_{y=0} \tag{5.26}$$

Where V is the flow velocity in the channel, D^{eff} the effective oxygen diffusivity in the considered medium, and h the channel depth. α stands for the ratio between the channel/GDL interface and the active surface (Figure 5.8). Two cases can be considered:

- In the case of a macroscopic diffusive medium:

$$\alpha = \frac{W_{channel}}{W_{channel} + W_{rib}} \tag{5.27}$$

$\alpha = 1$ if the channel rib surface is negligible; in many cases $\alpha = 0.5$.

- In the case of a microscopic diffusion medium:

$$\alpha = \frac{W_{channel}}{\gamma(W_{channel} + W_{rib})} \tag{5.28}$$

2. At the electrode interface ($y = \delta$):

$$D^{eff} \left.\frac{\partial c_{O_2}}{\partial y}\right|_{y=\delta} = -\frac{j_f}{4F} \tag{5.29}$$

Only the first boundary condition (5.26) differs from the classical Warburg approach, where the oxygen concentration at $y = 0$ is constant. As shown in section 5.1, the decrease of the time-averaged oxygen concentration along the air channel contributes significantly to the diffusion impedance; this can be accounted for thanks to a very simple modification of the boundary condition at the channel/GDL interface (5.30) that corresponds to that of the local Warburg impedance (5.7):

$$c_{O_2}(x, y = 0, t) = c_{O_2}^{channel}(x,t) = c_{O_2}^{*} \frac{IS_{O_2} - d\int_0^x j_f(x')dx'}{IS_{O_2}(1+H)} \tag{5.30}$$

AC effects are also significant and they have to be considered through equation (5.26), as shown in the following. As for the previous model approaches, the AC signal of each variable X is decomposed into its steady-state value $\langle X \rangle_t$ and a small sinusoidal component of amplitude $\Delta\bar{X}$ which leads to the following expressions:

$$\begin{aligned}
E(t) &= \langle E \rangle_t + \Delta\bar{E}\exp(i\omega t) \\
j(x,t) &= \langle j(x) \rangle_t + \Delta\bar{j}(x)\exp(i\omega t) \\
j_f(x,t) &= \langle j_f(x) \rangle_t + \Delta\bar{j}_f(x)\exp(i\omega t) \\
\eta_{act}(x,t) &= \langle \eta_{act}(x) \rangle_t + \Delta\bar{\eta}_{act}(x)\exp(i\omega t) \\
c_{O_2}(x,y,t) &= \langle c_{O_2}(x,y) \rangle_t + \Delta\bar{c}_{o_2}(x,y)\exp(i\omega t)
\end{aligned} \tag{5.31}$$

DC solution

In steady state, the capacitive current is null and the cathode potential (according to equations (5.22) - (5.24)) is given by:

$$\langle E \rangle_t = E_0 - R_{hf} \langle j(x) \rangle_t - b \ln\left[\frac{\langle j(x) \rangle_t c_{O_2}^{*}}{j_0 \langle c_{O_2}(x, y = \delta) \rangle_t}\right] \tag{5.32}$$

- In the case of an under-saturated flow ($P_{H_2O} < P_{sat}$), the steady-state oxygen concentration at the electrode interface is written (cf. appendix B.1.1):

$$\langle c_{O_2}(x, y = \delta) \rangle_t = \frac{c_{O_2}^{*}}{1+H}\left[1 - \frac{\int_0^x \langle j(x') \rangle_t dx'}{S_{O_2}\int_0^L \langle j(x') \rangle_t dx'}\right] - \frac{\langle j(x) \rangle_t \delta}{4FD^{eff}} \tag{5.33}$$

- And in the case of a saturated flow ($P_{H_2O} = P_{sat}$) (cf. appendix B.1.2):

$$\langle c_{O_2}(x, y=\delta)\rangle_t = c^*_{O_2}\left(1-\frac{P_{sat}}{P}\right)\left[1-\frac{\int_0^x \langle j(x')\rangle_t\, dx'}{S_{O_2}\int_0^L \langle j(x')\rangle_t\, dx'}\right] - \frac{\langle j(x)\rangle_t\,\delta}{4FD^{eff}} \tag{5.34}$$

Remember that $c^*_{O_2}$ is the dry air inlet oxygen concentration (21% of P/RT), S_{O_2} the air stoichiometry and P_{sat} the vapor saturation pressure depending on temperature (1.33). H stands for the absolute humidity at the inlet, that is to say for the ratio between the water and dry air molar flow rates. In equations (5.33) and (5.34), the oxygen stoichiometric coefficient S_{O_2} can be replaced by the flow velocity V, according to:

$$S_{O_2} = \frac{\varphi^{channel,in}_{O_2}}{\frac{\langle j\rangle_{x,t}}{4F}S_{diff}} = \frac{c^{in}_{O_2} V S_{channel}}{\frac{\langle j\rangle_{x,t}}{4F}S_{diff}} \tag{5.35}$$

where $\langle j\rangle_{x,t}$ is the time- and space-averaged value of the current density (over the whole cell), $S_{diff} = L \times W_{channel}/\alpha$ the diffusion area perpendicular to the electrode surface and $S_{channel} = h \times W_{channel}$ the channel section (Figure 5.8). $c^{in}_{O_2} = c^*_{O_2}\frac{1}{1+H}$ stands for the oxygen concentration at the channel inlet (cf. (B.9) in appendix B.1).

Inserting these expressions in equation (5.35) yields finally:

$$S_{O_2} = \frac{c^*_{O_2} V \alpha h}{\frac{\langle j\rangle_{x,t}}{4F}L(1+H)} \;\rightarrow\; V = S_{O_2}\frac{\langle j\rangle_{x,t} L(1+H)}{4F c^*_{O_2}\alpha h} \tag{5.36}$$

AC solution

The solution of the system (5.25),(5.27)-(5.30) leads to the expression of the local Warburg impedance:

$$\frac{\Delta\bar{c}_{O_2}}{\Delta\bar{j}_f}(y=\delta) = -\frac{\tanh\left(\sqrt{\frac{i\omega}{D^{eff}}}\delta\right)}{4F\sqrt{i\omega D^{eff}}};\; \frac{\Delta\eta_{act}}{\Delta j_f} = \frac{b}{\langle j(x)\rangle_t} + \frac{b}{\langle c_{O_2}(x,\delta)\rangle_t}\frac{\tanh\left(\sqrt{\frac{i\omega}{D^{eff}}}\delta\right)}{4F\sqrt{i\omega D^{eff}}} \tag{5.37}$$

The first term of the second equation ($b/\langle j(x)\rangle_t$) is the charge transfer resistance. The second term - which depends on the diffusive medium characteristics - is the local Warburg impedance $Z^{W,loc}$ (5.14) accounting for oxygen consumption in contrast to the classical 1D Warburg impedance that assumes a constant concentration along the electrode. It depends thus also on the steady-state local concentration at the electrode - given by (5.33) or (5.34) - and thus on the oxygen stoichiometry.

The solution of the system that takes into account the propagation of oxygen concentration oscillations (5.25)-(5.29) yields the 2D local concentration impedance (the detailed derivation is given in appendix B.2):

$$\frac{\Delta\bar{c}_{O_2}}{\Delta\bar{j}_f}(x,\delta) = -\frac{\frac{e^{-\frac{x}{X}}}{4F\alpha hV}}{\cosh^2\left(\sqrt{\frac{i\omega}{D^{eff}}}\delta\right)}\frac{\int_0^x e^{\frac{x'}{X}}\Delta\bar{j}_f(x')dx'}{\Delta\bar{j}_f(x)} - \frac{\tanh\left(\sqrt{\frac{i\omega}{D^{eff}}}\delta\right)}{4F\sqrt{i\omega D^{eff}}} \tag{5.38}$$

$$\text{with } X = \frac{V}{i\omega + \frac{1}{\alpha h}\sqrt{i\omega D^{eff}}\tanh\left(\sqrt{\frac{i\omega}{D^{eff}}}\delta\right)} \tag{5.39}$$

The first term on the right hand side of equation (5.38) tends to zero when V tends to infinity. In this case, the expression of $\Delta\bar{c}_{O_2}/\Delta\bar{j}_f$ corresponds the classical Warburg approach (5.37). One can also notice that this term depends on the upstream variations of the faradic current density $\Delta j_f(x')$ (with $x' \leq x$), which are unknown.

As a consequence, solving this equation is not as simple as for the classical approach. Actually, there is no explicit solution but as shown in appendix B.2, the local conductance can be expressed as:

$$\frac{-\Delta\boldsymbol{J}}{\Delta E} = \left(\boldsymbol{M}_c\boldsymbol{L}_j + \boldsymbol{M}_j\right)^{-1}\boldsymbol{M}_c\boldsymbol{P} \tag{5.40}$$

where $\Delta\boldsymbol{J} = \left[\Delta\bar{j}(x_1)\ \Delta\bar{j}(x_2)\ \ldots\ \Delta\bar{j}(x_n)\right]^t$ is a column vector of the local amplitudes of the current density oscillations, the electrodes being discretized into n segments from the air inlet to the outlet. In practice, these segments can correspond to those of a segmented cell for an experimental validation of the analytical results [PBSM11]. Note that the negative sign has to be used in (5.40) in order to take account of the phase shift between the current and the voltage variations. $\boldsymbol{P}$ is a column vector and $\boldsymbol{M}_c$, $\boldsymbol{L}_j$ and $\boldsymbol{M}_j$ are $n \times n$ matrices; their elements are functions of the position along the air channel x_i $(1 \leq i \leq n)$, of the five local impedance parameters $R_{hf}(x_i)$, $b(x_i)$, $\delta(x_i)$, $D^{eff}(x_i)$ and $C_{dl}(x_i)$, of the flow velocity V, and of the oscillation angular frequency $\omega = 2\pi\nu$.

Asymptotic study

When the frequency tends toward zero, and if the current density is uniform, it is possible to derive a simple analytical expression of the global impedance (see appendix B.3):

$$\frac{\Delta\bar{E}}{-\langle\Delta\bar{j}\rangle_x} = R_{hf} + \frac{b}{\langle j\rangle_{x,t}} + \frac{b}{4F\left\langle c_{O_2}(y=\delta)\right\rangle_{x,t}}\left(\frac{L}{2\alpha hV} + \frac{\delta}{D^{eff}}\right) \tag{5.41}$$

According to equation (5.41), the global impedance is the sum of the high frequency resistance R_{hf}, the charge transfer resistance $b/\langle j\rangle_{x,t}$ and the mass transfer resistance which is made up of two terms:

- One term results from mass transfer through the diffusive media and depends on the time- and space-averaged value of the oxygen concentration, and therefore on the air stoichiometry:

$$R_{diff} = \frac{b}{4F\left\langle c_{O_2}(y=\delta)\right\rangle_{x,t}}\frac{\delta}{D^{eff}} \tag{5.42}$$

- The second term is a consequence of convection along the air channel:

$$R_{conv} = \frac{b}{4F\left\langle c_{O_2}(y=\delta)\right\rangle_{x,t}} \frac{L}{2\alpha h V} \tag{5.43}$$

This convection resistance (that does not exist in steady-state) could explain the difference between the low frequency resistance and the slope of the polarization curve (cf. Figure 5.7); it is proportional to a time constant defined by L/V which characterizes the air flow through the cathode compartment (from the channel inlet to the outlet). This hypothesis will be studied in more detail in chapter 6.4.

Equation (5.41) shows that convection or inertial effects linked to the oscillations of the oxygen concentration can be neglected - over the whole frequency range - if:

$$\frac{L}{2\alpha h V} \ll \frac{\delta}{D^{eff}} \tag{5.44}$$

That is to say, if the non-dimensional number M is much lower than 1:

$$M = \frac{LD^{eff}}{2V\alpha h\delta} = \frac{1}{2}\frac{c^*_{O_2}/(1+H)}{S_{O_2}\left\langle j\right\rangle_{x,t}/4F}\frac{D^{eff}}{\delta} \ll 1 \tag{5.45}$$

Criterion (5.45) has to be checked after the estimation of δ and D^{eff} with the classical Warburg model.

5.2.2 Comparison of diffusive and convective effects on the cell impedance response

For the sake of simplicity, all the results presented in this section were obtained assuming that the main resistance for oxygen diffusion appears in the gas diffusion layer. In practice, it could also result from oxygen transport through the micro-porous layer, the macro-pores of the electrode, as well as through a water or liquid layer coating the catalyst particles. The discussion about the main origin(s) of the oxygen diffusion resistance with the pseudo-2D impedance models derived in this chapter is out of the scope of this section and is presented in chapter 6.3.2. A first estimation of the diffusing limiting layer with the classical 1D Warburg impedance is presented in chapter 3.6.3. Similarly, all parameters - including the Tafel slope $b(x)$, the exchange current density $j_0(x)$ and the high frequency resistance $R_{hf}(x)$ - except the oxygen concentration are set to standard values (Table 5.2). This amounts to neglect the variations of these parameters as functions of the local current density, as well as of other local effects like membrane hydration. It is assumed that the cathode is fed with air.

Steady-state solution

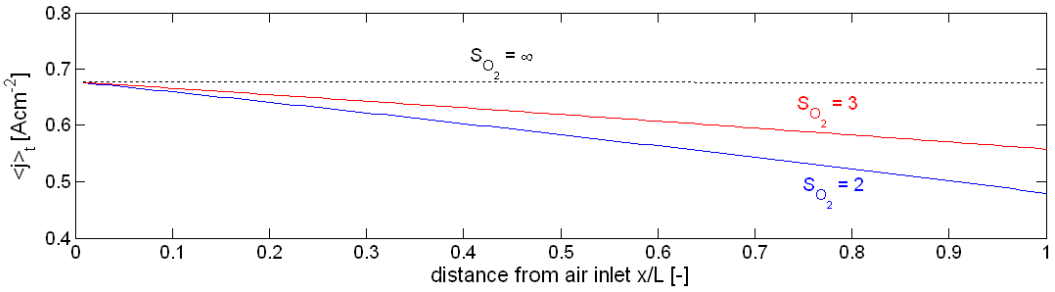
First of all, in the absence of experimental results, it is necessary to simulate the steady-state profile of the current density $\left\langle j(x)\right\rangle_t$ to be able to calculate the steady state concentration profile at the electrode $\left\langle c_{O_2}(x,\delta)\right\rangle_t$ required to construct the spectrum. For usual stoichiometric ratios

[2] macroscopic exchange current density: $\gamma = 100$

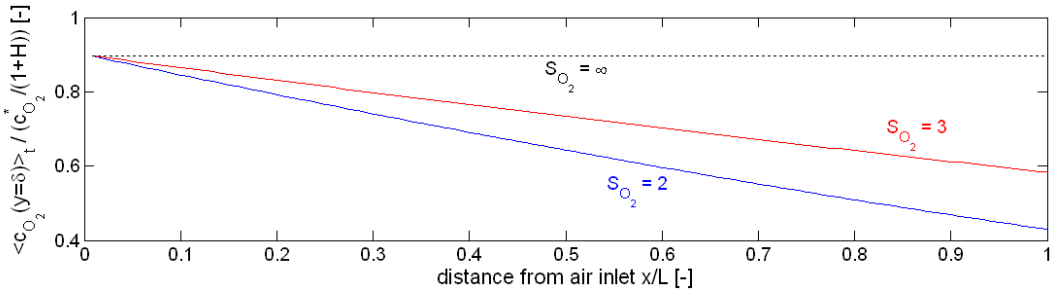
[3] corresponds to a RH at 60°C of 60%

High frequency resistance	R_{hf}	$[\Omega cm^2]$	0.1	[SZWG96, RUKD08]
Tafel slope	b	$[mV]$	50	[ABDO98]
Exchange current density[2]	j_0	$[Acm^{-2}]$	$1.5\,10^{-4}$	[SPK05a]
Diffusive medium thickness	δ	$[\mu m]$	200	[CCD+10]
Oxygen effective diffusivity	D^{eff}	$[m^2 s^{-1}]$	$3.5\,10^{-5} \times 0.4^2$	[BSL02, SPK05a]
Double layer capacity	C_{dl}	$[Fcm^{-2}]$	0.02	[SZWG96, RUKD08]
Temperature	T	$[°C]$	60	
Absolute pressure	P	$[bar]$	1	
Channel length	L	$[cm]$	30	
Channel depth	h	$[mm]$	0.7	
Channel to active surface ratio	α	$[-]$	0.5	
Absolute humidity	H	$[-]$	0.13[3]	
Potential	E	$[V]$	0.5	[SZWG96]
Amplitude of potential variation	$\Delta E/E$	$[-]$	0.05	

Table 5.2: *Values of the parameters used for the analysis of the influence of convective versus diffusive effects on the impedance response of a PEMFC. The impedance parameters are set to standard values that correspond also to those identified with our PEMFC (cf. experimental results in chapters 3 and 6) in similar operating conditions. The parameters defining the cell geometry correspond to those of cell 2 (cf. chapter 3.5.1).*



(a)



(b)

Figure 5.9: *Steady-state current density (a) and normalized oxygen concentration at the reaction interface (b) along the channel for three values of the air stoichiometric ratio.*

($S_{O_2} = 2,3$), the current density (obtained from (5.32) and (5.33)) decreases significantly (Figure 5.9) as a result from oxygen consumption along the air channel (the other parameters remaining uniform): oxygen depletion is responsible for a drop of about one third of the current density between inlet and outlet for an air stoichiometry of $S_{O_2} = 2$.

Dynamic solution

The transient solutions are calculated starting from the steady-state profiles of current density and of oxygen concentration. The *local impedances* are derived according to (5.40):

$$Z_i = \frac{\Delta\bar{E}}{-\Delta\bar{j}(x_i)}_{1\leq i\leq n} \tag{5.46}$$

The *global impedance* is obtained by dividing the potential amplitude by the averaged value of the local current density amplitudes:

$$Z_G = \frac{\Delta\bar{E}}{\frac{-1}{n}\sum_{1}^{n}\Delta\bar{j}(x_i)} \tag{5.47}$$

Note that the global impedance is not equal to the average of the local values.

Figure 5.10 shows local and global spectra obtained with the classical 1D Warburg approach and with the "convecto-diffusive" model described above for different values of the stoichiometric ratio S_{O_2}. In the case of the Warburg model, the steady-state oxygen concentration is chosen equal to the average of the local concentrations calculated with the 2D model in steady-state conditions - that is to say $\langle c_{O_2}(\delta)\rangle_{x,t} = \left(\langle c_{O_2}(0,\delta)\rangle_t + \langle c_{O_2}(L,\delta)\rangle_t\right)/2$ - so that the diffusion losses due to a finite stoichiometry are accounted for. Of course, for an infinite stoichiometry, the problem becomes one-dimensional: all the curves are superimposed (this case is not drawn).

The curves of Figure 5.10 show that the convection effect is mainly significant at low frequencies ($\nu \leq 10\,Hz$), even for values of the air stoichiometry as high as 10. This effect can be difficult to detect experimentally because when a low frequency arc due to diffusion limitations is already present, convection does not create a new arc but tends to widen the latter, which is usually attributed only to the diffusion impedance. In the shown example, the effective diffusion coefficient corresponds to a gaseous diffusion in the GDL without significant diffusion limitations: therefore, no low frequency arc can be observed in the spectra obtained with the classical Warburg model. The LF loops derived with the convecto-diffusive impedance are created exclusively by convection effects. It can be noticed that the M number - which is inversely proportional to the air stoichiometry - reaches 2.9 when $S_{O_2} = 2$, which means that the impact of convection on the low frequency impedance is about 3 times more significant than that of diffusion. The spectra show that even for a stoichiometry of 3 ($M = 1.8$), neglecting the convection effect would lead to an overestimation of the diffusive losses. Furthermore, it can be seen on these curves that the decrease of the LF loop following an increase of the air stoichiometry is not only due to an enhanced diffusion, but also to a large extent to the decrease of convective effects.

The slope of the polarization curve should correspond to the intersection of the red curve relative to the Warburg model with the real axis (Figure 5.10). For almost all positions along the channel, the low frequency resistance obtained with the convecto-diffusive model is higher than the slope of the polarization curve, which is linked to the AC measuring method: the low frequency resistance measured by EIS is not strictly equal to the slope of the polarization curve because of the propagation of oxygen concentration oscillations by convection. This discrepancy will be analyzed in more detail in chapter 6.4.

At the local level, the convection effect is more significant near the outlet of the channel ($x/L = 1$) because the concentration of oxygen depends on upstream processes. The oxygen concentration is constant at the inlet ($x/L = 0$), but it is subjected to fluctuations downstream which depend on

the diffusive media characteristics (δ and D^{eff}), the angular frequency ω, the flow velocity V, ... Here, the diffusive loop at the inlet is smaller than the Warburg loop because the global Warburg spectrum is calculated with a steady-state oxygen concentration (in equation (5.37)) equal to the space-average value between the inlet and outlet.

Figure 5.11 shows a comparison between local and global impedance spectra obtained with the convecto-diffusive model Z^{osc} and the local Warburg impedance $Z^{W,loc}$ accounting for oxygen depletion along the channel (5.15). The spectra are plotted in the conditions of Table 5.2 for two stoichiometries: $S_{O_2} = 3$ and $S_{O_2} = 10$. The local oxygen concentration at the electrode corresponds to the steady-state solution, which is the same for both approaches $\langle c_{O_2}(x=0,y)\rangle_t$ (equation (5.12) or (5.33)), since convection has an influence only in AC conditions. The local current density was calculated by an iterative procedure with a Tafel law starting from the local concentrations.

In both cases, the low frequency loop increases from the air inlet to the outlet. At the channel inlet ($x = 0$), the spectra derived with Z^{osc} and $Z^{W,loc}$ coincide: this is consistent, since AC effects appear only downstream in the channel. However, over the whole electrode length, the low frequency arcs obtained with the local Warburg impedance $Z^{W,loc}$ remain smaller than those obtained with the convecto-diffusive impedance Z^{osc} accounting in addition for oxygen concentration oscillation. The same difference can be observed for the global impedance spectra determined with both models. Even at air stoichiometries as high as 10, the discrepancy between the spectra obtained with both approaches remains significant. These curves indicate that AC induced concentration oscillations propagating along the channel by convection have a predominant impact on the LF impedance and have thus to be taken into account for an accurate description of the mass transport impedance in fuel cells.

Globally, over the whole channel length, the impedance calculated with the convecto-diffusive model shows a low frequency arc larger than the arc obtained with the classical or the local Warburg model accounting for oxygen consumption, even for rather high values of the air stoichiometry. As a result, it can be concluded that neglecting convection effects along the air channel direction in the mass transport impedance model would most probably lead to an overestimation of the diffusion thickness δ and an underestimation of the effective diffusion coefficient D^{eff}. Applying the values of the parameters given in Table 5.2 to the criteria defined by equation (5.44) gives:

$$\frac{\delta}{D^{eff}} \approx 40\ sm^{-1} \qquad \text{and} \qquad \frac{L}{2h\alpha V} = \frac{c^*_{O_2}/(1+H)}{2S_{O_2}\langle j\rangle_{x,t}/4F} \approx \frac{210}{S_{O_2}}\ sm^{-1} \tag{5.48}$$

As a consequence, assuming that the convection effects are negligible when the M number is lower than $1/10$ would mean that the Warburg model is valid only for stoichiometries higher than 50 in these conditions. Of course, the greater the diffusion resistance[4] (δ/D^{eff}), the lower the convection effect for a given stoichiometry.

Figure 5.12 illustrates these results by showing the oscillations of oxygen concentration at the electrode ($\Delta\bar{c}_{O_2}(x,\delta)$) as functions of the frequency and of the position, the air stoichiometric ratio S_{O_2} being set to 2. The dotted curves correspond to the assumption that the concentration in the channel is constant but not uniform: this description is two-dimensional because it takes account of the decrease of the time-averaged concentration along the channel, but $\langle c_{O_2}(x,y)\rangle_t$ is deliberately kept constant in time, *i.e.* upstream AC effects are not considered. This corresponds to a description of the diffusion impedance by the local Warburg model presented in section 5.1. The

[4] δ/D^{eff} should not be mistaken for the diffusion (electrical) resistance R_d (3.39).

plain curves show the oxygen concentration simulated with the 2D convecto-diffusive accounting for the propagation of the concentration oscillations at the velocity of the air flow in the channel direction. The two upper graphs of Figure 5.12 show the modulus of the oscillations at the electrode $|\Delta\bar{c}_{O_2}(x,\delta,\omega)|/c^*_{O_2}$ as a function of the frequency (on the left) and of the normalized distance from the inlet (on the right). The two lower graphs show the corresponding phase $\Phi(\Delta\bar{c}_{O_2}(x,\delta,\omega)$. The oscillation of the potential $\Delta\bar{E}$ defines the origin of the phases.

For low frequencies ($\nu \rightarrow 0\ Hz$), the oxygen concentration at the electrode is in phase with the potential (that is in phase opposition with the current density), this for the two models and any of the positions along the channel. Indeed, a 1D diffusion medium is a low-pass filter. However, it is noticeable that there is an amplification of the concentration oscillation from the inlet to the outlet depicted by the convecto-diffusive model. Here, the amplitude of this amplification near the outlet for standard operating conditions is of the same order of magnitude as the 1D-diffusive oscillation itself. It results from the upstream oxygen consumption, which creates a wave of concentration carried toward the outlet with the flow velocity V, even if the potential oscillation is low. Actually, this effect does not depend on the amplitude of the potential oscillation (here, $\Delta\bar{E}/E = 5\%$).

When the frequency approaches the convection frequency V/L, the convecto-diffusive model shows concentration oscillations that may increase and decrease as a function of the position (see the red curve on the right for $\nu = 10\ Hz$), while the classical model still predicts the local 1D diffusion oscillation of concentration. This phenomenon does not become negligible when the convection frequency V/L is exceeded, but only for values higher than the diffusion frequency D^{eff}/δ^2 (see the black curve on the right for $\nu = 100\ Hz$).

In conclusion, the pseudo-2D convecto-diffusive model allowed to confirm the experimental observations of Schneider *et al.* [SFK$^+$07, SKWS07] that the LF loop in PEMFC impedance spectra is due to a large extent to concentration oscillation propagating along the flow fields by convection. Global and local impedance spectra obtained with this model showed that the low frequency loop is significantly affected by convective processes in the direction of the channel, which could lead to misinterpretations of the diffusion limitations when this phenomenon is not considered. The 2D convecto-diffusive impedance has been analytically derived without introducing any unknown parameter. This expression could explain why the low frequency resistance is generally higher than the slope of the polarization curve. This will be studied in more detail in chapter 6.4. A non-dimensional number was proposed to check if this "convection" effect is negligible or not as a function of the working conditions and over the whole frequency range.

An important assumption upon which the model is based is that the diffusion or dispersion along the channel direction is neglected. In practice, the tortuosity of the channels leads to a "turbulent diffusion" along the direction of the channel that can smoothen the concentration wave.

5.3 Conclusions about the Two-Dimensional Mass Transport Models

In the above sections, the influence of phenomena appearing parallel to the electrode surface on the impedance pattern of a PEMFC is investigated. Two impedance expressions are derived accounting for gas consumption and for the effect of convective phenomena along the channel. As oxygen transport is considered simultaneously in the directions perpendicular and parallel to the electrode surface, these models are two-dimensional.

The first approach is a simple improvement of the classical 1D Warburg impedance that accounts

for oxygen depletion along the gas channel. Starting from experimental data from the literature, numerical simulations show that conclusions about the origin of the low frequency loop of PEMFC impedance spectra are significantly affected by oxygen consumption along the electrode. Oxygen consumption in the channel direction has thus to be taken into account in the oxygen transport impedance modeling. The results also put forward the existence of a critical value of the air stoichiometry below which, close to the air channel exit, no oxygen can access to the active layer. This diffusion impedance model does not take account of time dependent current variation effects on the gas concentration. However, experimental proofs have been brought by Schneider *et al.* [SFK$^+$07, SKWS07] that they influence significantly the measured impedance spectra and they should be included in the impedance modeling.

Thus, concentration oscillations that are induced by the measuring signal and that propagate along the gas channel by convection are implemented in a second approach. The resulting 2D convecto-diffusive impedance expression highlights the influence of these AC induced phenomena on the pattern of global and local impedance spectra. It can be pointed out that the concentration oscillations influence the impedance spectra mainly in the low frequency domain and neglecting them would lead to misinterpretations of the diffusion losses. Furthermore, this approach yields a possible explanation of the commonly observed discrepancy between the low frequency limit of the impedance spectra and the slope of the polarization curve. A non-dimensional number M (5.45) allows to estimate the contribution of these "convective" phenomena to the LF impedance as a function of the working conditions and over the whole frequency range.

These pseudo-2D mass transport impedance models allow to estimate in which conditions a description by a classical one-dimensional diffusion impedance is justified. Furthermore, they warn about misinterpretations of the origin of the low frequency loop observed in experimental impedance spectra that are caused by oxygen depletion along the channel direction. This opens up the following perspectives:

- The interpretation of experimental impedance spectra with the pseudo-2D impedances in order to assess the improvement obtained with these models. The results of these investigations are presented in the following chapter. In more detail, the experimental studies concern the identification of the possible oxygen diffusion limiting layer, as well as the phase (liquid or gas) in which oxygen diffuses. Comparing the results obtained with the local Warburg impedance with those of the convecto-diffusive impedance allows to quantify experimentally the impact of concentration oscillations on the interpretation of impedance spectra. Furthermore, the hypothesis can be confirmed that the propagation of concentration oscillations is mainly at the origin of the discrepancy between the low frequency limit of the impedance spectra and the slope of the polarization curve.

- It has to be mentioned that several improvements have still to be brought to the expression of the oxygen transport impedance: the above presented approaches are based on simple descriptions of mass transport mechanisms in the direction perpendicular to the electrode surface (pure diffusion, presence of a reaction interface). All phenomena investigated in the one-dimensional models presented in chapter 4, *i.e.* the influence of a possible convective flux due to water vapor evacuation and the fact that the reaction sites are distributed along the electrode depth, are neglected. It would be interesting to develop a mass transport impedance model that accounts for all these phenomena. However, the complexity of such a model

would most probably not allow the independent estimation of its main parameters starting from experimental results.

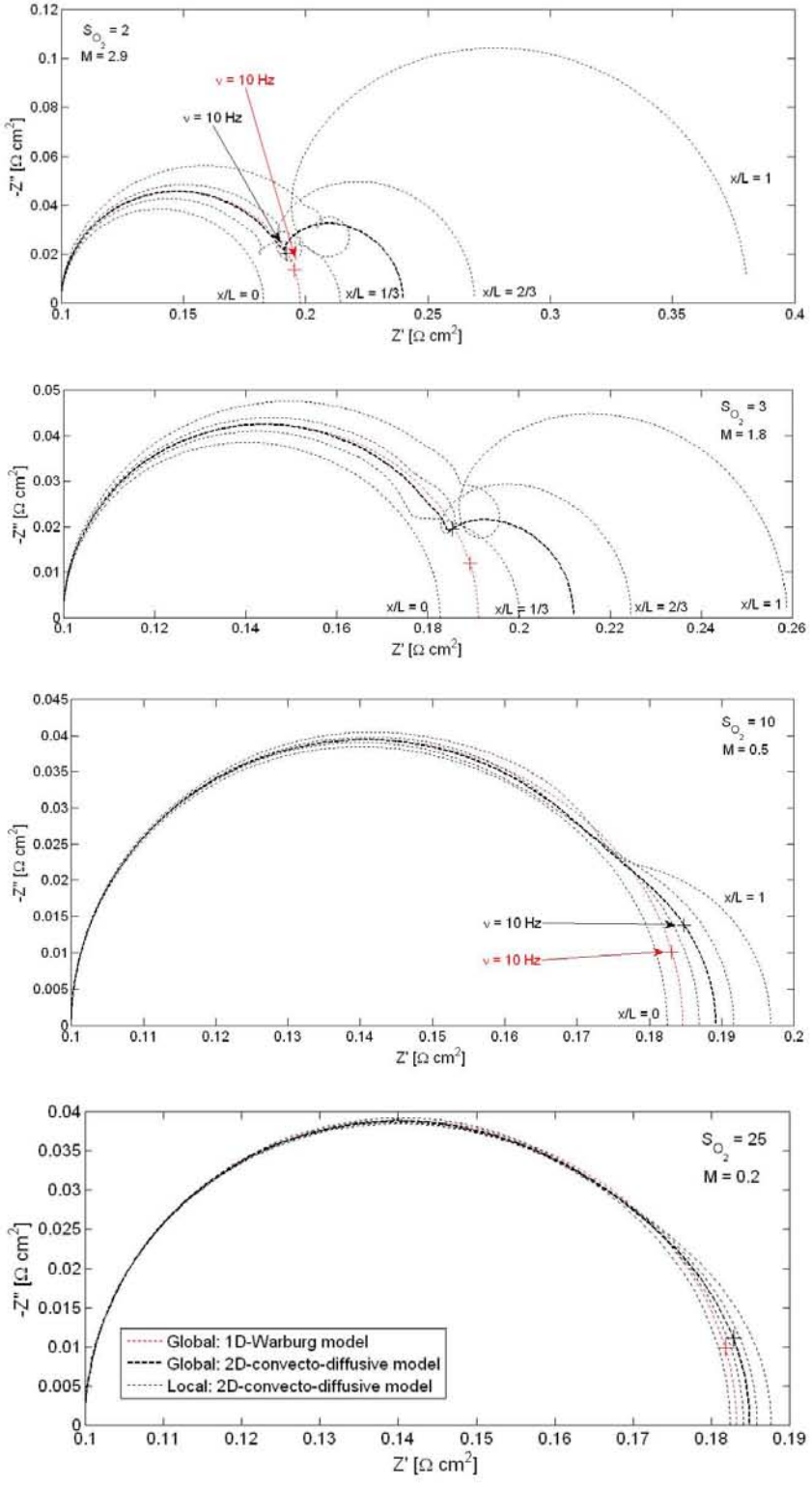


Figure 5.10: *Local and global impedance spectra derived from the convecto-diffusive model and the classical 1D Warburg expression (equation (5.37) with* $\langle c_{O_2}(\delta)\rangle_{x,t} = \left(\langle c_{O_2}(0,\delta)\rangle_t + \langle c_{O_2}(L,\delta)\rangle_t\right)/2$*) for* 4 *different values of* S_{O_2} *comprised between* 2 *and* 25 *(*$M = 1.4, 0.8, 0.2, 0.1$*). The intersection of the red curves (Warburg model) with the real axis should give the slope of the polarization curve, which is not the case in practice.*

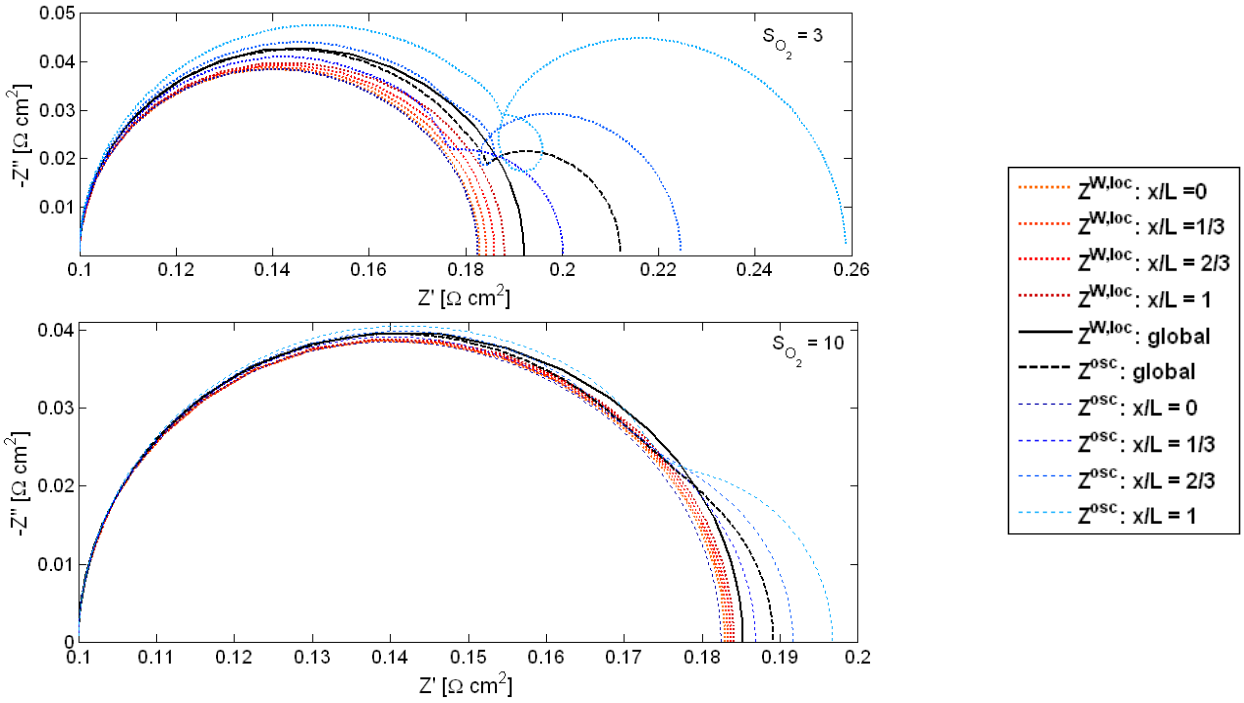


Figure 5.11: *Local and global impedance spectra derived from the convecto-diffusive model (blue lines) and the local Warburg impedance accounting for oxygen depletion along the channel (red lines calculated with equation* (5.15)*). The spectra are plotted in the conditions of Table 5.2 with* $S_{O_2} = 3, 10$.

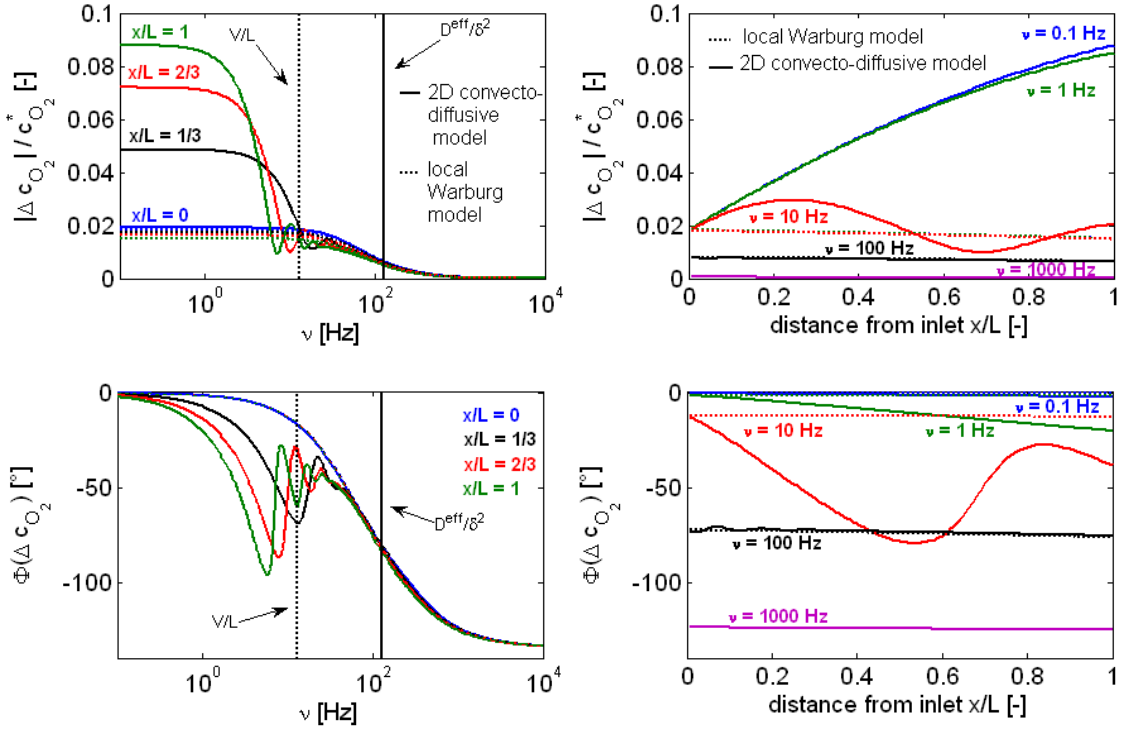


Figure 5.12: *Modulus and phase* Φ *of the oxygen concentration oscillation at the electrode* $\Delta\bar{c}_{O_2}(x,\delta,\omega)$ *as a function of the frequency (first column) and of the distance from the inlet (second column) using the convecto-diffusive model (plain lines) and the local Warburg approach (dotted lines);* $S_{O_2} = 2$.

6 Experimental Validation of the Models

This chapter presents some results of parameter estimation starting from the one- and two-dimensional oxygen transport models derived in the previous chapters. The comparison of experimental and numerical results allows to confirm some of the main hypotheses.

In a first part, a comparison between the impedance parameters estimated using the finite Warburg element and the 1D convecto-diffusive impedance is presented: this makes it possible to assess the impact of convection perpendicular to the electrode on the impedance spectra of PEMFC and the error made when it is neglected.

In a second part, the values of the diffusion parameters estimated using the 1D finite Warburg impedance (cf. section 3.6.3) are compared to those determined with the pseudo-2D oxygen transport impedances, which emphasizes the significance of the phenomena occuring along the channel direction (oxygen depletion and concentration oscillations). Then, the 2D convecto-diffusive impedance is used for the estimation of the local diffusion parameters δ and D^{eff} with MEA using GDL of different thickness, with and without a MPL.

The derivation of the 2D convecto-diffusive impedance in section 5.2 put forward that the oscillations of the oxygen concentration are probably at the origin of the discrepancy between the low frequency limit of the impedance spectra and the slope of the polarization curve. This hypothesis is tested experimentally in the last part of this chapter.

The impedance spectra presented in this chapter are measured with the segmented cells described in chapter 3.5.

6.1 Convective Oxygen Transport Perpendicular to the Electrode

In chapter 4.1, a one-dimensional oxygen transport model was derived considering convection perpendicular to the electrode in addition to diffusion. The resulting expression of the convecto-diffusive impedance is obtained using a convection-diffusion equation instead of a diffusion equation in the case of the classical Warburg impedance. The main hypothesis of the model is that all of the water flows through the porous media in vapor phase. This allows to express the velocity of the convective flux $V = (2\alpha - 1)\frac{j_f}{4F}\frac{RT}{P}$ (4.7) as a function of a water transport coefficient α (the fraction of produced water that is evacuated at the cathode outlet). Note that this hypothesis is not necessarily valid in all cases and may lead to an overestimation of V when water flows through the GDL in liquid phase. Three limiting cases can be distinguished:

- $\alpha = 0$: all of the produced water flows through the membrane toward the anode (convection in the same direction as diffusion).
- $\alpha = 0.5$: purely diffusive oxygen transport (Warburg impedance).

- $\alpha = 1$: all of the produced water is evacuated at the cathode outlet (convection in the direction opposite to diffusion).

If air is humidified, the values of α can be lower than 0 or higher than 1, the flux of water through the membrane being possibly negative (from the cathode to the anode) or greater than $N_{H_2O}^{prod} = j_{cell}/2F$.

The numerical results obtained with the 1D convecto-diffusive impedance (cf. section 4.1) indicate that the impact of convection can be neglected if the cell is operated at low current density ($j_{cell} < 0.5\ Acm^{-2}$) and if the voltage drop caused by oxygen diffusion remains low compared to the other sources of voltage loss. However, for high current densities, the model predicts a growing influence of convection on the low frequency loop (the convective flux velocity being an increasing function of the current density). This was confirmed experimentally in our group by A. Thomas. Some of these results are presented in the following.

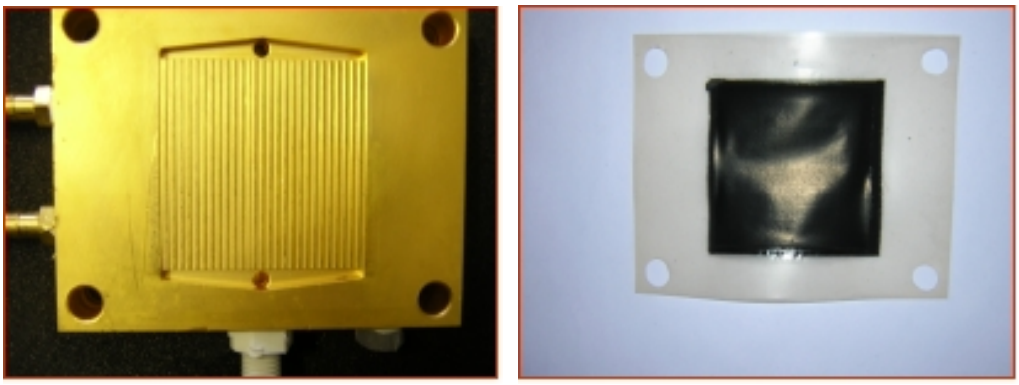


Figure 6.1: *Flow field plates (gold plated brass; the anode and the cathode plates are symmetrical with* 28 *parallel channels) and MEA (Johnson Matthey Technologies;* $A_{geom} = 23.88\ cm^2$*) of the single cell used for experimental studies performed by A. Thomas.*

The experimental results are obtained with a single cell of active area $A_{geom} = 23.88\ cm^2$ (Figure 6.1). The flow field plates (Figure 6.1(a)) are made of gold plated brass. The anode and the cathode plates are symmetrical with 28 vertical parallel channels. The MEA (Johnson Matthey Technologies) consists of a 30 μm thick PFSA (Gore) polymer membrane and Pt/C electrodes ($\approx 10\ \mu m$) with a platinum load of 0.2 $mg_{Pt}cm^{-2}$ at the anode and 0.6 $mg_{Pt}cm^{-2}$ at the cathode. The electrodes are covered with a MPL and a GDL (SGL 10 BB, $\delta_{GDL} = 420\ \mu m$; Sigracet®). This cell was designed initially to study the influence of a temperature difference ΔT between the anode and cathode plates on the water transport coefficient α. Actually, the first results showed that it is possible to vary α over a wide range of values (from 0.25 to 1.3) through the variation of ΔT [TMD+11]. This made possible the measurement of the impedance spectra presented below. Moreover, the major result of these studies is that the transport of water in the direction perpendicular to the membrane occurs like in a heat pipe in three stages:

- Evaporation under the effect of a locally higher temperature at the electrode.
- Convection and/or diffusion in gas phase through the porous media (GDL, MPL and catalyst layer).
- And eventually, condensation in the gas channel.

Discussing this description would be out of the scope of this work (one can refer to [TMD+11]), but its consequences in term of impedance are of great interest.

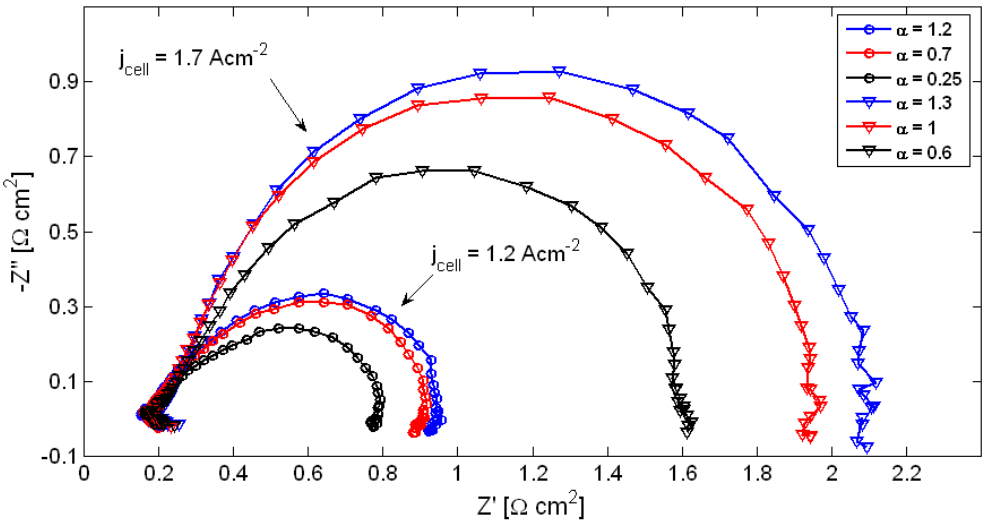


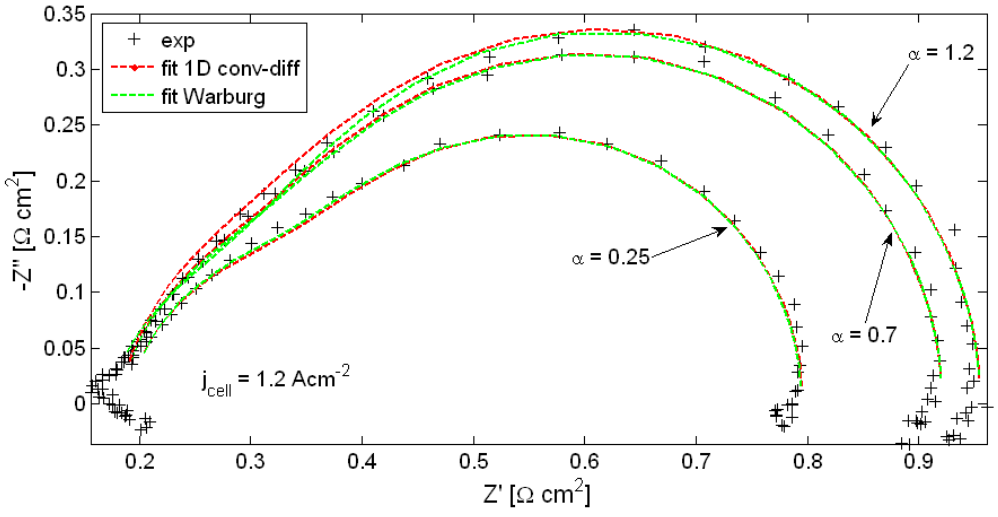
Figure 6.2: *Impedance spectra measured with the single cell of Figure 6.1 (open dots: $j_{cell} = 1.2\ Acm^{-2}$; triangles: $j_{cell} = 1.7\ Acm^{-2}$) for different values of the water transport coefficient. α is controlled by the temperature difference between the anode and the cathode flow field plates.*

Figure 6.2 shows impedance spectra measured at two different current densities ($j_{cell} = 1.2\ Acm^{-2}$ and $j_{cell} = 1.7\ Acm^{-2}$) for three different values of the water transport coefficient per operating point. The cell is operated with pure hydrogen ($S_{H_2} = 1.4$) and air ($S_{air} = 3$) in co-flow, at atmospheric pressure and at a mean temperature of $60°C$. The gases are saturated with vapor and consequently, α can reach values above 1 and below 0. As expected, the cell impedance increases with α. Inversely, it can be concluded from these curves that a convective flow in the same direction as diffusion ($\alpha < 0.5$) can improve oxygen transport through the catalyst layer, which should result in better cell performances [TMD+11]. The comparison of spectra measured at $1.2\ Acm^{-2}$ with those measured at $1.7\ Acm^{-2}$ confirms that the impact of convection is more important at high current densities (section 4.1).

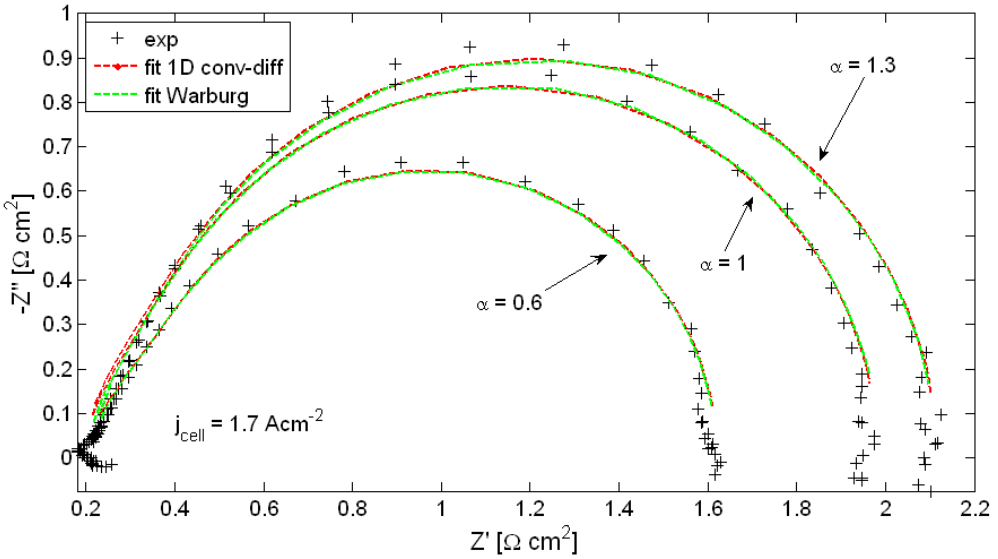
The experimental data are fitted (Figure 6.3) with an impedance expression corresponding to a Randles EEC in which the mass transport is accounted for either by a classical finite Warburg impedance (3.38) (green dotted lines) or by the 1D convecto-diffusive impedance (4.27) (red dotted lines). Note that α is determined directly by measuring the water output at the outlet of each electrode. The simultaneous estimation of the 6 parameters of the EEC, including those of the convecto-diffusive impedance (R_{hf}, R_{ct}, C_{dl}, D^{eff}, δ and α) was not possible, probably because α is correlated with other parameters.

The data at $j_{cell} = 1.2\ Acm^{-2}$ are fitted over frequencies comprised between $0.16\ Hz$ and $200\ Hz$. The results do not depend on the frequency range (Table 6.1). The values of the high frequency parameters (R_{hf}, R_{ct}, C_{dl}) are typical of PEMFC (cf. experimental results of chapter 3 and [RUKD08, SZWG96]). They are not significantly affected by the choice of the mass transport model, except for the charge transfer resistance, most probably because of correlation(s) with other parameters at intermediate frequencies (cf. Figure 3.12 in section 3.3).

The values of the diffusion parameters (D^{eff}, δ) are calculated with a macroscopic point of view (considering an oxygen flux relative to the MEA flat surface). They are in ranges typical of gas



(a) $j_{cell} = 1.2\ Acm^{-2}$



(b) $j_{cell} = 1.7\ Acm^{-2}$

Figure 6.3: *Impedance spectra of Figure 6.2 with fitting curves for different values of the water transport coefficient. Green lines: Randles EEC with the finite Warburg impedance. Red lines: Randles EEC with the 1D convecto-diffusive impedance.*

diffusion in PEMFC backing layers (cf. section 3.6.3 and [BSL02, GFP+06]). The choice of the oxygen transport model modifies mostly the value of the diffusion coefficient D^{eff}. For $\alpha = 0.25$, the value of D^{eff} obtained with the Warburg impedance is higher than with the convecto-diffusive model, the convective flux being oriented in the same direction as diffusion. For $\alpha = 0.7$ and $\alpha = 1.2$ (convection opposite to diffusion) the tendency is inverted: the diffusivities estimated with the Warburg impedance are lower than with the 1D convecto-diffusive impedance. Furthermore, the difference increases with the water transport coefficient. These results are consistent with the expectations and confirm the validity of the 1D convecto-diffusive impedance model, at least from a qualitative point of view.

	α $[-]$	R_{hf} $[\Omega cm^2]$	R_{ct} $[\Omega cm^2]$	C_{dl} $[F cm^{-2}]$	D^{eff} $[m^2 s^{-1}]$	δ $[\mu m]$
Warburg		0.194	0.173	0.016	$2.02\,10^{-6}$	350
Conv-diff 1D	0.25	0.193	0.169	0.016	$1.87\,10^{-6}$	341
Warburg		0.186	0.173	0.018	$1.89\,10^{-6}$	353
Conv-diff 1D	0.7	0.186	0.177	0.018	$1.99\,10^{-6}$	357
Warburg		0.176	0.114	0.015	$1.67\,10^{-6}$	348
Conv-diff 1D	1.2	0.186	0.192	0.020	$2.31\,10^{-6}$	381

Table 6.1: *Impedance parameters identified from the impedance spectra of Figure 6.3(a); at* $j_{cell} = 1.2\ Acm^{-2}$.

The diffusion thickness δ does not vary significantly with the oxygen transport impedance. Convection can possibly affect the diffusion thickness indirectly by means of the content of liquid water present in the gas pores: when the convective flux from the cathode to the channel ($\alpha > 0.5$) increases, more water is (probably) present in the porous media of the cathode. On a macroscopic point of view, an increase of the liquid water content in the gas pores would lead to an increase of the tortuosity and thus to higher values of δ (cf. hypotheses in section 6.3). On the contrary, if α is lower than 0.5, it is likely that there is less liquid water in the cathode (convection oriented from the air channel to the membrane). In this case, a decrease of the diffusion thickness can be observed. The values of δ estimated with the 1D convecto-diffusive impedance at $1.2\ Acm^{-2}$ are consistent with this explanation, which is not the case for the values of D^{eff} (Table 6.1): the diffusion coefficients should rather remain constant or decrease with V. The model being based on the assumption that water is evacuated in pure vapor phase, it is possible that V is overestimated; in spite of the evaporation and condensation processes in (or at the boundaries of) the porous media (heat pipe effect), some water may be evacuated in liquid form, which is not considered here.

	α $[-]$	R_{hf} $[\Omega cm^2]$	R_{ct} $[\Omega cm^2]$	C_{dl} $[F cm^{-2}]$	D^{eff} $[m^2 s^{-1}]$	δ $[\mu m]$
Warburg		0.209	0.157	0.014	$3.02\,10^{-6}$	462
Conv-diff 1D	0.6	0.195	0.063	0.010	$3.03\,10^{-6}$	488
Warburg		0.202	0.229	0.017	$3.34\,10^{-6}$	501
Conv-diff 1D	1	0.186	0.030	0.015	$3.65\,10^{-6}$	561
Warburg		0.214	0.345	0.019	$3.69\,10^{-6}$	520
Conv-diff 1D	1.3	0.184	0.040	0.011	$4.19\,10^{-6}$	610

Table 6.2: *Impedance parameters identified from the impedance spectra of Figure 6.3(b); at* $j_{cell} = 1.7\ Acm^{-2}$.

The fitting curves at $j_{cell} = 1.7\ Acm^{-2}$ (Figure 6.3(b)) depend on the frequency range, which shows that the EEC is not fully appropriate in these conditions. Because of this difficulty, the interpretation of the results is limited and must be considered with care. Some results obtained with a frequency range identical for both models ($0.32\ Hz - 100\ Hz$) are summarized in Table 6.2.

This frequency range is chosen so that the quality of the fitting curves (the residual deviation) is similar in both cases.

The values of the charge transfer resistance identified with the 1D convecto-diffusive impedance are one order of magnitude smaller than those obtained with the Warburg impedance. This shows that these impedance models are not appropriate in these operating conditions and that there must be phenomena governing the cell impedance at high current densities that are not considered in the models (possible evacuation of water in liquid phase) and/or correlations between the parameters in these conditions. Nevertheless, the values of the main transport parameters show the same tendency as those estimated at $j_{cell} = 1.2\ Acm^{-2}$: when $\alpha > 0.5$ (convective flux oriented from the cathode to the channel), D^{eff} and δ are higher with the convecto-diffusive model than with the Warburg impedance.

The main conclusions of this section can be summarized as follows:

- As expected, the finite Warburg impedance tends to overestimate the diffusion coefficient in the presence of a convective flux in the same direction as oxygen diffusion ($\alpha > 0.5$) and to underestimate it when the convection is oriented in the direction opposite to the diffusion ($\alpha < 0.5$).
- The discrepancy between the diffusion parameters identified with both models increases with the current density.
- At high current densities, a consistent parameter estimation is not possible. This can be explained by correlations between the model parameters or by phenomena not considered in the 1D convecto-diffusive impedance, like evacuation of water in liquid phase. This is certainly the most important shortcoming of this model.
- Note eventually that the values of D^{eff} and δ estimated with both transport models do not vary drastically: at moderate current densities and for a first estimation of the diffusion parameters, convection perpendicular to the electrode can be neglected. This is consistent with the results of the numerical investigations presented in section 4.1.

6.2 Estimation of the Local Impedance Parameters with the Pseudo 2D Impedance Models

The results of parameter estimation in chapter 3.6.3 point out that the one-dimensional Warburg impedance yields a good estimate of the order of magnitude of the diffusion parameters. However, a clear identification of the main origin of the diffusion impedance (backing and/or active layer(s)) is not possible. Furthermore, the profiles of δ and D^{eff} along the air channel seem to lead in some cases to conflicting conclusions, which shows that probably, some of the main assumptions of the Warburg model are not realistic.

Therefore, in this section we compare results obtained with:

- The 1D finite Warburg impedance $Z^{W,1D}$ (cf. equation (3.38) in section 3.2.2).
- The local Warburg impedance $Z^{W,loc}_{c_{O_2}}$ (6.2) accounting for oxygen depletion.
- The 2D convecto-diffusive impedance $Z^{osc}_{c_{O_2}}$ (6.3) accounting in addition for concentration oscillations in the air channel.

The analysis is done starting from the local impedance spectra of Figure 3.24 (section 3.6): they are measured at a mean current density $\langle j_{cell} \rangle_t = 0.5\ Acm^{-2}$, so that convective effects in the direction perpendicular to the electrode can be neglected. Note also that the effects of the finite proton conduction and of gas consumption in the pores of the catalyst layer are not considered in this section (surface electrode description). The impedance parameters, the current density and the oxygen concentration are assumed uniform over each segment of the instrumented cells (cell 1: $N_{seg} = 18$; cell 2: $N_{seg} = 20$; cf. section 3.5.1). The electrode/membrane interface is located at $x = 0$ and the GDL/channel interface at $x = \delta$.

The expression of the local Warburg impedance accounting for oxygen depletion along the channel length $Z^{W,loc}_{c_{O_2}}(y_n)$ (5.14) is recalled:

$$Z^{W,loc}_{c_{O_2}}(y_n) = \frac{b(y_n)}{4F \langle c_{O_2}(0,y_n) \rangle_t \sqrt{i\omega D^{eff}(y_n)}} \tanh\left(\sqrt{\frac{i\omega}{D^{eff}(y_n)}}\right) \tag{6.1}$$

where y_n denotes the position of the n$^{\text{th}}$ segment (with $1 \leq n \leq N_{seg}$). Using this diffusion impedance in a Randles equivalent circuit, the expression of the local cell impedance becomes:

$$Z^{W,loc}(y_n) = R_{hf}(y_n) + \frac{1}{\frac{1}{\frac{b(y_n)}{\langle j(y_n) \rangle_t} + Z^{W,loc}_{c_{O_2}}(y_n)} + i\omega C_{dl}(y_n)} \tag{6.2}$$

When taking into account the propagation of the concentration oscillations, the local cell impedance is derived from (5.40), which leads to:

$$\begin{aligned} Z^{osc}(y_n) &= \frac{\Delta E_{cell}}{-\Delta j(y_n)} \\ &= \underbrace{R_{hf}(y_n)}_{\text{Ohmic resistance}} + \underbrace{\frac{\frac{b(y_n)}{\langle j(y_n) \rangle_t}}{1 + \frac{i\omega C_{dl}(y_n)}{\langle j(y_n) \rangle_t}}}_{\text{Reaction kinetics}} - \underbrace{\left(1 - \frac{\frac{i\omega C_{dl}(y_n)}{\langle j(y_n) \rangle_t}}{1 + \frac{i\omega C_{dl}(y_n)}{\langle j(y_n) \rangle_t}}\right) \frac{b(y_n)}{\langle c_{O_2}(0,y_n) \rangle_t} \frac{\Delta c_{O_2}(0,y_n)}{\Delta j(y_n)}}_{\text{Mass transfer impedance } Z^{osc}_{c_{O_2}}} \end{aligned} \tag{6.3}$$

The first term of (6.3) accounts for the finite electronic and ionic conductivity of the MEA, the second for the reaction kinetics and the last term stands for oxygen transport. In this last term, the ratio of the concentration and current density oscillations $\frac{\Delta c_{O_2}(0,y_n)}{\Delta j(y_n)}$ (in segment n) is given by (5.38):

$$\frac{\Delta c_{O_2}(0,y_n)}{\Delta j(y_n)} = \underbrace{-\frac{\frac{e^{-\frac{y_n}{X}}}{4F\alpha h V}}{\cosh^2\left(\sqrt{\frac{i\omega}{D^{eff}(y_n)}}\delta(y_n)\right)} \frac{\sum_{n'=1}^{n} e^{\frac{y_{n'}}{X}} \Delta j(y_{n'}) \Delta y}{\Delta j(y_n)}}_{\text{Convecto-diffusive impedance } Z_{conv-diff}} - \underbrace{\frac{\tanh\left(\sqrt{\frac{i\omega}{D^{eff}(y_n)}}\delta(y_n)\right)}{4F\sqrt{i\omega D^{eff}(y_n)}}}_{\text{Warburg impedance } Z_W} \tag{6.4}$$

$$\text{with } X = \frac{V}{i\omega + \frac{1}{\alpha h}\sqrt{i\omega D^{eff}(y_n)} \tanh\left(\sqrt{\frac{i\omega}{D^{eff}(y_n)}}\delta(y_n)\right)} \tag{6.5}$$

where Δy stands for the length of one segment: $\Delta y = L/N_{seg}$.

The first term in (6.4) stands for a convecto-diffusive contribution to the oxygen transport impedance and the second one for a purely diffusive contribution. The latter is the same as in the Warburg impedances ($Z^{W,1D}$ and $Z^{W,loc}$). The flow velocity V is assumed constant along the channel. It is a function of the oxygen stoichiometry S_{O_2}, of the operating conditions and of the channel dimensions (h, L, α): $V = S_{O_2} \frac{\langle j \rangle_{x,t} L(1+H)}{4F c^*_{O_2} \alpha h}$ (5.36). For an infinitely high air velocity $V \longrightarrow \infty$, the convecto-diffusive term $Z_{conv-diff}$ tends to zero and Z^{osc} (6.3) reduces to $Z^{W,loc}$ (6.2).

The expression of the time-averaged oxygen concentration at the reaction interface $\langle c_{O_2}(0,y_n) \rangle_t$ is the same in both pseudo-2D approaches (cf. equations (5.33) and (5.8)). Since the measurements are done in under-saturated conditions, it comes:

$$\langle c_{O_2}(0,y_n) \rangle_t = \frac{c^*_{O_2}}{1+H} \left[1 - \frac{\sum_{n'=1}^{n} \langle j(y_{n'}) \rangle_t}{S_{O_2} \sum_{n'=1}^{N_{seg}} \langle j(y_{n'}) \rangle_t} \right] - \frac{\langle j(y_n) \rangle_t \, \delta(y_n)}{4F D^{eff}(y_n)} \tag{6.6}$$

Independently of the model, the cell impedance depends on:

- The high frequency resistance $R_{hf}(y_n)$.
- The Tafel slope $b(y_n)$.
- The double-layer capacity $C_{dl}(y_n)$.
- The effective diffusivity $D^{eff}(y_n)$.
- The diffusion thickness $\delta(y_n)$.

These parameters are determined by fitting the experimental spectra using a complex nonlinear least square method (cf. chapter 3.3). The results depend on the operating conditions and on the channel dimensions in the case of the 2D convecto-diffusive impedance Z^{osc} (Table 6.3).

Parameter		Cell 1 co-flow	Cell 1 counter-flow	Cell 2 counter-flow
Channel depth h	$[mm]$	0.6	0.5	0.7
Channel length L	$[m]$	0.33	0.33	0.3
Ratio channel/GDL interface α	$[-]$	1/1.6	1/1.6	1/2
Cell temperature T_{cell}	$[^\circ C]$	56.1	55.9	50
Relative humidity hydrogen RH_{H_2}	$[-]$	0	0	0.6
Relative humidity air RH_{air}	$[-]$	0.74	0.75	0.6

Table 6.3: *Model parameters used for fitting the local impedance spectra of Figure 3.24 with the 2D convecto-diffusive impedance* (6.3)*. The spectra are measured at a mean current density* $\langle j_{cell} \rangle_t = 0.5\, Acm^{-2}$ *with* $S_{H_2} = 1.2$ *and* $S_{air} = 3$.

Figure 6.4 shows the local impedance spectra measured with cell 2 (in counter-flow) and their respective fitting curves obtained with the local Warburg impedance $Z^{W,loc}$ (blue lines) and with the 2D convecto-diffusive impedance Z^{osc} (green lines). The impedance spectra are fitted between 0.2 Hz and 200 Hz. With the 2D convecto-diffusive impedance, the shape of spectra differs from

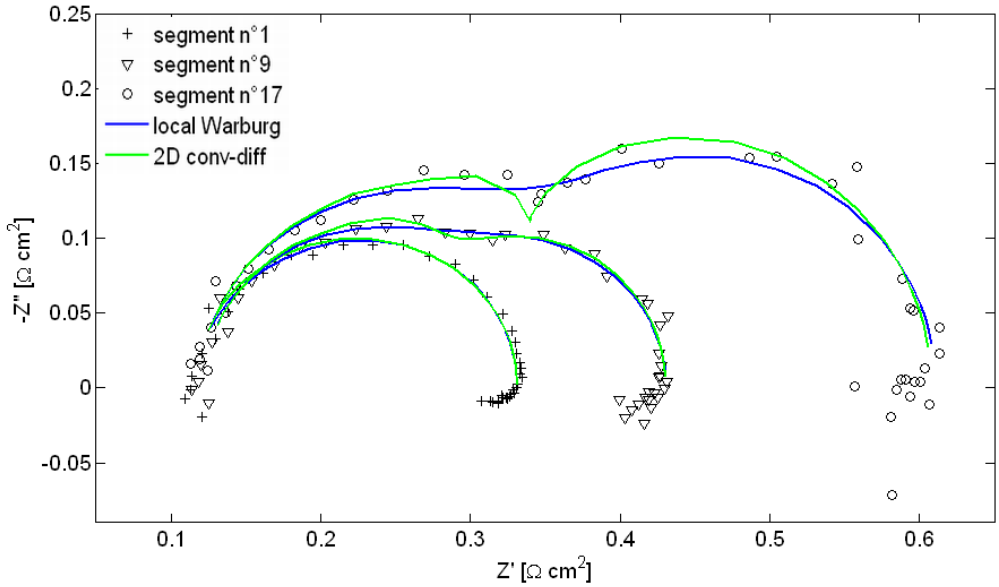


Figure 6.4: *Local impedance spectra measured with cell 2 in counter-flow and corresponding fitting curves obtained with the local Warburg impedance $Z^{W,loc}$ (blue lines) and with the 2D convecto-diffusive impedance Z^{osc} (green lines); $\langle j_{cell} \rangle_t = 0.5\ Acm^{-2}$, $S_{O_2} = 3$ and $h = 0.7\ mm$. Segment 1 corresponds to the air inlet.*

that obtained with the local Warburg impedance, especially close to the air channel outlet, when the low frequency loop is the most pronounced: with Z^{osc}, the spectra exhibit a clear separation of the two loops, which is not the case with $Z^{W,loc}$. The same tendency can be observed with cell 1 as shown in appendix C.0.1 (Figure C.1(a) and C.1(b)).

It is worth mentioning that the values of the local diffusion parameters estimated with the convecto-diffusive impedance depend on the channel depth h. The real channel depth (machined in the flow field plates) is 0.8 *mm* for cell 1 and 0.7 *mm* for cell 2. However, a parameter estimation over the entire channel length is not always possible with these values. Consequently, we chose the highest ones allowing an estimation over the entire electrode length: 0.6 *mm* for cell 1 in co-flow and 0.5 *mm* in counter-flow. For cell 2, it was not necessary to modify the depth of the channel ($h = 0.7\ mm$). Note that in a running fuel cell, the actual channel depth is lower than that measured in the flow field plates alone because the GDL tends to penetrate into the channel. Furthermore, the possible presence of liquid water reduces also the hydraulic diameter. A sensitivity analysis is presented in appendix C.0.2 (Figure C.2).

High frequency parameters

Figure 6.5 shows the profiles of the high frequency parameters (b, R_{hf} and C_{dl}) estimated starting from local impedance spectra measured with cell 2 (Figure 6.4) using $Z^{W,1D}$ (black dots), $Z^{W,loc}_{c_{O_2}}$ (blue dots) and $Z^{osc}_{c_{O_2}}$ (green dots). These curves confirm that the choice of the mass transport impedance has no impact on the high frequency parameters, except for the Tafel slope b (Figure 6.5(b)): the convecto-diffusive impedance leads to a rather flat profile, whereas the values obtained with the Warburg impedances ($Z^{W,loc}_{c_{O_2}}$ and $Z^{W,1D}$) increase along the channel. This can be explained by considering the shape of the spectra in Figure 6.4: with the convecto-diffusive impedance, the clear separation of the low and high frequency loops reduces the diameter of this latter, and thus the Tafel slope. The separation is not observed using the local or the 1D Warburg impedance. More

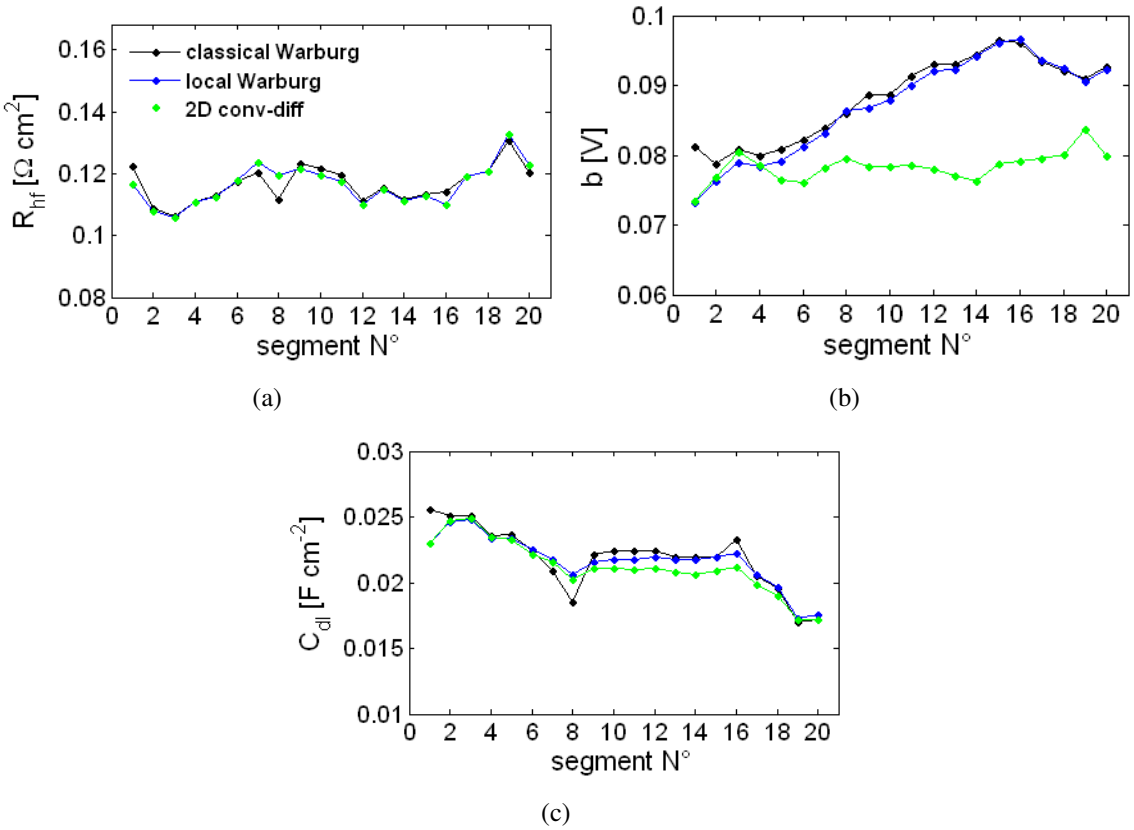


Figure 6.5: *High frequency impedance parameters estimated starting from local spectra measured with cell 2 (Figure 6.4) using $Z^{W,1D}$ (black dots), $Z^{W,loc}_{c_{O_2}}$ (blue dots) and $Z^{osc}_{c_{O_2}}$ (green dots): (a) high frequency resistance R_{hf}, (b) Tafel slope b, (c) double-layer capacity C_{dl}.*

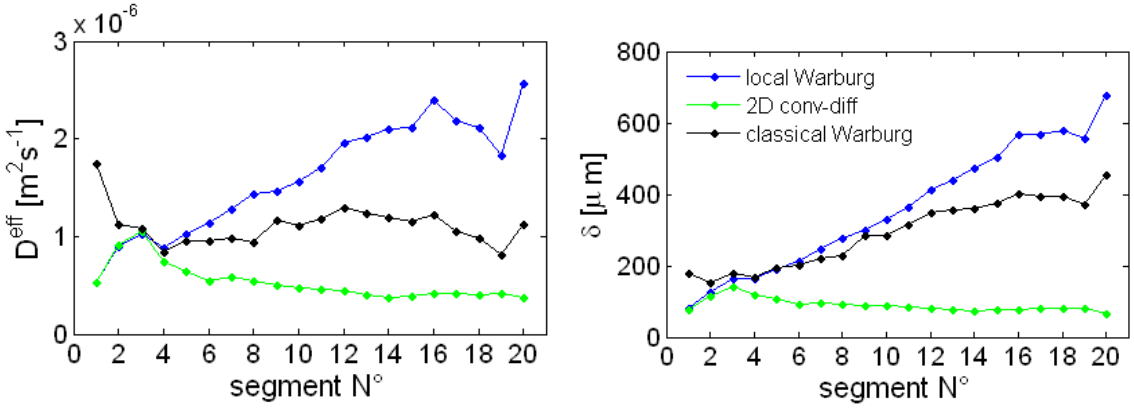
generally, this difference in the profiles of the Tafel slope results from correlations between the charge transfer resistance and the other parameters at intermediate frequencies (cf. Figure 3.12 in section 3.3). The results obtained with cell 1 in co- and counter-flow are given in appendix C.0.3. They lead to the same conclusions.

Low frequency parameters

Figure 6.6 shows the profiles of the diffusion parameters D^{eff} and δ estimated starting from the local spectra of cell 2, with the three oxygen transport impedances and using a macroscopic approach (with reference to the MEA flat surface A_{geom}). As seen previously in section 3.6.3 and further in this section, a microscopic point of view (referring to the electrochemically active area γA_{geom}) affects only the values of these parameters but not the shape of their profiles.

Gas consumption and concentration oscillations being negligible near the air channel inlet, the results should be similar with the three models over the first segment(s)[1]. However, a slight difference is observed between the parameters obtained using the 1D Warburg impedance $Z^{W,1D}$ and those estimated using the pseudo-2D transport impedances ($Z^{W,loc}_{c_{O_2}}$ and $Z^{osc}_{c_{O_2}}$). This can be explained by the fact that $Z^{W,1D}$ does not consider gas humidification: accounting for the absolute humidity

[1] The values of the first and of the last segment are to be considered carefully because of possible discrepancies in the active area compared to the other segments.



(a) (b)

Figure 6.6: *Diffusion parameters identified with cell 2 in counter-flow using $Z^{W,1D}$ (black dots), $Z^{W,loc}_{c_{O_2}}$ (blue dots) and $Z^{osc}_{c_{O_2}}$ (green dots). (a) effective diffusivity D^{eff}; (b) diffusion thickness δ.*

H reduces the oxygen concentration $\langle c_{O_2}(0,y_n)\rangle_t$ (6.6), which results in a decrease of D^{eff}.

The values of the effective diffusivity D^{eff} identified with the three impedances (Figure 6.6(a)) are in ranges expected for gas diffusion in the pores of backing layers [BSL02]. When using the local Warburg impedance $Z^{W,loc}_{c_{O_2}}$ instead of the 1D Warburg impedance $Z^{W,1D}$, a steeper increase of D^{eff} is observed over the electrode. This results from the boundary condition at the reaction interface: $Z^{W,loc}_{c_{O_2}}$ accounts for a decrease of $\langle c_{O_2}(0,y_n)\rangle_t$ along the channel, which is not the case of $Z^{W,1D}$. The profiles obtained with $Z^{osc}_{c_{O_2}}$ completely differ from the two others: the local variations of δ and D^{eff} along the channel are much less important and no clear tendency between the inlet and outlet can be observed. **The comparison of the profiles obtained with $Z^{W,loc}$ and Z^{osc} (accounting both for oxygen consumption) clearly shows that the AC induced concentration oscillations have a more important impact on the impedance parameters than the decreasing time-averaged oxygen concentration.** These results confirm that concentration oscillations can lead to misinterpretations of the low frequency loop if they are not taken into account in the models. The same conclusions can be drawn starting from the data measured with cell 1 (Figure C.5 in appendix C.0.4).

In addition, the local Tafel slope b identified using the 2D convecto-diffusive impedance does not exhibit an increase along the cathode, contrary to what is observed when using the Warburg impedances $Z^{W,1D}$ or $Z^{W,loc}_{c_{O_2}}$: this shows that the oxygen transport model has also an impact on the estimation of the parameters governing the impedance of the cell at intermediate frequencies.

6.3 Analysis of Oxygen Transport with the 2D Convecto-Diffusive Impedance

The profiles of the diffusion parameters presented in the previous section highlight the necessity of considering concentration oscillations propagating along the channel direction when modeling the fuel cell impedance in order to avoid misleading conclusions. **In this section, δ and D^{eff} are estimated using the 2D convecto-diffusive impedance only.** We open a discussion about the limiting layer for oxygen transport starting from the spectra presented in the previous section plus

complementary tests carried out with GDL of different thickness, with and without a MPL.

Again, the most obvious interpretations of the profiles of δ and D^{eff} are linked to the amount of water present in the MEA. They are based on the following simple hypotheses:

- The water content increases along the air channel.
- This increase is assumed to be more pronounced in co- than in counter-flow.

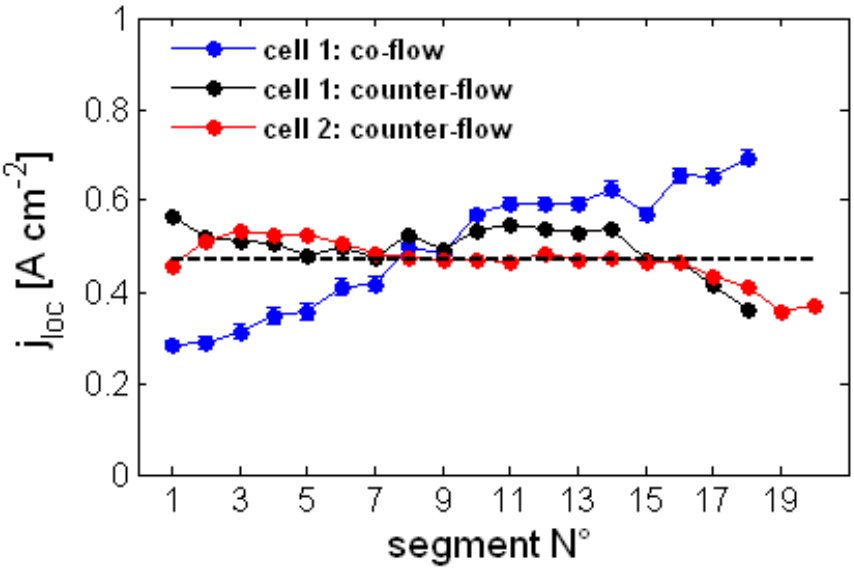


Figure 6.7: *Local current densities of cell 1 and cell 2 in co- and in counter-flow;* $j_{cell} = 0.5\ Acm^{-2}$, $S_{H_2} = 1.2$ *and* $S_{air} = 3$.

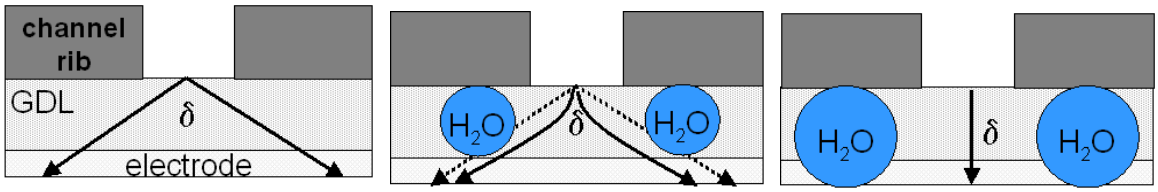
- However, according to Figure 6.7, the local current densities being the highest at the outlet of the air channel of cell 1 in co-flow, there is probably no excess of liquid water in the GDL or catalyst layer (no flooding), at least when $j_{cell} \leq 0.5\ Acm^{-2}$.
- According to the works of A. Thomas [TMD+11], water is evacuated through the GDL (mostly) in vapor phase (heat pipe effect, cf. section 6.1). These studies show furthermore that the electrode temperature rises with the current density, which could lead in some cases to drier conditions in the catalyst layer or in the GDL.

In addition, one can also consider that the impact of liquid water on D^{eff} and δ depends on the considered length scale (macroscopic or microscopic), or in other words, on the place where it accumulates:

- With a macroscopic point of view, the orders of magnitude of δ and D^{eff} seem to show that oxygen diffusion occurs in gas phase through the pores of the backing and active layers. Figure 6.8 depicts the probable stages of liquid water accumulation in the porous media and the resulting evolution of the diffusion thickness δ:
  - In dry conditions, oxygen diffuses under the channel ribs in order to reach the reaction sites (2D diffusion, Figure 6.8(a)). Then, further along the air channel or under the effect of a higher current density, water condensates preferentially under the channel ribs

[SWS+11], where the temperature is assumed to be the lowest (Figure6.8(b)). According to the experimental results of Reum [Reu08], in dry conditions or at high voltage, the local current density is higher under the ribs than below the channel, probably because the electrode and the membrane are better hydrated at these locations.

– A further increase of the amount of water in the GDL could lead to a shift from 2D to 1D diffusion of oxygen (Figure 6.8(c)) if the excess of liquid water under the channel ribs blocks the access to the active layer. Again, this tendency was confirmed experimentally by Reum [Reu08]: the local current density is higher below the air channel when the MEA is well hydrated.



(a) Dry conditions: 2D diffusion (b) Appearance of liquid water: 2D diffusion (c) Flooding: 1D diffusion

Figure 6.8: *Possible evolution of the diffusion thickness when liquid water accumulates in the GDL: (a) dry conditions (2D diffusion), (b) 2D diffusion in the presence of liquid water (c) 1D diffusion in the presence of liquid water.*

- The main question that arises from this description concerns the (expected) evolution of δ and D^{eff} between dry conditions (Figure 6.8(a)) and the case where an excess (or at least a large amount) of liquid water occupies the GDL (Figure 6.8(c)): δ should decrease; however, by no more than 40%. D^{eff} being a function of the porosity ($D^{eff} = \varepsilon^m D_{O_2}$, cf section 2.4.2), which decreases with the amount of liquid water, it should decrease as well.
- With a microscopic point of view, oxygen diffusion is assumed to occur through a film of liquid water and/or ionomer covering the agglomerates, which is consistent with the orders of magnitude of δ and D^{eff} estimated experimentally. In this case, an increase in the liquid water content is expected to result in higher values of δ. In addition, the diffusivity of oxygen through the electrolyte depending on its water content, D^{eff} should increase as well.

These scenarios are only hypotheses. Detailed investigations are necessary to confirm them. However, in the absence of alternative explanations, the profiles of the diffusion parameters presented in the following are interpreted according to these hypotheses. These interpretations may differ from those proposed in section 3.6.3 and page 171: this is due to the difference in the profiles of δ and D^{eff} obtained with the 2D convecto-diffusive impedance compared to those obtained with the 1D and local Warburg impedances (Figure 6.6).

6.3.1 First results about oxygen transport through the cathode

The experimental data presented in this section are measured with cell 1 and 2 (cf. previous section) using the MEA (Johnson Matthey) presented in section 3.5.1.

Figure 6.9 shows the profiles of the diffusion parameters identified using the 2D convecto-diffusive impedance. The results correspond to macroscopic (Figures 6.9(a) and 6.9(b)) and microscopic (Figures 6.9(c) and 6.9(d)) descriptions of the oxygen flux. The electrode roughness γ is

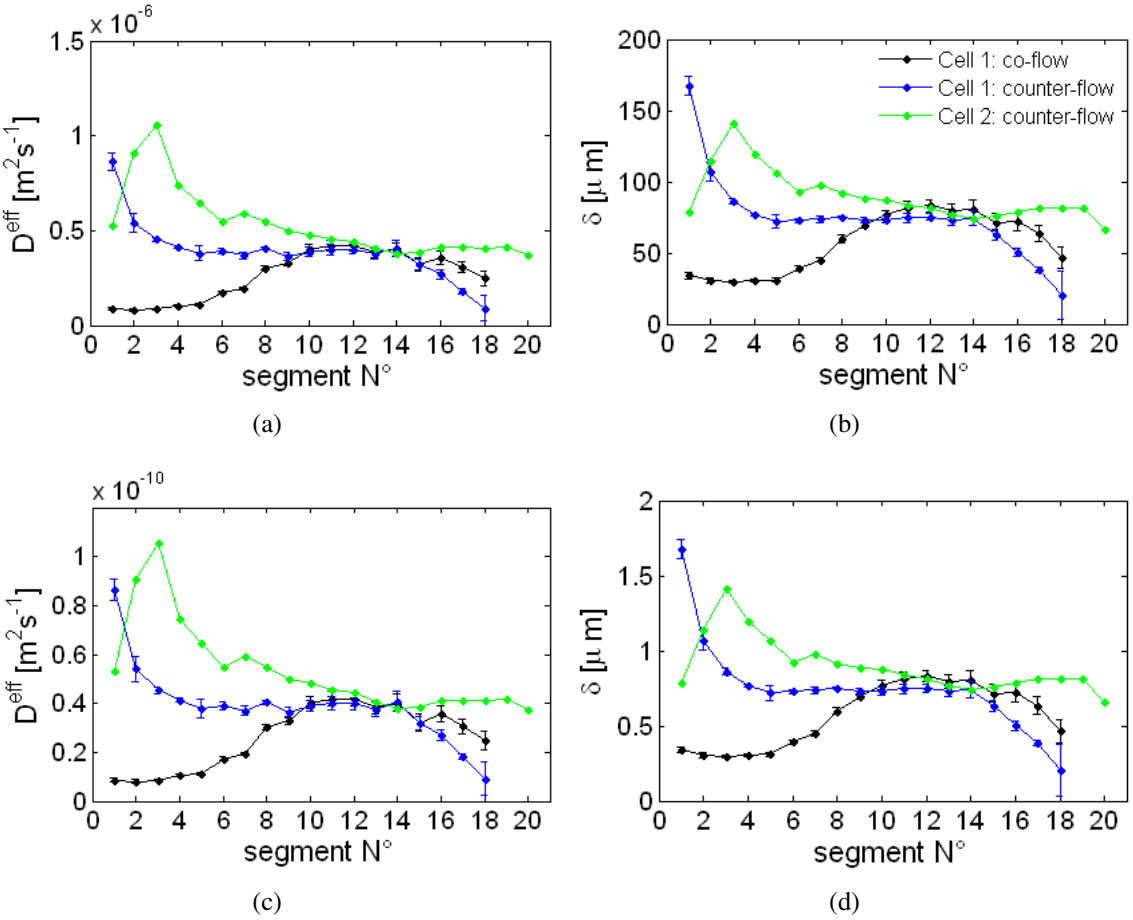


Figure 6.9: *Diffusion parameters identified starting from local spectra measured with cell 1 and 2 using the 2D convecto-diffusive impedance: (a) - (b) macroscopic point of view; (c) - (d) microscopic point of view;* $\gamma = 100$.

set to 100. With a macroscopic point of view, the values of D^{eff} and δ vary in ranges expected for gas diffusion in the pores of the GDL or active layer [BSL02]. With a microscopic point of view, the parameters are in ranges characteristic of liquid diffusion in the ionomer and/or liquid layer covering the agglomerates [BSL02, CYH$^+$99].

In all cases, the profiles of the diffusion parameters can be divided into three parts:

At the channel inlet

The diffusion parameters determined with cell 1 in co-flow are the lowest at the air inlet. They remain almost constant over the first third of the channel and then increase. This can be interpreted with a microscopic point of view: according to the previous hypotheses (cf. pp. 177), hydration is less important at the air channel inlet resulting in a low diffusivity of dissolved oxygen in the ionomer present in the active layer. In these conditions, less liquid water is expected to be present in the pores of the active layer which leads to lower values of the diffusion thickness δ supposing oxygen diffuses in liquid phase through a liquid water or ionomer film.

For a gas supply in counter-flow, the diffusion parameters are the highest at the air inlet and decrease over the first segments. The MEA being a priori better hydrated than in co-flow,

these profiles could be interpreted in terms of gas diffusion through the GDL and active layer (macroscopic description). In this case, the decrease of D^{eff} and δ would correspond to condensation under the channel ribs of the vapor (Figure 6.8(c)) and to the shift from 2D to 1D diffusion described above. However, the difference between the values obtained with cell 1 and cell 2 over the first segments is difficult to explain with these hypotheses, except maybe by considering that condensation would occur further along the channel with cell 2.

At the center of the cell

Whatever the flow configuration or the cell used, there is no significant difference between the values of δ and D^{eff} obtained in the three cases. One can probably conclude that over the second third of the air channel, the MEA operates optimally, independently of the cell geometry and of the direction of the gas flows. In the absence of significant variations of δ and D^{eff}, one can imagine that the oxygen transport is governed by phenomena occurring in the active layer (at the microscopic scale and in liquid phase) as well as in the pores of the active and backing layers (at the macroscopic scale and in gas phase). The increase of D^{eff} and δ with the MEA water content (along the channel) at the microscopic scale could compensate their decrease entailed by liquid water accumulation in the pores of the GDL.

At the channel outlet

In all cases, the diffusion parameters decrease near the cathode outlet (although slightly with cell 2). In co-flow, the decrease of δ and D^{eff} can be explained (on a macroscopic scale) by an excess of liquid water under the channel rib (cf. scenario in Figure 6.8(c); vapor condenses first under the channel rib). The current density being the highest at the air outlet in co-flow (Figure 6.7), this seems to confirm that the accumulation of liquid water is limited to the parts of the MEA located under the channel ribs: the access to the active sites is thus not reduced significantly.

This interpretation remains possibly valid in counter-flow. However, the decrease of δ and D^{eff} can also be explained from a microscopic point of view: the air channel outlet faces the hydrogen inlet, which could result in local drying of the MEA. More precisely, since the flow of water through the membrane is oriented from the cathode to the anode, one can expect that this drying occurs in the active layer. This would result in a decrease of δ and D^{eff} according to the scenarios described on page 179. Hydrogen being humidified in cell 2 but not in cell 1, this effect is less pronounced in cell 2 leading to higher values of D^{eff} and δ. The profiles in Figure 6.9 are consistent with this interpretation.

With the (1D and local) Warburg impedances, the diffusion parameters δ and D^{eff} increase continuously along the channel, independently of the gas flow direction (Figure 6.6), which does not provide enough information for a consistent interpretation of their profile. On the contrary, the values of δ and D^{eff} obtained with the 2D convecto-diffusive impedance show different profiles over the channel length depending on the gas flow direction (Figure 6.9). This allows to make some first interpretations of the diffusion parameter profiles in terms of humidification. Note however that they are to be considered carefully because they are based on relatively simple scenarios about the impact of liquid water on oxygen diffusion. Further investigations are thus necessary to confirm them.

Finally, another striking result in Figure 6.9 is the apparent similarity between the profiles of δ and D^{eff}. This similarity can be understood by considering the profiles of the mass diffusion

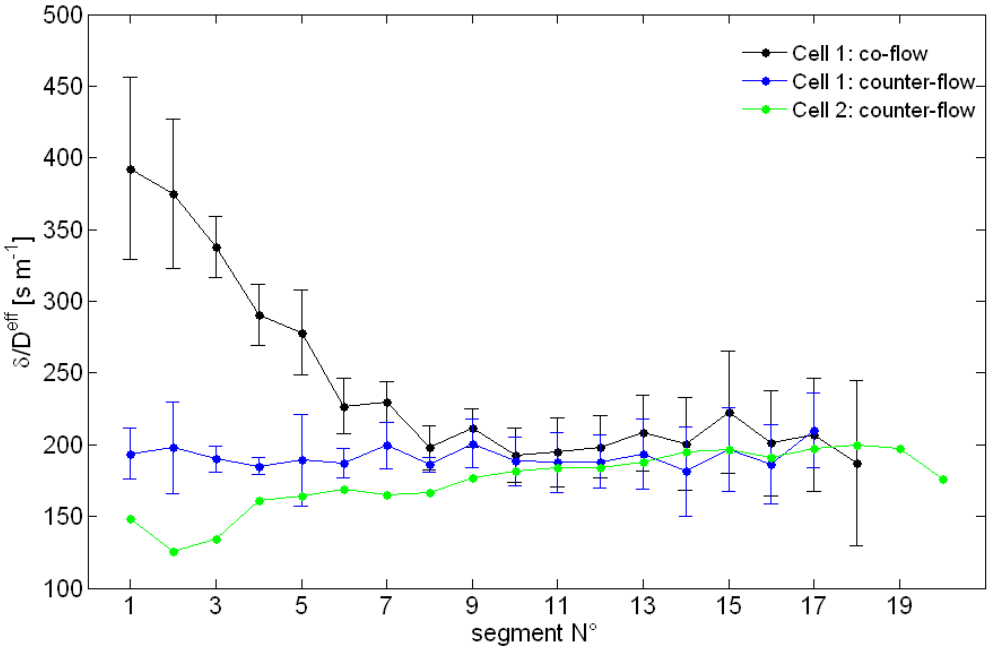


Figure 6.10: *Local mass diffusion resistance δ/D^{eff} determined with the diffusion parameters in Figure 6.9; macroscopic point of view.*

resistance δ/D^{eff}[2], which appears nearly uniform over the channel length (Figure 6.10), except with cell 1 in co-flow. The mass diffusion resistance seems thus to be governed mostly by the hydration of the active layer.

6.3.2 Role of Gas Diffusion Layer and Micro Porous Layer in oxygen transport

In order to complete the previous results, a series of measurements is performed using MEA with backing layers of different thickness. Keeping the operating conditions identical in each case allows to investigate the role of the GDL in oxygen diffusion. In some cases, a micro-porous layer (MPL) is used, which provides information about its impact on the ORR and on oxygen diffusion.

The measurements are carried out with cell 1 (one serpentine flow field, 18 segments and a MEA with $A_{geom} = 5.94\ cm^2$; Johnson Matthey) at pressure $P = 1\ atm$, temperature $T = 60°C$ and with current densities ranging between $j_{cell} = 0.17\ Acm^{-2}$ and $j_{cell} = 0.84\ Acm^{-2}$. The cell is fed with dry hydrogen ($S_{H_2} = 1.4$) and humidified air ($S_{O_2} = 3$, $RH = 90\%$) in counter-flow. Segment 1 corresponds to the air inlet. The characteristics of the three GDL (Sigracet®) are given in Table 6.4.

	GDL series	MPL	Thickness $[\mu m]$	Reference
GDL 1	GDL 25 BC	$\surd$	235	[Sigb]
GDL 2	GDL 10 BB	$\surd$	420	[Siga]
GDL 3	GDL 25 BA	-	190	[Sigb]

Table 6.4: *Characteristics of the Sigracet® backing layers used in this study.*

[2] δ/D^{eff} should not be mistaken for the diffusion (electrical) resistance R_d (3.39).

The impedance spectra are fitted between 0.2 Hz and 200 Hz using the 2D convecto-diffusive impedance. The parameters describing the channel geometry are given in Table 6.5. Again, the channel depth h is set to the highest value allowing parameter estimation over the entire cathode surface (0.7 mm instead of the actual depth 0.8 mm).

Channel depth h	$[mm]$	0.7
Channel length L	$[m]$	0.33
Ratio channel/GDL interface α	$[-]$	$1/1.6$

Table 6.5: *Parameters describing the channel geometry that are needed to fit the impedance data measured with GDL 1 - 3.*

Role of the gas diffusion layer (GDL)

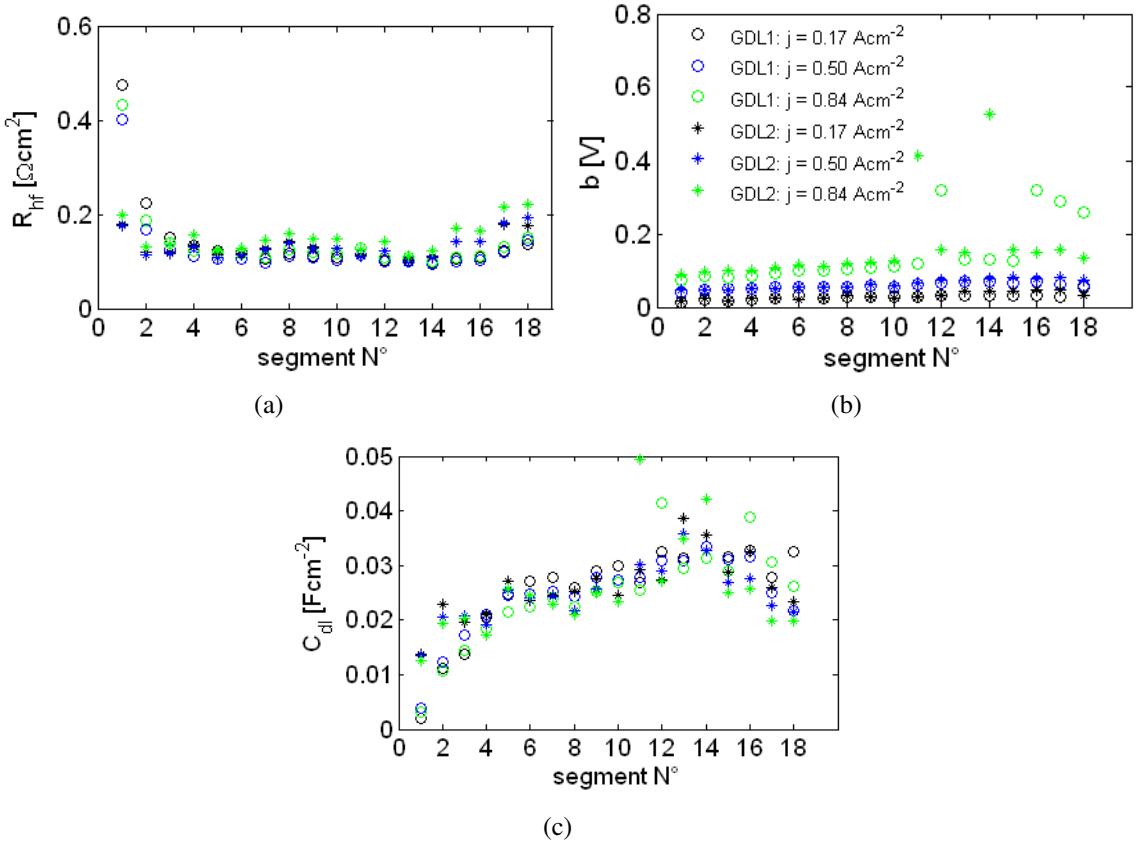
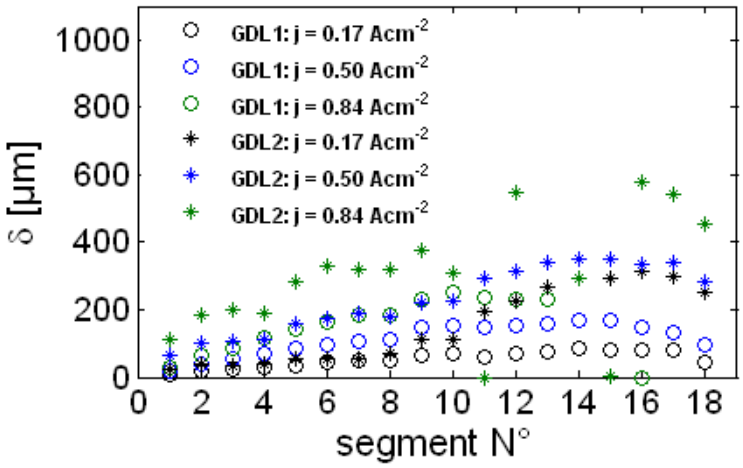


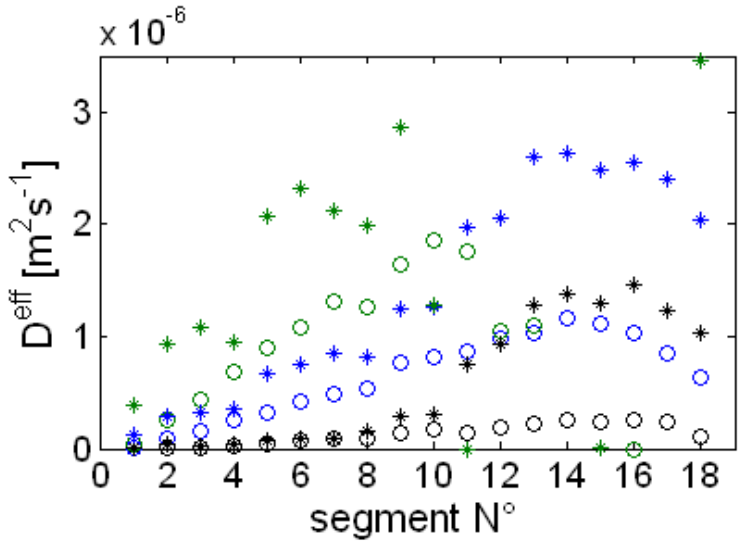
Figure 6.11: *High frequency parameters identified with cell 1 using GDL 1 ($\delta_{GDL1} = 235\ \mu m$) and GDL 2 ($\delta_{GDL2} = 420\ \mu m$) at different current densities: (a) high frequency resistance R_{hf}, (b) Tafel slope b and (c) double-layer capacity C_{dl}.*

Figure 6.11 shows profiles of the high frequency parameters (R_{hf}, C_{dl} and b) estimated at different current densities. The open dots correspond to the data of GDL 1 ($\delta_{GDL1} = 235\ \mu m$) and the stars to those of GDL 2 ($\delta_{GDL2} = 420\ \mu m$). According to these curves, R_{hf}, b and C_{dl} do not depend on the GDL thickness. Furthermore, it can be seen that the high frequency parameters do

not vary significantly with the current density, except the Tafel slope b which increases continuously. The values of b are in the same ranges as those obtained from global impedance spectra (cf. section 3.4). These results are thus consistent with those presented in chapter 3.



(a)



(b)

Figure 6.12: *Diffusion parameters of cell 1 using GDL 1 ($\delta_{GDL1} = 235\ \mu m$) and GDL 2 ($\delta_{GDL2} = 420\ \mu m$) at different current densities: (a) diffusion thickness δ, (b) effective diffusion coefficient D^{eff}.*

Figure 6.12 shows the profiles of δ (Figure 6.12(a)) and D^{eff} (Figure 6.12(b)) determined with a macroscopic point of view: consequently, the values of δ are of the same order as the GDL thickness and those of D^{eff} vary in ranges characteristic of gas diffusion through the MEA porous materials. In the case of a microscopic description, the diffusion thickness δ has to be divided by the electrode roughness γ and the effective diffusivity by γ^2, which leads to values characteristic of oxygen diffusion through the ionomer or through liquid water.

At the lowest current density ($\langle j_{cell} \rangle_t = 0.17\ Acm^{-2}$) and close to the air channel outlet, the diffusion parameters do not depend on the GDL thickness, which means that in these (dry) conditions, the catalyst layer is probably the limiting layer for oxygen diffusion. At higher current densities, a

difference is observed between the diffusion parameters identified with both GDL over the whole length of the channel. At the highest current density ($\langle j_{cell} \rangle_t = 0.84\ Acm^{-2}$), the estimated values of δ and D^{eff} range between:

$$\begin{aligned} \text{GDL 1:} \quad & 30\ \mu m \leq \delta \leq 260\ \mu m \\ & 0.1\,10^{-6} m^2 s^{-1} \leq D^{eff} \leq 2.1\,10^{-6} m^2 s^{-1} \\ \text{GDL 2:} \quad & 10\ \mu m \leq \delta \leq 570\ \mu m \\ & 0.4\,10^{-6} m^2 s^{-1} \leq D^{eff} \leq 3\,10^{-6} m^2 s^{-1} \end{aligned}$$

The values of the diffusion thickness identified with GDL 2 ($\delta_{GDL2} = 420\ \mu m$) are thus up to two times higher than with GDL 1 ($\delta_{GDL1} = 235\ \mu m$). The values of D^{eff} estimated with GDL 2 are also higher than starting from GDL 1. This can be explained by the higher temperature difference between the electrode and the flow field plate [TMD+11], the vapor flux being oriented from the highest to the lowest temperature (in our case from the electrode to the channel). This temperature gradient increases with the GDL thickness, which results in a better removal of water from the active layer.

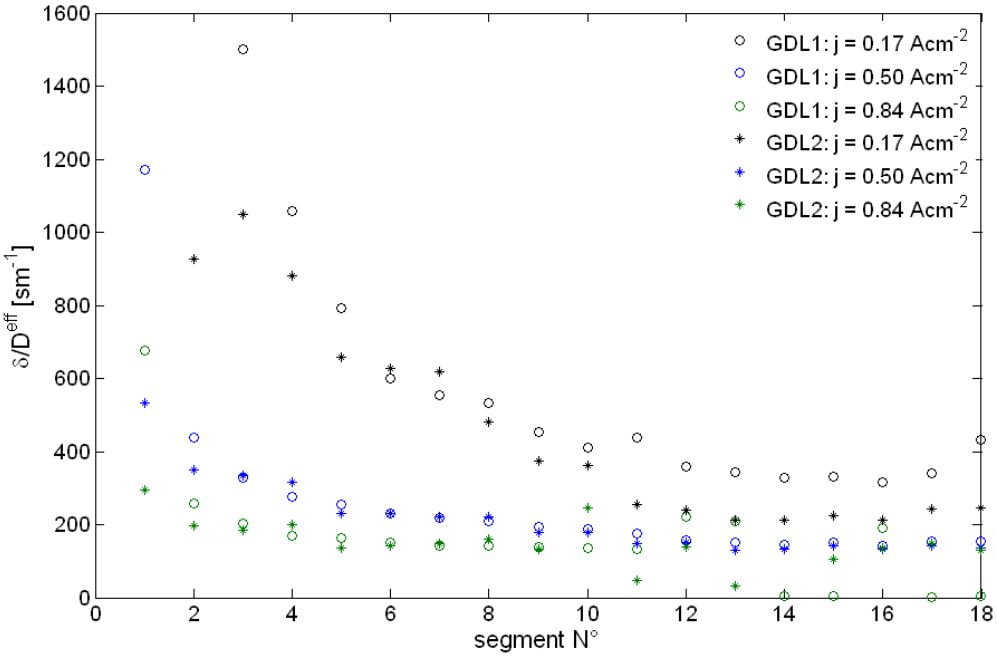


Figure 6.13: *Mass diffusion resistance δ/D^{eff} determined starting from the diffusion parameters of GDL 1 and GDL 2 (Figure 6.12).*

Finally, the profiles of the mass diffusion resistance δ/D^{eff} are plotted in Figure 6.13, for different values of the average current density. Like previously, δ/D^{eff} seems rather uniform, except at the inlet of the air channel when the amount of water in the MEA is the lowest. The values measured at low current density ($j = 0.17\ Acm^{-2}$) result probably from dry conditions over most of the MEA surface: the difference between the values obtained with GDL 1 and with GDL 2 is probably not significant considering the dispersion of the initial data and the low sensitivity of the impedance to the transport parameters at low current density. The dispersion of the results is also important at the exit of the air channel when $j = 0.87\ Acm^{-2}$. Apart from these two cases, there

is no pronounced difference between the values obtained with GDL 1 and GDL 2, which tends to confirm that the mass diffusion resistance δ/D^{eff} is governed mainly by phenomena occuring in the active layer.

Role of the micro-porous layers (MPL)

It is commonly accepted that MPL improve the electronic contact between the catalyst and backing layers and allow a better water management [PWC05]. However, there is still no consensus about the reason(s) for this better water management [PW04a, QK02a, PWC05]; the authors suggest generally that the MPL retains the water produced by the ORR in the membrane, or that it enhances the water flux through the cathode GDL to the channel (cf. section 1.5.3).

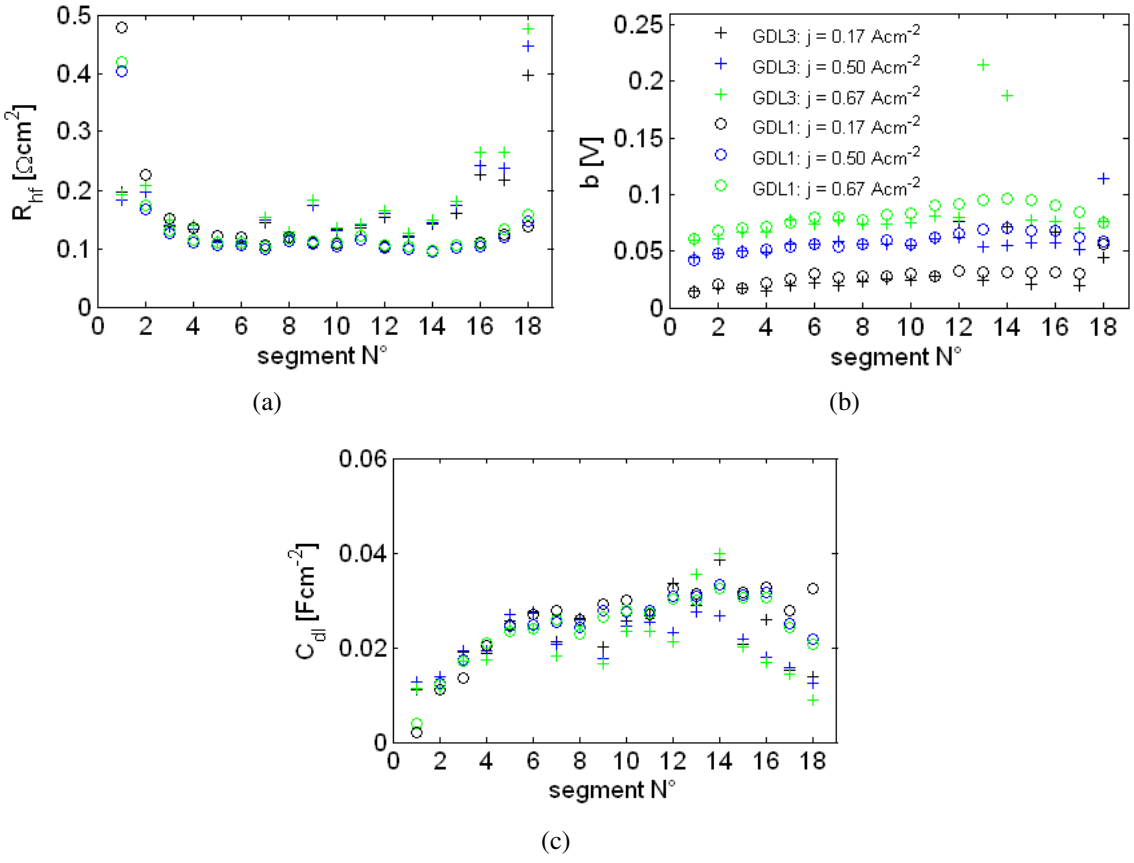
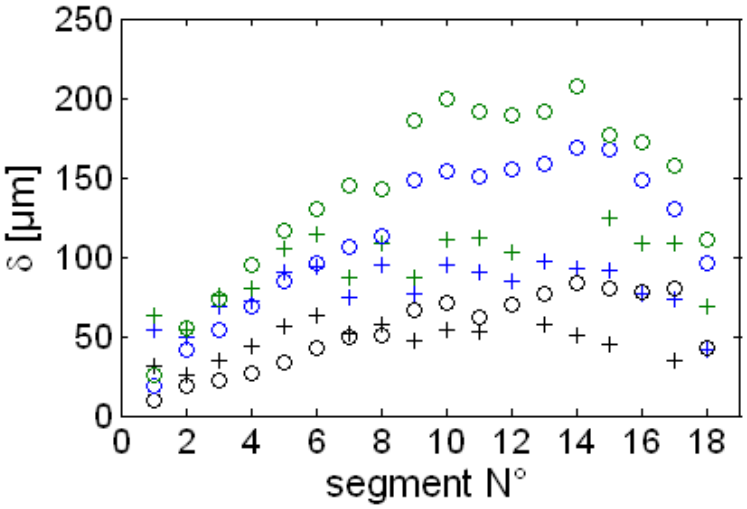


Figure 6.14: *High frequency parameters identified with GDL 1 ($\delta_{GDL1} = 235\ \mu m$ with MPL) and GDL 3 ($\delta_{GDL3} = 190\ \mu m$ without MPL) at different current densities: (a) high frequency resistance R_{hf}, (b) Tafel slope b and (c) double-layer capacity C_{dl}.*

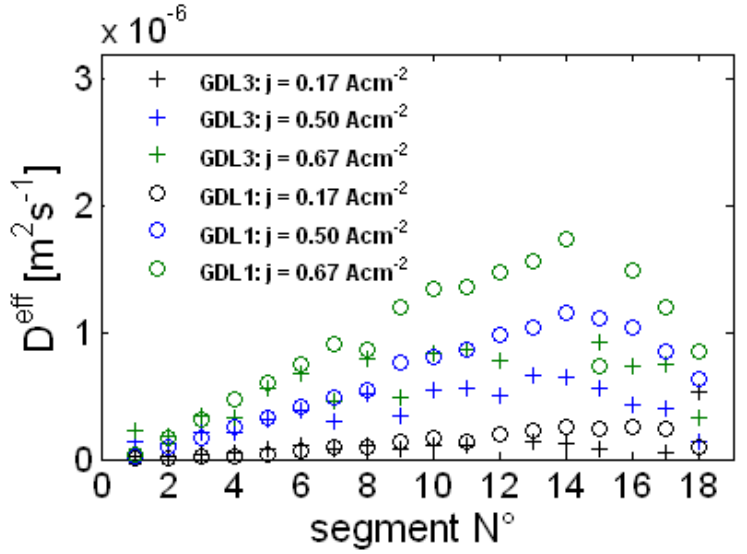
Figure 6.14 shows the profiles of the high frequency parameters (R_{hf}, C_{dl} and b) estimated with GDL 1 ($\delta_{GDL1} = 235\ \mu m$ with MPL) and GDL 3 ($\delta_{GDL3} = 190\ \mu m$ without MPL) at different current densities[3]. The high frequency resistance (Figure 6.14(a)) is slightly lower when a MPL is used (while the double-layer capacity is slightly higher), possibly because of a better electronic contact between the MEA components or of a better hydration of the ionomer. This is

[3] Again, the values of segments 1 and 18 have to be considered carefully because of a possible discrepancy of their active area compared to that of the other segments (MEA centering).

consistent with the hypothesis that MPL would enhance the back-flow of water toward the membrane [PWC05]. On the other hand, the MPL has no significant impact on the Tafel slope (Figure 6.14(b)). In accordance with the previous observations, b increases with the current density, whereas R_{hf} and C_{dl} do not depend on j_{cell}.



(a)



(b)

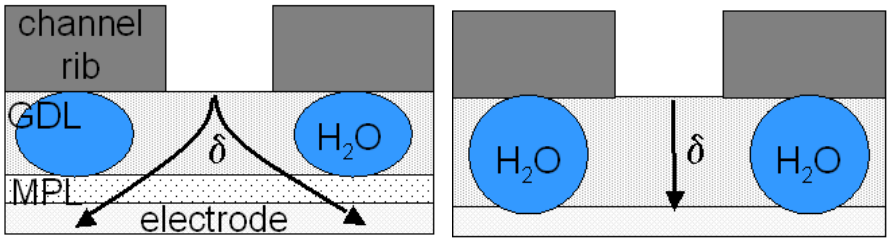
Figure 6.15: *Diffusion parameters identified with GDL 1 ($\delta_{GDL1} = 235\ \mu m$ with MPL) and GDL 3 ($\delta_{GDL3} = 190\ \mu m$ without MPL) at different current densities: (a) diffusion thickness δ, (b) effective diffusion coefficient D^{eff}.*

Figure 6.15 shows the profiles of the diffusion parameters δ and D^{eff} identified starting from the data of GDL 1 (with MPL) and GDL 3 (without MPL). The numerical values in Figure 6.15 correspond to a macroscopic description (surface electrode). Those of δ are close to the actual GDL thickness. When choosing a microscopic approach, they are in ranges expected for a liquid water film or an electrolyte layer covering the agglomerates of the catalyst layer. The values of D^{eff} are in ranges of either gas diffusion (macroscopic point of view), or liquid diffusion (microscopic

description).

At low current densities ($\langle j_{cell} \rangle_t = 0.17\ Acm^{-2}$), the presence of a MPL does not seem to have a significant impact on oxygen diffusion. This confirms that, in these conditions, the main resistance for oxygen diffusion is (in) the catalyst layer. Again, with increasing current density, the diffusion parameters obtained with both GDL diverge. At the highest current density ($\langle j_{cell} \rangle_t = 0.67\ Acm^{-2}$), the values of δ and D^{eff} range between (Figure 6.15):

$$\begin{aligned} &\text{GDL 1:} && 30\ \mu m \leq \delta \leq 190\ \mu m \\ & && 0.1\,10^{-6} m^2 s^{-1} \leq D^{eff} \leq 1.3\,10^{-6} m^2 s^{-1} \\ &\text{GDL 3:} && 60\ \mu m \leq \delta \leq 120\ \mu m \\ & && 0.1\,10^{-6} m^2 s^{-1} \leq D^{eff} \leq 0.8\,10^{-6} m^2 s^{-1} \end{aligned}$$



(a) GDL with MPL: 2D diffusion (b) GDL without MPL: 1D diffusion

Figure 6.16: *Water accumulation under the channel ribs and interpretation in term of diffusion thickness for a MEA with (a) and without (b) MPL: with MPL the catalyst layer is better supplied with oxygen but δ increases because the mean path toward the catalyst layer is larger (constriction effect).*

The diffusion parameters corresponding to GDL 1 (with MPL) are up to two times higher than those of GDL 3 (without MPL), although their actual thickness are close to each other ($\delta_{GDL1} = 235\ \mu m$, $\delta_{GDL3} = 190\ \mu m$). A possible explanation of this discrepancy is depicted in Figure 6.16: the MPL being highly hydrophobic, it retains liquid water that accumulates under the channel ribs in the backing layers. Without MPL, liquid water accumulation under the channel ribs is expected to be extended to the catalyst layer and to lead to a reduction of the diffusion thickness (1D diffusion, Figure 6.16(b)). With a MPL, the liquid water remains in the GDL and oxygen can diffuse through the entire catalyst layer (2D diffusion, Figure 6.16(a)). This can also explain the higher values of D^{eff} measured with GDL 1 than with GDL 3: a lower water content leading to higher porosities. This interpretation is consistent with the fact that over the first third of the air channel, where the MEA water content is lower, δ does not seem sensitive to the presence of the MPL. It is also consistent with the scenario proposed at the beginning of section 6.3 and with the experimental observations of section 6.3.1: liquid water accumulation in the GDL leads to a simultaneous decrease of the diffusion thickness δ and of the effective diffusion coefficient D^{eff}.

The curves in Figure 6.17 show the profiles of the mass diffusion resistance δ/D^{eff}. Like previously, δ/D^{eff} is mostly sensitive to the hydration of the active layer and consequently, it decreases steeply over the first segments. Then, there seems to be no significant effect of the presence of a MPL on δ/D^{eff}; however, it has to be kept in mind that the maximum average current density reaches only 0.67 Acm^{-2}, which is a moderate value.

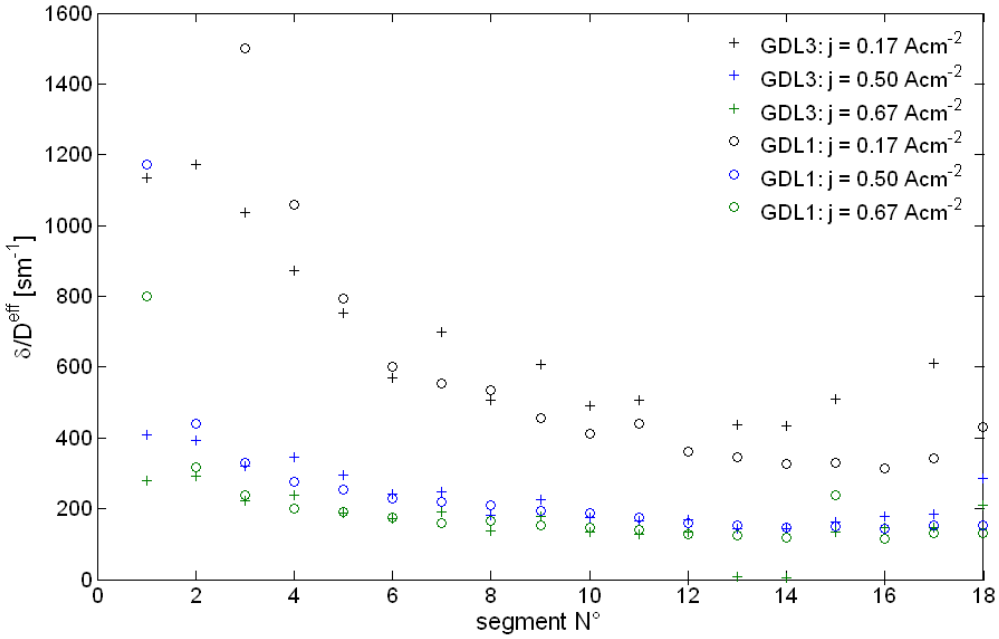


Figure 6.17: *Mass diffusion resistance δ/D^{eff} determined starting from the diffusion parameters of GDL 1 and GDL 3 (Figure 6.15).*

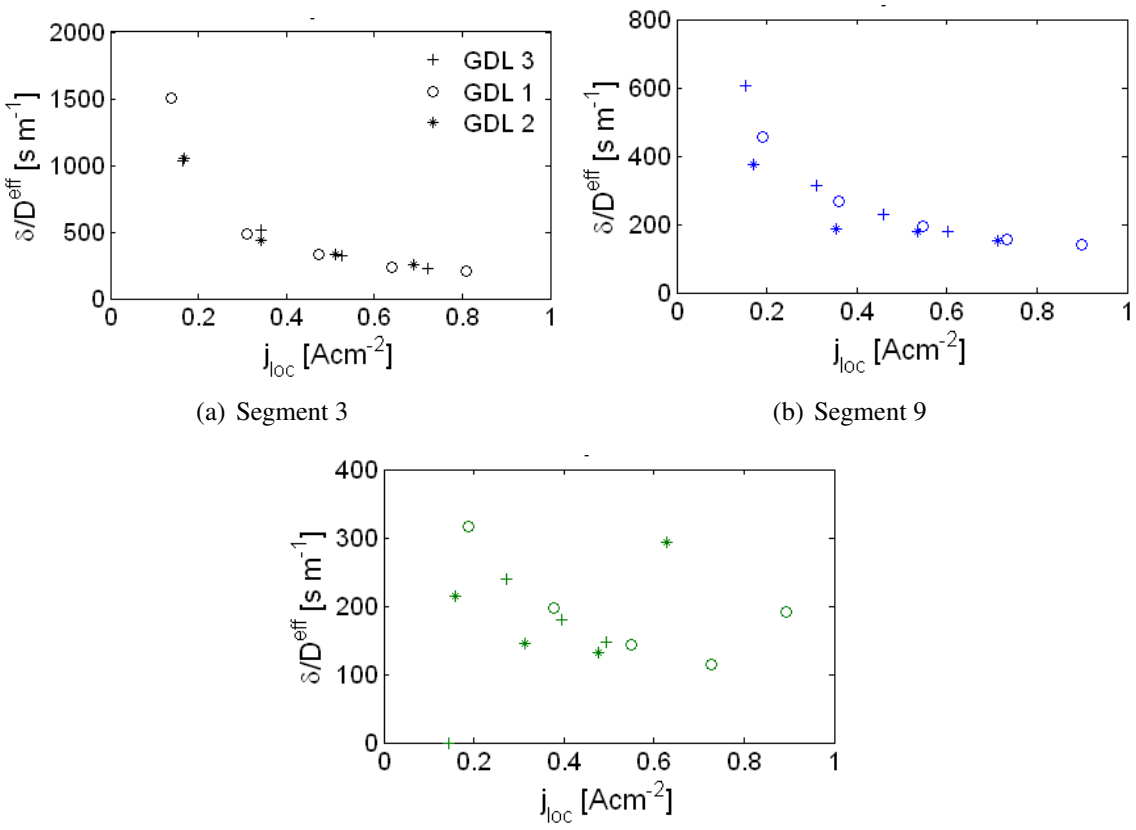
The profiles measured at $j = 0.17\ Acm^{-2}$ reflect mostly the higher dispersion of the data at low current density. They also show that probably, the hydration of the MEA is not optimal over a large part of the surface.

6.3.3 Role of the current density

Figures 6.12 and 6.15 show that independently of the GDL thickness and of the presence of a MPL, δ and D^{eff} increase with the current density. These evolutions seem to show that the amount of liquid water in the GDL tends to decrease at higher current density. Actually, an increase of the current density can result in various effects:

- A higher water production rate, with a subsequent better hydration of the active layer and consequently, an increase of δ and D^{eff} (considering oxygen diffusion through the microscopic layer of ionomer and/or liquid water covering the catalyst particles). On the contrary, if water leaves the active layer in liquid phase, one can also expect a decrease of δ and D^{eff} resulting from its presence within the GDL.
- A rise in the temperature of the electrodes and in the temperature difference between the electrodes and the flow field plates, which improves the convecto/diffusive flux of vapor toward the gas channels and which could consequently reduce the amount of liquid water in the GDL.

Starting from this reasoning, an increase of the current density could have different effects in terms of water management. As an increase of δ and D^{eff} with the current density is observed, it seems that in our conditions, there is a better hydration of the active layer resulting in an enhanced oxygen diffusion on a microscopic scale (through a liquid water or electrolyte film) and a drying of the GDL which allows a better diffusion through the gas pores on a macroscopic scale.



(a) Segment 3

(b) Segment 9

(c) Segment 16

Figure 6.18: *Mass diffusion resistance δ/D^{eff} determined with GDL 1, GDL 2 and GDL 3 for different segments along the air channel as a function of the current density.*

This interpretation is confirmed by the evolutions of the mass diffusion resistance δ/D^{eff} (Figure 6.18, for segments 3, 9 and 16) with the (local) current density: δ/D^{eff}, which is sensitive mostly to the hydration of the active layer, decreases significantly with the current density. This tendency is less marked in segment 16 (and more generally, at the exit of the air channel), possibly because of the higher dispersion of the initial data and/or because there is more liquid water in the GDL.

It would be interesting to repeat these experiments with higher average current densities in order to see whether other phenomena (drying of the active layer or on the contrary excess of water in the GDL) can be observed.

6.3.4 Conclusion of the section

To summarize the above results about oxygen transport through the porous layer of the cathode, the following conclusions can be drawn:

- The GDL is clearly not the only layer limiting oxygen transport.
- At high current densities, δ and D^{eff} depend on the characteristic of the GDL (the thickness and the presence of a MPL), showing that this layer becomes limiting in these conditions.

- At low current densities and near the air channel inlet (dry conditions), the diffusion parameters δ and D^{eff} do not depend on (the thickness of) the GDL, although they remain sensitive to the current density. This seems to show that the main resistance for oxygen transport originates mostly from the active layer. Note however that the parameter estimation is difficult to perform at low current densities, since the impedance data are significantly noised.

- The mass diffusion resistance δ/D^{eff} being independent of the GDL thickness and of the presence of a MPL, but decreases with the current density, we conclude that it seems to be sensitive mostly to the hydration of the active layer, at least in our operating conditions (average current density $\leq 0.84\ Acm^{-2}$).

- The presence of a MPL leads to higher diffusion coefficients at high current densities, probably because this layer limits liquid water accumulation under the channel ribs, which results in a 2D diffusion instead of a 1D diffusion when no MPL is present.

- When a MPL is present, a decrease of the high frequency resistance R_{hf} is observed. This can possibly be explained by a better electrical contact between the MEA components or by a better hydration of the ionomer. This latter explanation would be consistent with the hypothesis that MPL enhance the back-flow of the water produced by the ORR to the membrane [PWC05].

- The main effect of the current density seems to be in term of hydration of the ionomer in the catalyst layer. Its water content increases with the current density while that in the GDL decreases possibly. This could explain the increase of δ and D^{eff} with the current density (observed with all samples). In addition, this interpretation is confirmed by the evolution of the mass diffusion resistance δ/D^{eff}.

6.4 Low Frequency Limit of the 2D Convecto-Diffusive Impedance

The derivation of the pseudo 2D convecto-diffusive impedance in section 5.2 shows that convection is probably at the origin of the frequently observed discrepancy between the low frequency limit of the impedance spectra R_{lf} and the steady-state resistance R_{DC} determined from the slope of the polarization curve (DC: direct current). Figure 6.19 shows clearly that R_{DC} is lower than R_{lf} (the interception of the spectra with the real axis) even when considering local impedances: this difference is not linked to non-uniformities over the MEA surface. According to the 2D convecto-diffusive model, it corresponds to the additional resistance resulting from convection in the direction of the air channel R_{conv}. Our objective is thus to test this assumption experimentally. This is done starting from local impedance spectra measured with cell 2 in counter-flow: $\langle j_{cell}\rangle_t = 0.5\ Acm^{-2}$, $S_{H_2} = 1.2$, $S_{air} = 3$ and $RH_{H_2,air} = 0.6$ (Figure 6.19).

The expression of the low frequency limit ($\omega \to 0$) of the amplitude of the concentration oscillations $\Delta c_{O_2}(x=0,y)$ is derived in appendix B.3 (assuming the local current oscillations $\Delta j(y)$ uniform). At the position y_n along the channel direction, we have:

$$\Delta c_{O_2}(x=0,y_n) = -\left(\frac{y_n}{\alpha h V} + \frac{\delta}{D^{eff}}\right)\frac{\langle \Delta j\rangle_{y_n}}{4F} \tag{6.7}$$

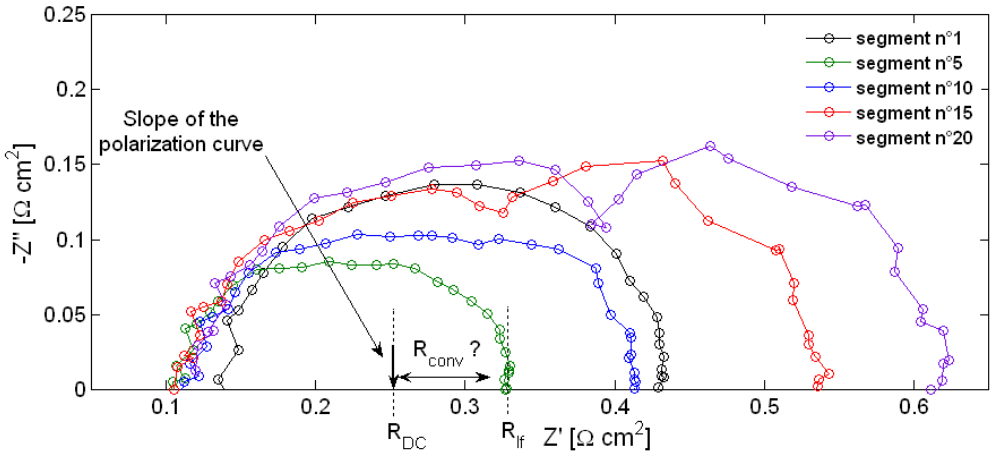


Figure 6.19: *Local spectra measured with cell 2 in counter-flow at a mean current density of* 0.5 Acm^{-2} *($S_{H_2} = 1.2$, $S_{air} = 3$, $RH_{H_2,air} = 0.6$): discrepancy between the low frequency limit R_{lf} of the impedance spectra and the steady-state resistance R_{DC} derived from the slope of the local polarization curves (DC: direct current).*

Introducing (6.7) in the expression of the local cell impedance $Z^{osc}(y_n)$ (6.3) allows to derive an analytical expression of its low frequency limit:

$$\lim_{\omega \to 0} \frac{\Delta E_{cell}}{-\langle \Delta j \rangle_{y_n}} = R_{hf}(y_n) + \frac{b(y_n)}{\langle j(y_n) \rangle_t} + \frac{b(y_n)}{4F \langle c_{O_2}(x=0,y_n) \rangle_t} \left(\frac{y_n}{\alpha h V} + \frac{\delta(y_n)}{D^{eff}(y_n)} \right) \tag{6.8}$$

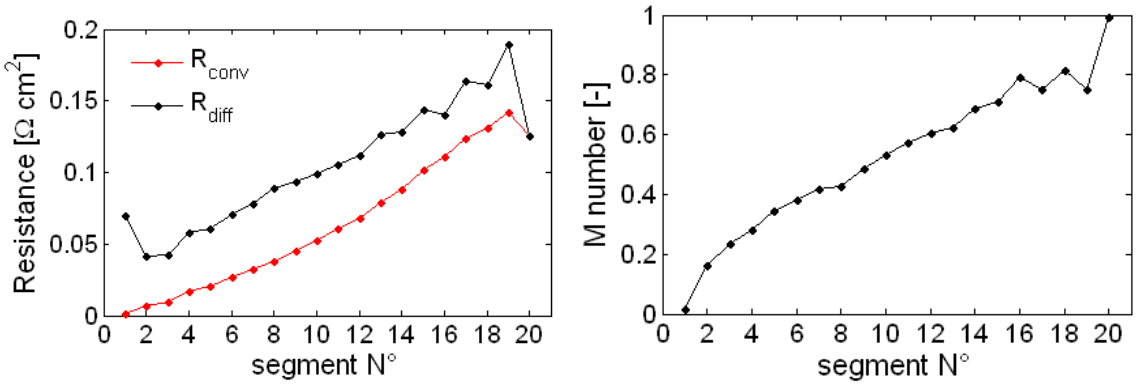
According to equation (6.8), the intercept of the local (and global) impedance spectra with the real axis is the sum of the high frequency resistance $R_{hf}(y_n)$, of the charge transfer resistance $R_{ct}(y_n) = b(y_n) / \langle j(y_n) \rangle_t$ and of the oxygen transport resistance, composed of two terms:

$$\text{The diffusion impedance:} \quad R_{diff}(y_n) = \frac{b(y_n)}{4F \langle c_{O_2}(x=0,y_n) \rangle_t} \frac{\delta(y_n)}{D^{eff}(y_n)} \tag{6.9}$$

$$\text{The convection impedance:} \quad R_{conv}(y_n) = \frac{b(y_n)}{4F \langle c_{O_2}(x=0,y_n) \rangle_t} \frac{y_n}{\alpha h V} \tag{6.10}$$

R_{diff} and R_{conv} (and thus the low frequency resistance (6.8)) can be calculated knowing the impedance parameters of the electrical equivalent circuit. Their profiles (Figure 6.20(a)) show that the convection resistance is null at the cathode inlet and rises along the channel due to the increasing impact of the concentration oscillations. Initially, R_{conv} is slightly higher than zero because on segment 1, y_n is low but not null. R_{diff} increases along the channel because of oxygen depletion. Again, the values of the first and last segments are to be considered carefully due to possible discrepancies in their active area compared to the other segments. Figure 6.20(b) shows the profile of the corresponding M number - $M = \frac{y_n D^{eff}}{2V \alpha h \delta}$ (5.45) - giving the ratio between the contributions of convection and diffusion to the low frequency resistance: at the channel inlet, M is almost equal to zero and convection can be neglected. At the cell outlet, the contribution of convection to the oxygen transport resistance is close to that of diffusion ($M \approx 0.8$ in segment 19).

Figure 6.21 shows a comparison between the low frequency limit of the local impedance spectra



(a) (b)

Figure 6.20: *Profiles of (a) R_{conv} and R_{diff}, the two terms in the low frequency limit of the oxygen transport impedance and (b) of their ratio (M number).*

R_{lf} (blue dots) and the sum $R_{hf}+R_{ct}+R_{diff}+R_{conv}$ (red dots) calculated with (6.8) starting from the impedance parameters. Over the first 12 segments, their values fit very well together. The slight difference observed on the last segments could have different origins:

- Non-uniform current density oscillations ($\langle \Delta j \rangle_t$) or a varying air flow rate along the channel, whereas the model assumes that they are constant over the whole MEA.
- Physical phenomena (adsorption of reaction intermediates, platinum dissolution and/or oxidation... cf. section 3.1.2) leading to an inductive impedance in the low frequency domain, which would affect the determination of R_{lf}.

It is worth mentioning that the value of the channel depth h has no impact on the estimation of R_{conv}, because this resistance depends on the product $h \times V$ (the gas flow rate) assumed uniform along the channel.

According to equation (6.8), the steady-state resistance R_{DC} can be obtained by subtracting the convection resistance R_{conv} from the low frequency resistance R_{lf}. For this, the steady-state resistance R_{DC} of each segment is derived from the slope of the polarization curve (Figure 6.22) at $j = j_{loc}$ (with j_{loc} measured at $j_{glob} = 0.5\ Acm^{-2}$). Note that the actual values of the local current density j_{loc} vary between 0.35 Acm^{-2} and 0.55 Acm^{-2}.

Figure 6.23 presents the profiles of:

- The low frequency resistance R_{lf} identified from the intercept of the local impedance spectra with the real axis (red dots).
- R_{lf} minus the convection resistance, $R_{lf} - R_{conv}$ (black dots).
- The steady-state resistance R_{DC} derived from the slope of the local polarization curves (blue dots).

At the cell inlet, the discrepancy between the three curves is the smallest, because the impact of convection on the impedance is negligible. The discrepancy between R_{lf} and R_{DC} increases significantly along the channel: at the cell outlet, R_{lf} is about 2 times higher than the steady-state

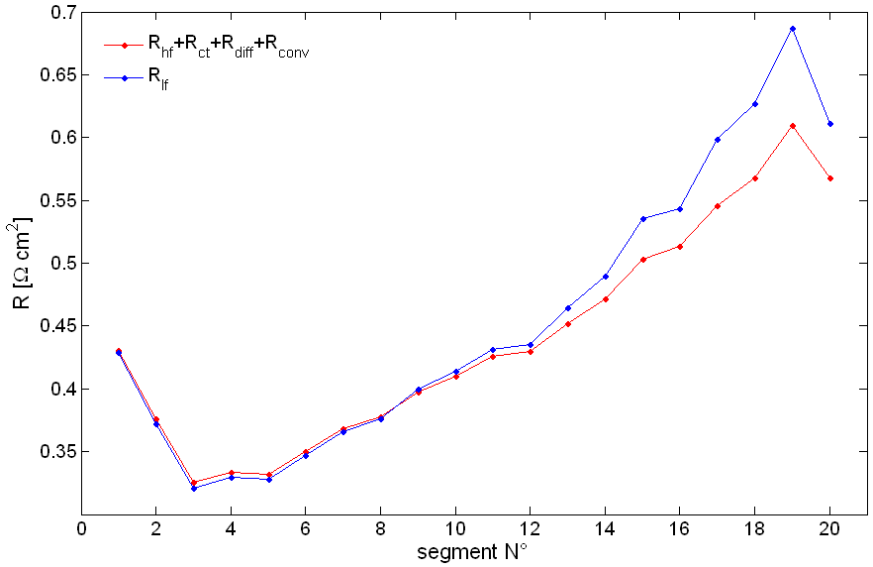


Figure 6.21: *Low frequency resistances of cell 2 calculated starting from the intercept of the local impedance spectra with the real axis R_{lf} (blue dots) and from the low frequency limit of the 2D convecto-diffusive impedance* (6.8) *(red dots).*

resistance R_{DC}. The discrepancy between R_{DC} and the values obtained by EIS is significantly reduced after subtracting the convection resistance R_{conv} from R_{lf}. However, a difference remains, which seems to be quite uniform, with variations $(R_{lf} - R_{conv} - R_{DC})$ of about 20% of the average value of R_{DC} over segments 2 to 19 (Figure 6.24). By comparison, $(R_{lf} - R_{DC})$ reaches almost 70% of R_{DC} at the air outlet.

Two main conclusions can be drawn from these results:

- Considering the convection resistance R_{conv} allows to reduce the discrepancy between the low frequency limit of the impedance spectra and the steady-state resistance derived from the slope of the polarization curves.
- However, the concentration oscillations are not the only origin of this difference. After subtracting R_{conv} from R_{lf}, a remaining discrepancy of about 20% is still observed. This discrepancy is most probably an artifact that comes from the fact that the intercept of the impedance spectra with the real axis is not observed at 0 Hz, but - depending on the segment - at frequencies comprised between 0.79 Hz and 0.13 Hz: inductive loops (linked to physical phenomena) and/or a pronounced scattering (possibly because of the impact of liquid water on the impedance) in the low frequency domain (cf. section 3.3).

6.5 Summary of the Chapter

A first set of experiments is used for analyzing global impedance spectra in the presence of a convective flux (characterized by the water transport coefficient α) in the direction perpendicular to the electrode (1D convecto-diffusive model 4.1). One can notice that the Warburg impedance tends to overestimate D^{eff} if this convective flux adds to diffusion ($\lambda < 0.5$) and to underestimate D^{eff} when it is oriented in the direction opposite to diffusion ($\lambda < 0.5$). Logically, this tendency is more pronounced at high current densities. However, above $j_{cell} = 1.2\ Acm^{-2}$, the parameter

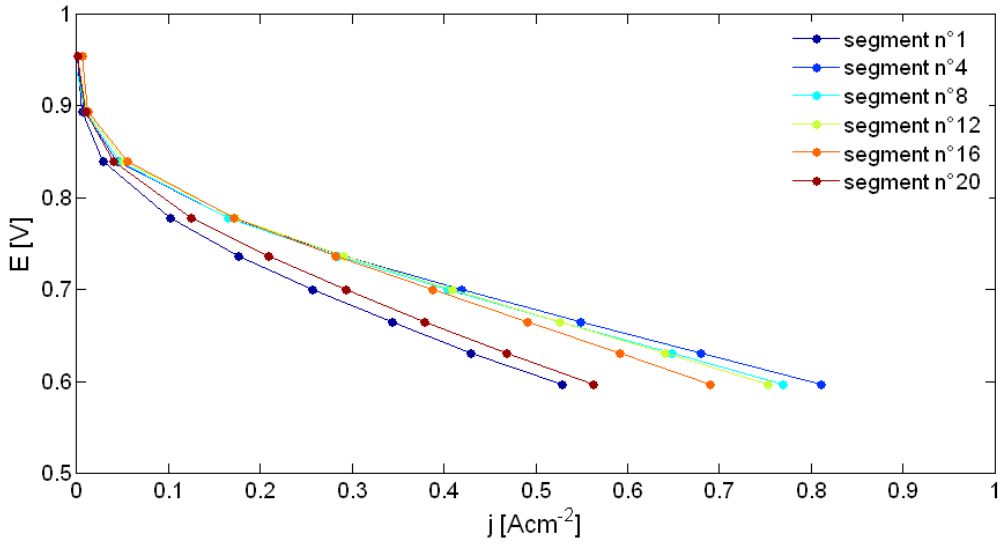


Figure 6.22: *Local polarization curves of cell 2;* $j_{glob} = 0.5\ Acm^{-2}$. $S_{H_2} = 1.2$, $S_{air} = 3$.

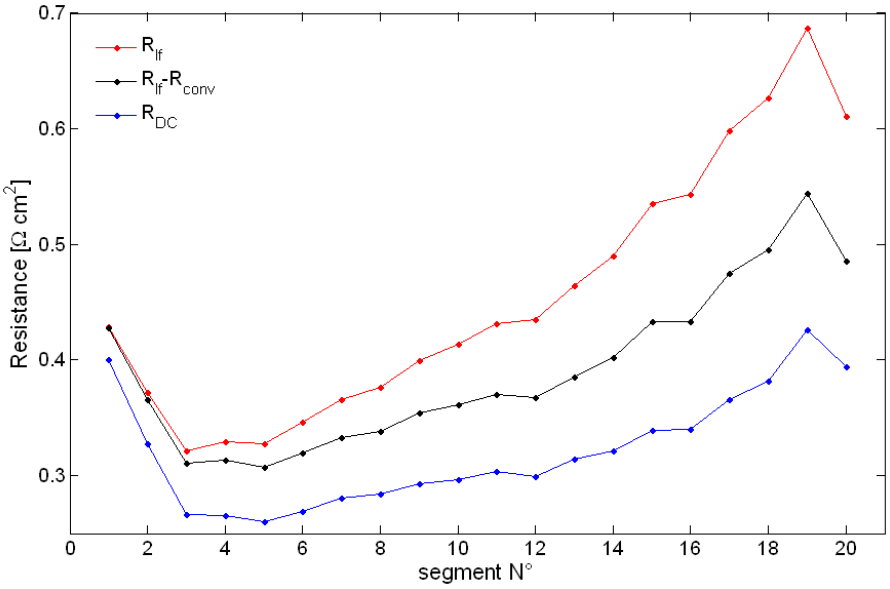


Figure 6.23: *Low frequency resistance* R_{lf} *determined from the intercept of the local impedance spectra with the real axis (red dots),* R_{lf} *minus the convection resistance* R_{conv} *(black dots) and steady-state resistance* R_{DC} *derived from the slope of the local polarization curves (blue dots). According to* (6.8)*, one should have* $R_{DC} = R_{lf} - R_{conv}$.

estimation is not possible, probably because the model parameters are correlated with each other or because other phenomena govern the impedance. This shortcoming could also be linked to the model hypothesis that all water is expected to be evacuated in vapor form, which is most certainly not realistic. The evacuation of liquid water should be included in the model. Note that in any case, convection perpendicular to the electrode does not modify drastically the values of δ and of D^{eff}, at least in the analyzed conditions. This leads to the conclusion that it can be neglected for a first estimation of the diffusion parameters, all the more so at moderate current density.

In the second part of the chapter, the diffusion parameters δ and D^{eff} estimated starting from

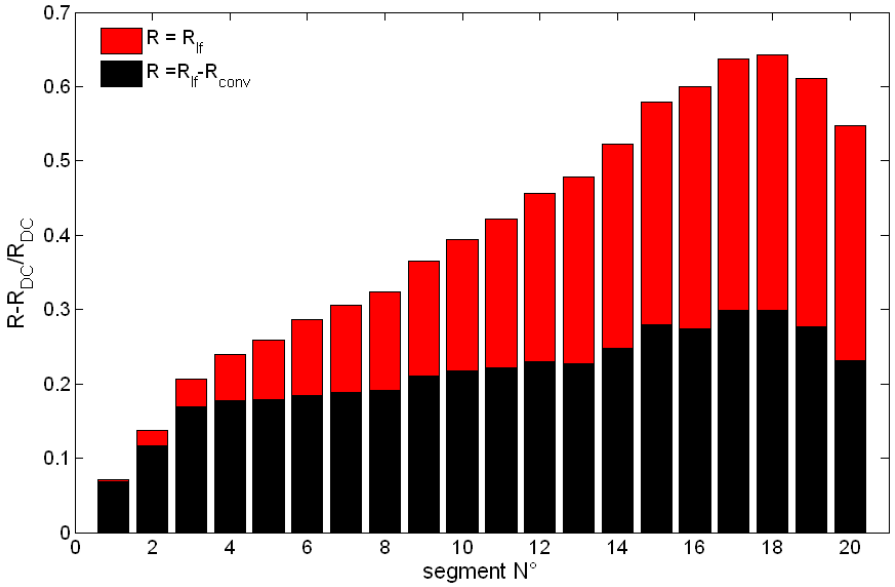


Figure 6.24: *Residual difference between R_{lf} or $R_{lf} - R_{conv}$ and the steady-state resistance R_{DC}: $\Delta R = R/R_{DC} - 1$. Red bars: $R = R_{lf}$; black bars: $R = R_{lf} - R_{conv}$.*

local impedance spectra using the classical Warburg impedance or the two pseudo-2D impedances are compared with each other: the results point out that AC induced concentration oscillations propagating along the channel by convection and oxygen consumption affect significantly the estimation of the local (and thus global) impedance parameters. This study shows that concentration oscillations govern the impedance at low frequencies, which confirms the necessity of including them in the oxygen transport models. Furthermore, the choice of the model affects also the estimation of the Tafel slope: with the 2D convecto-diffusive impedance, b remains uniform along the channel, whereas it increases with the (1D and local) Warburg impedances.

In the third part of the chapter, a discussion is opened about the limiting layer for oxygen transport and the phase in which it diffuses (gas or liquid) starting from the profiles of δ and D^{eff} identified with the 2D convecto-diffusive impedance. The first results are completed by a series of tests carried out using GDL of different thickness, with and without a MPL. It seems that at low current densities and near the air channel inlet (dry conditions), microscopic oxygen diffusion through a liquid water or electrolyte film in the active layer is limiting for oxygen transport, whereas the impact of the GDL increases with the current density. Furthermore, some preliminary conclusions about the role of MPL can be drawn: at high current densities, the MEA with MPL exhibits a higher diffusion coefficient, most probably because it avoids blocking of the reaction sites by liquid water accumulation under the channel ribs. The high frequency resistance is also lower with a MPL, which could be explained by a better electrical contact between the MEA components or a better ionomer hydration. However, these conclusions have to be considered carefully, because they rely on scenarios about liquid water accumulation in the MEA and about their effects on oxygen transport that must be confirmed experimentally (at different current densities, gas humidification, gas flow rates ...). Note also that the spectra measured at low current density are significantly noised.

Finally, the last part of the chapter is a discussion about a commonly observed shortcoming of EIS: the discrepancy between the low frequency limit of the impedance spectra R_{lf} and the steady-state resistance derived from the slope of the polarization curve R_{DC}. It appears clearly that the

convection resistance R_{conv} resulting from concentration oscillations along the channel represents the main contribution to this discrepancy. However, accounting for this phenomenon does not suffice to obtain identical values of R_{lf} and R_{DC}: there remains a difference equal to about 20% of the steady-state resistance R_{DC}, independently of the location along the channel. This could be due to artifacts of impedance spectroscopy or to the physical phenomena leading to the existence of a low frequency inductive loop like adsorption of reaction intermediates, oxidation, etc.

7 Conclusions and Perspectives

The main objective of this Ph.D thesis is to contribute to a better understanding of the low frequency loop in the impedance spectra of H_2/air PEMFC. This low frequency loop is usually associated with oxygen transport and it can be the source of information about the main origin(s) of the so-called diffusion impedance.

For this, different oxygen transport impedances alternative to the 1D finite Warburg element are proposed. They account for various processes in addition to diffusion in the directions perpendicular and parallel to the electrode. These expressions are implemented in an equivalent electrical circuit aiming to simulate the impedance of the cell. By comparing experimental and numerical results, it is possible to determine the impedance parameters characterizing the physical and electrochemical processes occurring in the MEA. In order to perform impedance measurements with a spatial resolution over the MEA surface, instrumented cells with a segmented current collection at the cathode, designed and built in our group, are used.

In a first step, the cell impedance is modeled by a Randles EEC, in which the oxygen transport is represented by the one-dimensional finite Warburg element. In chapter 3, a sensitivity analysis shows that in typical operating conditions and over the frequency range 0.4 Hz - 200 Hz, the model parameters are sufficiently uncorrelated to allow their simultaneous estimation. Furthermore, it is confirmed that the anode has no significant impact on the estimation of the cathode parameters and that its contribution to the cell impedance can be neglected. Some preliminary results are presented in this chapter, with the aim to test the limits of the hypotheses leading to the expression of the Warburg impedance (one-dimensional description, oxygen transport by diffusion only, surface reaction, uniform concentration along the air channel). The estimated values of the model parameters (R_{hf}, R_{ct}, C_{dl}, R_d^{1D}, τ_d) are in ranges usually encountered in the literature, which confirms the validity of this EEC for a first interpretation of local impedance spectra. Then, the impedance parameters are used for an estimation of those characterizing the charge transfer at the electrode (b, α_c) and the oxygen diffusion (δ, D^{eff}, ε). At this stage, the only possible interpretation of their profiles (along the air channel) seems to be in terms of water content.

The profiles of the oxygen diffusion parameters δ and D^{eff} are interpreted with reference to two different length scales (macroscopic point of view: referring to the MEA flat surface A_{geom}; microscopic point of view: referring to the catalytic active area γA_{geom}). Depending on the considered length scale, the identified values of the diffusion parameters are actually in ranges typical of gas diffusion through the pores of the backing and active layers (macroscopic approach) or of liquid diffusion through an electrolyte or liquid water film covering the agglomerates. However, their profiles obtained with the 1D Warburg impedance lead sometimes to contradicting interpretations and thus, a clear identification of the layer limiting the oxygen transport and of the phase in which it diffuses is not possible. This confirms the necessity of a more elaborate model.

One-dimensional and pseudo two-dimensional models accounting for phenomena not considered in the classical Warburg approach are developed in chapters 4 and 5. In a first step, the impact of these phenomena on the cell impedance is analyzed numerically.

The first 1D impedance model considers convection in the direction perpendicular to the elec-

trode. The second accounts for the finite proton conductivity and oxygen consumption in the catalyst layer:

- Convection in the direction perpendicular to the electrode depends on the vapor flux though the GDL characterized by the water transport coefficient α. The usual description of oxygen transport leading to the Warburg impedance assumes a purely diffusive flux ($\alpha = 0.5$), which is not always verified. Numerical and experimental results are presented in sections 4.1 and 6.1. Both lead to the same conclusions, which are:
  - The classical Warburg impedance tends to underestimate the diffusion parameters when convection is oriented in the direction opposite to diffusion. On the contrary, if the convective flux is in the same direction as diffusion, D^{eff} and δ are overestimated.
  - At high current densities, parameter estimation is not possible with the 1D convecto-diffusive impedance: phenomena not considered in the model (like the evacuation of liquid water) may govern the cell impedance or there may be correlations between the parameters in these conditions.
  - At moderate current densities ($j_{cell} \leq 0.5\ Acm^{-2}$) and for a first estimation of the diffusion parameters, convection perpendicular to the electrode can be neglected.
- The second one-dimensional model allows to analyze the impact on the cell impedance of the finite proton conduction of the ionomer in the catalyst layer and of oxygen consumption along the thickness of the electrode. This model is based on the works of Eikerling and Kornyshev [EK99]. The numerical simulations lead to two main conclusions:
  - It can be shown that the straight line at 45° observed at high frequencies is not caused by diffusion (Warburg behavior) but is related to the porous structure of the electrode. This straight line always exists, whatever the values of the model parameters. However, it extends to lower frequencies with increasing values of the protonic resistance ρ_p. ρ_p does not affect the high frequency resistance, but it has a significant impact on the size of the spectra at intermediate and low frequencies, and thus on the low frequency resistance.
  - The impedances related to macroscopic oxygen diffusion and to proton transport through ionomer in the catalyst layer seem to appear in the same frequency range: they govern the impedance at intermediate frequencies. This leads to the conclusion that macroscopic (gas) diffusion in the catalyst layer is not at the origin of the separate low frequency loop observed usually in PEMFC impedance spectra (for frequencies $\leq 10\ Hz$). This loop seems thus to be caused by (i) macroscopic gas diffusion through the GDL, by (ii) microscopic diffusion through a liquid or electrolyte film covering the agglomerates of the active layer, or by (iii) phenomena occurring in the channel direction (oxygen depletion and concentration oscillations induced by the AC measuring signal). It would be interesting to include this electrode model in the cell impedance description. However, considering its complexity (no analytical solution, numerical solution only by discretizing the electrode in a finite number of slices), it is possible that some parameters are correlated, which would make their independent estimation impossible.

In the pseudo 2D models, all transport phenomena perpendicular to the electrode, apart from diffusion, are neglected, but the impact of oxygen depletion in terms of DC and AC effects on the cell impedance is considered:

- The first oxygen transport impedance is a simple expression alternative to the classical Warburg impedance that accounts for a decrease in the steady-state oxygen concentration along the gas channel as alternative boundary condition. Numerical studies with this local Warburg impedance show that oxygen consumption affects the local impedance spectra at low frequencies ($\nu \leq 10\ Hz$) and thus their interpretation in terms of oxygen transport through the cathode porous media. Furthermore, this approach allows to estimate easily the critical conditions (air stoichiometry, GDL thickness, current density ...) for which no oxygen reaches the reaction sites near the air channel outlet. These results are published in the *Journal of the Electrochemical Society* [MMD$^+$10a].

- Experimental works of Schneider *et al.* [SFK$^+$07, SKWS07] put forward that the AC measuring signal induces concentration oscillations that propagate along the air channel by convection and influence the impedance spectra especially in the low frequency domain: their results indicate that the low frequency loop seems to originate mainly from the propagation of these concentration oscillations. Starting from these observations, a pseudo-2D convecto-diffusive oxygen transport impedance is derived in the second part of chapter 5 considering these concentration oscillations. The first numerical results put forward that convection along the air channel affects the impedance spectra mainly in the low frequency domain and that their neglect would lead to wrong conclusions about oxygen transport. A non-dimensional number M is introduced that allows to estimate in which conditions this convective flux is negligible compared to diffusion. Furthermore, it appears that the concentration oscillations can be a possible explanation of the currently observed discrepancy between the low frequency limit of impedance spectra and the steady-state resistance derived from the slope of the PEMFC polarization curve. This hypothesis is confirmed experimentally in chapter 6.4.

The numerical results obtained with the pseudo-2D models are compared to experimental results in chapter 6. Firstly, a comparison of the profiles of δ and D^{eff} obtained starting from parameter estimation with the 1D Warburg impedance and with the two pseudo-2D impedances (local Warburg impedance and 2D convecto-diffusive impedance) is presented. The results confirm that oxygen consumption and concentration oscillations have to be included in the modeling: they affect significantly the profiles of the (estimated) diffusion parameters. In addition, it can be shown that the choice of the oxygen transport model affects also the identification of the Tafel slope b: b is nearly uniform along the air channel with the 2D convecto-diffusive impedance, whereas it increases between the inlet and outlet with the finite Warburg impedance. This discrepancy is most probably due to correlations between the parameters of the Randles EEC at intermediate frequencies, which confirms once again the interest of the 2D convecto-diffusive impedance.

Then, a discussion is opened about the limiting layer for oxygen transport and about the phase in which oxygen diffuses (gas or liquid) starting from local spectra measured in co- and counterflow and using GDL of different thickness, with and without MPL. The profiles of the diffusion parameters δ and D^{eff} are interpreted in terms of water content in the MEA. The 2D convecto-diffusive impedance allows more consistent conclusions than the finite Warburg impedance, which are:

- At low current densities and near the air channel inlet (dry conditions), δ and D^{eff} do not depend on the characteristics of the GDL. This leads to the conclusion that, in these conditions, the main contribution to the oxygen transport impedance results from the active layer.

- At high current densities, the diffusion parameters depend on the characteristics of the GDL (the thickness and the presence of a MPL) showing that this layer becomes limiting in these conditions.

- The mass diffusion resistance δ/D^{eff} decreases when the current density increases, but it is independent of the GDL characteristics: this seems to show that δ/D^{eff} is sensitive mainly to the hydration of the ionomer present in the active layer.

- The presence of a MPL leads to lower values of the high frequency resistance R_{hf} (associated with electronic conduction) and to a higher diffusion coefficient D^{eff} at high current densities. These results are consistent with the hypothesis that MPL enhance the back-flow of the water produced by the ORR to the membrane [PWC05].

Finally, the last part of chapter 6 is a discussion about the discrepancy between the low frequency limit of the impedance spectra R_{lf} and the steady-state resistance derived from the slope of the polarization curve R_{DC}. It can be shown that the convection resistance R_{conv} associated with the propagation of concentration oscillations in the air channel reduces significantly the difference between R_{lf} and R_{DC}. However, concentration oscillations are not its only origin: a difference of about 20% of R_{DC} is still observed when subtracting R_{conv} from R_{lf}, which could be explained by an inductive behavior and/or by a pronounced scattering (possibly because of the impact of liquid water on the impedance) of the spectra at low frequencies.

To summarize the results of this work, it was shown the one- and two-dimensional expressions of the oxygen transport impedance derived in this work allow more consistent interpretations of local (and global) impedance spectra of H_2/air PEMFC than the finite Warburg element. Depending on the working conditions, several phenomena can be neglected before the others and the impedance model should be chosen accordingly. It would be interesting to derive a model including all the phenomena that are considered separately in this work. However, such a model may be too complex to allow the simultaneous estimation of all model parameters and it could be more reasonable to adapt the hypotheses to the analyzed system.

This work confirms also that the low frequency loop is caused mainly by concentration oscillations in the gas channel. They have to be considered in order to avoid misinterpretations of the impedance spectra.

Some other perspectives of this Ph.D thesis are beginning to be developed within the framework of three projects that started recently in our group:

- The Ph.D thesis of Anthony Thomas, who focuses mostly on the impact of a temperature difference (between the anode and cathode plates) on the net flux of water through the membrane (*i.e.* on the water transport coefficient). The main objectives of this work are to come to a detailed understanding of the mechanisms governing water fluxes through the cell. In this context, the identification of the diffusion coefficients δ and D^{eff} thanks to EIS brings useful information.

- The Ph.D thesis of Adrien Lamibrac, who addresses the interplay between transport phenomena and PEMFC aging/degradations, mostly during stop and start sequences. EIS is one of the most adapted tools to monitor (vs. time) the local performance of a segmented cell subjected to various solicitations.

- The H2E ("Hydrogène Horizon Energy") program in which the fuel cell group participates, under the leadership of Air Liquide, mostly by applying the experimental methods and techniques developed during these three Ph.D theses, with the objective to improve the efficiency and the reliability of the fuel cells and fuel cell systems made by Axane.

Appendices

A Determination of the Species Concentration with the 1D Warburg Diffusion Model

This appendix gives a detailed derivation of the expressions of the reactant concentrations in DC and AC conditions according to the one-dimensional Warburg approach in the case of a Redox reaction whose rate follows a Butler-Volmer law (3.14). It is assumed that $j_f > 0$ and $\eta_{act} > 0$ so that the reductant is the consumed species and the oxidant the produced species in the forward reaction direction.

In AC conditions, the system properties $X(t)$ (with $X = j_f$ and η_{act}) oscillate around their steady-state values $\langle X \rangle_t$ which provokes an oscillation of the species concentrations $\Delta c_k(x,t)$ (with $k = Ox$, Red). In an established periodic regime, the concentration variations take the form:

$$\Delta c_k(x,t) = c_k(x,t) - \langle c_k(x) \rangle_t = \Delta \bar{c}_k(x) \exp(i\omega t), \quad \text{with } k = Red/Ox \tag{A.1}$$

The mass transport is described by the Fick equations:

$$1^{st}\text{Fick's law:} \qquad \mp \frac{j_f}{\frac{n}{n_{Red}}F} = -D_k^{eff} \left.\frac{\partial c_k}{\partial x}\right|_{x=0} \tag{A.2}$$

$$2^{nd}\text{Fick's law:} \qquad \frac{\partial c_k}{\partial t} = D_k^{eff} \frac{\partial^2 c_k}{\partial x^2} \tag{A.3}$$

For convenience, the sign of the consumed species (Red) will be noted at the upper side and the one of the produced species (Ox) at the lower side in the following equations.

The time-averaged value of the reactant concentration $\langle c_k(x) \rangle_t$ corresponds to the steady-state solution the 2nd Fick diffusion equation:

$$0 = D_k^{eff} \frac{\partial^2 \langle c_k(x) \rangle_t}{\partial x^2} \tag{A.4}$$

in the boundary conditions of the Warburg approach (Figure 3.10):

$$\text{At } x = \delta: \quad \langle c_k(x = \delta) \rangle_t = c_k^* \tag{A.5}$$

$$\text{At } x = 0: \quad N_k = \mp \frac{\langle j_f \rangle_t}{\frac{n}{n_{Red}}F} = -D_k^{eff} \left.\frac{\partial \langle c_k \rangle_t}{\partial x}\right|_{x=0} \tag{A.6}$$

This yields:

$$\langle c_k(x)\rangle_t = c_k^* \mp \frac{\langle j_f\rangle_t}{\frac{n}{n_{Red}}F}\frac{\delta - x}{D_k^{eff}} \tag{A.7}$$

In order to determine the concentration variations $\Delta\bar{c}_k(x)$, the 2nd Fick law has to be solved in AC conditions where the boundary conditions take the form:

$$\text{At } x=\delta: \quad \Delta\bar{c}_k(x=\delta) = 0 \tag{A.8}$$

$$\text{At } x=0: \quad \mp\frac{\Delta\bar{j}_f}{\frac{n}{n_{Red}}F} = -D_k^{eff}\left.\frac{\partial\Delta\bar{c}_k}{\partial x}\right|_{x=0} \tag{A.9}$$

Inserting the concentration variation (A.1) in the 2nd Fick equations (A.3) leads to:

$$i\omega\,\Delta\bar{c}_k(x) = D_k^{eff}\frac{\partial^2\Delta\bar{c}_k(x)}{\partial x^2} \tag{A.10}$$

whose general solution is:

$$\Delta\bar{c}_k(x) = A\cosh\left(\sqrt{\frac{i\omega}{D_k^{eff}}}x\right) + B\sinh\left(\sqrt{\frac{i\omega}{D_k^{eff}}}x\right) \tag{A.11}$$

The boundary condition at the reaction interface (A.9) allows to determine the factor B:

$$\mp\frac{\Delta\bar{j}_f}{\frac{n}{n_{Red}}F} = -D_k^{eff}\sqrt{\frac{i\omega}{D_k^{eff}}}\left[A\sinh\left(\sqrt{\frac{i\omega}{D_k^{eff}}}(x=0)\right) + B\cosh\left(\sqrt{\frac{i\omega}{D_k^{eff}}}(x=0)\right)\right] \tag{A.12}$$

$$\Rightarrow B = \pm\frac{\Delta\bar{j}_f}{\frac{n}{n_{Red}}F\sqrt{i\omega D_k^{eff}}} \tag{A.13}$$

The factor A is obtained with the boundary condition at the diffusion medium inlet (A.8):

$$A = -B\tanh\left(\sqrt{\frac{i\omega}{D_k^{eff}}}\delta\right) = \mp\frac{\Delta\bar{j}_f}{\frac{n}{n_{Red}}F\sqrt{i\omega D_k^{eff}}}\tanh\left(\sqrt{\frac{i\omega}{D_k^{eff}}}\delta\right) \tag{A.14}$$

The local instantaneous reagent concentration is finally obtained by combining (A.7) and (A.11):

$$\begin{aligned} c_k(x,t) &= \Delta c_k(x,t) + \langle c_k(x)\rangle_t \\ &= \mp\frac{\Delta\bar{j}_f}{\frac{n}{n_{Red}}F\sqrt{i\omega D_k^{eff}}}\frac{\sinh\left(\sqrt{\frac{i\omega(\delta-x)^2}{D_k^{eff}}}\right)}{\cosh\left(\sqrt{\frac{i\omega\delta^2}{D_k^{eff}}}\right)}e^{i\omega t} + c_k^* \mp \frac{\langle j_f\rangle_t}{\frac{n}{n_{Red}}F}\frac{\delta - x}{D_k^{eff}} \end{aligned} \tag{A.15}$$

B Detailed Derivation of the Expressions of the 2D Convecto-Diffusive Impedance Model

In the following, the solution of the equations of the 2D convecto-diffusive impedance model accounting for oxygen concentration variations in the gas channel is presented in detail. Appendix B.1 presents the solution in steady state and appendix B.2 the dynamic solution.

B.1 Derivation of the Steady-State Oxygen Concentration

The local oxygen concentration in steady-state $c_{O_2}(x,y)$ can be determined with the oxygen molar ratio $y_{O_2}(x)$ in the channel $(y=0)$ given by:

$$y_{O_2}(x) = \frac{N_{O_2}(x)}{N_{O_2}(x) + N_{N_2} + N^{vap}_{H_2O}(x)} \tag{B.1}$$

where N_i denotes the molar flux density of species i ($i = O_2$, N_2, H_2O) in x-direction. Nitrogen being inert its flux is uniform along the channel length. We can write the oxygen and the water vapor molar flux density (in $mol/s/m^2$) as functions of the current density $j(x)$:

$$N_{O_2}(x) = N^{in}_{O_2} - \int_0^x \frac{j(x)}{4F} dx \tag{B.2}$$

In the case of the vapor flux density, a distinction has to be made between an under-saturated and a saturated flow.

B.1.1 Under-saturated flow: $P_{H_2O} < P_{sat}$

It is necessary to make an assumption about the amount of water produced at the cathode that passes through the membrane in the direction of the anode compartment. The influence of the water transfer coefficient on the impedance response has been discussed in section 4.1. For thin membranes this coefficient is commonly of about 50% (half of the produced water crosses the membrane)[CCD+09]. This leads to the following expression of the vapor flux density:

$$N_{H_2O}^{vap}(x) = N_{H_2O}^{in} + \frac{1}{2}\int_0^x \frac{j(x)}{2F}dx \tag{B.3}$$

Inserting (B.2) and (B.3) in (B.1) yields:

$$y_{O_2}(x) = \frac{N_{O_2}^{in} - \int_0^x \frac{j(x)}{4F}dx}{N_{O_2}^{in} + N_{N_2} + N_{H_2O}^{in}} \tag{B.4}$$

Assuming air behaving like an ideal gas, the oxygen concentration in the channel is given by:

$$c_{O_2}(x, y=0) = y_{O_2}(x)\frac{P}{RT} \tag{B.5}$$

Where P is the total pressure, R the ideal gas constant and T the temperature. The oxygen (or air) stoichiometry S_{O_2} is defined as the ratio between the molar flux at the air channel inlet $N_{O_2}^{in}$ and the consumed amount:

$$S_{O_2} = \frac{N_{O_2}^{in}}{\int_0^L \frac{j(x)}{4F}dx} \tag{B.6}$$

The nitrogen molar flux density is proportional to oxygen molar flux density at the channel inlet. $c_{O_2}^*$ denoting the oxygen concentration in dry air ($0.21P/RT$), it comes:

$$\frac{c_{O_2}^*}{P/RT} = \frac{N_{O_2}^{in}}{N_{N_2} + N_{O_2}^{in}} \tag{B.7}$$

The molar flux density of water vapor at the cathode inlet is a function of the oxygen molar flux density and of the absolute humidity H (expressed in mol_{H_2O}/mol_{dryair}):

$$N_{H_2O}^{in} = H(N_{O_2}^{in} + N_{N_2}) \tag{B.8}$$

which makes it possible to express the oxygen concentration at the cathode inlet as:

$$c_{O_2}^{in} = \frac{c_{O_2}^*}{1+H} \tag{B.9}$$

Combining equations (B.3) - (B.9) leads finally to:

$$c_{O_2}(x, y=0) = \frac{c_{O_2}^*}{1+H}\left[1 - \frac{\int_0^x j(x)dx}{S_{O_2}\int_0^L j(x)dx}\right] \tag{B.10}$$

In order to obtain the oxygen concentration at the electrode/membrane interface ($y = \delta$), it is necessary to consider the decrease due to the Fickian diffusion (cf. appendix A). The diffusion medium is characterized by its thickness δ and its effective diffusivity D^{eff}. The model remains valid whatever is this diffusion medium: the backing layer, the catalyst layer, or a small liquid or polymer layer coating the carbon-platinum aggregates:

$$c_{O_2}(x,y=\delta) = \frac{c^*_{O_2}}{1+H}\left[1 - \frac{\int_0^x j(x)dx}{S_{O_2}\int_0^L j(x)dx}\right] - \frac{j(x)\delta}{4FD^{eff}} \tag{B.11}$$

B.1.2 Saturated flow: $P_{H_2O} = P_{sat}$

The vapor molar flux density is imposed by:

$$N^{vap}_{H_2O}(x) = \frac{P_{sat}}{P - P_{sat}}(N_{O_2}(x) + N_{N_2}) \tag{B.12}$$

Assuming the oxygen consumption can be neglected by comparison with the sum of air and vapor molar fluxes $\left(N_{O_2}(x) + N_{N_2} \approx N^{in}_{O_2} + N_{N_2}\right)$, the oxygen concentration in the channel becomes:

$$c_{O_2}(x,y=0) = c^*_{O_2}\left(1 - \frac{P_{sat}}{P}\right)\left[1 - \frac{\int_0^x j(x)dx}{S_{O_2}\int_0^L j(x)dx}\right] \tag{B.13}$$

Note that in usual conditions, with an air stoichiometric ratio of 2.5, a temperature of 70°C ($P_{sat} = 3\,10^4$ Pa) and a total pressure of 10^5 Pa, the decrease in the oxygen flux density along the cathode compartment represents only 6% of the molar flux density of saturated air at the channel inlet.

Finally, the oxygen concentration at the electrode/membrane interface is given by:

$$c_{O_2}(x,y=\delta) = c^*_{O_2}\left(1 - \frac{P_{sat}}{P}\right)\left[1 - \frac{\int_0^x j(x)dx}{S_{O_2}\int_0^L j(x)dx}\right] - \frac{j(x)\delta}{4FD^{eff}} \tag{B.14}$$

B.2 Derivation of the Convecto-Diffusive Impedance

B.2.1 Local amplitude of the oxygen concentration oscillations at the electrode $\Delta c_{O_2}(x,y=\delta)$

The flow velocity V being constant, the system formed by equations (5.25), (5.26) and (5.29) is linear and the oxygen concentration $c_{O_2}(x,y)$ can be replaced by the amplitude of the oscillations $\Delta c_{O_2}(x,y)$ according to (5.31):

$$i\omega\Delta c_{O_2}(x,y) = D^{eff}\frac{\partial^2\Delta c_{O_2}}{\partial y^2}(x,y) \tag{B.15}$$

$$i\omega\Delta c_{O_2}(x,y=0) + V\frac{\partial\Delta c_{O_2}}{\partial x}(x,y=0) = \frac{D^{eff}}{\alpha h}\frac{\partial\Delta c_{O_2}}{\partial y}(x,y=0) \tag{B.16}$$

$$D^{eff}\frac{\partial\Delta c_{O_2}}{\partial y}(x,y=\delta) = -\frac{\Delta j_f(x)}{4F} \tag{B.17}$$

Remember that the overline used in (5.31) to denote the amplitude of complex numbers is omitted for the sake of simplicity.

Integrating (B.15) with respect to y yields:

$$\Delta c_{O_2}(x,y) = A(x)\cosh\left(\sqrt{\frac{i\omega}{D^{eff}}}y\right) + B(x)\sinh\left(\sqrt{\frac{i\omega}{D^{eff}}}y\right) \tag{B.18}$$

$A(x)$ and $B(x)$ are functions of x that can be determined from the boundary conditions.

- At the diffusion layer - channel interface $(y=0)$:

$$A(x) = \Delta c_{O_2}^{y=0}(x) \tag{B.19}$$

- At the electrode - membrane interface (B.17) ($y=\delta$, equation (B.17)):

$$B(x) = -\frac{\Delta j_f(x)}{4F\sqrt{i\omega D^{eff}}\cosh\left(\sqrt{\frac{i\omega}{D^{eff}}}\delta\right)} - \tanh\left(\sqrt{\frac{i\omega}{D^{eff}}}\delta\right)\Delta c_{O_2}^{y=0}(x) \tag{B.20}$$

Introducing (B.19) and (B.20) into (B.18) gives the amplitude of the concentration oscillations in the diffusion layer $\Delta c_{O_2}(x,y)$ as a function of the concentration oscillation amplitude in the channel $\Delta c_{O_2}^{y=0}(x)$:

$$\begin{aligned}\Delta c_{O_2}(x,y) = &\left[\cosh\left(\sqrt{\frac{i\omega}{D^{eff}}}y\right) - \tanh\left(\sqrt{\frac{i\omega}{D^{eff}}}\delta\right)\sinh\left(\sqrt{\frac{i\omega}{D^{eff}}}y\right)\right]\Delta c_{O_2}^{y=0}(x)\\ &- \frac{\sinh\left(\sqrt{\frac{i\omega}{D^{eff}}}y\right)}{4F\sqrt{i\omega D^{eff}}\cosh\left(\sqrt{\frac{i\omega}{D^{eff}}}\delta\right)}\Delta j_f(x)\end{aligned} \tag{B.21}$$

At the diffusion layer - channel interface, $\Delta c_{O_2}^{y=0}(x)$ verifies equation (B.16):

$$\left[\frac{i\omega}{V} + \frac{1}{\alpha hV}\sqrt{i\omega D^{eff}}\tanh\left(\sqrt{\frac{i\omega}{D^{eff}}}\delta\right)\right]\Delta c_{O_2}^{y=0} + \frac{\partial\Delta c_{O_2}^{y=0}}{\partial x} = -\frac{1}{\alpha hV}\frac{1}{4F\cosh\left(\sqrt{\frac{i\omega}{D^{eff}}}\delta\right)}\Delta j_f(x) \tag{B.22}$$

This ordinary differential equation can be written:

$$K_1 \Delta c_{O_2}^{y=0} + \frac{\partial \Delta c_{O_2}^{y=0}}{\partial x} = K_2 \Delta j_f(x) \tag{B.23}$$

with

$$\begin{aligned} K_1 &= \frac{i\omega}{V} + \frac{1}{\alpha h V}\sqrt{i\omega D^{eff}}\tanh\left(\sqrt{\frac{i\omega}{D^{eff}}}\delta\right) \\ K_2 &= -\frac{1}{\alpha h V}\frac{1}{4F\cosh\left(\sqrt{\frac{i\omega}{D^{eff}}}\delta\right)} \end{aligned} \tag{B.24}$$

The homogeneous solution of equation (B.23) is:

$$\Delta c_{O_2}^{y=0}(x) = A e^{-K_1 x} \tag{B.25}$$

A special solution can be found by supposing that the parameter A in (B.25) depends on x:

$$\begin{aligned} &\frac{\partial A}{\partial x} e^{-K_1 x} = K_2 \Delta j_f(x) \\ &\Rightarrow A(x) = \int_0^x K_2 e^{K_1 x'} \Delta j_f(x') dx' \end{aligned} \tag{B.26}$$

The complete solution of (B.23) is then given by:

$$\Delta c_{O_2}^{y=0}(x) = e^{-K_1 x} \cdot \int_0^x K_2 e^{K_1 x'} \Delta j_f(x') dx' \tag{B.27}$$

The amplitude of the concentration oscillations at the electrode $c_{O_2}(x, y=\delta)$ can finally be determined by introducing (B.27) into (B.21):

$$\Delta c_{O_2}(x,\delta) = -\frac{e^{-\frac{x}{X}}}{4F\alpha h V \cosh^2\left(\sqrt{\frac{i\omega}{D^{eff}}}\delta\right)} \int_0^x e^{\frac{x'}{X}} \Delta j_f(x') dx' - \frac{\tanh\left(\sqrt{\frac{i\omega}{D^{eff}}}\delta\right)}{4F\sqrt{i\omega D^{eff}}} \Delta j_f(x) \tag{B.28}$$

with

$$X = \frac{V}{i\omega + \frac{1}{\alpha h}\sqrt{i\omega D^{eff}}\tanh\left(\sqrt{\frac{i\omega}{D^{eff}}}\delta\right)} \tag{B.29}$$

Equation (B.28) shows that the amplitude of the oxygen concentration oscillations at the electrode $\Delta c_{O_2}(x,\delta)$ depends on the amplitude of the faradaic current density oscillations *upstream* $\Delta j_f(x' \leq x)$.

B.2.2 Convecto-diffusive impedance accounting for concentration oscillations in the channel

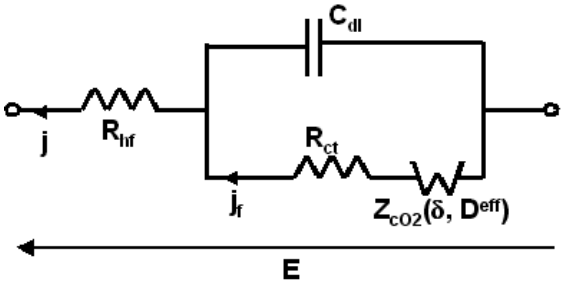


Figure B.1: *Common electrical equivalent circuit for the cathode of a PEMFC. R_{hf} stands for the high frequency resistance, R_{ct} for the charge transfer resistance resulting from the irreversibility of the electrochemical reaction and $Z_{c_{O_2}}$ stands for the oxygen diffusion impedance. C_{dl} represents the double layer capacity.*

In order to derive the cell impedance, let us express the amplitude of the oscillations of the faradaic current density $\Delta j_f(x)$ as a function of that of the total current density $\Delta j(x)$. Contrary to $\Delta j_f(x)$, $\Delta j(x)$ can be measured thanks to a segmented cell. According to the equivalent circuit of the Figure B.1, $\Delta j_f(x)$ can be written in terms of $\Delta j(x)$ and of the amplitude of the oxygen concentration oscillations at the reaction interface $\Delta c_{O_2}(x,\delta)$:

$$\Delta j(x) = \Delta j_f(x) + i\omega\Delta Q \tag{B.30}$$

where Q stands for the charge of the electrical double layer:

$$\Delta\eta_{act} = \frac{\Delta Q}{C_{dl}} \text{ with } \Delta\eta_{act} = b\frac{\Delta j_f(x)}{\langle j(x)\rangle_t} - b\frac{\Delta c_{O_2}(x,\delta)}{\langle c_{O_2}(x,\delta)\rangle_t} \tag{B.31}$$

Combining (B.30) and (B.31) leads finally to:

$$\Delta j_f(x) = \frac{\Delta j(x) + i\omega bC_{dl}\frac{\Delta c_{O_2}(x,\delta)}{\langle c_{O_2}(x,\delta)\rangle_t}}{1+\frac{i\omega bC_{dl}}{\langle j(x)\rangle_t}} \tag{B.32}$$

Replacing Δj_f in equation (B.28) by (B.32), it comes:

$$\begin{aligned}\Delta c_{O_2}(x,\delta) = &-\frac{e^{-\frac{x}{X}}}{4F\alpha hV\cosh^2\left(\sqrt{\frac{i\omega}{D^{eff}}}\delta\right)}\left[\int_0^x \frac{e^{\frac{x'}{X}}}{1+\frac{i\omega bC_{dl}}{\langle j(x')\rangle_t}}\Delta j(x')dx' + \int_0^x \frac{\frac{i\omega bC_{dl}}{\langle c_{O_2}(x',\delta)\rangle_t}e^{\frac{x'}{X}}}{1+\frac{i\omega bC_{dl}}{\langle j(x')\rangle_t}}\Delta c_{O_2}(x',\delta)dx'\right] \\ &- \frac{\tanh\left(\sqrt{\frac{i\omega}{D^{eff}}}\delta\right)}{4F\sqrt{i\omega D^{eff}}\left(1+\frac{i\omega bC_{dl}}{\langle j(x)\rangle_t}\right)}\Delta j(x) - \frac{\tanh\left(\sqrt{\frac{i\omega}{D^{eff}}}\delta\right)\frac{i\omega bC_{dl}}{\langle c_{O_2}(x,\delta)\rangle_t}}{4F\sqrt{i\omega D^{eff}}\left(1+\frac{i\omega bC_{dl}}{\langle j(x)\rangle_t}\right)}\Delta c_{O_2}(x,\delta)\end{aligned} \tag{B.33}$$

Since there is no explicit solution to (B.33), it is necessary to discretize the channel length ($x \in [0;L]$) into n segments where all variables remain constant. In this case, the integral of a function Φ becomes:

$$\int_0^{x_i} \Phi(x')dx' = \Delta x \sum_{k=1}^{i} \Phi(x_k) \tag{B.34}$$

Δx denotes the length of one segment ($n\Delta x = L$) and x_i the abscissa of the end of the i^{th} segment. With this convention, (B.33) can be written as:

$$\begin{aligned}\Delta c_{O_2}(x_i,\delta) = &-\frac{\Delta x}{4F\alpha hV\cosh^2\left(\sqrt{\frac{i\omega}{D^{eff}}}\delta\right)}\sum_{k=1}^{i}\left[\frac{e^{\frac{x_k}{X_k}-\frac{x_i}{X_i}}}{1+\frac{i\omega bC_{dl}}{\langle j(x_k)\rangle_t}}\Delta j(x_k)+\frac{\frac{i\omega bC_{dl}}{\langle c_{O_2}(x_k,\delta)\rangle_t}e^{\frac{x_k}{X_k}-\frac{x_i}{X_i}}}{1+\frac{i\omega bC_{dl}}{\langle j(x_k)\rangle_t}}\Delta c_{O_2}(x_k,\delta)\right]\\ &-\frac{\tanh\left(\sqrt{\frac{i\omega}{D^{eff}}}\delta\right)}{4F\sqrt{i\omega D^{eff}}\left(1+\frac{i\omega bC_{dl}}{\langle j(x_i)\rangle_t}\right)}\Delta j(x_i)-\frac{\tanh\left(\sqrt{\frac{i\omega}{D^{eff}}}\delta\right)\frac{i\omega bC_{dl}}{\langle c_{O_2}(x_i,\delta)\rangle_t}}{4F\sqrt{i\omega D^{eff}}\left(1+\frac{i\omega bC_{dl}}{\langle j(x_i)\rangle_t}\right)}\Delta c_{O_2}(x_i,\delta)\end{aligned} \tag{B.35}$$

In order to simplify the equations, let us define four functions $\Psi^1_{i,k}$, $\Psi^2_{i,k}$, Ψ^3_i and Ψ^4_i, as follows:

$$\Psi^1_{i,k} = \frac{\frac{\Delta x}{4F\alpha hV}}{\cosh^2\left(\sqrt{\frac{i\omega}{D^{eff}}}\delta\right)}\frac{e^{\frac{x_k}{X_k}-\frac{x_i}{X_i}}}{1+\frac{i\omega bC_{dl}}{\langle j(x_k)\rangle_t}} \tag{B.36}$$

$$\Psi^2_{i,k} = \frac{\frac{\Delta x}{4F\alpha hV}}{\cosh^2\left(\sqrt{\frac{i\omega}{D^{eff}}}\delta\right)}\frac{\frac{i\omega bC_{dl}}{\langle c_{O_2}(x_k,\delta)\rangle_t}e^{\frac{x_k}{X_k}-\frac{x_i}{X_i}}}{1+\frac{i\omega bC_{dl}}{\langle j(x_k)\rangle_t}} \tag{B.37}$$

$$\Psi^3_i = \frac{\tanh\left(\sqrt{\frac{i\omega}{D^{eff}}}\delta\right)}{4F\sqrt{i\omega D^{eff}}\left(1+\frac{i\omega bC_{dl}}{\langle j(x_i)\rangle_t}\right)} \tag{B.38}$$

$$\Psi^4_i = \frac{\tanh\left(\sqrt{\frac{i\omega}{D^{eff}}}\delta\right)\frac{i\omega bC_{dl}}{\langle c_{O_2}(x_i,\delta)\rangle_t}}{4F\sqrt{i\omega D^{eff}}\left(1+\frac{i\omega bC_{dl}}{\langle j(x_i)\rangle_t}\right)} \tag{B.39}$$

Thus, equation (B.35) becomes:

$$\sum_{k=1}^{i-1}\Psi^2_{i,k}\Delta c_{O_2}(x_k,\delta)+\left(1+\Psi^4_i+\Psi^2_{i,i}\right)\Delta c_{O_2}(x_i,\delta) = -\sum_{k=1}^{i-1}\Psi^1_{i,k}\Delta j(x_k)-\left(\Psi^1_{i,i}+\Psi^3_i\right)\Delta j(x_i) \tag{B.40}$$

Equation (B.40) can be written as a matrix product:

$$\begin{bmatrix}1+\Psi^4_1+\Psi^2_{1,1} & 0 & \cdots & 0\\ \Psi^2_{2,1} & \ddots & \ddots & \vdots\\ \vdots & \ddots & \ddots & 0\\ \Psi^2_{n,1} & \cdots & \Psi^2_{n,n-1} & 1+\Psi^4_n+\Psi^2_{n,n}\end{bmatrix}\begin{bmatrix}\Delta c_{O_2}(x_1,\delta)\\ \vdots\\ \vdots\\ \Delta c_{O_2}(x_n,\delta)\end{bmatrix} = -\begin{bmatrix}\Psi^3_1+\Psi^1_{1,1} & 0 & \cdots & 0\\ \Psi^1_{2,1} & \ddots & \ddots & \vdots\\ \vdots & \ddots & \ddots & 0\\ \Psi^1_{n,1} & \cdots & \Psi^1_{n,n-1} & \Psi^3_n+\Psi^1_{n,n}\end{bmatrix}\begin{bmatrix}\Delta j(x_1)\\ \vdots\\ \vdots\\ \Delta j(x_n)\end{bmatrix} \tag{B.41}$$

With

$$\boldsymbol{M}_c = \begin{bmatrix}1+\Psi^4_1+\Psi^2_{1,1} & 0 & \cdots & 0\\ \Psi^2_{2,1} & \ddots & \ddots & \vdots\\ \vdots & \ddots & \ddots & 0\\ \Psi^2_{n,1} & \cdots & \Psi^2_{n,n-1} & 1+\Psi^4_n+\Psi^2_{n,n}\end{bmatrix} \tag{B.42}$$

and

$$\boldsymbol{M}_j = \begin{bmatrix} \Psi_1^3 + \Psi_{1,1}^1 & 0 & \cdots & 0 \\ \Psi_{2,1}^1 & \ddots & \ddots & \vdots \\ \vdots & \ddots & \ddots & 0 \\ \Psi_{n,1}^1 & \cdots & \Psi_{n,n-1}^1 & \Psi_n^3 + \Psi_{n,n}^1 \end{bmatrix} \tag{B.43}$$

equation (B.41) simplifies to:

$$\boldsymbol{M}_c \Delta \boldsymbol{c}_{O_2}^{y=\delta} = -\boldsymbol{M}_j \Delta \boldsymbol{j} \tag{B.44}$$

Assuming a linear behavior for small sinusoidal perturbations, the potential variation can be derived from equations (5.22) and (5.23) as a function of the variations of the faradaic current density and of the concentration:

$$\Delta E = -R_{hf}\Delta j(x) - b\frac{\Delta j_f(x)}{\langle j(x)\rangle_t} + b\frac{\Delta c_{O_2}(x,\delta)}{\langle c_{O_2}(x,\delta)\rangle_t} \tag{B.45}$$

Replacing $\Delta j_f(x)$ by its expression as a function of $\Delta j(x)$ (B.32) yields:

$$\begin{aligned} \Delta E &= -R_{hf}\Delta j(x) - \frac{b}{\langle j(x)\rangle_t}\left(\frac{\Delta j(x) + i\omega b C_{dl}\frac{\Delta c_{O_2}(x,\delta)}{\langle c_{O_2}(x,\delta)\rangle_t}}{1+\frac{i\omega b C_{dl}}{\langle j(x)\rangle_t}}\right) + b\frac{\Delta c_{O_2}(x,\delta)}{\langle c_{O_2}(x,\delta)\rangle_t} \\ &= -\left(R_{hf} + \frac{\frac{b}{\langle j(x)\rangle_t}}{1+\frac{i\omega b C_{dl}}{\langle j(x)\rangle_t}}\right)\Delta j(x) + \left(1 - \frac{\frac{i\omega b C_{dl}}{\langle j(x)\rangle_t}}{1+\frac{i\omega b C_{dl}}{\langle j(x)\rangle_t}}\right)\frac{b\Delta c_{O_2}(x,\delta)}{\langle c_{O_2}(x,\delta)\rangle_t} \end{aligned} \tag{B.46}$$

Let us define the functions Ψ_i^5 and Ψ_i^6 in order to simplify the notations:

$$\Psi_i^5 = R_{hf} + \frac{\frac{b}{\langle j(x_i)\rangle_t}}{1+\frac{i\omega b C_{dl}}{\langle j(x_i)\rangle_t}} \tag{B.47}$$

$$\Psi_i^6 = \left(1 - \frac{\frac{i\omega b C_{dl}}{\langle j(x_i)\rangle_t}}{1+\frac{i\omega b C_{dl}}{\langle j(x_i)\rangle_t}}\right)\frac{b}{\langle c_{O_2}(x_i,\delta)\rangle_t} \tag{B.48}$$

Thus, equation (B.46) becomes:

$$\begin{bmatrix} \Delta c_{O_2}(x_1,\delta) \\ \vdots \\ \vdots \\ \Delta c_{O_2}(x_n,\delta) \end{bmatrix} = \begin{bmatrix} \frac{\Psi_i^5}{\Psi_i^6} & 0 & \cdots & 0 \\ 0 & \ddots & \ddots & \vdots \\ \vdots & \ddots & \ddots & 0 \\ 0 & \cdots & 0 & \frac{\Psi_n^5}{\Psi_n^6} \end{bmatrix} \begin{bmatrix} \Delta j(x_1) \\ \vdots \\ \vdots \\ \Delta j(x_n) \end{bmatrix} + \begin{bmatrix} \frac{\Delta E}{\Psi_i^6} \\ \vdots \\ \vdots \\ \frac{\Delta E}{\Psi_n^6} \end{bmatrix} \tag{B.49}$$

Or, in a more compact form:

$$\Delta \boldsymbol{c}_{O_2}^{y=\delta} = \boldsymbol{L}_j \Delta \boldsymbol{j} + \boldsymbol{P}\Delta E \tag{B.50}$$

with

$$\boldsymbol{L}_j = \begin{bmatrix} \frac{\Psi_i^5}{\Psi_i^6} & 0 & \cdots & 0 \\ 0 & \ddots & \ddots & \vdots \\ \vdots & \ddots & \ddots & 0 \\ 0 & \cdots & 0 & \frac{\Psi_n^5}{\Psi_n^6} \end{bmatrix} \quad \text{(B.51)} \qquad \text{and} \qquad \boldsymbol{P} = \begin{bmatrix} \frac{1}{\Psi_i^6} \\ \vdots \\ \vdots \\ \frac{1}{\Psi_n^6} \end{bmatrix} \quad \text{(B.52)}$$

Combining (B.44) and (B.50) yields the local electric conductance:

$$\frac{-\Delta \boldsymbol{j}}{\Delta E} = \left(\boldsymbol{M}_c \boldsymbol{L}_j + \boldsymbol{M}_j\right)^{-1} \boldsymbol{M}_c \boldsymbol{P} \tag{B.53}$$

The negative sign of the current perturbation in (B.53) takes account of the phase shift between the total current and the voltage of the cell and has to be applied in order to obtain a positive impedance.

B.3 Asymptotic Study

When the frequency tends toward zero equation (B.29) takes the form:

$$\lim_{\omega \to 0} X = \frac{V}{i\omega \left(1 + \frac{\delta}{\alpha h}\right)} \tag{B.54}$$

In this case the capacitive current can be neglected compared to the faradaic current and (B.28) becomes:

$$\Delta c_{O_2}(x, \delta) = -\frac{1}{\alpha h V} \int_0^x \frac{\Delta j(x')}{4F} dx' - \frac{\delta}{D^{eff}} \frac{\Delta j(x)}{4F} \tag{B.55}$$

In the absence of information about the local current density variation $\Delta j(x)$, it can be assumed to be uniform. Thus, the integration of equation (B.55) leads to:

$$\Delta c_{O_2}(x, \delta) = -\left(\frac{x}{\alpha h V} + \frac{\delta}{D^{eff}}\right) \frac{\langle \Delta j \rangle_x}{4F} \tag{B.56}$$

And therefore, for the overall cell:

$$\langle \Delta c_{O_2}(y = \delta) \rangle_x = -\left(\frac{L}{2\alpha h V} + \frac{\delta}{D^{eff}}\right) \frac{\langle \Delta j \rangle_x}{4F} \tag{B.57}$$

The global electric impedance can be derived from (B.46) and (B.57) at low frequencies:

$$\frac{\Delta E}{-\langle \Delta j \rangle_x} = R_{hf} + \frac{b}{\langle j \rangle_{x,t}} + \frac{b}{4F \langle c_{O_2}(y = \delta) \rangle_{x,t}} \left(\frac{L}{2\alpha h V} + \frac{\delta}{D^{eff}}\right) \tag{B.58}$$

By replacing the flow velocity by its expression as a function of the stoichiometry (5.36), it comes:

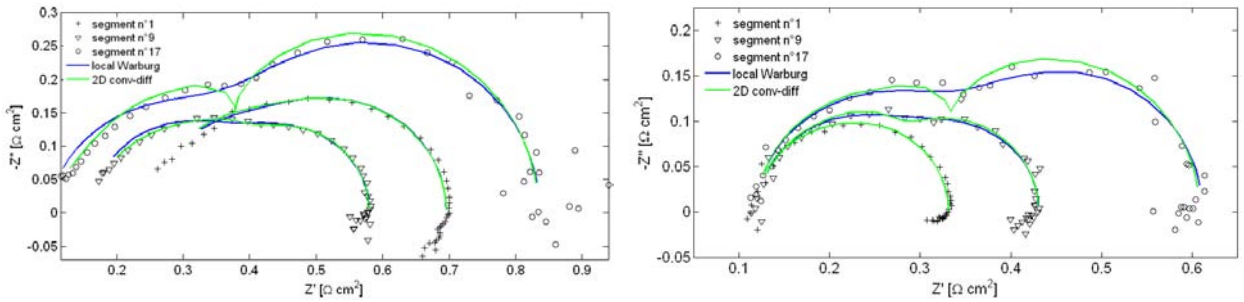
$$\frac{\Delta E}{-\langle \Delta j \rangle_x} = R_{hf} + \frac{b}{\langle j \rangle_{x,t}} + \frac{b}{4F \langle c_{O_2}(y = \delta) \rangle_{x,t}} \left(\frac{1}{2} \frac{c_{O_2}^* / (1 + H)}{S_{O_2} \langle j \rangle_{x,t} / 4F} + \frac{\delta}{D^{eff}}\right) \tag{B.59}$$

The mean oxygen concentration at the electrode $\langle c_{O_2}(y=\delta)\rangle_{x,t}$ can be determined by the integration of equation (B.11) or (B.14). Expressions (B.54) to (B.59) are valid only for low frequencies.

C Figures Completing the Experimental Study with the Pseudo-2D Impedances

The graphs presented below aim to complete the experimental study of section 6.2.

C.0.1 Local impedance spectra measured with cell 1



(a) co-flow (b) counter-flow

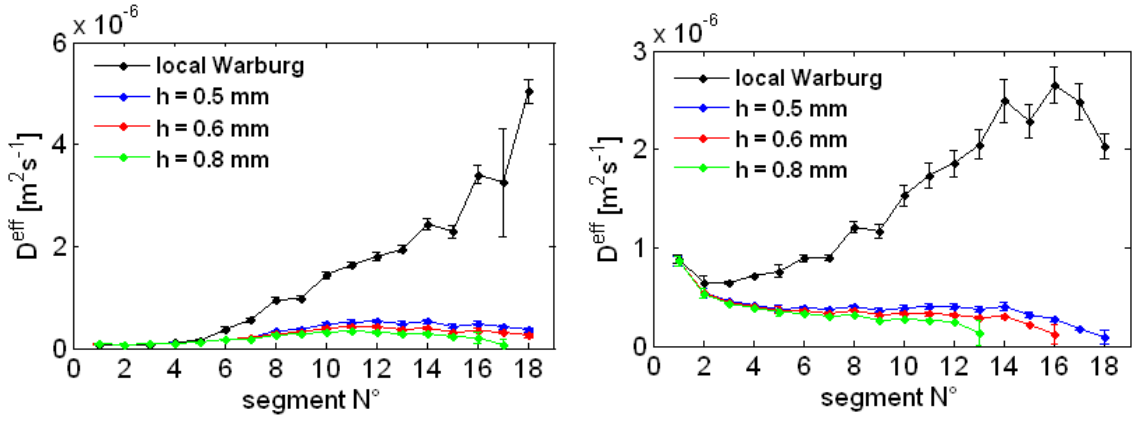
Figure C.1: *Local spectra measured with cell 1 and their fitting curves obtained using the local Warburg impedance $Z^{W,loc}$ (6.2) and the 2D convecto-diffusive impedance Z^{osc} (6.3). For the fitting curves in co-flow (a), the channel depth h is set to 0.6 mm and for those in counter-flow (b) $h = 0.5$ mm; $\langle j_{cell} \rangle_t = 0.5\ Acm^{-2}$, $S_{O_2} = 3$.*

Fitting curves of local impedance spectra of cell 1 in co- (Figure C.1(a)) and in counter-flow (Figure C.1(b)) obtained using the local Warburg (blue lines) and the 2D convecto-diffusive impedance (green lines). The shapes of the spectra obtained with the 2D convecto-diffusive impedance clearly differ from those of the local Warburg impedance when the low frequency loop enlarges: with Z^{osc}, the spectra exhibit a clear separation of the two loops, which is not the case with $Z^{W,loc}$.

C.0.2 Impact of the channel depth on the parameter estimation

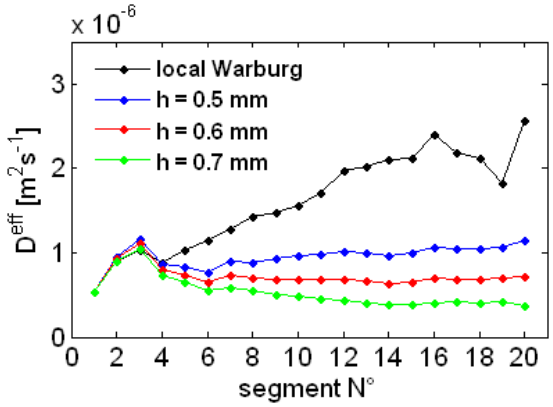
The values of the local diffusion parameters estimated with the convecto-diffusive impedance depend on the channel depth h. This is highlighted by the curves in Figure C.2 which show the profiles of D^{eff} estimated starting from the spectra of cell 1 and 2 with different values of h [1]. The real channel depth measured in the flow field plates is 0.8 *mm* for cell 1 and 0.7 *mm* for cell 2.

[1] The parameters determined with cell 1 result from a series of 5 measurements under identical conditions. As a consequence, their corresponding standard deviations are indicated. The data of cell 2 result from only one set of measurements.



(a) Cell 1: co-flow

(b) Cell 1: counter-flow



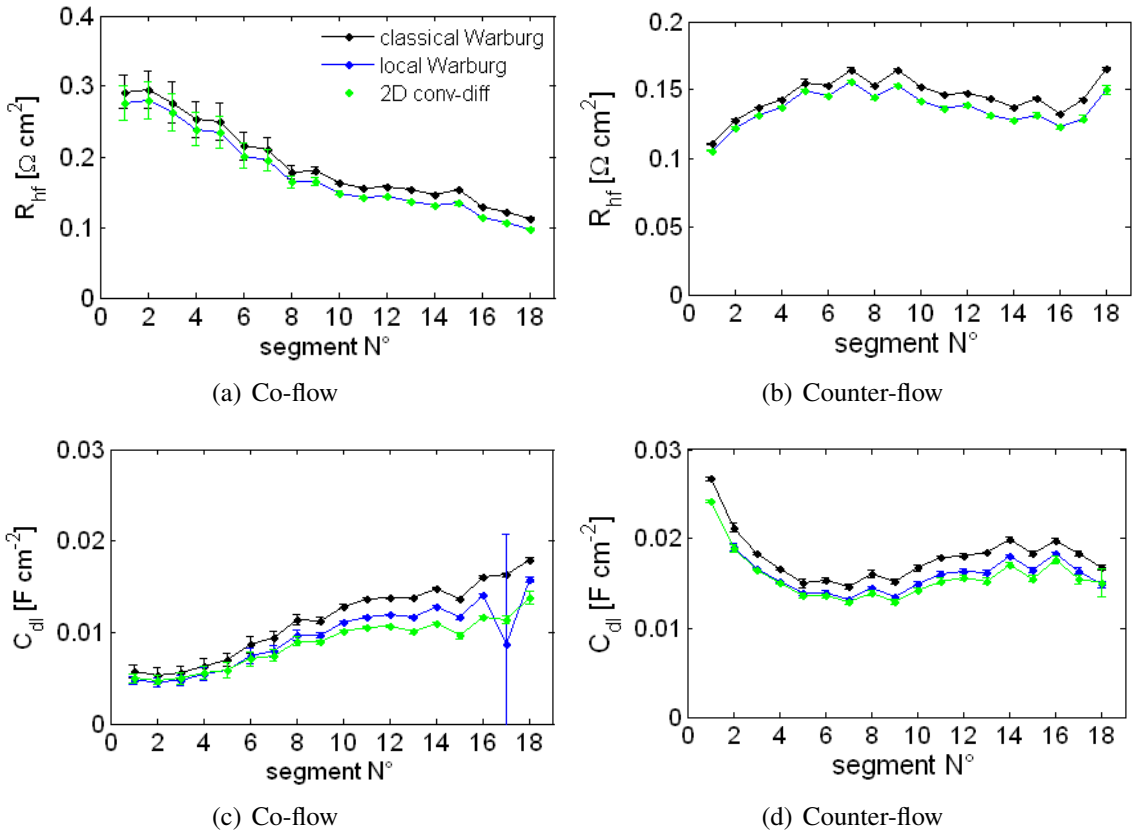
(c) Cell 2: counter-flow

Figure C.2: *Impact of the channel depth h on the estimation of the local diffusion coefficients with the 2D convecto-diffusive impedance: (a) cell 1 in co-flow, (b) cell 1 in counter-flow, (c) cell 2 in counter-flow.*

In the case of cell 1, the convecto-diffusive impedance does not allow a parameter estimation over the entire channel length when the channel depth is set to its real value. The graphs in Figure C.2 show that an identification of the diffusion parameters is possible for all segments only when reducing the channel depth. In this case, the values of D^{eff} (and of δ) obtained with the convecto-diffusive impedance are closer to those obtained with the local Warburg impedance. This can be explained by the fact that reducing the channel depth while keeping the air flux constant results in an increase of the air velocity V. Note that in a running fuel cell, the actual channel depth must be lower than that measured in the flow field plates alone because the GDL tend to penetrate into the channel. Furthermore, the possible presence of liquid water reduces also the hydraulic diameter of the channels. Consequently, the value that was chosen is the highest allowing a parameter estimation over the entire electrode length: 0.6 *mm* for cell 1 in co-flow, 0.5 *mm* in counter-flow. For cell 2, it was not necessary to modify the depth of the channel ($h = 0.7$ *mm*).

C.0.3 High frequency impedance parameters identified with cell 1

Figure C.3 shows the profiles of the high frequency impedance parameters (R_{hf} and C_{dl}) identified starting from local impedance spectra measured with cell 1 in co- (Figure C.1(a)) and in counter-



(a) Co-flow (b) Counter-flow

(c) Co-flow (d) Counter-flow

Figure C.3: *High frequency impedance parameters identified starting from the local impedance spectra measured with cell 1 in co- (Figure C.1(a)) and in counter-flow (Figure C.1(b)) with the 1D Warburg (black dots), the local Warburg (blue dots) and the convecto-diffusive impedance (green dots): (a)-(b) high frequency resistance R_{hf}, (c)-(d) double-layer capacity C_{dl}.*

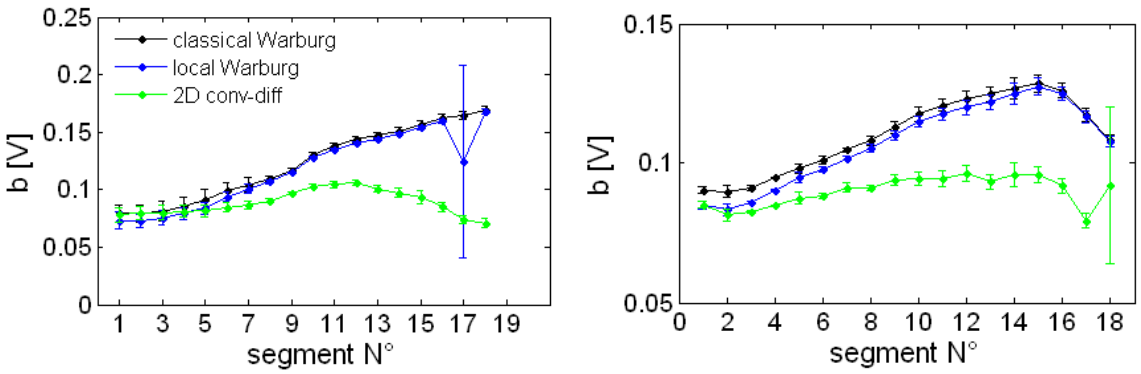
flow (Figure C.1(b)). These curves confirm that the choice of the oxygen transport model has no impact on the high frequency parameters, except for the Tafel slope b (Figure C.4): the convecto-diffusive impedance leads to a rather flat profile, whereas the values obtained with the Warburg impedances increase along the channel.

C.0.4 Diffusion parameters D^{eff} and δ identified starting from cell 1

Figure C.5 shows the profiles of the diffusion parameters D^{eff} (Figures C.5(a) and C.5(b)) and δ (Figures C.5(c) and C.5(d)) estimated starting from local spectra measured with cell 1 and using a macroscopic approach (with reference to the MEA flat surface A_{geom}). These profiles confirm the conclusions obtained with the data of cell 2:

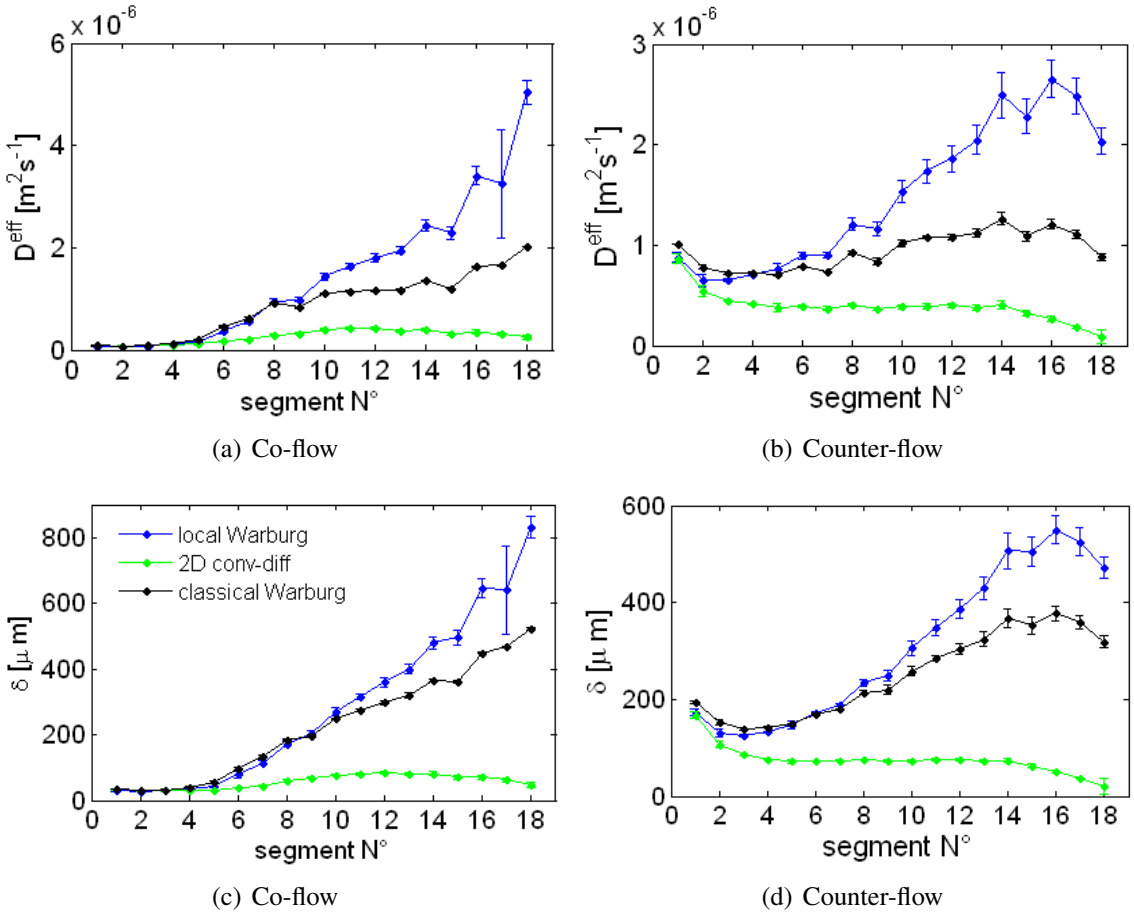
- Gas consumption and concentration oscillations being negligible near the air channel inlet, the values of the diffusion parameters identified with the three models should be the same for the first segment(s). A slight difference is observed between the parameters obtained with the 1D Warburg impedance and those estimated with the pseudo-2D transport impedances because $Z^{W,1D}$ does not account for gas humidification. This discrepancy is less pronounced for a gas supply in co-flow, because the inlet of the dry hydrogen faces the air inlet leading to a lower value of the absolute humidity H than in counter-flow.

- The values of the effective diffusivity D^{eff} identified with the three impedances (Figures C.5(a) and C.5(b)) are in ranges expected for gas diffusion in the pores of backing or active layers [BSL02].
- When using $Z^{W,loc}$ instead of $Z^{W,1D}$, a steeper increase of D^{eff} over the electrode is observed, which results from the consideration of a decrease in the oxygen concentration along the channel. The comparison of the profiles of δ and of D^{eff} obtained with $Z^{W,loc}$ and Z^{osc} (accounting both for oxygen consumption) clearly shows that the signal oscillations have a more important impact on the impedance parameters than the decreasing oxygen concentration. They have thus to be included in the oxygen transport model.



(a) Co-flow (b) Counter-flow

Figure C.4: *Tafel slope b identified starting from local impedance spectra measured with cell 1 (a) in co-(Figure C.1(a)) and (b) in counter-flow (Figure C.1(b)) with the 1D Warburg (black dots), the local Warburg (blue dots) and the convecto-diffusive impedance (green dots).*



(a) Co-flow (b) Counter-flow

(c) Co-flow (d) Counter-flow

Figure C.5: *Diffusion parameters identified for cell 1 in co- and counter-flow using the 1D Warburg (black dots), the local Warburg (blue dots) and the convecto-diffusive impedance (green dots). (a)-(b) effective diffusivity D^{eff}; (c)-(d) diffusion thickness δ.*

Bibliography

[ABD01] O. Antoine, Y. Bultel, and R. Durand. Oxygen reduction reaction kinetics and mechanism on platinum nanoparticles inside Nafion®. *J. Electroanal. Chem.*, 499(1):85–94, 2001.

[ABDO98] O. Antoine, Y. Bultel, R. Durand, and P. Ozil. Electrocatalysis, diffusion and ohmic drop in PEMFC: Particle size and spatial discrete distribution effects. *Electrochim. Acta*, 43(24):3681–3691, 1998.

[AD00] O. Antoine and R. Durand. RRDE study of oxygen reduction on Pt nanoparticles inside Nafion: H_2O_2 production in PEMFC cathode conditions. *J. Appl. Electrochem.*, 30(7):839–844, 2000.

[ADP06] Peter Atkins and Julio De Paula. *Atkins' Physical Chemistry*. Oxford University Press, 8th edition, March 2006.

[Adz98] R. Adzic. *Recent Advances in the Kinetics of Oxygen Reduction*. Wiley-VCH, ISBN: 0-471-24673-5, 1998.

[AlB+10] F. Alcaide, G. Àlvarez, J.A. Blazquez, P.L. Cabot, and O. Miguel. Development of a novel portable-size PEMFC short stack with electrodeposited Pt hydrogen diffusion anodes. *Int. J. Hydrogen Energy*, 35:5521–5527, 2010.

[ANS08] G. Alberti, R. Narducci, and M. Sganappa. Effects of hydrothermal/thermal treatments on the water-uptake of Nafion membranes and relations with changes of conformation, counter-elastic force and tensile modulus of the matrix. *J. Power Sources*, 178(2):575–583, 2008.

[APBDSS+92] Arvind Parthasarathy, Bhasker Dave, Supramaniam Srinivasan, A. John Appleby, and Charles R. Martin. The Platinum Microelectrode/Nafion Interface: An Electrochemical Impedance Spectroscopic Analysis of Oxygen Reduction Kinetics and Nafion Characteristics. *J. Electrochem. Soc.*, 139(6):1634–1641, 1992.

[Arc42] G.E. Archie. Electrical Resistivity Log as an Aid in Determining Some Reservoir Characteristics. *Trans. AIME*, **146**:54–61, 1942.

[AST99] P. Argyropoulos, K. Scott, and W.M. Taama. Gas evolution and power performance in direct methanol fuel cells. *J. Appl. Electrochem.*, 29(6):661–669, 1999.

[AZS+07] R.R. Adzic, J. Zhang, K. Sasaki, M.B. Vukmirovic, M. Shao, J.X. Wang, A.U. Nilekar, M. Mavrikakis, J.A. Valerio, and F. Uribe. Platinum monolayer fuel cell electrocatalysts. *Top. Catal.*, 46(3-4):249–262, 2007.

[BAL] BALLARD®. www.ballard.com.

[BBO04] M. Bautista, Y. Bultel, and P. Ozil. Polymer electrolyte membrane fuel cell modelling: d.c. and a.c. solutions. *Chem. Eng. Res. Des.*, 82(7):907–917, 2004.

[BD03] T. Berning and N. Djilali. A 3D, multiphase, multicomponent model of the cathode and anode of a PEM fuel cell. *J. Electrochem. Soc.*, 150(12):A1589–A1598, 2003.

[BE97a] K. Broka and P. Ekdunge. Modelling the PEM fuel cell cathode. *J. Appl. Electrochem.*, 27(3):281–289, 1997.

[BE97b] K. Broka and P. Ekdunge. Oxygen and hydrogen permeation properties and water uptake of Nafion® 117 membrane and recast film for PEM fuel cell. *J. Appl. Electrochem.*, 27(2):117–124, 1997.

[BGA+02] Y. Bultel, L. Genies, O. Antoine, P. Ozil, and R. Durand. Modeling impedance diagrams of active layers in gas diffusion electrodes: Diffusion, ohmic drop effects and multistep reactions. *J. Electroanal. Chem.*, 527(1-2):143–155, 2002.

[Boi05] M. Boillot. *Validation expérimentale d'outils de modélisation d'une pile à combustible de type PEM*. PhD thesis, INPL-ENSIC, Nancy, 2005.

[BR73] J.O. Bockris and A.K.N Reddy. *Modern Electrochemistry*. Plenum Publishing Corporation, 1973.

[Bru35] H.C. Bruggeman. Berechnung verschiedenr Physikalischer Konstanten von heterogenen Substanzen. *Ann. Physik (Leipzig)*, **24**:636–679, 1935.

[BSL02] R.B. Bird, W.E. Stewart, and E.N. Lightfood. *Transport Phenomena*. John Wiley and Sons, New York, ISBN: 0-471-41077-2, 2002.

[BWJ+05] Y. Bultel, K. Wiezell, F. Jaouen, P. Ozil, and G. Lindbergh. Investigation of mass transport in gas diffusion layer at the air cathode of a PEMFC. *Electrochim. Acta*, 51(3):474–488, 2005.

[CCD+09] T. Colinart, A. Chenu, S. Didierjean, O. Lottin, and S. Besse. Experimental study on water transport coefficient in Proton Exchange Membrane Fuel Cell. *J. Power Sources*, 190(2):230–240, 2009.

[CCD+10] S. Chupin, T. Colinart, S. Didierjean, Y. Dubé, K. Agbossou, G. Maranzana, and O. Lottin. Numerical investigation of the impact of gas and cooling flow configurations on current and water distributions in a polymer membrane fuel cell through a pseudo-two-dimensional diphasic model. *J. Power Sources*, 195(16):5213–5227, 2010.

[CD03] P. Choi and R. Datta. Sorption in proton-exchange membranes. An explanation of Schroeder's paradox. *J. Electrochem. Soc.*, 150(12):E601–E607, 2003.

[CEM+09] M. Cavarroc, A. Ennadjaoui, M. Mougenot, P. Brault, R. Escalier, Y. Tessier, J. Durand, S. Roualdès, T. Sauvage, and C. Coutanceau. Performance of plasma sputtered fuel cell electrodes with ultra-low Pt loadings. *Electrochem. Commun.*, 11(4):859–861, 2009.

[CES94] M. Cappadonia, J.W. Erning, and U. Stimming. Proton conduction of Nafion® 117 membrane between 140 K and room temperature. *J. Electroanal. Chem.*, 376(1-2):189–193, 1994.

[CGB+09] R. N. Carter, W. Gu, B. Brady, P. T. Yu, K. Subramanian, and H. A. Gasteiger. Electrode degradation mechanisms studies by current distribution measurements. In W Vielstich, H. A. Gasteiger, and H. Yokokawa, editors, *Handbook of Fuel Cells*, volume 6, chapter 56, page 829. Wiley-VCH, 2009.

[CL99] S.Y. Cha and W.M. Lee. Performance of proton exchange membrane fuel cell electrodes prepared by direct deposition of ultrathin platinum on the membrane surface. *J. Electrochem. Soc.*, 146(11):4055–4060, 1999.

[Col08] T. Colinart. *Gestion de l'eau et performances électriques d'une pile à combustible: des pores de la membrane à la cellule*. PhD thesis, INPL-LEMTA, Nancy, 2008.

[Coo03] W. Grover Coors. Protonic ceramic fuel cells for high-efficiency operation with methane. *J. Power Sources*, 118(1-2):150–156, May 2003.

[Cos01] P. Costamagna. Transport phenomena in polymeric membrane fuel cells. *Chem. Eng. Sci.*, 56(2):323–332, 2001.

[CR01] M. Ciureanu and R. Roberge. Electrochemical impedance study of PEM fuel cells. Experimental diagnostics and modeling of air cathodes. *J. Phys. Chem. B*, 105(17):3531–3539, 2001.

[CSY+09] S. Chen, W. Sheng, N. Yabuuchi, P.J. Ferreira, L.F. Allard, and Y. Shao Horn. Origin of oxygen reduction reaction activity on Pt_3Co nanoparticles: Atomically resolved chemical compositions and structures. *Journal of Physical Chemistry C*, 113(3):1109–1125, 2009.

[CT02] B.E. Conway and B.V. Tilak. Interfacial processes involving electrocatalytic evolution and oxidation of H_2, and the role of chemisorbed H. *Electrochim. Acta*, 47(22-23):3571–3594, 2002.

[CW99] M. Ciureanu and H. Wang. Electrochemical impedance study of electrode-membrane assemblies in PEM fuel cells. I. Electro-oxidation of H_2 and H_2/CO mixtures on Pt-based gas-diffusion electrodes. *J. Electrochem. Soc.*, 146(11):4031–4040, 1999.

[CYH+99] X. Cheng, B. Yi, M. Han, J. Zhang, Y. Qiao, and J. Yu. Investigation of platinum utilization and morphology in catalyst layer of polymer electrolyte fuel cells. *J. Power Sources*, 79(1):75–81, 1999.

[Dai08] J. Dailly. *Synthèse et caractérisation de nouveaux matériaux de cathode pour piles à combustible à conduction protonique PCFC (Protonic Ceramic Fuel Cell)*. PhD thesis, Université de Bordeaux 1, 2008.

[DB67] A. Damjanovic and V. Brusic. Electrode kinetics of oxygen reduction on oxide-free platinum electrodes. *Electrochim. Acta*, 12(6):615–628, 1967.

[DDM+] L. Dubau, J. Durst, F. Maillard, L. Guétaz, M. Chatenet, J. André, and E. Rossinot. Further insights into the durability of Pt3Co/C electrocatalysts: formation of "hollow" Pt nanoparticles induced by the Kirkendall effect. *Electrochim. Acta*, In Press, Accepted Manuscript.

[Des08] J. Deseure. Coupling RTD and EIS modelling to characterize operating non-uniformities on PEM cathodes. *J. Power Sources*, 178(1):323–333, 2008.

[DJK+03] H. Dohle, R. Jung, N. Kimiaie, J. Mergel, and M. Müller. Interaction between the diffusion layer and the flow field of polymer electrolyte fuel cells - Experiments and simulation studies. *J. Power Sources*, 124(2):371–384, 2003.

[DLGM96] J.-P. Diard, B. Le Gorrec, and C. Montella. *Cinétique électrochimique*. Hermann, Editeur des Sciences et des Arts, ISBN-13: 978-2705662950, 1996.

[DLGM+98] J. P. Diard, B. Le Gorrec, C. Montella, C. Poinsignon, and G. Vitter. Impedance measurements of polymer electrolyte membrane fuel cells running on constant load. *J. Power Sources*, 74(2):244–245, August 1998.

[DLM+10] J. Dillet, O. Lottin, G. Maranzana, S. Didierjean, D. Conteau, and C. Bonnet. Direct observation of the two-phase flow in the air channel of a proton exchange membrane fuel cell and of the effects of a clogging/unclogging sequence on the current density distribution. *J. Power Sources*, 195(9):2795–2799, 2010.

[DMC+10] L. Dubau, F. Maillard, M. Chatenet, J. André, and E. Rossinot. Nanoscale compositional changes and modification of the surface reactivity of Pt_3Co/C nanoparticles during proton-exchange membrane fuel cell operation. *Electrochim. Acta*, 56(2):776–783, 2010.

[Don02] W.R.M. Donis. *Diagnosis of PEMFC Stack Failures via Electrochemical Impedance Spectroscopy*. PhD thesis, University of Victoria, 2002.

[DSVA06] M.K. Debe, A.K. Schmoeckel, G.D. Vernstrom, and R. Atanasoski. High voltage stability of nanostructured thin film catalysts for PEM fuel cells. *J. Power Sources*, 161(2):1002–1011, 2006.

[DT10] V.A. Danilov and M.O. Tade. An alternative way of estimating anodic and cathodic transfer coefficients from PEMFC polarization curves. *Chemical Engineering Journal*, 156(2):496–499, 2010.

[EAP98] S. Escribano, P. Aldebert, and M. Pineri. Volumic electrodes of fuel cells with polymer electrolyte membranes: Electrochemical performances and structural analysis by thermoporometry. *Electrochim. Acta*, 43(14-15):2195–2202, 1998.

[Eik06] M. Eikerling. Water management in cathode catalyst layers of PEM fuel cells. *J. Electrochem. Soc.*, 153(3):E58–E70, 2006.

[EK99] M. Eikerling and A.A. Kornyshev. Electrochemical impedance of the cathode catalyst layer in polymer electrolyte fuel cells. *J. Electroanal. Chem.*, 475(2):107–123, 1999.

[FDN+06] N. Fouquet, C. Doulet, C. Nouillant, G. Dauphin Tanguy, and B. Ould Bouamama. Model based PEM fuel cell state-of-health monitoring via ac impedance measurements. *J. Power Sources*, 159(2):905–913, 2006.

[FJW98] A. Fischer, J. Jindra, and H. Wendt. Porosity and catalyst utilization of thin layer cathodes in air operated PEM-fuel cells. *J. Appl. Electrochem.*, 28(3):277–282, 1998.

[FMB91] Donald R. Franceschetti, J.Ross Macdonald, and Richard P. Buck. Interpretation of finite-length-Warburg-type impedances in supported and unsupported electrochemical cells with kinetically reversible electrodes. *J. Electrochem. Soc.*, 138(5):1368–1371, 1991.

[FN92] Thomas Fuller and John Newman. Experimental determination of the transport number of water in Nafion 117 membrane. *J. Electrochem. Soc.*, 139(5):1332–1337, 1992.

[Fre05] V. Freger. Diffusion impedance and equivalent circuit of a multilayer film. *Electrochem. Commun.*, 7(9):957–961, 2005.

[Fri03] W. Friede. *Modélisation et caractérisation d'une pile à combustible du type PEM*. PhD thesis, INPL, Nancy, 2003.

[FSD05] J. Fimrite, H. Struchtrup, and N. Djilali. Transport phenomena in polymer electrolyte membranes I. Modeling framework. *J. Electrochem. Soc.*, 152(9):A1804–A1814, 2005.

[GAPP98] L. Giorgi, E. Antolini, A. Pozio, and E. Passalacqua. Influence of the PTFE content in the diffusion layer of low-Pt loading electrodes for polymer electrolyte fuel cells. *Electrochim. Acta*, 43(24):3675–3680, 1998.

[GBLG09] W. Gu, D.R. Baker, y. Liu, and H.A. Gasteiger. Proton exchange membrane fuel cell (PEMFC) down- the-channel performance model. In W. Vielstich, H.A. Gasteiger, and H. Yokokawa, editors, *Handbook of Fuel Cells - Fundamentals, Technology and Applications*, volume 6, page 631. John Wiley and Sons, Ltd, Chichester, 2009.

[GCG+98] F. Gloaguen, P. Convert, S. Gamburzev, O.A. Velev, and S. Srinivasan. An evaluation of the macro-homogeneous and agglomerate model for oxygen reduction in PEMFCs. *Electrochim. Acta*, 43(24):3767–3772, 1998.

[GCT+03] Q. Guo, M. Cayetano, Y.-M. Tsou, E.S. De Castro, and R.E. White. Study of the ionic conductivity profiles of the air cathode of a PEMFC by AC impedance spectroscopy. *J. Electrochem. Soc.*, 150(11):A1440–A1449, 2003.

[GD97] F. Gloaguen and R. Durand. Simulations of PEFC cathodes: An effectiveness factor approach. *J. Appl. Electrochem.*, 27(9):1029–1035, 1997.

[Geb00] G. Gebel. Structural evolution of water swollen perfluorosulfonated ionomers from dry membrane to solution. *Polymer*, 41(15):5829–5838, 2000.

[GFI+06] J.T. Gostick, M.W. Fowler, M.A. Ioannidis, M.D. Pritzker, Y.M. Volfkovich, and A. Sakars. Capillary pressure and hydrophilic porosity in gas diffusion layers for polymer electrolyte fuel cells. *J. Power Sources*, 156(2):375–387, 2006.

[GFP+06] J.T. Gostick, M.W. Fowler, M.D. Pritzker, M.A. Ioannidis, and L.M. Behra. In-plane and through-plane gas permeability of carbon fiber electrode backing layers. *J. Power Sources*, 162(1):228–238, 2006.

[GJL+03] P. Gode, F. Jaouen, G. Lindbergh, A. Lundblad, and G. Sundholm. Influence of the composition on the structure and electrochemical characteristics of the PEFC cathode. *Electrochim. Acta*, 48(28):4175–4187, 2003.

[GLS02] P. Gode, G. Lindbergh, and G. Sundholm. In-situ measurements of gas permeability in fuel cell membranes using a cylindrical microelectrode. *J. Electroanal. Chem.*, 518(2):115–122, 2002.

[HL01] C. Hitz and A. Lasia. Experimental study and modeling of impedance of the her on porous Ni electrodes. *J. Electroanal. Chem.*, 500(1-2):213–222, 2001.

[HMT94] James T. Hinatsu, Minoru Mizuhata, and Hiroyasu Takenaka. Water uptake of perfluorosulfonic acid membranes from liquid water and water vapor. *J. Electrochem. Soc.*, 141(6):1493–1498, 1994.

[HPK08] D. Harvey, J.G. Pharoah, and K. Karan. A comparison of different approaches to modelling the PEMFC catalyst layer. *J. Power Sources*, 179(1):209–219, 2008.

[Hun01] R.J. Hunter. *Foundations of Colloid Science*. Oxford University Press Inc., New York, 2001.

[HWO+] Vicky Mei Wen Huang, Shao-Ling Wu, Mark E. Orazem, Nadine Pébère, Bernard Tribollet, and Vincent Vivier. Local Electrochemical Impedance Spectroscopy: a Review and Some Recent Developments. *Electrochim. Acta*, In Press, Accepted Manuscript.

[IJL+02] J. Ihonen, F. Jaouen, G. Lindbergh, A. Lundblad, and G. Sundholm. Investigation of mass-transport limitations in the solid polymer fuel cell cathode. II. Experimental. *J. Electrochem. Soc.*, 149(4):A448–A454, 2002.

[IML04] J. Ihonen, M. Mikkola, and G. Lindbergh. Flooding of gas diffusion backing in PEFCs: Physical and electrochemical characterization. *J. Electrochem. Soc.*, 151(8):A1152–A1161, 2004.

[IPSV00] G. Inzelt, M. Pineri, J.W. Schultze, and M.A. Vorotyntsev. Electron and proton conducting polymers: Recent developments and prospects. *Electrochim. Acta*, 45(15-16):2403–2421, 2000.

[JCD05] N.H. Jalani, P. Choi, and R. Datta. TEOM: A novel technique for investigating sorption in proton-exchange membranes. *J. Membr. Sci.*, 254(1-2):31–38, 2005.

[JL03] F. Jaouen and G. Lindbergh. Transient techniques for investigating mass-transport limitations in gas diffusion electrodes. I. Modeling the PEFC cathode. *J. Electrochem. Soc.*, 150(12):A1699–A1710, 2003.

[JLS02] F. Jaouen, G. Lindbergh, and G. Sundholm. Investigation of mass-transport limitations in the solid polymer fuel cell cathode. I. Mathematical model. *J. Electrochem. Soc.*, 149(4):A437–A447, 2002.

[JLW03] F. Jaouen, G. Lindbergh, and K. Wiezell. Transient techniques for investigating mass-transport limitations in gas diffusion electrodes. II. Experimental characterization of the PEFC cathode. *J. Electrochem. Soc.*, 150(12):A1711–A1717, 2003.

[JOPT06] J.-B. Jorcin, M.E. Orazem, N. Pébère, and B. Tribollet. CPE analysis by local electrochemical impedance spectroscopy. *Electrochim. Acta*, 51(8-9):1473–1479, 2006.

[JS65] M.F.L. Johnson and W.E. Stewart. Pore structure and gaseous diffusion in solid catalysts. *J. Catal.*, 4(2):248–252, 1965.

[Ker01] J.A. Kerres. Development of ionomer membranes for fuel cells. *J. Membr. Sci.*, 185(1):3–27, 2001.

[KJN09] A. Kirubakaran, Shailendra Jain, and R.K. Nema. A review on fuel cell technologies and power electronic interface. *Renewable and Sustainable Energy Reviews*, 13(9):2430–2440, December 2009.

[KKL$^+$02] C.S. Kong, D.-Y. Kim, H.-K. Lee, Y.-G. Shul, and T.-H. Lee. Influence of pore-size distribution of diffusion layer on mass-transport problems of proton exchange membrane fuel cells. *J. Power Sources*, 108(1-2):185–191, 2002.

[KL09] S.G. Kandlikar and Z. Lu. Fundamental research needs in combinedwater and thermal management within a proton exchange membrane fuel cell stack under normal and cold-start conditions. *Journal of Fuel Cell Science and Technology*, 6(4):0440011–04400113, 2009.

[KLSC95] Junbom Kim, Seong-Min Lee, Supramaniam Srinivasan, and Charles E. Chamberlin. Modeling of proton exchange membrane fuel cell performance with an empirical equation. *J. Electrochem. Soc.*, 142(8):2670–2674, 1995.

[KMIY10] Masanobu Kumagai, Seung-Taek Myung, Takuma Ichikawa, and Hitoshi Yashiro. Evaluation of polymer electrolyte membrane fuel cells by electrochemical impedance spectroscopy under different operation conditions and corrosion. *J. Power Sources*, 195(17):5501–5507, September 2010.

[KPK03] C.-H. Kim, S.-I. Pyun, and J.-H. Kim. An investigation of the capacitance dispersion on the fractal carbon electrode with edge and basal orientations. *Electrochim. Acta*, 48(23):3455–3463, 2003.

[KPSS04] K.-D. Kreuer, S.J. Paddison, E. Spohr, and M. Schuster. Transport in proton conductors for fuel-cell applications: Simulations, elementary reactions, and phenomenology. *Chemical Reviews*, 104(10):4637–4678, 2004.

[KSP04] H. Kim, N.P. Subramanian, and B.N. Popov. Preparation of PEM fuel cell electrodes using pulse electrodeposition. *J. Power Sources*, 138(1-2):14–24, 2004.

[Kul03] A.A. Kulikovsky. Quasi-3D modeling of water transport in polymer electrolyte fuel cells. *J. Electrochem. Soc.*, 150(11):A1432–A1439, 2003.

[KW97] R. Krishna and J.A. Wesselingh. Review article number 50: The Maxwell-Stefan approach to mass tranfer. *Chem. Eng. Sci.*, 52(6):861–911, 1997.

[LAC+09] O. Lottin, B. Antoine, T. Colinart, S. Didierjean, G. Maranzana, C. Moyne, and J. Ramousse. Modelling of the operation of Polymer Exchange Membrane Fuel Cells in the presence of electrodes flooding. *International Journal of Thermal Sciences*, 48(1):133–145, 2009.

[Las99] A. Lasia. *Electrochemical Impedance Spectroscopy and Its Applications, Modern Aspects of Electrochemistry*, volume 32. B. E. Conway, J. Bockris, and R. White, Edts., Kluwer Academic/Plenum Publishers, New York, 1999.

[LCAH06] J.-M. Le Canut, R.M. Abouatallah, and D.A. Harrington. Detection of membrane drying, fuel cell flooding, and anode catalyst poisoning on PEMFC stacks by electrochemical impedance spectroscopy. *J. Electrochem. Soc.*, 153(5):A857–A864, 2006.

[LD03] J. Larminie and A. Dicks. *Fuel Cell Systems Explained*. John Wiley and Sons Ltd, England, ISBN: 978-0-470-84857-9, 2003.

[LE08] J. Liu and M. Eikerling. Model of cathode catalyst layers for polymer electrolyte fuel cells: The role of porous structure and water accumulation. *Electrochim. Acta*, 53(13):4435–4446, 2008.

[LHVN04] G. Lin, W. He, and T. Van Nguyen. Modeling liquid water effects in the gas diffusion and catalyst layers of the cathode of a PEM fuel cell. *J. Electrochem. Soc.*, 151(12):A1999–A2006, 2004.

[LHVZM99] W.-K. Lee, C.-H. Ho, J.W. Van Zee, and M. Murthy. Effects of compression and gas diffusion layers on the performance of a PEM fuel cell. *J. Power Sources*, 84(1):45–51, 1999.

[LM04] S. Litster and G. McLean. PEM fuel cell electrodes. *J. Power Sources*, 130(1-2):61–76, 2004.

[LMM+98] S.J. Lee, S. Mukerjee, J. McBreen, Y.W. Rho, Y.T. Kho, and T.H. Lee. Effects of Nafion impregnation on performances of PEMFC electrodes. *Electrochim. Acta*, 43(24):3693–3701, 1998.

[LPS+99] F. Lufrano, E. Passalacqua, G. Squadrito, A. Patti, and L. Giorgi. Improvement in the diffusion characteristics of low Pt-loaded electrodes for PEFCs. *J. Appl. Electrochem.*, 29(4):445–448, 1999.

[LPZ99] M. Laporta, M. Pegoraro, and L. Zanderighi. Perfluorosulfonated membrane (Nafion): FT-IR study of the state of water with increasing humidity. *Phys. Chem. Chem. Phys.*, 1(19):4619–4628, 1999.

[LRWW99] J.C. Lagarias, J.A. Reeds, M.H. Wright, and P.E. Wright. Convergence properties of the Nelder-Mead simplex method in low dimensions. *SIAM Journal on Optimization*, 9(1):112–147, 1999.

[LSVZ03] W.-K. Lee, S. Shimpalee, and J.W. Van Zee. Verifying predictions of water and current distributions in a serpentine flow field polymer electrolyte membrane fuel cell. *J. Electrochem. Soc.*, 150(3):A341–A348, 2003.

[Mac06] D.D. MacDonald. Reflections on the history of electrochemical impedance spectroscopy. *Electrochim. Acta*, 51(8-9):1376–1388, 2006.

[Mar04] N. Martz. *Strukturelle und elecktrochemische Charakterisierung von Pt/X-Katalysatoren für Membran-Brennstoffzellen*. PhD thesis, Technische Universität Darmstadt, 2004.

[MBK05] A.-K. Meland, D. Bedeaux, and S. Kjelstrup. A Gerischer phase element in the impedance diagram of the polymer electrolyte membrane fuel cell anode. *J. Phys. Chem. B*, 109(45):21380–21388, 2005.

[MBZ+08] M. Mathias, D. Baker, J. Zhang, Y. Liu, and W. Gu. Frontiers in application of impedance diagnostics to H_2-fed polymer electrolyte fuel cells. In *ECS Transactions*, volume 13, pages 129–152, General Motors - Fuel Cell Activities, 30500 Mound Road, Warren, MI 48090, United States, 2008.

[ME04] F. Meier and G. Eigenberger. Transport parameters for the modelling of water transport in ionomer membranes for PEM-fuel cells. *Electrochim. Acta*, 49(11):1731–1742, 2004.

[MHM94] O.J. Murphy, G.D. Hitchens, and D.J. Manko. High power density proton-exchange membrane fuel cells. *J. Power Sources*, 47(3):353–368, 1994.

[MK07] A.-K. Meland and S. Kjelstrup. Three steps in the anode reaction of the polymer electrolyte membrane fuel cell. Effect of CO. *J. Electroanal. Chem.*, 610(2):171–178, 2007.

[MKB06] A.-K. Meland, S. Kjelstrup, and D. Bedeaux. Rate limiting proton hydration in the anode of the polymer electrolyte membrane fuel cell. *J. Membr. Sci.*, 282(1-2):96–108, 2006.

[MLC+08] G. Maranzana, O. Lottin, T. Colinart, S. Chupin, and S. Didierjean. A multi-instrumented polymer exchange membrane fuel cell: Observation of the in-plane non-homogeneities. *J. Power Sources*, 180(2):748–754, 2008.

[MM04] K.A. Mauritz and R.B. Moore. State of understanding of Nafion. *Chemical Reviews*, 104(10):4535–4585, 2004.

[MMB05] R. Makharia, M.F. Mathias, and D.R. Baker. Measurement of catalyst layer electrolyte resistance in PEFCs using electrochemical impedance spectroscopy. *J. Electrochem. Soc.*, 152(5):A970–A977, 2005.

[MMD+10a] J. Mainka, G. Maranzana, J. Dillet, S. Didierjean, and O. Lottin. Effect of oxygen depletion along the air channel of a PEMFC on the warburg diffusion impedance. *J. Electrochem. Soc.*, 157(11):B1561–B1568, 2010.

[MMD+10b] J. Mainka, G. Maranzana, J. Dillet, S. Didierjean, and O. Lottin. Origin of diffusion impedance at the cathode of a Proton Exchange Membrane Fuel Cell. In Detlef Stolten and Thomas Grube, editors, *18th World Hydrogen Energy Conference 2010 - WHEC 2010 : Parallel Sessions Book 1: Fuel Cell Basics / Fuel Infrastructures*, Schriften des Forschungszentrums Jülich / Energy & Environment, pages 37–44. Forschungszentrum Jülich GmbH, Zentralbibliothek, Verlag, Essen (Germany), May 16-21 2010. ISBN: 978-3-89336-651-4 ISSN: 1866-1793.

[MMD+10c] G. Maranzana, C. Moyne, J. Dillet, S. Didierjean, and O. Lottin. About internal currents during start-up in proton exchange membrane fuel cell. *J. Power Sources*, 195(18):5990–5995, 2010.

[MMGL02] F. Maillard, M. Martin, F. Gloaguen, and J.-M. Léger. Oxygen electroreduction on carbon-supported platinum catalysts. Particle-size effect on the tolerance to methanol competition. *Electrochim. Acta*, 47(21):3431–3440, 2002.

[NK03] J.H. Nam and M. Kaviany. Effective diffusivity and water-saturation distribution in single- and two-layer PEMFC diffusion medium. *International Journal of Heat and Mass Transfer*, 46(24):4595–4611, 2003.

[NNAO09] Soshin Nakamura, Hisao Nishikawa, Tsutomu Aoki, and Yasuji Ogami. The diffusion overpotential increase and appearance of overlapping arcs on the Nyquist plots in the low humidity temperature test conditions of polymer electrolyte fuel cell. *J. Power Sources*, 186(2):278–285, January 2009.

[NP85] L. Nyikos and T. Pajkossy. Fractal dimension and fractional power frequency-dependent impedance of blocking electrodes. *Electrochim. Acta*, 30(11):1533–1540, 1985.

[OCCP06] R. O'Hayre, S.-W. Cha, W. Colella, and F. B. Prinz. *Fuel Cell Fundamentals*. John Wiley and Sons, New York, ISBN-13: 978-0471741480, 2006.

[OLCP02] R. O'Hayre, S.-J. Lee, S.-W. Cha, and F.B. Prinz. A sharp peak in the performance of sputtered platinum fuel cells at ultra-low platinum loading. *J. Power Sources*, 109(2):483–493, 2002.

[OT08] Mark E. Orazem and Bernard Tribollet. An integrated approach to electrochemical impedance spectroscopy. *Electrochim. Acta*, 53(25):7360–7366, October 2008.

[OXT96] T. Okada, G. Xie, and Y. Tanabe. Theory of water management at the anode side of polymer electrolyte fuel cell membranes. *J. Electroanal. Chem.*, 413(1-2):49–65, 1996.

[PBSM11] L.C. Pérez, L. Brandão, J.M. Sousa, and A. Mendes. Segmented polymer electrolyte membrane fuel cells-A review. *Renewable and Sustainable Energy Reviews*, 15(1):169–185, 2011.

[PMS91] Arvind Parthasarathy, Charles R. Martin, and Supramaniam Srinivasan. Investigations of the O_2 Reduction Reaction at the Platinum/Nafion® Interface Using a Solid-State Electrochemical Cell. *J. Electrochem. Soc.*, 138(4):916–921, April 1991.

[POT+98] V.A. Paganin, C.L.F. Oliveira, E.A. Ticianelli, T.E. Springer, and E.R. Gonzalez. Modelistic interpretation of the impedance response of a polymer electrolyte fuel cell. *Electrochim. Acta*, 43(24):3761–3766, 1998.

[PSAM92] Arvind Parthasarathy, Supramaniam Srinivasan, A.John Appleby, and Charles R. Martin. Temperature dependence of the electrode kinetics of oxygen reduction at the platinum/nafion® interface - a microelectrode investigation. *J. Electrochem. Soc.*, 139(9):2530–2537, 1992.

[PSL+01] E. Passalacqua, G. Squadrito, F. Lufrano, A. Patti, and L. Giorgi. Effects of the diffusion layer characteristics on the performance of polymer electrolyte fuel cell electrodes. *J. Appl. Electrochem.*, 31(4):449–454, 2001.

[PW04a] U. Pasaogullari and C.-Y. Wang. Two-phase transport and the role of microporous layer in polymer electrolyte fuel cells. *Electrochim. Acta*, 49(25):4359–4369, 2004.

[PW04b] U. Pasaogullari and C.Y. Wang. Liquid Water Transport in Gas Diffusion Layer of Polymer Electrolyte Fuel Cells. *J. Electrochem. Soc.*, 151(3):A399–A406, 2004.

[PWC05] U. Pasaogullari, C.-Y. Wang, and K.S. Chen. Two-phase transport in polymer electrolyte fuel cells with bilayer cathode gas diffusion media. *J. Electrochem. Soc.*, 152(8):A1574–A1582, 2005.

[QK02a] Z. Qi and A. Kaufman. Enhancement of PEM fuel cell performance by steaming or boiling the electrode. *J. Power Sources*, 109(1):227–229, 2002.

[QK02b] Z. Qi and A. Kaufman. Improvement of water management by a microporous sublayer for PEM fuel cells. *J. Power Sources*, 109(1):38–46, 2002.

[RAB+09] H. Rabat, C. Andreazza, P. Brault, A. Caillard, F. Béguin, C. Charles, and R. Boswell. Carbon/platinum nanotextured films produced by plasma sputtering. *Carbon*, 47(1):209–214, 2009.

[Rai90] I.D. Raistrick. Impedance studies of porous electrodes. *Electrochim. Acta*, 35(10):1579–1586, 1990.

[Ram05] J. Ramousse. *Transferts couples masse-charge-chaleur dans une cellule de pile à combustible à membrane polymère*. PhD thesis, INPL-LEMTA, Nancy, 2005.

[Ran47] J.E.B. Randles. Kinetics of rapid electrode reactions. *Discussion of the Faraday Society*, **1**:11, 1947.

[RDL+05] J. Ramousse, J. Deseure, O. Lottin, S. Didierjean, and D. Maillet. Modelling of heat, mass and charge transfer in a PEMFC single cell. *J. Power Sources*, 145(2):416–427, 2005.

[RDLM08] J. Ramousse, S. Didierjean, O. Lottin, and D. Maillet. Estimation of the effective thermal conductivity of carbon felts used as PEMFC Gas Diffusion Layers. *International Journal of Thermal Sciences*, 47(1):1–6, 2008.

[Reu08] M. Reum. *Sub-millimeter resolved measurement of current density and membrane resistance in Polymer Electrolyte Fuel Cells (PEMFC)*. PhD thesis, Swiss Federal Institue of Technology Zürich (ETHZ), 2008.

[RL01] A. Rowe and X. Li. Mathematical modeling of proton exchange membrane fuel cells. *J. Power Sources*, 102(1-2):82–96, 2001.

[RLDM09] J. Ramousse, O. Lottin, S. Didierjean, and D. Maillet. Heat sources in proton exchange membrane (PEM) fuel cells. *J. Power Sources*, 192(2):435–441, 2009.

[RO07] S.K. Roy and M.E. Orazem. Error analysis of the impedance response of PEM fuel cells. *J. Electrochem. Soc.*, 154(8):B883–B891, 2007.

[RO08] S.K. Roy and M.E. Orazem. Guidelines for evaluation of error structure for impedance response of Polymer Electrolyte Membrane (PEM) fuel cells. In *ECS Transactions*, volume 13, pages 153–169, Department of Chemical Engineering, University of Florida, Gainesville, FL 32611, 2008.

[RO09] S.K. Roy and M.E. Orazem. Graphical estimation of interfacial capacitance of PEM fuel cells from impedance measurements. *J. Electrochem. Soc.*, 156(2):B203–B209, 2009.

[ROT07] S.K. Roy, M.E. Orazem, and B. Tribollet. Interpretation of low-frequency inductive loops in PEM fuel cells. *J. Electrochem. Soc.*, 154(12):B1378–B1388, 2007.

[RRGD02] L. Rubatat, A.L. Rollet, G. Gebel, and O. Diat. Evidence of elongated polymeric aggregates in Nafion. *Macromolecules*, 35(10):4050–4055, 2002.

[RSD+10] S. Rodat, S. Sailler, F. Druart, P.-X. Thivel, Y. Bultel, and P. Ozil. EIS measurements in the diagnosis of the environment within a PEMFC stack. *J. Appl. Electrochem.*, 40(5):911–920, 2010.

[Rub03] L. Rubatat. *Nouveau modèle structural des membranes Nafion®, polymère de référence pour l'application pile à combustible basse température*. PhD thesis, Université Joseph Fourier - Grenoble I, 2003.

[RUKD08] M.A. Rubio, A. Urquia, R. Kuhn, and S. Dormido. Electrochemical parameter estimation in operating proton exchange membrane fuel cells. *J. Power Sources*, 183(1):118–125, 2008.

[SB58] John C. Slattery and R. Byron Bird. Calculation of the diffusion coefficient of dilute gases and of the self-diffusion coefficient of dense gases. *AIChE J.*, 4(2):137–142, 1958.

[SBWS08] I.A. Schneider, M.H. Bayer, A. Wokaun, and G.G. Scherer. Impedance response of the proton exchange membrane in polymer electrolyte fuel cells. *J. Electrochem. Soc.*, 155(8):B783–B792, 2008.

[Sch03] P. Schroeder. Über Erstarrungs- unde Quellungserscheinungen von Gelantine. *Z. Phys. Chem.*, 45:57, 1903.

[SCL01] J.M. Song, S.Y. Cha, and W.M. Lee. Optimal composition of polymer electrolyte fuel cell electrodes determined by the AC impedance method. *J. Power Sources*, 94(1):78–84, 2001.

[SDFP04] R.F. Silva, M. De Francesco, and A. Pozio. Tangential and normal conductivities of Nafion® membranes used in polymer electrolyte fuel cells. *J. Power Sources*, 134(1):18–26, 2004.

[SENVS03] N.P. Siegel, M.W. Ellis, D.J. Nelson, and M.R. Von Spakovsky. Single domain PEMFC model based on agglomerate catalyst geometry. *J. Power Sources*, 115(1):81–89, 2003.

[SENVS04] N.P. Siegel, M.W. Ellis, D.J. Nelson, and M.R. Von Spakovsky. A two-dimensional computational model of a PEMFC with liquid water transport. *J. Power Sources*, 128(2):173–184, 2004.

[SES96] Y. Sone, P. Ekdunge, and D. Simonsson. Proton conductivity of Nafion 117 as measured by a four-electrode AC impedance method. *J. Electrochem. Soc.*, 143(4):1254–1259, 1996.

[SFK+07] I.A. Schneider, S.A. Freunberger, D. Kramer, A. Wokaun, and G.G. Scherer. Oscillations in gas channels. *J. Electrochem. Soc.*, 154(4):B383–B388, 2007.

[SFM+07] V.R. Stamenkovic, B. Fowler, B.S. Mun, G. Wang, P.N. Ross, C.A. Lucas, and N.M. Markovic. Improved oxygen reduction activity on $Pt_3Ni(111)$ via increased surface site availability. *Science*, 315(5811):493–497, 2007.

[Siga] Sigracet®. http://www.servovision.com/fuel_cell_components/gdl_10.pdf.

[Sigb] Sigracet®. http://www.servovision.com/fuel_cell_components/gdl_24_25.pdf.

[SKVK09] K. Saminathan, V. Kamavaram, V. Veedu, and A.M. Kannan. Preparation and evaluation of electrodeposited platinum nanoparticles on in situ carbon nanotubes grown carbon paper for proton exchange membrane fuel cells. *Int. J. Hydrogen Energy*, 34(9):3838–3844, 2009.

[SKWS07] I.A. Schneider, D. Kramer, A. Wokaun, and G.G. Scherer. Oscillations in gas channels: II. Unraveling the characteristics of the low frequency loop in air-fed PEFC impedance spectra. *J. Electrochem. Soc.*, 154(8):B770–B782, 2007.

[SM09] V.R. Stamenkovic and N.M. Markovic. Oxygen reduction on platinum bimetallic alloy catalysts. In W. Vielstich, H.A. Gasteiger, and H. Yokokawa, editors, *Handbook of Fuel Cells - Fundamentals, Technology and Applications*, volume 5, page 18. John Wiley and Sons, Ltd, Chichester, 2009.

[SOH+07] M.M. Saleh, T. Okajima, M. Hayase, F. Kitamura, and T. Ohsaka. Exploring the effects of symmetrical and asymmetrical relative humidity on the performance of H_2/air PEM fuel cell at different temperatures. *J. Power Sources*, 164(2):503–509, 2007.

[SPK05a] W. Sun, B.A. Peppley, and K. Karan. An improved two-dimensional agglomerate cathode model to study the influence of catalyst layer structural parameters. *Electrochim. Acta*, 50(16-17):3359–3374, 2005.

[SPK05b] W. Sun, B.A. Peppley, and K. Karan. Modeling the Influence of GDL and flow-field plate parameters on the reaction distribution in the PEMFC cathode catalyst layer. *J. Power Sources*, 144(1):42–53, 2005.

[SR89] T.E. Springer and I.D. Raistrick. Electrical impedance of a pore wall for the flooded-agglomerate model of porous gas-diffusion electrodes. *J. Electrochem. Soc.*, 136(6):1594–1603, 1989.

[SSF+08] D.U. Sauer, T. Sanders, B. Fricke, T. Baumhöfer, K. Wippermann, A.A. Kulikovsky, H. Schmitz, and J. Mergel. Measurement of the current distribution in a direct methanol fuel cell-Confirmation of parallel galvanic and electrolytic operation within one cell. *J. Power Sources*, 176(2):477–483, 2008.

[SSP+10] N. Saibuathong, Y. Saejeng, K. Pruksathorn, M. Hunsom, and N. Tantavichet. Catalyst electrode preparation for PEM fuel cells by electrodeposition. *J. Appl. Electrochem.*, 40:903–910, 2010.

[SVD81] D.B. Sepa, M.V. Vojnovic, and A. Damjanovic. Reaction intermediates as a controlling factor in the kinetics and mechanism of oxygen reduction at platinum electrodes. *Electrochim. Acta*, 26(6):781–793, 1981.

[SWG93] T.E. Springer, M.S. Wilson, and S. Gottesfeld. Modeling and experimental diagnostics in polymer electrolyte fuel cells. *J. Electrochem. Soc.*, 140(12):3513–3526, 1993.

[SWS+11] K. Seidenberger, F. Wilhelm, T. Schmitt, W. Lehnert, and J. Scholta. Estimation of water distribution and degradation mechanisms in polymer electrolyte membrane fuel cell gas diffusion layers using a 3D Monte Carlo model. *J. Power Sources*, 196(12):5317–5324, June 2011.

[SZG91] T.E. Springer, T.A. Zawodzinski, and S. Gottesfeld. Polymer electrolyte fuel cell model. *J. Electrochem. Soc.*, 138(8):2334–2342, 1991.

[SZWG96] T.E. Springer, T.A. Zawodzinski, M.S. Wilson, and S. Gottesfeld. Characterization of polymer electrolyte fuel cells using AC impedance spectroscopy. *J. Electrochem. Soc.*, 143(2):587–599, 1996.

[TCB00] V. Tricoli, N. Carretta, and M. Bartolozzi. Comparative investigation of proton and methanol transport in fluorinated ionomeric membranes. *J. Electrochem. Soc.*, 147(4):1286–1290, 2000.

[TDRS88] E.A. Ticianelli, C.R. Derouin, A. Redondo, and S. Srinivasan. Methods to advance technology of proton exchange membrane fuel cells. *J. Electrochem. Soc.*, 135(9):2209–2214, 1988.

[TI] Inc Toray Industries. www.torayca.com/index2.html.

[TMD+11] A. Thomas, G. Maranzana, S. Didierjean, O. Lottin, J. Dillet, and A. Lamibrac. Thermal management of a Proton Exchange Membrane Fuel Cell. In *Proceedings of the Fundamentals and Developments of Fuel Cells Conference 2011*. 19th-21st January 2011, Grenoble, France (ISBN : 978-2-7566-2970-7), 2011.

[TMTD00] T. Thampan, S. Malhotra, H. Tang, and R. Datta. Modeling of conductive transport in proton-exchange membranes for fuel cells. *J. Electrochem. Soc.*, 147(9):3242–3250, 2000.

[Tor02] S. Torquato. *Random Heterogeneous Materials: Microstructure and Macroscopic Properties*. Springer, ISBN-13: 978-0387951676, 2002.

[UW04] S. Um and C.Y. Wang. Three-dimensional analysis of transport and electrochemical reactions in polymer electrolyte fuel cells. *J. Power Sources*, 125(1):40–51, 2004.

[VAT92] N.R.K. Vilambi, E.B. Anderson, and E.J. Taylor. High utilization supported catalytic metal-containing gas-diffusion electrode, process for making it, and and cells utilizing it, 1992.

[VDHRD04] P.C. Van Der Heijden, L. Rubatat, and O. Diat. Orientation of drawn Nafion at molecular and mesoscopic scales. *Macromolecules*, 37(14):5327–5336, 2004.

[Ver94] Mark W. Verbrugge. Selective electrodeposition of catalyst within membrane electrode structures. *J. Electrochem. Soc.*, 141(1):46–53, 1994.

[VK04] P.J.S. Vie and S. Kjelstrup. Thermal conductivities from temperature profiles in the polymer electrolyte fuel cell. *Electrochim. Acta*, 49(7):1069–1077, 2004.

[Wag02] N. Wagner. Characterization of membrane electrode assemblies in polymer electrolyte fuel cells using a.c. impedance spectroscopy. *J. Appl. Electrochem.*, 32(8):859–863, 2002.

[War99] E. Warburg. Über das Verhalten sogenannter unpolarisirbarer Elektroden gegen Wechselstrom. *Annalen der Physik und Chemie*, **69**:493–499, March 1899.

[WBB+04] M.V. Williams, E. Begg, L. Bonville, H.R. Kunz, and J.M. Fenton. Characterization of gas diffusion layers for PEMFC. *J. Electrochem. Soc.*, 151(8):A1173–A1180, 2004.

[WS03] N. Wagner and M. Schulze. Change of electrochemical impedance spectra during CO poisoning of the Pt and Pt-Ru anodes in a membrane fuel cell (PEFC). *Electrochim. Acta*, 48(25-26):3899–3907, 2003.

[WSML98] N. Wagner, W. Schnurnberger, B. Müller, and M. Lang. Electrochemical impedance spectra of solid-oxide fuel cells and polymer membrane fuel cells. *Electrochim. Acta*, 43(24):3785–3793, 1998.

[WSONL05] H. Wendt, E.V. Spinacé, A. Oliveira Neto, and M. Linardi. Electrocatalysis and electrocatalysts for low temperature fuel cells: Fundamentals, state of the art, research and development. *Quim. Nova*, 28(6):1066–1075, 2005.

[WYW+08] J. Wu, X.Z. Yuan, H. Wang, M. Blanco, J.J. Martin, and J. Zhang. Diagnostic tools in PEM fuel cell research: Part I Electrochemical techniques. *Int. J. Hydrogen Energy*, 33(6):1735–1746, 2008.

[XSA+06] Zhong Xie, Chaojie Song, Bernhard Andreaus, Titichai Navessin, Zhiqing Shi, Jiujun Zhang, and Steven Holdcroft. Discrepancies in the Measurement of Ionic Conductivity of PEMs Using Two- and Four-Probe AC Impedance Spectroscopy. *J. Electrochem. Soc.*, 153(10):E173–E178, October 2006.

[YCP+08] S.J. Yoo, Y.-H. Cho, H.-S. Park, J.K. Lee, and Y.-E. Sung. High utilization of Pt nanocatalysts fabricated using a high-pressure sputtering technique. *J. Power Sources*, 178(2):547–553, 2008.

[YW08] Q. Yan and J. Wu. Modeling of single catalyst particle in cathode of PEM fuel cells. *Energy Conversion and Management*, 49(8):2425–2433, 2008.

[YWCSZ07] X. Yuan, H. Wang, J. Colin Sun, and J. Zhang. AC impedance technique in PEM fuel cell diagnosis-A review. *Int. J. Hydrogen Energy*, 32(17):4365–4380, 2007.

[YY85] R.S. Yeo and H.L. Yaeger. Structural and transport properties of perfluorinated ion-exchange membranes. In *Modern Aspects of Electrochemistry*, volume 16, chapter 6, pages 437–504. Conway, B.E. and White, R.E. and Bockris, J. O'M., 1985.

[ZDR+93] Thomas A. Zawodzinski, Charles Derouin, Susan Radzinski, Ruth J. Sherman, Van T. Smith, Thomas E. Springer, and Shimshon Gottesfeld. Water uptake by and transport through Nafion® 117 membranes. *J. Electrochem. Soc.*, 140(4):1041–1047, 1993.

[ZJSD+93] Thomas A. Zawodzinski Jr., Thomas E. Springer, John Davey, Roger Jestel, Cruz Lopez, Judith Valerio, and Shimshon Gottesfeld. Comparative study of water uptake by and transport through ionomeric fuel cell membranes. *J. Electrochem. Soc.*, 140(7):1981–1985, 1993.

[ZRI04] J.M. Zalc, S.C. Reyes, and E. Iglesia. The effects of diffusion mechanism and void structure on transport rates and tortuosity factors in complex porous structures. *Chem. Eng. Sci.*, 59(14):2947–2960, 2004.

[ZTS+06] J. Zhang, Y. Tang, C. Song, J. Zhang, and H. Wang. PEM fuel cell open circuit voltage (OCV) in the temperature range of 23°C to 120 °C. *J. Power Sources*, 163(1 SPEC. ISS.):532–537, 2006.

[ZX95] Y. Zhang and Z. Xu. Atomic radii of noble gas elements in condensed phases. *Am. Mineral.*, 80:670–675, 1995.

[ZZZ+06] X. Zhu, H. Zhang, Y. Zhang, Y. Liang, X. Wang, and B. Yi. An ultrathin self-humidifying membrane for PEM fuel cell application: Fabrication, characterization, and experimental analysis. *J. Phys. Chem. B*, 110(29):14240–14248, 2006.

Abstract

The aim of this Ph.D thesis is to contribute to a better understanding of the low frequency loop in impedance spectra of H_2/air fed PEMFC and to bring information about the main origin(s) of the oxygen transport impedance through the porous media of the cathode via locally resolved EIS.

Different expressions of the oxygen transport impedance alternative to the one-dimensional finite Warburg element are proposed. They account for phenomena occurring in the directions perpendicular and parallel to the electrode plane that are not considered usually: convection through the GDL and along the channel, finite proton conduction in the catalyst layer, and oxygen depletion between the cathode inlet and outlet. A special interest is brought to the oxygen concentration oscillations induced by the AC measuring signal that propagate along the gas channel and to their impact on the local impedance downstream. These expressions of the oxygen transport impedance are used in an equivalent electrical circuit modeling the impedance of the whole cell.

Experimental results are obtained with instrumented and segmented cells designed and built in our group. Their confrontation with numerical results allows to identify parameters characterizing the physical and electrochemical processes in the MEA.

Keywords

Fuel cells, PEMFC, local electrochemical impedance spectroscopy, segmented cell, porous media, modeling, gas diffusion electrode.

Résumé

Cette thèse apporte des éléments de compréhension de la boucle basse fréquence des spectres d'impédance de PEMFC H_2/air.

Différentes expressions de l'impédance de transport de l'oxygène alternatives à l'élément de Warburg sont proposées. Elles prennent en compte des phénomènes de transport dans les directions perpendiculaire et parallèle à l'électrode qui sont habituellement négligés: convection à travers la GDL et le long du canal d'air, résistance protonique de la couche catalytique et appauvrissement en oxygène entre l'entrée et la sortie de la cellule. Une attention particulière est portée sur les oscillations de concentration induites par le signal de mesure qui se propagent le long du canal d'air. Ces différentes expressions de l'impédance de transport de l'oxygène sont utilisées dans un circuit électrique équivalent destiné à simuler l'impédance de la cellule.

Une comparaison entre résultats expérimentaux et théoriques permet d'identifier les paramètres du circuit électrique. A partir de ces paramètres, il est possible d'analyser les mécanismes physiques et électro-chimiques qui se produisent dans la pile, ainsi que de tirer certaines conclusions sur les phénomènes de transport de l'oxygène dans les milieux poreux de la cathode. Pour cela, nous avons utilité des cellules segmentées et instrumentées conçues et fabriquées au laboratoire.

Mots-clés

Pile à combustible, PEMFC, spectroscopie d'impédance locale, cellule instrumentée, milieux poreux, modélisation, cathode.